THE UNIVERSITY *of* EDINBURGH

Modelling porosity and permeability in early cemented carbonates

Aleksandra Maria Hosa

THE UNIVERSITY *of* EDINBURGH

A Thesis Submitted for the Degree of Doctor of Philosophy

School of GeoSciences
University of Edinburgh

2016

Declaration

I declare that this thesis has been composed solely by myself and that it has not been submitted, either in whole or in part, in any previous application for a degree. Except where otherwise acknowledged, the work presented is entirely my own.

Aleksandra Hosa

May 2016

Abstract

Cabonate-hosted hydrocarbon reservoirs will play an increasingly important role in the energy supply, as 60% of the world's remaining hydrocarbon resources are trapped within carbonate rocks. The properties of carbonates are controlled by deposition and diagenesis, which includes calcite cementation that begins immediately after deposition and may have a strong impact on subsequent diagenetic pathways. This thesis aims to understand the impact of early calcite cementation on reservoir properties through object-based modelling and Lattice Boltzmann flow simulation to obtain permeability. A Bayesian inference framework is also developed to quantify the ability of Lattice Boltzmann method to predict the permeability of porous media.

Modelling focuses on the impact of carbonate grain type on properties of early cemented grainstones and on the examination of the theoretical changes to the morphology of the pore space. For that purpose process-based models of early cementation are developed in both 2D (Calcite2D) and 3D (Calcite3D, which also includes modelling of deposition). Both models assume the existence of two grain types: polycrystalline and monocrystalline, and two early calcite cement types specific to these grain types: isopachous and syntaxial, respectively. Of the many possible crystal forms that syntaxial cement can take, this thesis focuses on two common rhombohedral forms: a blocky form $01\bar{1}2$ and an elongated form $40\bar{4}1$.

The results of the 2D and 3D modelling demonstrate the effect of competition of growing grains for the available pore space: the more monocrystalline grains

present in the sample, the stronger this competition becomes and the lesser the impact of each individual grain on the resulting early calcite cement volume and porosity.

The synthetic samples with syntaxial cements grown of the more elongated crystal form $40\bar{4}1$ have lower porosity for the same monocrystalline grains content than synthetic samples grown following more blocky crystal form $01\bar{1}2$. Moreover, permeability at a constant porosity is reduced for synthetic samples with the form $40\bar{4}1$. Additionally, synthetic samples with form $40\bar{4}1$ exhibit greater variability in the results as this rhombohedral form is more elongated and has the potential for producing a greater volume of cement.

The results of the 2D study suggest that for samples at constant porosity the higher the proportion of monocrystalline grains are in the sample, the higher the permeability. The 3D study suggests that for samples with crystal form $01\bar{1}2$ at constant porosity the permeability becomes lower as the proportion of monocrystalline grains increase, but this impact is relatively minor. In the case of samples with crystal form $40\bar{4}1$ the results are inconclusive. This dependence of permeability on monocrystalline grains is weaker than in the 2D study, which is most probably a result of the bias of flow simulation in the 2D as well as of the treatment of the porous medium before the cement growth model is applied. The range of the permeability results in the 2D modelling may be artificially overly wide, which could lead to the dependence of permeability on sediment type being exaggerated.

Poroperm results of the 2D modelling ($10 - 8000mD$) are in reasonable agreement with the data reported for grainstones in literature ($0.1 - 5000mD$) as well as for the plug data of the samples used in modelling (porosity $22 - 27\%$, permeability $200 - 3000mD$), however permeability results at any given porosity have a wide range due to the bias inherent to the 2D flow modelling. Poroperm results in the 3D modelling ($10 - 30,000mD$) exhibit permeabilities above the range of that reported in the literature or the plug data, but the reason for that is that

the initial synthetic sediment deposit has very high permeability ($58,900mD$). However, the trend in poroperm closely resembles those reported in carbonate rocks.

As the modelling depends heavily on the use of Lattice Boltzmann method (flow simulation to obtain permeability results), a Bayesian inference framework is presented to quantify the predictive power of Lattice Boltzmann models. This calibration methodology is presented on the example of Fontainebleau sandstone. The framework enables a systematic parameter estimation of Lattice Boltzmann model parameters (in the scope of this work, the relaxation parameter τ), for the currently used calibrations of Lattice Boltzmann based on Hagen-Poiseuille law. Our prediction of permeability using the Hagen-Poiseuille calibration suggests that this method for calibration is not optimal and in fact leads to substantial discrepancies with experimental measurements, especially for highly porous complex media such as carbonates.

We proceed to recalibrate the Lattice Boltzmann model using permeability data from porous media, which results in a substantially different value of the optimal τ parameter than those used previously (0.654 here compared to 0.9). We augment our model introducing porosity-dependence, where we find that the optimal value for τ decreases for samples of higher porosity. In this new semi-empirical model one first identifies the porosity of the given medium, and on that basis choses an appropriate Lattice Boltzmann relaxation parameter. These two approaches result in permeability predictions much closer to the experimental permeability data, with the porosity-dependent case being the better of the two. Validation of this calibration method with independent samples of the same rock type yields permeability predictions that fall close to the experimental data, and again the porosity-dependent model provides better results. We thus conclude that our calibration model is a powerful tool for accurate prediction of complex porous media permeability.

Acknowledgements

First and foremost I would like to thank my sponsors: BG Group and Petrobras. Without their financial support the completion of this project would not have been possible.

I am also vary grateful to my supervisor, Rachel Wood. Not only did she take me in when I decided to discontinue my graduate study at Caltech and move back to the UK, but she also allowed me great freedom in choosing the topic of my thesis. Her help and support along the way were invaluable. I also really appreciate the fact that she allowed me to take a time off from my PhD to pursue internships (two summers at Statoil in Bergen, Norway).

I would also like to thank my second supervisor, Rink van Dijke from Heriot-Watt, with whom I conducted many constrictive discussions about various modelling approaches at the beginning of my PhD work. My great thanks go also toward Andrew Curtis, who by now is my 'honorary' supervisor. Without him the Bayesian calibration work (Chapter 6) would not have been possible.

I would like to extend very special thanks to Tony Dickson, with whom I had numerous discussions concerning calcite cementation in carbonates that were crucial in deciding modelling implementations. I would also like to thank the colleagues from the International Centre for Carbonate Reservoirs, who proved to be a very stimulating environment to work in.

I would like to thank the IT team at the School of GeoSciences for helping me with any technical problems. I would also like to thank the UK National Supercomputing Service Archer for awarding us the computational time that allowed me to simulate flow in multiple outputs of my cementation models.

I would like to thank my fellow students at the School of GeoSciences for creating a great atmosphere to work. I particularly would like to thank Sophie Harland, who was very supportive, especially in my final months of writing-up. In the grand analogy of the scientific community as a family, Sophie is my identical twin sister from whom I was separated at birth. Sister - because we are both supervised by Rachel Wood; twin - because we both started and finished our PhD studies more or less at the same time; identical - because our projects are very similar (pore-scale modelling in carbonates); separated at birth - because, sadly, due to the fact that we had different sponsors and the resulting confidentiality issues, we could not share and discuss our work to an extent we would like to. Please excuse me for this effusion, but this analogy was just too good not to put it here.

Naturally, I would like to thank my family. My parents were always very supportive in my choosing whatever I want to do in my life, even if it meant studying geology at MIT instead of something that objectively would make more sense, such as computer science (because computer science is what people go to MIT for). My sister, Asia, was pivotal in getting me to come to the University of Edinburgh in the first place (to work as a research associate in the CCS group). I fell in love with the city instantly and enjoyed the environment of the School of GeoSciences so much that I could not stay away and evacuated from Caltech after just half a year. Asia has has since moved to Paris, but I am still here. My brother, Piotr, has also been a great comfort, especially since he came to study in Glasgow 1 year after I started my PhD.

My boyfriend Panos deserves his own paragraph. I can confidently say that without him this thesis would not come to be, and it is not only because be spotted me some serious amount of computational time on various clusters when

I was desperate. He also read most of the chapters of my thesis and put in hundreds, if not thousands, of 'the' and 'a', which basically doubled my word count. He is not a native English speaker, but he has been fortunate enough that his first language *does* have the notion of articles, unlike my wretched first language (Polish). If some chapter of this thesis is disturbingly undersaturated (or oversaturated) in definite and indefinite articles, that is because Panos has not read it. However, I am not sure if I *want* to thank him, as over the past few months he has blatantly disregarded my many requests to terminate my life. He also fed me so much chocolate, when I stayed at his place in Zurich during my writing-up, that I gained a significant amount of weight, which I do not appreciate in the slightest. But custom dictates that I thank him, so there.

Contents

List of Tables

List of Figures

Chapter 1

Introduction

Carbonate-hosted hydrocarbon reservoirs will play an increasingly important role in the energy supply industry, as 60% of the world's remaining hydrocarbon resources are trapped within carbonate rocks (Sun and Sloan, 2003; Sayers, 2008), and this proportion is likely to increase. Carbonate rocks are very complex, partially due to the heterogeneity of sediment grain types, but also due to diagenesis, which in carbonates can take many divergent pathways, leading to a multitude of rock types.

The complexity of carbonate diagenesis results from various processes, involving any combination of the following mechanisms: dissolution, neomorphism and replacement of minerals, compaction of grains, and cementation (Scoffin, 1987; Tucker and Wright, 1990; Moore, 1989). Specific diagenetic pathways depend on factors occurring at the basin scale, such as the chemistry of both the rock and interstitial fluids, and conditions during burial history, such as temperature and pressure.

Diagenesis is a major control on the evolution of porosity and permeability within carbonate rocks, and so predicting diagenetic characteristics through increased

understanding of the controls is of great interest. Although diverse, carbonate-hosted hydrocarbon reservoirs have a set of common cement types, which can be used to produce geologically-guided models of cementation.

Given that carbonate rocks are often 'unique', rock modelling at the pore scale has been widely used to predict subsurface hydrocarbon reservoir rock properties such as absolute permeability, capillary pressure, and relative permeability. The undeniable advantage of synthetic rock models is that simulations are much more flexible and considerably less expensive than data obtained via experiments. Importantly, such models can be used to test hypotheses as to the impact of specific diagenetic events on flow properties.

However, while the majority of remaining hydrocarbon reserves are found within carbonate rocks, only a small portion of synthetic (or digital) rock research is dedicated to carbonates (Biswal *et al.*, 2007; Mousavi *et al.*, 2013; Okabe and Blunt, 2004; van der Land *et al.*, 2013; Harland *et al.*, 2015). This can be attributed to the complexity of carbonate rock fabrics and typically, published process-based carbonate rock models, capture only one specific type of carbonate or a specific process of formation (Mousavi *et al.*, 2013; Biswal *et al.*, 2007). Nevertheless, these models report successful prediction of rock petrophysical properties within the range of experimental data. As George E. P. Box, a mathematician and a pioneer in Bayesian inference, once stated: 'all models are wrong, but some are useful'.

1.1 Thesis Aims and Objectives

This thesis tests the following hypotheses:

- Hypothesis 1: Early cements exert a major control on porosity and permeability in carbonate grainstone rocks.

- Hypothesis 2: Grainstone sediment type, understood here as the ratio of monocrystalline to polycrystalline grains, controls the properties of early cemented grainstones.
- Hypothesis 3: Crystal form of syntaxial cement controls the properties of early cemented grainstones.
- Hypothesis 4: A Bayesian uncertainty quantification framework can provide a robust prediction for the permeability using Lattice Boltzmann method.

This thesis undertakes pore-scale rock modelling as a means to achieve an understanding as to how early diagenetic calcite cements influence the physical properties (porosity and permeability) of carbonate rocks. Also explored is the role of initial carbonate sediment type in controlling the distribution of such early calcite cements, as grain crystallinity can act as a strong influence on the type of cement seeded (Lander *et al.*, 2008). Sediment type is characterised as the ratio of monocrystalline grains (consisting of a single calcite crystal) to polycrystalline grains (consisting of multiple, often sub-resolution crystals). This thesis will focus upon early marine cements in calcite-dominated grainstones.

Grainstone fabrics were selected because they are known for having good reservoir quality (high permeability and producibility) and as such are of particular interest to hydrocarbon recovery (Lucia, 2007; Neilson *et al.*, 1998). Contrary to sandstones, where most quartz cement is precipitated by cooling, ascending formation water at burial depths of several kilometers (McBride, 1989), cementation in carbonates can begin in the marine environment just after deposition and continuing through vadose, shallow, intermediate, and deep-burial environments (Ahr, 2008). A focus on early marine cements is made as these cement types may influence subsequent diagenetic pathways (van der Land *et al.*, 2013).

Meteoric, marine and burial diagenesis may either destroy or enhance original porosity depending on compaction, cementation and dissolution. In case of early oil emplacement, specific diagenetic processes or cementation can be inhibited, so

that only cements that developed very early are present (Neilson *et al.*, 1998). In such cases it is the morphology of the pore space determined by early cementation that controls the fluid flow in the reservoir.

The two types of grains under consideration in this thesis have different types of early calcite cement associated with them (Lucia, 2007), both of which are common in reservoir rocks (Figure 1.1). Syntaxial cement, sometimes also called epitaxial (Knoerich and Mutti, 2006), is associated exclusively with monocrystalline grains, while isopachous cement is the most common early marine cement developed on polycrystalline grains (Moore, 1989). This thesis postulates that due to differences in the morphology of these cement forms, their relative volumes, which are controlled by the sediment type, have varying impacts on pore space morphology and therefore on permeability.

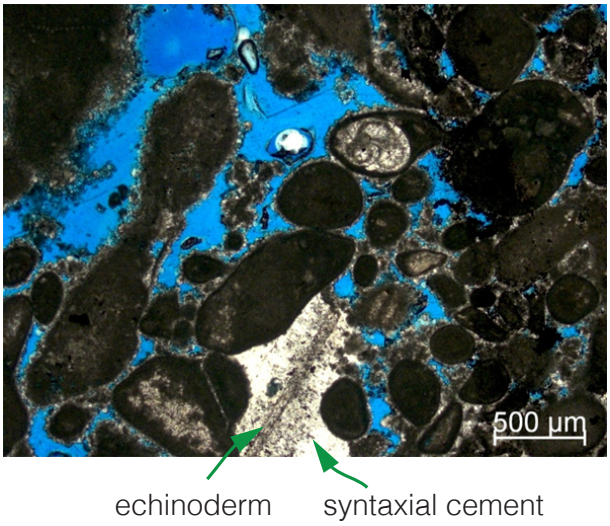

Figure 1.1: Thin section image of a Cretaceous shallow marine grainstone reservoir rock from the Campos basin, Brazil. Syntaxial cement (white) is surrounding a monocrystalline echinoderm fragment. Other grains, which are polycrystalline, are surrounded by a thinner coating of isopachous fringes.

In order to investigate the dependence of rock properties on sediment type, a pore-scale cementation modelling methodology is developed and implemented in both 2D and 3D. The model is object- and process-based and focuses on maintaining

the geometries of isopachous and syntaxial cements. Processes modelled include cementation as well as deposition in the 3D implementation of the model. The model aims to simulate cementation as it occurs in natural carbonates, taking into account the geometries of the developing cements, as well as such local phenomena such as grain-grain impact (or impingement).

The model is used to generate multiple synthetic rock samples of varying sediment type, i.e. the ratio of monocrystalline and polycrystalline grains. The Lattice Boltzmann method is then utilised to quantify the permeability of these synthetic samples. Furthermore, during the course of the work, it was found that a method of calibrating the Lattice Boltzmann model parameters was required. As such, a Bayesian uncertainty quantification framework for the robust prediction of permeability was developed.

To summarise, the objectives of this thesis are as follows:

1. Develop a 2D model of early calcite cementation that differentiates between grain types based on their crystallinity (monocrystalline and polycrystalline) and produces two early marine cement types associated with grain types (syntaxial and isopachous).

2. Apply the 2D cementation model on a natural reservoir rock image that has been stripped of cement. Generate multiple cemented synthetic samples based on varying deposit types (ratio of monocrystalline to polycrystalline grains).

3. Determine porosity and quantify the permeability (via Lattice Boltzmann flow simulation) of the generated cemented synthetic 2D samples. Investigate any trends in these properties as a function of the deposit type.

4. Develop a methodology to generate a 3D porous medium with characteristics, such as grain shape and size distribution, as observed in 2D thin section images.

5. Develop a 3D model of early calcite cementation that differentiates between grain types based on their crystallinity (monocrystalline and polycrystalline) and produces two early marine cement types associated with grain types (syntaxial and isopachous).

6. Apply the 3D cementation model to synthetic 3D deposit. Generate multiple cemented synthetic samples based on varying deposit types (ratio of monocrystalline to polycrystalline grains).

7. Determine porosity and quantify the permeability of the generated cemented synthetic 3D samples. Investigate any trends in these properties as a function of the deposit type.

8. Develop a Bayesian calibration framework for model parameters used in Lattice Boltzmann simulations so as to improve the predictive power of this flow simulation model.

1.2 Terminology

In this thesis, the outputs of the cementation models are termed *synthetic rock samples* or *synthetic samples* to distinguish them from the term *samples*, which is typically reserved for natural rock specimens. Similarly, all of the results of porosity or permeability derived for the synthetic rock samples are termed *synthetic data*, to distinguish it from *data*, which is usually reserved for experimental results.

1.3 Controls on Porosity and Permeability in Carbonates

Carbonate pore space is inherently heterogenous and multiscale, much more so than clastic rocks. While sandstones exhibit decreasing permeability with porosity, determining such trends for carbonates is difficult. This is due to extreme variability in carbonate depositional environments and susceptibility to a range of post-depositional processes that result in complex pore structures comprising length scales from tens of nanometres to several centimetres. In reservoir rocks, this heterogeneity results in reservoir quality characteristics, such as porosity and permeability, that are diverse for different carbonate rock types. As a result, carbonate reservoirs are a topic of their own and are usually given a separate treatment (Tucker and Wright, 1990; Lucia, 2007; Moore, 2001).

Permeability depends on factors such as porosity, connectivity and tortuosity and these dependencies have been empirically formulated. For instance, Bernabé *et al.* (2010) report that in simple cubic 3D networks, permeability (κ) depends on the connectivity of pore space and obeys a 'universal' power law:

$$\kappa \propto (z - z_c)^{\lambda} \tag{1.1}$$

where the exponent λ is a function of the standard deviation of the pore radius distribution, z is the coordination number, defined as the number of branches meeting at a node, and z_c is the percolation threshold expressed in terms of the coordination number, typically taken to have a value of 1.5.

Assuming that a porous bed can be regarded as a bundle of capillaries of equal length and constant cross-section, Kozeny and Carman proposed the following semi-empirical formula (Kozeny, 1927; Carman, 1937; Bear, 1972; Dullien, 1991):

$$\kappa = \frac{\phi^3}{\xi \cdot T^2 \cdot S^2} \tag{1.2}$$

which relates the permeability κ to four structural parameters: the porosity ϕ, the specific surface area of the pore/solid interface S, the shape factor ξ, and the hydraulic tortuosity T, defined as the ratio between the effective channel length due to the tortuous path and the length of the porous body.

The three factors: porosity, connectivity and tortuosity are explored in the following sections.

1.3.1 Porosity

Porosity is one of the most important controls on permeability; flow can not occur if there is no space for it. Pore space in carbonate rocks is usually physically complex, genetically diverse, and distinct from that of other sedimentary rocks. Carbonate porosity generally differs significantly from that of sandstone, with which it commonly is compared, in that the amount of pore space is typically smaller. In carbonate rocks, interparticle porosity is volumetrically less important, while intraparticle, intercrystal, moldic and other pore types play much more important role (Choquette and Pray, 1970). Moreover, pore size and shape can be much more varied, and both the pre- and post-depositional conditions are more important in forming and modifying porosity than in the case of sandstones.

The loss of porosity in carbonates with depth, due to mechanical compaction, dissolution of grain boundaries and cementation, is well studied. Some of the studies include one by Schmoker and Halley (1982), who surveyed carbonate rock porosity throughout the south Florida peninsula to depths of 5500m. They found that porosity decreases exponentially as a function of depth (Figure 1.2a). In a subsequent study, they discuss porosity-depth data for Pleistocene to Paleocene aged carbonates from the same area. Such rocks, found at shallower depths (2 to 830 m) (Halley and Schmoker, 1983), confirm the exponential relationship. Halley and Schmoker (1983) note that mechanical compaction is probably not the primary cause of porosity loss with depth. Early cementation is likely to

strengthen the sediment fabric and inhibit grain readjustment, fracturing, and deformation processes that are involved in mechanical compaction. They conclude that steady cementation as a function of time or depth is responsible for the decrease of porosity observed in their data.

In a yet later work, Scholle and Halley (1985) examined the porosity of Holocene and Pleistocene aged carbonates from the reservoirs in south-eastern USA. They find that data from reservoirs in south Arkansas and north Louisiana are a very good match to the curve found by Schmoker and Halley (1982) and the data from Alabama, Louisiana and Florida, albeit not falling exactly on the curve, confirm the exponential decrease of porosity with depth. Through experimental, observational, and geochemical data they show that porosity loss through burial diagenesis results from both physical and chemical compaction and from cementation.

In a study of Mississippian carbonates from the Williston Basin, on the border between USA and Canada, Brown (1997) found that average porosity decreases as a function of depth and that this decrease is approximately exponential for all carbonate lithologies (Figure 1.2b). Brown concludes that the greatest control on the rate of porosity loss with depth is the lithology of the carbonate and observes that grainstones tend to lose the least porosity as burial progresses. The process that is identified as responsible for most of the porosity loss is cementation rather than mechanical compaction, which is common in shelf limestones, as noted by Brown.

The relationship between permeability and depth is not so simple. For instance, the analysis of Paleogene aged carbonates of west-central Florida by Budd (2001) reveals significant scatter in permeability-depth data. Moreover, Budd demonstrates dependence of the permeability-depth relationship on carbonate lithology, with grainstones exhibiting a depth-dependent trend and wackestones not showing any trend (Figure 1.3). Similarly, the relationship between porosity

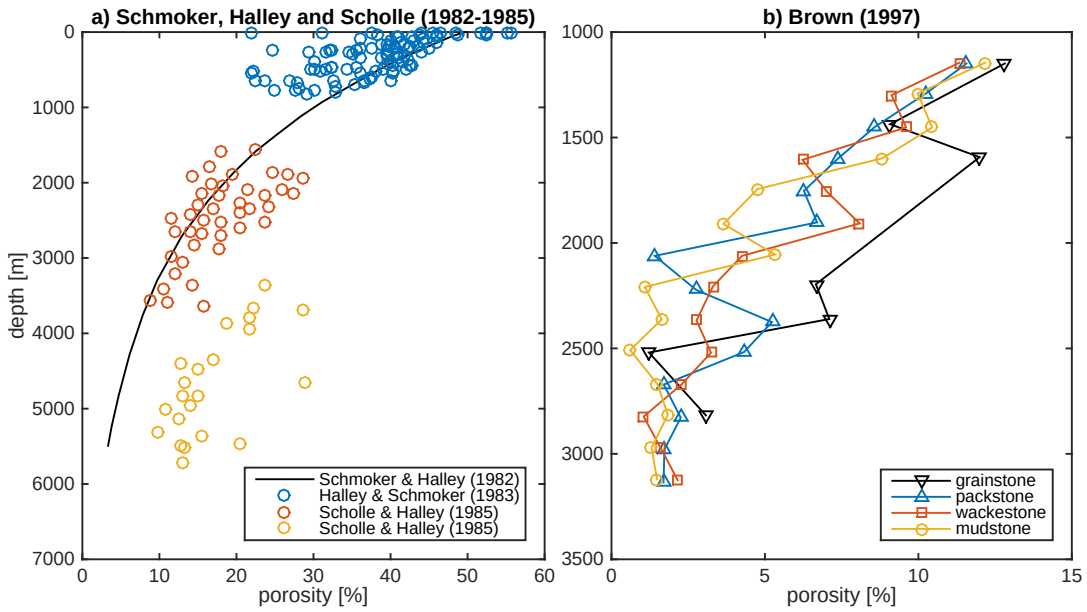

Figure 1.2: Porosity vs depth in carbonates; a) limestones of the south-eastern USA, including the best fit curve (black) for limestones in south Florida (Schmoker and Halley, 1982), shallow limestones in south Florida (blue) (Halley and Schmoker, 1983) and reservoir limestones from south Arkansas and north Louisiana (red) as well as from Alabama, Louisiana and Florida (yellow) (Scholle and Halley, 1985); b) mean porosity of fabrics at depth intervals for Mississippian carbonates from the Williston Basin (Brown, 1997).

and permeability of carbonates is complex and is shown to depend on the type of the rock (see Section 1.4).

Budd (2001) considered the typical causes of porosity loss: grain-to-grain chemical compaction, cementation, and mechanical compaction and investigated the degree to which they affect permeability loss. It was concluded that grain-to-grain pressure solution is the most detrimental to permeability. Pressure solution closes pore throats thus isolating pore bodies. Pore throats that remain open are also constricted, resulting in remaining flow paths consisting of progressively smaller pore throats. Cementation was determined to be the next strongest impact on permeability. An increase in cementation leads to a loss of permeability by the thinning of pore throats and an increase in the surface area and tortuosity of pores. Lastly, mechanical compaction was found to be the least effective process in reducing permeability relative to an incremental decrease in porosity. In this case permeability reduction is achieved mostly by the loss of porosity, increases in pore-throat lengths, and increases in the tortuosity of flow paths due to closer packing.

1.3.2 Pore connectivity and tortuosity

One reason why the relationship between porosity and permeability in carbonates is so complicated is the connectivity of pores. High porosity is obsolete if the pores are completely disconnected from each other. Jiang *et al.* (2011) demonstrated that changes in pore connectivity are more important than the changes in the porosity of the rock. Jiang's study considers Fontainebleau and Berea sandstones, which are quite simple porous media. The connectivity of pores in carbonates is more complicated, as the multitude of different carbonate pore types can connect in a multitude of ways. For example, separate vugs often constitute the largest volume fraction of porosity within carbonates but, due to the fact that they are disconnected pore bodies, alone they do not contribute to fluid flow and permeability. Carbonate pores are multi-scale and sometimes the level of

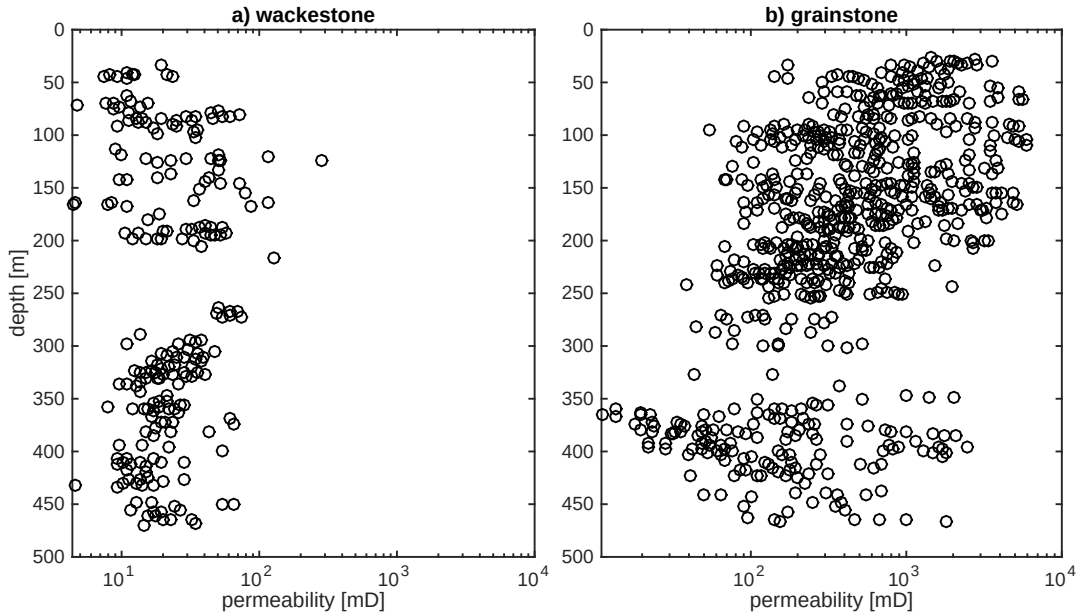

Figure 1.3: Permeability vs depth in Paleogene carbonates of west-central Florida (Budd, 2001); a) wackestones exhibit no trend, b) grainstones exhibit large scatter but overall demonstrate permeability decreasing with depth.

connectivity differs for pores of different sizes in one sample (Sok *et al.*, 2010; Hebert *et al.*, 2014; Oyewole *et al.*, 2015), e.g. the networks of micropores and macropores in one sample can have two distinct pore network structures and connectivity.

To characterise the connectivity of pores in a sample, the coordination number (z) is often used. The coordination number is defined as the number of branches (pore throats) meeting at a node (pore body) (Fauzi *et al.*, 2002). Since a 3D model is needed, this parameter is not directly measurable from a 2D cross section. Doyen (1988), however, defined a pseudo 2D coordination number as the total number of throats divided by the total number of pore elements in a thin section. Fauzi *et al.* (2002) demonstrated on an example of sandstones that permeability increases rapidly at small coordination number and that the relationship is not linear.

The other aspect of the morphology of the pore space that plays a role in

permeability is the tortuosity (T) of the flow paths. Tortuosity is one of the most important parameters when assessing fluid-flow properties in reservoirs but remains difficult to quantify (Makhloufi *et al.*, 2013). It is a measure of flow path complexity and is typically defined as the length of the fluid pathway between two points divided by the distance between these points (1.2). The more tortuous the path is, the longer it takes for the fluid to flow from one end to the other and as a result the permeability is reduced. Carbonates tend to have highly tortuous flow paths, which may occur due to the patchiness of cement (Lønøy, 2006) or from the break-up and rotation of skeletal grains during compaction (Budd, 2002).

In a study on modelling syntaxial quartz overgrowths, Jin *et al.* (2003) note that syntaxial cement tends to grow toward pore bodies, and thus it increases the tortuosity of the pore space in the sample. Pore-lining cements, such as isopachous cements, also lead to an increase in the tortuosity through the constriction of pore throats (Budd, 2001). However, we are not aware of any studies comparing the impact of different cement types on tortuosity.

1.4 Carbonate Classifications and Porosity-Permeability Relationship (Poroperm)

A correlation between low permeability and low porosity is a fundamental characteristic of porous media (Nelson, 1994) and is observed in sandstones, which are usually dominated by relatively simple intergranular porosity. Since carbonates are more complex in terms of pore structure, carbonate porosity-permeability relationships (poroperm from this point onwards) does not necessarily follow this trend. Regarding unconsolidated carbonate sediment, Enos and Sawatsky (1981) demonstrated an *inverse* relationship in the poroperm of modern carbonate sediments: lower-porosity (40%) grain-supported sediments exhibit higher permeabilities (up to $50,000mD$) than higher-porosity (up to 75%) mud-supported sediments, which have lower permeabilities (less than $100mD$). However, due to the

fact that the diagenesis for any given sediment type may take multiple different paths, the resulting poroperm data are extremely scattered (Ehrenberg and Nadeau, 2005).

Carbonates often show highly heterogeneous and convoluted pore networks, which makes the conversion from porosity to permeability difficult (Blunt *et al.*, 2013). Carbonate pore systems do not divide into simple pore bodies and pore throats, as is the case for sandstones, but rather are multi-scaled, complex pore systems. That is why so much work has been put into classifications of carbonates based on the pore type (Choquette and Pray, 1970; Lucia, 1995; Lønøy, 2006; Mousavi *et al.*, 2013).

Choquette and Pray (1970) distinguish several types of porosity in three groups (Figure 1.4):

- Fabric selective, which can be related to sedimentary or diagenetic components that constitute the texture or fabric and include:
  - Interparticle or intercrystal porosity, which are defined as the pore space between the grains or crystals of the rock respectively, where the pores are not bigger than the particles.
  - Intraparticle porosity, which is the empty space within the grains, typical for many skeletal grains that are not completely solid throughout their volume.
  - Moldic porosity, which is a form of secondary porosity developed by the preferential dissolution of shell fragments or other particles.
  - Fenestral porosity, that occurs due to the presence of fenestrae, which are irregular cavities found in muddy carbonate sediments. They take a number of forms, e.g. laminoid fenestrae, which are long and parallel to the sediment laminae and are produced by the decay of organic material, or birdseye fenestrae, which are irregular and formed by gas entrapments.

  - Shelter porosity, which is a type of primary interparticle porosity created by the sheltering effect of relatively large sedimentary particles which prevent the infilling of pore space by finer clastic particles.
  - Growth-framework porosity, which occurs due to growth of organisms in organic or inorganic boundstones.

- Non fabric selective, which can overprint the fabric selective porosity types, and include:

  - Fracture porosity, which can be found in any type of carbonate rock and occurs due to the stress that the rock undergoes.
  - Channel, vug and cavern (large-scale channel or vug) pore types, which occur as a result of dissolution. Vuggy porosity is defined as pore space that is significantly larger than grains or crystals.

- Fabric selective or not:

  - Breccia porosity, which conserves the porosity of the source material and introduces pore space between broken rock fragments.
  - Boring and burrow porosity, which occur due to organic intervention.
  - Shrinkage porosity, which consist of cavities produced within a solidified mass due to volume contraction on solidification.

Lucia (1995) proposed a division of all pore space into interparticle (intergrain and intercrystal) and vuggy pores. Lucia noted that in non-vuggy carbonate rocks, permeability and capillary properties can be described in terms of particle size, sorting, and interparticle porosity. Thus he proposed a classification of particle size and sorting in limestones using a modified Dunham approach, distinguishing between grain-dominated fabrics (grainstone and grain-dominated packstone) and mud-dominated fabrics (mud-dominated packstone, wackestone and mudstone) (Figure 1.5).

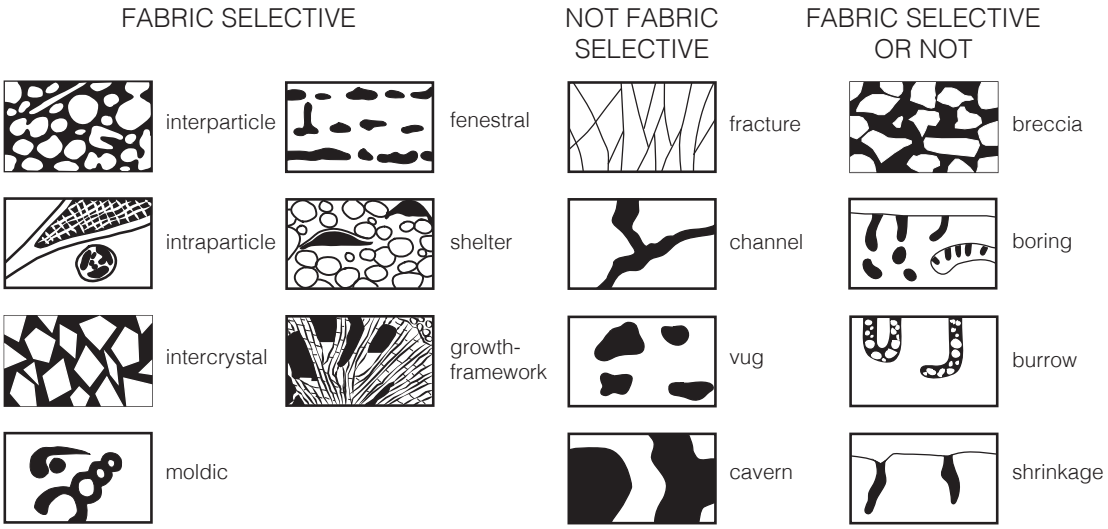

Figure 1.4: A classification of pores types in carbonate rocks (Choquette and Pray, 1970).

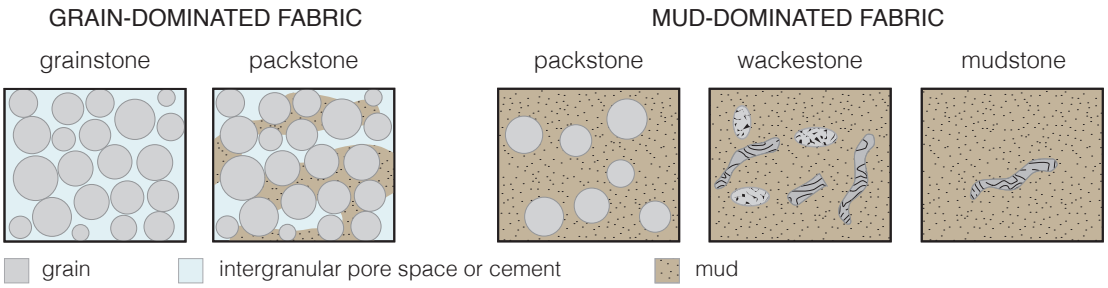

Figure 1.5: Classification of particle size and sorting in limestones using a modified Dunham approach adapted from Lucia (1995).

Lucia used the classification to examine carbonate poroperm relationships. Figure 1.6 shows that clear poroperm relationships exist for each of these petrophysical classes. Rock fabrics associated with the petrophysical classes described by Lucia have a predictable pattern of occurrence in a carbonate platform based on sedimentological processes and stratigraphic stacking. Of these facies, grainstones and grain-dominated packstones make for the best quality reservoirs and are therefore of particular interest.

Lucia noted that vuggy pore space needs to be described to complete the petrophysical characterisation. Vuggy pore space can be divided into separate vugs and touching vugs on the basis of vug interconnection. Separate vugs are connected only through the interparticle pore network and as such they contribute little to permeability and should be subtracted from total porosity to obtain interparticle porosity for permeability estimation.

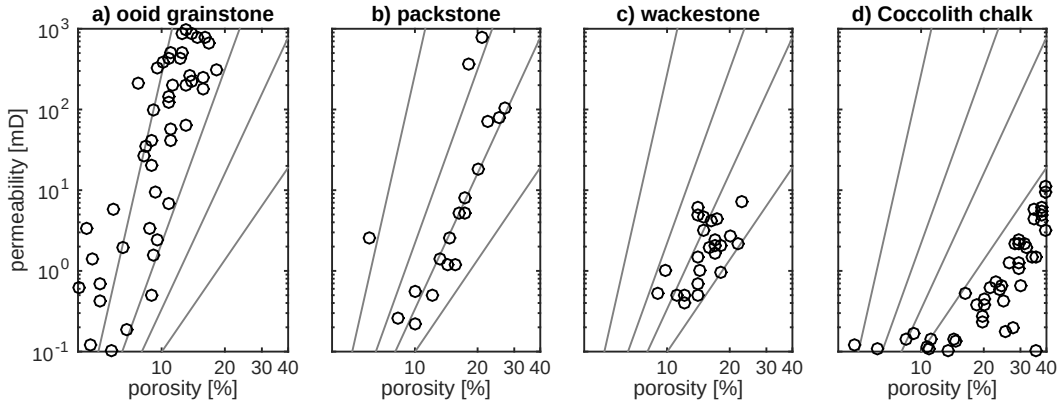

Figure 1.6: Permeability vs interparticle porosity for non-vuggy limestone rock fabrics adapted from Lucia (1995); a) $400\mu m$ ooid grainstone Ste. Genevieve, Illinois (Choquette and Steinen, 1985) b) grain-dominated packstone from Wolfcamp, west Texas, a poorly sorted mixture of $80 - 300\mu m$ grains and micrite (Lucia and Conti, 1987), c) wackestones with microporosity between $5\mu m$ crystals, Shuaiba, United Arab Emirates (Moshier *et al.*, 1988), d) Coccolith chalk, Cretaceous (Scholle, 1977).

Lønøy (2006) based his system on the work of Choquette and Pray (1970) and incorporated elements of the classification by Lucia (1995). His modifications

include incorporation of porosity distribution as a major new element in the classification. Lønøy's subdivision of interparticle porosity is based on pore size instead of grain size and sorting. Interparticle and intercrystalline porosity types are subdivided into twelve classes, as each of them can be described as either micro, meso or macro as well as either uniform or patchy. Figure 1.7 presents poroperm data for these twelve classes and demonstrates that permeability is generally higher for samples with macropores and lower for samples with smaller pores.

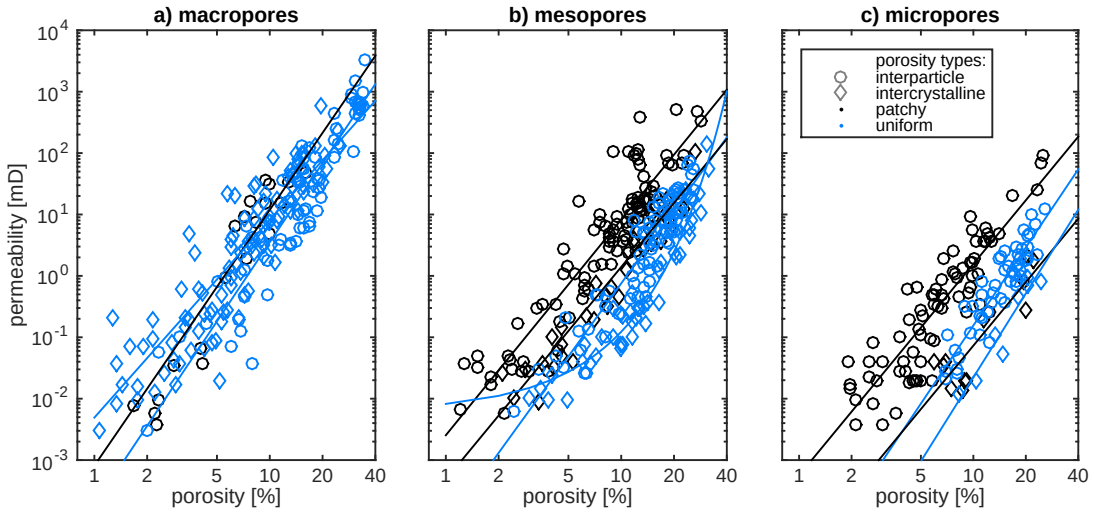

Figure 1.7: Poroperm for interparticle and intercrystalline pores based on the classification and data from Lønøy (2006): a) interparticle macropores ($> 100\mu m$ pore diameter) and intercrystalline macropores ($> 60\mu m$), b) interparticle mesopores ($50-100\mu m$) and intercrystalline mesopores ($20-60\mu m$), c) interparticle micropores ($10-50\mu m$) and intercrystalline micropores ($10-20\mu m$). All data are fitted with logarithmic curves, except for uniform intercrystalline microporosity, which is fitted with a linear function.

Moreover, in Lønøy's classification moldic porosity is subdivided into moldic micropores and moldic macropores. A new pore-type category: mudstone microporosity, is introduced and represented by four classes (Tertiary chalk, Cretaceous chalk, and uniform and patchy chalky micropores). Overall, Lønøy

describes 20 pore-type classes in carbonates and demonstrates a predictable relation between porosity and permeability of these classes.

Mousavi *et al.* (2013) slightly modified the classification of Lønøy (2006) for the purposes of process-based pore-scale modelling. A division of carbonate rocks into three types was proposed: muddy, grainy, and mixed, based on the carbonate content (grain, mud, and cement). Each type is further divided into subtypes on the basis of pore geometries defined by existing classifications. Muddy rock type is divided into two subtypes: interparticle porosity or microporosity and touching-vug porosity. Both grainy and mixed rock types have ten subtypes: interparticle porosity and intercrystalline porosity (each of three sizes after Lønøy (2006)), intraparticle porosity, moldic porosity with two pore sizes and touching-vug porosity.

These classifications however are performed based on petrographically observable textures, and as such they often fail to accurately predict flow properties, especially multiphase flow. Gomes *et al.* (2008) presented a carbonate reservoir rock typing workflow which included usage of both single-phase data (porosity, permeability) and two-phase data (capillary pressure curve) coupled with sedimentological descriptions. It was shown that combining a depositional facies model with a diagenetic facies model results in a model based on petrophysical groups that accurately predicts absolute permeability. Hamon (2003) used a similar procedure and demonstrated trends in the poroperm relationships for individual petrophysical groups. However, it must be highlighted that single-phase data might be poor indicators of controls of two-phase flow properties.

1.4.1 Poroperm behaviour of grainstone fabrics

In carbonate grainstones, the predominant poroperm trend that is observed is permeability decreasing with porosity. Figure 1.8 illustrates that as the occlusion of intergrain pore space proceeds with cementation (from 20% to 7%

porosity), permeability decreases, shifting the poroperm data points towards smaller porosity and permeability (Lucia, 2007). This mechanism is thought to be the cause of trends observed in Figures 1.6a and 1.7.

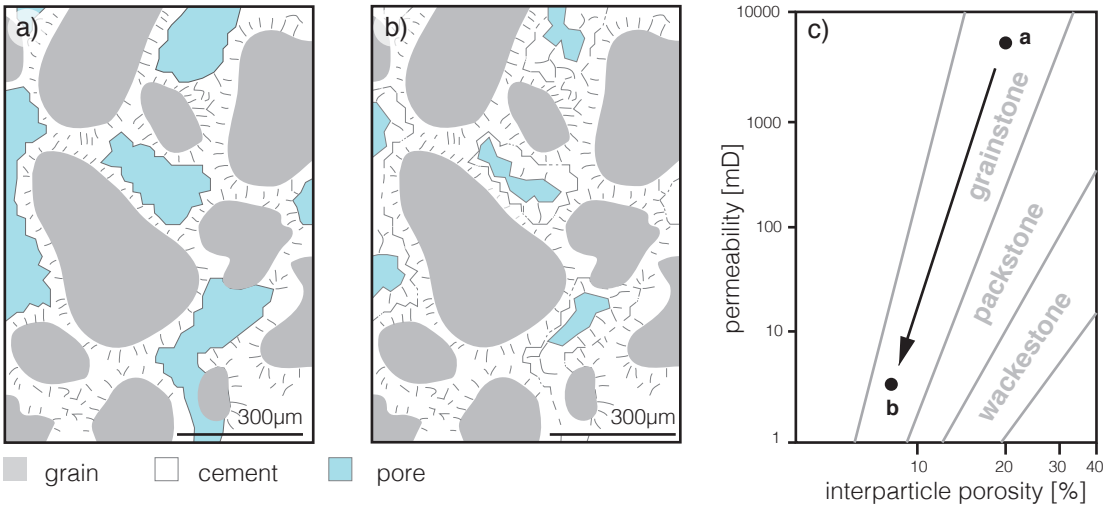

Figure 1.8: Decreasing permeability with decreasing porosity resulting from occlusion of intergrain pore space (Lucia, 2007). As 20% intergrain pore space in sample *a* is reduced by cementation to 7% in sample *b*, permeability is systematically reduced.

Key studies of the petrophysical characteristics of carbonate grainstones are those by Budd (2001, 2002); Melzer and Budd (2008). As mentioned previously, in a study of grain-supported Paleogene aged limestones of west-central Florida (oolite with sparse echinoderm fragments from depth $30 - 440m$), Budd (2001) found a systematic decline in mean and maximum permeability with depth (Figure 1.3). In contrast, wackestones exhibited no trend in permeability-depth data. The empirical permeability-depth relationship of Budd's grainstones resembles empirical porosity-depth relationships found for the same rocks by Halley and Schmoker (1983) (Figure 1.2a), although the rate of permeability loss is greater than porosity loss.

This study was extended by Melzer and Budd (2008), who added more samples of foraminifera-dominated grainstones from the same Eocene Avon Park Formation at depths of $300 - 500m$. The new samples, just like the old, are grainstones that are fairly homogenous in terms of size, sorting and grain types with variable

degrees of diagenesis represented by three diagenetic pathways: compaction-dominated, cementation-dominated and a mixture of both. Figure 1.9a shows the poroperm observed for cement-dominated samples. The best-fit for the cementation trend shown is an exponential function of permeability.

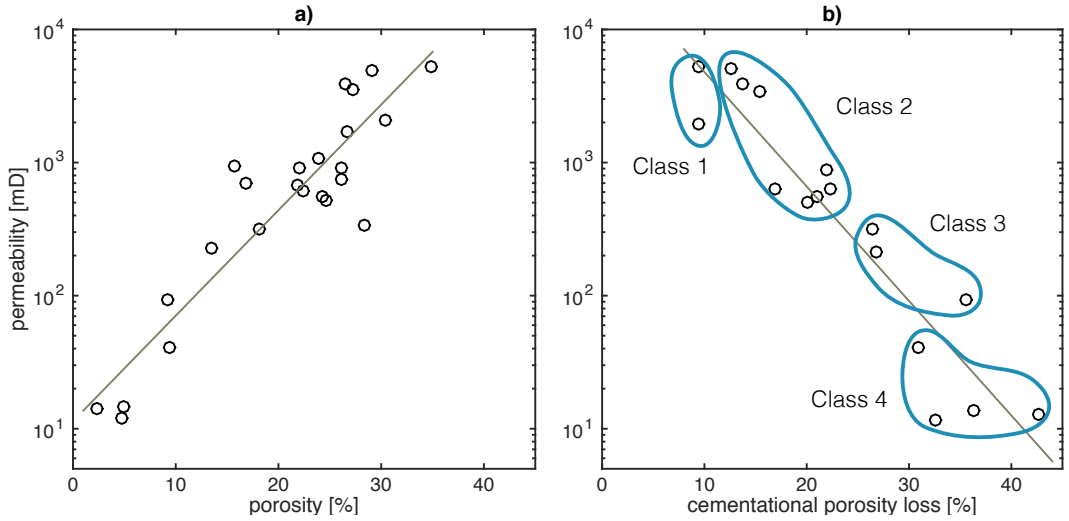

Figure 1.9: Poroperm relationships in grainstones. a) Permeability vs porosity of cement-dominated grainstones (Melzer and Budd, 2008). b) Permeability vs cementational porosity loss for samples dominated by cementation (Budd, 2002). In both cases data is fitted with an exponential function. Four classes of observed fabrics based on type and abundance of cement are distinguished: 1) little cement with syntaxial overgrowths in widely spaced echinoderm fragments and fringing cements, 2) more cement lining the pores, 3) partial-pore filling mosaics and 4) complete pore-filling mosaics.

In the analysis of thin sections of cemented rocks, it is usually difficult to separate the effects of porosity loss due to compaction and due to cementation. Budd's dataset included samples of variable levels of compaction and cementation and it was possible to quantify the two effects via thin-section point-count. Budd targets cement-dominated samples with less than 8% compactional porosity loss and compaction-dominated samples with less than 10% cementational porosity loss. Figure 1.9b demonstrates the trend of permeability vs cementational porosity

loss for cement-dominated grainstone, and distinguishes fabric classes based on type and abundance of cement.

Melzer and Budd (2008) concluded that in Paleogene grainstones of Florida pore geometries and permeability respond differently to compaction and cementation. The variations are due to different morphologies of the pore networks generated through these two processes. Cementation converts the original interparticle pore space to a system consisting of polyhedral and sheet-like pores connected by progressively smaller pore throats. In contrast, compaction does not generate a complex pore system and it tends to constrict the original interparticle porosity in the smaller pore throats. In cement-dominated samples, pore throats constrict as cementation progresses and they evolve from completely open voids to a mixture of open voids and polyhedral voids between cement crystals, and further to a mixture of polyhedral voids and sheet-like pores along compromise boundaries between cement crystals. In some cases a further evolution to sheet-like pores occurs.

1.5 Crystallinity of Carbonate Grains

This thesis focuses on grainstones and puts much emphasis on the distinction between grain types (monocrystalline vs polycrystalline) due to the fact that associated early calcite cement types (syntaxial vs isopachous respectively) have very different properties. Lander *et al.* (2008) demonstrated that the crystallinity of grains influences the volume of cement developed around them. Monocrystalline grains tend to produce large volumes of syntaxial overgrowth while polycrystalline grains develop thinner isopachous fringes (Scoffin, 1987). Besides volume, these two types of cement have different geometries and so their impact on the morphology of pore space varies.

1.5.1 Polycrystalline grains

Most carbonate grain types are polycrystalline (Scoffin, 1987). These include the majority of skeletal carbonates, as well as non-skeletal grains such as pellets and ooids. The crystallinity of the skeletal fragments may vary: it is homogenous prismatic for trilobites and ostracods, granular for foraminiferans, normal prismatic for brachiopods, foliated for bryozoans, brachiopods and oysters. The surfaces of these grains can be described as a mosaic of seeding sites with different crystal axes orientations and thus they develop cement typical for polycrystalline grains (Scoffin, 1987).

1.5.2 Monocrystalline grains

Most carbonate grains that can be considered monocrystalline are skeletal fragments of organisms belonging to the phylum Echinodermata. There are five major living classes (sea urchins, starfish, brittle stars, sea lilies and sea cucumbers) and several extinct classes. Echinoderms are exclusively marine and a common element in tropical and temperate areas. Calcareous remains of echinoderms rarely constitute more than 10% of modern sediment grains (Scoffin, 1987). However, in the past (especially in the Palaeozoic) they had much greater quantitative significance, even dominating the allochems (Walker *et al.*, 1990).

Figure 1.10 shows several thin sections of samples with a high content of monocrystalline grains (from 35% up to 80%). In each of these samples, the cement is dominated by syntaxial cement developed as overgrowth on the monocrystalline grains. The details of the allochem breakdown for each rock are presented in Table 1.1.

In actual fact, echinoderm fragments do not usually consist of a single calcite crystal, but are masses of sub-resolution crystals with almost perfectly aligned

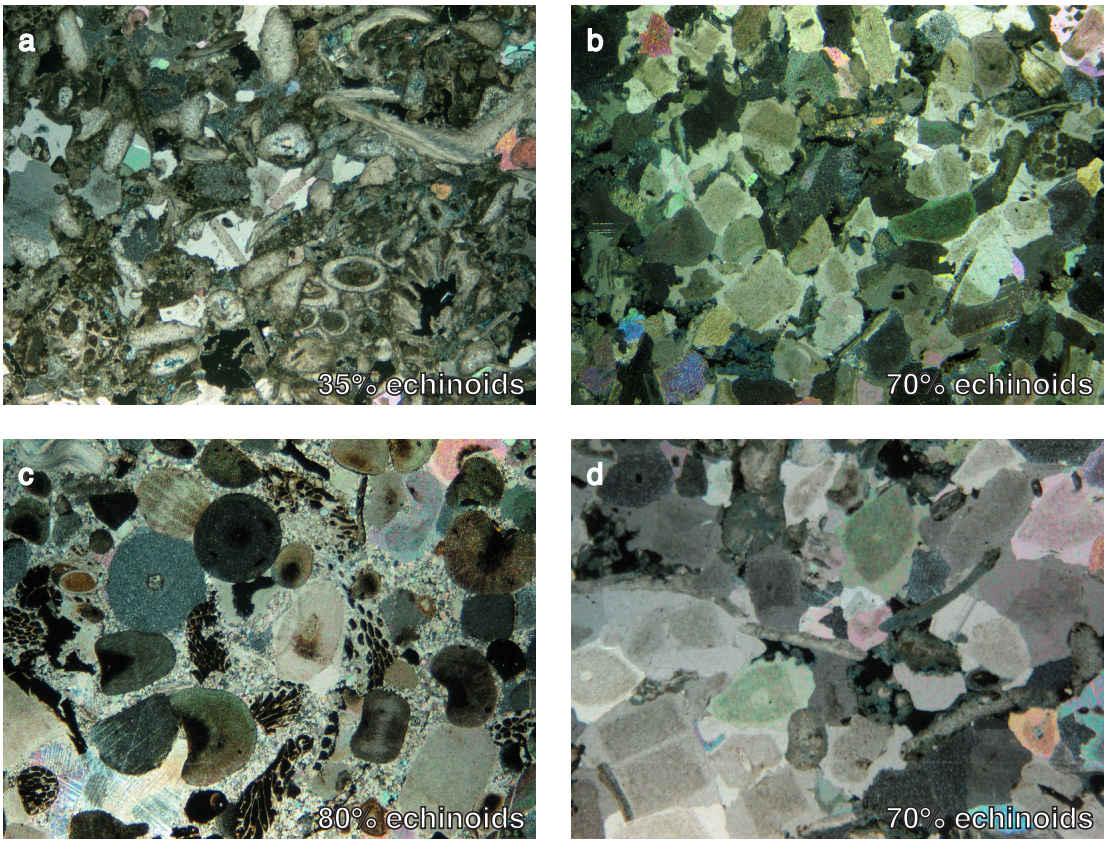

Figure 1.10: XPL images of monocrystalline rich rocks (Imperial College Rock Library): a) bioclastic limestone, b) echinoidal grainstone, c) crinoidal limestone and d) echinoidal bioclastic limestone. Field of view in each image is 1cm.

Table 1.1: Allochem content of monocrystalline rich rocks from Imperial College Rock Library.

Image	Rock	Allochem breakdown	Cement
a	bioclastic limestone	60% molluscs, 35% echinoids, 5% bryozoans	syntaxial overgrowth, crystals are up to 4mm
b	echinoidal grainstone	70% echinoid plates, 20% mollusc shell fragments, minor bryozoans	coarse grained ($4mm$) calcite crystals
c	crinoidal limestone (lower Carboniferous)	80% crinoid ossicles, 15% bryozoans, sparse ooliths and brachiopod valves	syntaxial overgrowth on crinoids (crystals bigger than $0.5mm$) and sparry calcite mosaic cement
d	echinoidal bioclastic limestone	70% echinoids, 10% bryozoans, minor intraclasts	coarse-grained sparry calcite (crystals up to $2.5mm$)

crystal axes. As such, they are normally treated as monocrystalline grains, as they are in this study.

1.6 Early Calcite Cement Types

The two types of early shallow marine calcite cements typical for grainstones considered in this thesis are the isopachous cement and the syntaxial cement or overgrowth (Figure 1.11). Syntaxial overgrowth is associated exclusively with grains that can be treated as monocrystalline, such as echinoderm fragments, while isopachous cement is the most volumetrically significant cement occurring around polycrystalline grains in the early stages of marine diagenesis (Walker *et al.*, 1990; Lucia, 2007; Ahr, 2008; Tucker and Wright, 1990; Flügel, 2010).

The choice to model only these two cement types was made for several reasons. Firstly, this work focuses on very early marine cementation, which occurs rapidly, before significant compaction takes place. Syntaxial and isopachous cements are both volumetrically significant early marine calcite cements. Secondly, as the overarching aim of this work is to understand the impact of the ratio of monocrystalline to polycrystalline grains on cemented rock properties, the focus is on cement types associated with these grain types.

1.6.1 Syntaxial cement

Syntaxial cement seeds on a monocrystalline grain, most notably echinoderm fragments, and grows in optical continuity to it (Scoffin, 1987). In a growing crystal, ions preferentially occupy the sites that result in greater release of energy. Non-euhedral faces of a grain provide a much greater release than euhedral faces (Mullin, 2001). As a result of this, calcite overgrowth proceeds rapidly until euhedral faces are achieved (epitaxial growth). Subsequently, the rate of growth

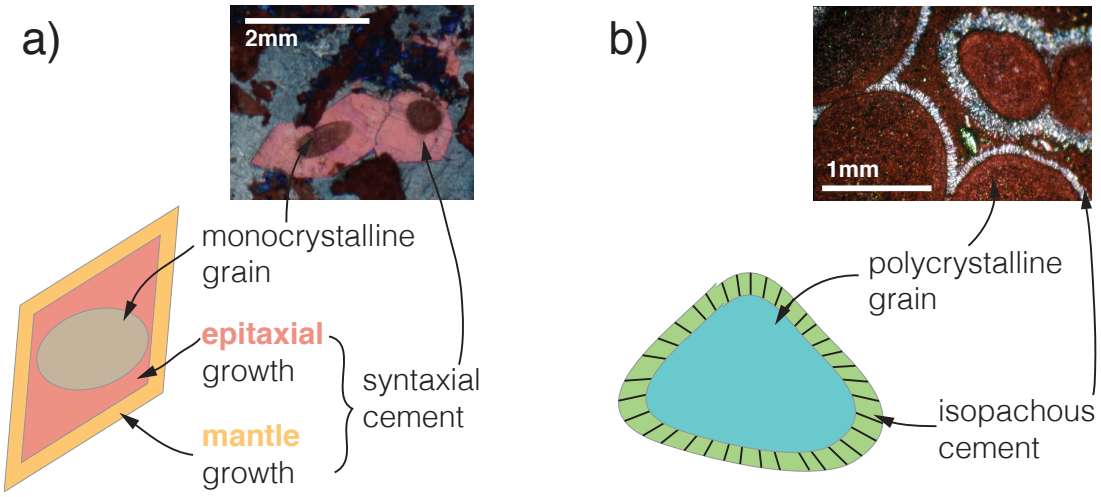

Figure 1.11: a) Monocrystalline grain (brown) with syntaxial cement. Red represents the epitaxial growth and orange represents concentric (mantle) growth. The thin section depicts Thamama Group rock, image courtesy of Cees van der Land. b) Isopachous calcite cement in a carbonate rock. The thin section depicts a beachrock from the Great Barrier Reef, image courtesy of Rachel Wood.

decreases considerably (mantle/concentric growth) (Dickson, 1983; Lander *et al.*, 2008) (Figure 1.11a). In the absence of any obstacles, monocrystalline grain grows rapidly until all faces are euhedral and the crystal form of calcite is achieved.

Due to the fact that early syntaxial cement growth occurs on non-euhedral faces and therefore is energetically favoured, syntaxial cements start to grow very early in the diagenesis, typically in the early marine stages (Lucia, 2007). Once the euhedral faces of the growing crystal are reached, cement growth can continue in a form of mantle growth, often continuing into the burial zone (Lucia, 2007).

1.6.2 Isopachous cement

Isopachous cement develops on grains that do not have the capacity to seed a single crystal. This includes typically polycrystalline grains, e.g. ooids, as well as grains where seeding sites are blocked so that growth of a single crystal is

impossible. This can be achieved by e.g. ooilitic coating on crinoid fragments as reported by Lucia and Murray (1967).

Isopachous cement occurs during the early stages of shallow marine diagenesis in the phreatic zone (Tucker and Wright, 1990; Moore, 1989). Isopachous calcite fringes may consist of fibrous, bladed or microcrystalline crystals which form a fringe of nearly constant thickness around grains (Figure 1.11b) (Lucia, 2007). The thickness of the fringe is typically $20 - 100\mu m$ (Tucker and Wright, 1990). Isopachous cement is common in grainstones and is particularly typical in beachrock (Tucker and Bathurst, 2009).

Isopachous fringes are essentially a collection of syntaxial overgrowths that form on small seeding sites provided by the many crystals on the surface of the polycrystalline grain. The crystals on the surface of the grain can be oriented in various directions, but those oriented normal to the substrate grow fastest and, as precipitation proceeds, they eliminate the crystals of other orientations (Scoffin, 1987). In similarity to syntaxial cements, once euhedral faces are achieved, precipitation slows down considerably.

1.6.3 Impact of early cements on pore space morphology and permeability

The pore space of sediments composed predominantly of echinoderm fragments (monocrystalline grains), which commonly have syntaxial overgrowths, is likely to be completely occluded by the cementation process (Lucia, 2007; Bjorlykke, 2010). However, in fabrics where monocrystalline grains are more sparse, cements tend to block local pore throats intermittently, creating a patchy cement distribution, and as such cementation may have a fairly low impact on porosity and permeability (Lønøy, 2006).

In contrast, isopachous cement tends to precipitate evenly around all polycrystalline grains. As such it does not penetrate deep into intergrain pore spaces (Lucia, 2007). By its nature, isopachous cement narrows all pore throats and, depending on the thickness of isopachous fringes, can close off most of pore throats, thus significantly reducing pore connectivity and permeability.

Therefore, the grain type plays an important role in determining the resulting pore space morphology of the final rock through the preferential development of cement type. If monocrystalline grains dominate the deposit, pores are likely to be completely occluded by syntaxial cements, and permeability can be significantly reduced. If the fraction of monocrystalline grains is low, pore spaces are less likely to be closed off by syntaxial overgrowths and the connectivity of the final rock depends more on the thickness of isopachous cement fringes. If isopachous fringes are thin, most of the primary connectivity is retained and the impact on permeability is small, but if they are thick, most pore throats may be closed and the effect on connectivity and permeability can be substantial.

1.6.4 Competition for growth space

Due to the proximity of grains to each other in any carbonate rock, syntaxial overgrowth almost always encounters other grains, which may or may not be developing their own syntaxial overgrowths. Thus the full crystal shape of calcite is never reached and instead of euhedral faces overgrowths form compromise boundaries (James and Jones, 2015; Dickson, 1983).

The average volume of syntaxial cement per grain in a cemented rock is dictated by the competition during growth: the more monocrystalline grains there are that develop syntaxial overgrowth, the smaller the average volume of cement produced per grain.

1.6.5 Impinging and 'shadow' effects

During cement growth, grains are very likely to impinge on one another, and thus deactivate seeding sites and create compromise boundaries with other grains before reaching euhedral faces of their own. Depending on the arrangement of the grains in the sample, impinging effects may lead to a 'shadow' effect. This effect is observed in natural carbonate rocks (J.A.D. Dickson, pers. comm.). It occurs due to the fact that once an obstacle is encountered during epitaxial growth, a portion of the seeding area on a non-euhedral face of the grain is blocked by it. As a result, no further syntaxial overgrowth will be seeded by that area.

Figure 1.12 illustrates how a single impinging grain limits the extent of the syntaxial overgrowth. Syntaxial cement can grow to its full extent shown in Figure 1.12a only in the absence of other grains. Once an obstacle is encountered, the seeding site of the growing cement that came in contact with the obstacle is blocked and the zone in the 'shadow' of the obstacle will not be produced. Thus, the fast epitaxial growth ceases and a smaller volume of cement is formed, as depicted in Figure 1.12b.

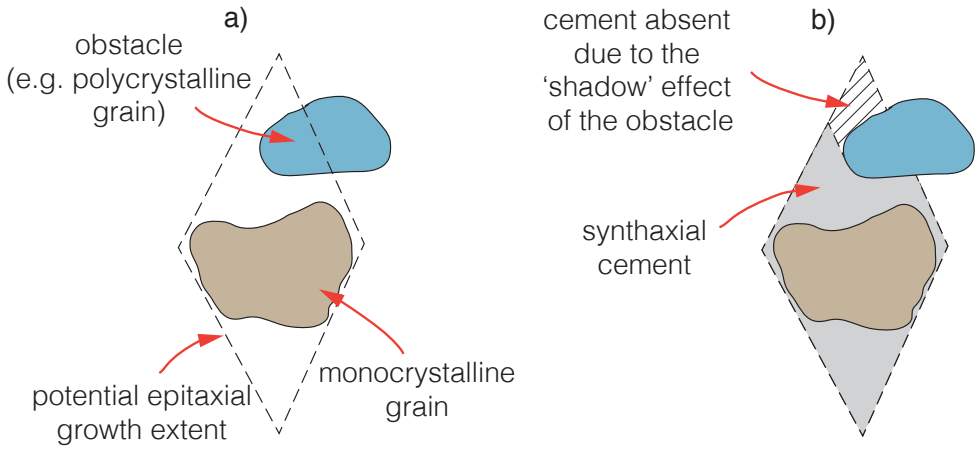

Figure 1.12: 'Shadow' effect of grains impinging on growing cement; a) extent of syntaxial overgrowth that would develop in the absence of obstacles, b) final cement geometry.

1.6.6 Crystal forms of calcite

Calcite belongs to a trigonal hexagonal scalenohedral crystal system with the following cell parameters: $a = b = 4.9896\mathring{A}$, $c = 17.061\mathring{A}$, $\alpha = \beta = 90°$, $\gamma = 120°$ (Kelly and Knowles, 2012) (Figure 1.13a). Over 800 different forms of calcite have been described, the most common of which are the rhombohedral and scalenohedral forms. This work focuses on the rhombohedral form, but even within this group many variations exist. Such variations include forms with Miller-Bravais indices $10\bar{1}1$, $40\bar{4}1$ and $01\bar{1}2$ (Figure 1.13b). The index $01\bar{1}2$ rhombohedron belongs to calcite forms most frequently observed in nature, and also most commonly derived in the laboratory (Massaro *et al.*, 2008). Another common rhombohedral form of calcite is $40\bar{4}1$ (Dickson, 1983). The main difference between these two rhombohedral forms is that $01\bar{1}2$ is more blocky and $40\bar{4}1$ is more elongated (Figure 1.13b), which results in different volumes of syntaxial cement produced. Figure 1.14 illustrates that in the absence of any obstacles, rhombohedral crystal form $40\bar{4}1$ produces significantly greater volume of epitaxial overgrowth than crystal form $01\bar{1}2$ (Dickson, 1983).

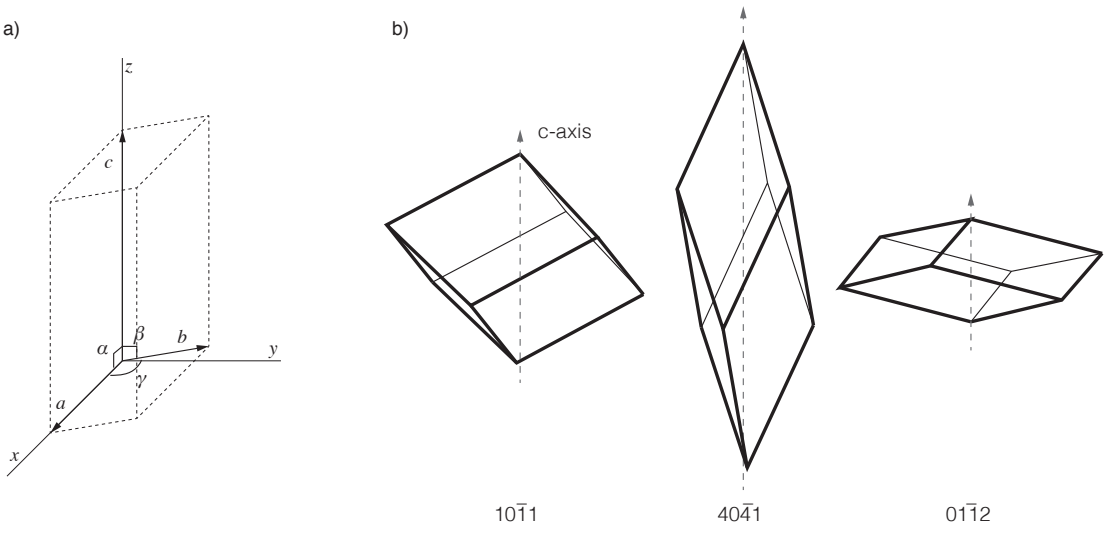

Figure 1.13: a) Calcite unit cell of dimensions $a = b = 4.9896\mathring{A}$, $c = 17.061\mathring{A}$ and $\alpha = \beta = 90°$, $\gamma = 120°$ (Kelly and Knowles, 2012). b) Three common rhombohedral forms of calcite (Dickson, 1983).

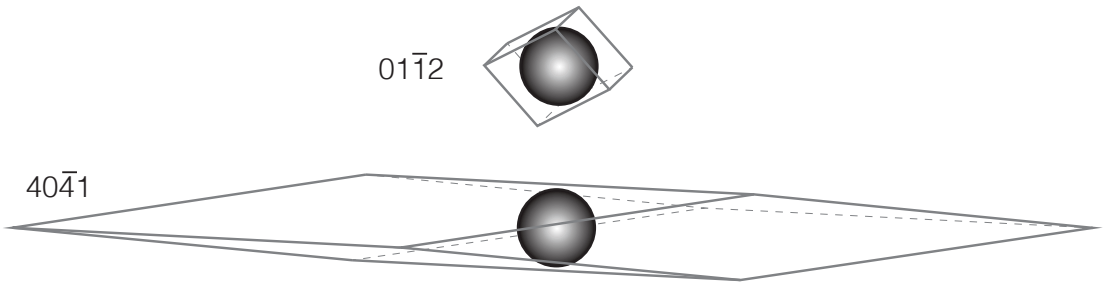

Figure 1.14: Comparison of the shape and size of crystals of the rhombohedral crystal form $01\bar{1}2$ and $40\bar{4}1$ circumscribed on two spheres of the same size. The length of crystal form $40\bar{4}1$ is 7.2 the length of form $01\bar{1}2$ and the volume is 5.8 times bigger, however the volume of the cement (the volume of rhombohedron diminished by the volume of the sphere) is 9.6 times greater in case $40\bar{4}1$.

Laboratory experiments suggest that the crystal form developed by calcite in supersaturated solutions diffusing in gels is influenced by the chemistry of the solution (Pastero *et al.*, 2003). Pastero *et al.* (2003) found that in an agarose gel crystal morphology terminated with a rhombohedral form $10\bar{1}4$, while in a Na-metasilicate gel two crystal forms developed: $01\bar{1}2$ and $10\bar{1}4$, with the relative abundance influenced by the pH of the solution and by the acidifying agent.

However, no quantitative studies on the abundance of the different crystal forms in the cement of carbonate rocks exist (J.A.D. Dickson, pers. comm.). Neither are there studies on the fraction of different crystal forms in a single rock sample (whether it consists only of a one crystal form or a mixture of various forms). Thus the approach in this work is to select crystal forms that are reported to be common ($01\bar{1}2$ and $40\bar{4}1$, Figure 1.14), and perform studies for each of these forms.

1.7 Synthetic Rock Modelling

The advantages of generating synthetic rocks by digital rock modelling are several. The procedure is time-saving, non-destructive, and easily reproducible.

Rock models are flexible and easily modified to study the impact of geological heterogeneity (modifications of rock components) on petrophysical parameters. The drawback is the replacement of the exact microstructure by an approximate model, as simplifications of the real fabrics are unavoidable in the modelling process. This is mostly the case due to the fact that the formation processes are not fully understood or due to computational constraints. An alternative to modelling are 3D imaging techniques, e.g. microcomputed tomography (μCT) (Pak *et al.*, 2015), however an important disadvantage of this method is that it is difficult to distinguish cement from grain in the resulting image.

Numerous digital rock modelling methods exist for sandstones reconstruction while only few carbonate rock models exist. The literature regarding the methodology of rock reconstruction can be split into two main approaches. The first one regards the statistical reconstruction of pore-scale rock models using probabilistic methods. In this approach, authors try to match certain morphological or statistical characteristics of the rock obtained via imaging techniques or experiments using stochastic processes. There is usually no underlying physical modelling.

In contrast, simulation-based models use either constitutive laws or they simulate the processes that occur during rock formation (deposition, compaction and diagenesis) in some other way. A subset of these simulation-based models are those that focus around grain growth. These still usually have a strong stochastic component and can be considered as hybrid models. We proceed to review the existing studies within these various approaches. Tables 1.2, 1.3 and 1.4 list all of the reviewed studies and some of their characteristics.

1.7.1 Statistical reconstruction models

Among the first studies involving statistical reconstruction methods, Adler *et al.* (1990, 1992) aimed to match statistics extracted from thin sections of

Table 1.2: Summary table of published statistical reconstruction models indicating author, rock type of focus and whether or not flow was simulated in the resulting model output. 'LB' indicates that the flow simulation was performed using Lattice Boltzmann method.

Study	Flow simulation	Rock type
Adler *et al.* (1990, 1992)	✓	Fontainebleau sandstone
Biswal *et al.* (1999)		Fontainebleau sandstone
Hazlett (1997)	✓(LB)	Berea sandstone
Yeong and Torquato (1998a,b)	✓	Fontainebleau sandstone
Liang *et al.* (2000b,a)	✓	sandstone, **dolomite**
Roberts (1997)		general
Manwart *et al.* (2000)		Fontainebleau sandstone, Berea sandstone
Thovert *et al.* (2001)		Fontainebleau sandstone
Roth *et al.* (2011)		**dolomite**
Okabe and Blunt (2004); Okabe (2004)	✓(LB)	Berea sandstone, **carbonate**
Okabe and Blunt (2007)	✓(LB)	**vuggy carbonate**
Wu *et al.* (2004)		soil
Wu *et al.* (2006)	✓(LB)	various, **carbonates** in van der Land *et al.* (2013)
Arns *et al.* (2003)		general
Daian *et al.* (2004)		sandstones
Fernandes *et al.* (1996)		Fontainebleau sandstone

Fontainebleau sandstone in order to recreate a 3D synthetic sample mimicking the natural sample. Flow simulations using a finite difference solver were performed on the resulting model outputs in order to assess how well the reconstructed geometries predict permeability. Two statistical properties of the rock were used to condition the models: the porosity and the correlation function between the pores assuming an isotropic medium. The modelling protocol however, as is the case with most statistical reconstructions, suffers due to the non-physical nature of the method. Targeted statistics are found insufficient to accurately approximate transport properties such as permeability, which is very sensitive to the pore connectivity in the reconstructed media. As such, permeability is underestimated by an order of magnitude.

Biswal *et al.* (1999) followed a similar statistical reconstruction approach to Adler *et al.* (1990). The porosity of the statistically reconstructed pore models was found to match that of the experimental sample (3D μCT sample of Fontainebleau sandstone) as did the two-point correlation function. However, multiple discrepancies resulting from the modelling framework were reported. The main differences between the reconstructed medium and the μCT sample were found in the degree of anisotropy and in the fluctuations of porosity and connectivity. Again, this was due to the the statistical reconstruction not being able to recreate the connectivity of the pore system of Fontainebleau sandstone.

As mentioned in Section 1.3.2, permeability is heavily influenced by pore connectivity. Stochastic reconstruction models based on matching porosity and correlation functions tend to fail in recreating the connectivity of pore networks and, in result, they suffer from a permeability mismatch when compared with experimental data. Multiple studies have tried to introduce additional constraints to address this issue. One such attempt is the work of Hazlett (1997). It was shown that global spatial correlation statistics (such as variograms) when complemented with local information of the pore geometry and connectivity, can adequately characterise 3D properties distributions of the rock and aid in predicting fluid transport properties.

In order to obtain this additional porosity spatial correlation structure, Hazlett extracted it from image statistics (a 3D μCT image of Berea sandstone) and attempted to match it with the reconstructed medium. Initially, in a reconstruction performed using only global statistics (variogram), a significant mismatch in the permeability between the synthetic media and the μCT images was found. After the reconstruction was supplemented with additional constraints to local connectivity, the permeability of the synthetic media approached that of the μCT images.

Hazlett's work was among the first studies to use a Lattice Boltzmann simulation on synthetically reconstructed media in order to quantify permeability of rock model outputs. Hazlett's predictions, albeit qualitatively correct, relied heavily on the statistics of a specific sample (in this case Berea sandstone). As such the predictive envelope of this modelling approach remains limited.

Another study regarding the reconstruction of 3D porous media using statistical information from natural rock images is that of Yeong and Torquato (1998a). This work attempted to capture more anisotropic information of the sample. In a subsequent study, Yeong and Torquato (1998b) augmented the methodology and attempted to inverse-engineer synthetic rock generation by statistically matching synthetic 3D samples to information obtained from 2D thin sections, a problem that does not have a unique solution. Multiple studies that use 2D statistical information in order to reproduce 3D reconstructed media followed (Liang *et al.*, 2000b,a; Roberts, 1997; Manwart *et al.*, 2000; Thovert *et al.*, 2001; Roth *et al.*, 2011). All of these studies, however, suffer from similar issues regarding poor prediction of the reconstructed pore network connectivity.

In another statistical reconstruction approach, Okabe (2004) and Okabe and Blunt (2004) used multi-point statistics in order to reconstruct a synthetic 3D sample. A high resolution 2D thin section image of a carbonate reservoir rock was used in conjunction with a 3D μCT image of Berea sandstone. The Lattice Boltzmann method was used to simulate flow through the generated synthetic samples and a

good agreement was reported with the permeability computed on the μCT image of Berea sandstone as well as with predictions using analysis of the 2D images and an effective medium approximation.

In an attempt to capture the more complex pore morphologies of a vuggy carbonate with statistical accuracy, Okabe and Blunt (2007) used multi-point statistics at different scales to reconstruct a 3D medium using a 2D thin section. Different scales were targeted in an effort to create a multi-scale model of a geologically accurate pore structure with realistic connectivities. The predicted permeabilities were in good agreement with the experimental values, despite the size of the reconstructed medium being smaller than conventional laboratory samples. No other geological process were modelled within this reconstruction framework.

Wu *et al.* (2004, 2006) developed a stochastic pore space reconstruction approach using 2D thin section images as an input. Notions from Markov Random Fields (MRF) theory, which is based on using only a small number of local conditions to predict global features based on training images were used. In order to identify the parameters associated with the MRF from the 2D thin sections, Wu *et al.* (2004) developed a Markov Chain Monte Carlo (MCMC) procedure to perform a probabilistic inference. The method generates 3D voxelised synthetic media based on the identified MRF parameters. A close match between the permeability of the synthetic media obtained via Lattice Boltzmann simulations and the corresponding experimental values for a range of materials was reported. All media used in the study were homogenous. Modelling more heterogenous media with complicated 3D topologies would require anisotropic MRF or more complicated models, inference of which is significantly harder.

An attempt at modelling carbonates using Wu's model was made by van der Land *et al.* (2013). A forward approach to model several diagenetic pathways originating from the same sediment image was utilised (a schematic image of a typical carbonate sediment). The 3D synthetic rock samples were generated

for each step along the various diagenetic pathways. The values of porosity and absolute permeability derived from these synthetic 3D rock models were within the range of values measured in natural media.

Arns *et al.* (2003) took quite a different approach. Integral geometry and the Kac theorem for the spectrum of the Laplace operator were used to define the effective shape of a grain in a system consisting of a distribution of arbitrarily shaped grains. They tried to find key morphological measures to create a stochastic reconstruction of a complex material made up of discrete pores or grains from a single 3D snapshot at any phase fraction of the sample rock. The reconstructed morphologies were shown to accurately predict the shear modulus of the natural sample as well as its effective conductivity. No tests were reported for transport properties of the stochastically reconstructed samples.

In an attempt to link and correlate the morphology and permeability of reservoir sandstones, Daian *et al.* (2004) used the concepts of renormalisation theory and upscaling. The data needed for multi-scale reconstructions are the pore and solid phase size distributions. The application of the classification model of Daian *et al.* (2004), to a series of reservoir rocks of widely varying porosity and permeability, showed that the method is able to provide a reasonably accurate estimation of permeability. However, once again this model does not involve any physical intuition or dynamic modelling of the spatiotemporal processes that govern carbonate growth, and as such is only useful as a morphology-permeability classifier.

In a similar modelling attempt, Fernandes *et al.* (1996) used Multiple Percolation Systems (MPS) to study invasion processes in porous media with a large pore size distribution. The authors concluded that despite conserving statistical properties such as the correlation function at the pore level, the use of MPS as a representation of a porous medium did not allow for the conservation of the geometrical structure of clusters of connected pores. Even after proposing updates to the MPS model, the connectivity function for the original porous

system and the updated MPS model differed significantly. As a result, so did the flow prediction, limiting the power of this model to predict transport properties.

1.7.2 Physically-inspired stochastic models of grain growth

Table 1.3: Summary table of published physically-inspired models of grain growth indicating author, simulated process and rock type of focus.

Study	Simulated processes	Rock type
Grest *et al.* (1985); Anderson *et al.* (1989); Forrest and Tang (1990)	grain growth	
Blikstein and Tschiptschin (1999)	grain growth	
Reiter (2005)	crystal growth	
Libbrecht (2007)	crystal growth	
Radhakrishnan and Zacharia (1995)	grain growth	
Pyle *et al.* (2013)	grain growth	
Wang *et al.* (2000)	grain growth	
Elsey *et al.* (2009); Elsey *et al.* (2011)	grain growth	
Esedoglu *et al.* (2010); Esedoglu (2010)	grain boundary motion	
Li *et al.* (2008)	grain boundary motion	
Lander *et al.* (2008)	crystal growth, quartz kinetics	sandstone

Some stochastic pore reconstruction models attempt to introduce physical intuition, albeit using a randomised algorithm. Among these hybrid methods are models of crystal or grain growth. One of the best known techniques for growth of an object is the Monte Carlo Potts model. A precursor to these studies is the seminal work by Grest *et al.* (1985). It was later implemented also by Anderson *et al.* (1989) and Forrest and Tang (1990). This model approximates curvature motion by a stochastic series of near-interface cell-flipping steps. While the basic

Monte Carlo method is relatively easy to implement, it is extremely slow and lacks sub-grid accuracy. Furthermore, the stochastic nature of the Monte Carlo evolution ensures that some type of averaging is needed to approximate the true continuum motion and that certain geometries are difficult to evolve due to lattice limitations. For example, the evolution of a simple circle by mean curvature is very difficult to capture accurately using Monte Carlo methods even on a well-resolved grid. Beyond these significant accuracy concerns, it is also difficult to connect the Monte Carlo method with some notion of real time in the simulation.

Similar to the Potts model, Blikstein and Tschiptschin (1999) developed a stochastic simulation model of grain growth. The medium is represented in a voxelised form and the stochasticity results from a Monte Carlo step of a trial growth. The Monte Carlo step involves an estimate of the free energy of growing a rock element in a voxel adjacent to others, with the energy of occupying a previously empty grid point, being dictated by a phenomenological constitutive law. This law, suggested by Burke (1949), states that the rate of boundary migration is inversely proportional to the average curvature radius. Depending on the crystallographic orientations that the authors promoted and on the neighbourhood of the proposed growth point, they calculated the free energies and used them to determine the probability at which a solid voxel is added. The voxel is added (or not) in a Monte Carlo random step.

This type of algorithm is equivalent to a probabilistic cellular automata type of algorithm in the sense that it uses a set of rules and neighbourhood interactions to update growing grains. It is additionally very similar to the algorithm used by Reiter (2005) to grow snowflakes. Its main limitations occur due to the difficulty in correctly assigning the free energies of adding a solid pixel at an arbitrary point. While Reiter's model is completely empirical as it contains some level of physical intuition, its solution using a continuum approach is susceptible to large model uncertainty. Moreover, it requires an enormous amount of Monte Carlo steps, and since many of them are rejected due to the algorithm, the model is computationally inefficient. Finally, description of more complicated growth

patterns that require non-local information would make the computational cost of the algorithm prohibitive.

Libbrecht (2007) derived a set of algorithms for simulating the diffusion-limited growth of faceted crystals using local cellular automata. It was demonstrated that this technique performs well for realistic crystal morphologies. Most importantly, a more rigorous physical foundation that connects the numerical code to the physics of attachment kinetics and diffusion dynamics was included. The growth code, however, has a heavy dependence on the underlying lattice geometry used, and the assumptions of diffusion-limited growth are not compatible with some geometries (including the shape of the crystal form of calcite).

As a further development of the Monte Carlo growth model, Radhakrishnan and Zacharia (1995) modified the algorithm of Anderson *et al.* (1989). This model resulted in an acceleration of the simulated grain growth and an early estimate of the grain growth exponent that is close to the theoretical value. These modifications eliminated grain coalescence during grain growth and the resulting grain size distribution provided an excellent log-normal fit.

Based on the work of Radhakrishnan and Zacharia (1995), Pyle *et al.* (2013) introduced a few modifications in order to generate polycrystal mosaics growing on a lattice. This study used tightly packed polycrystal morphologies for testing material strength rather than transport properties, and quantified the differences in the final material properties due to different types of crystals. In yet another Monte Carlo grain growth variation, Wang *et al.* (2000) developed a kinetic lattice Monte Carlo simulation-based model for deposition, surface self-diffusion, nucleation and film growth on cubic metal substrates. The method is kinetic as it contains serially multiple trajectories of deposited atoms on the structure. The study depends upon the cubic crystal system and as such is of limited applicability to crystals belonging to other systems, such as calcite.

The signed-distance-function based algorithm for multi-phase motion by mean

curvature described by Elsey *et al.* (2009) (also in Elsey *et al.* (2011), Esedoglu *et al.* (2010) and Esedoglu (2010)) can be thought of as a particular type of level-set method. It is a continuum model, that can be seen as a variation of threshold dynamics, described by Merriman *et al.* (1994), and based on constitutive equations relating motion with surface tension. In order to obtain the correct behaviour at triple junctions, Elsey made a stronger restriction on the level sets than ordinarily enforced. However, other hallmarks of the level-set method are retained: the interfaces are implicitly represented, sub-grid accuracy is obtained and the interface is sharp. On the other hand, standard level-set methods for evolution by mean curvature require the solution of a degenerate, highly nonlinear Partial Differential Equations (PDE). In contrast, the present algorithm is unconditionally stable (allowing much larger time steps to be taken), a feature inherited from its close connection to the diffusion-generated motion of threshold dynamics. In contrast to Monte Carlo approaches, the method retains the physical notion of time, and captures the experimental data reasonably well regarding the evolution of morphologies. However, Elsey's method still hinges on the underlying PDE that governs the physical processes, which is somewhat phenomenological, related to isotropic materials. Finally, the computational cost associated with the model is significantly larger than that of process-based models, since it involves the tracking of level sets.

The most involved continuous physically-inspired model of grain growth was developed by Li *et al.* (2008). Their continuum PDE model consists of four components:

1. the Navier-Stokes equations for fluid flow;

2. an advection-diffusion equation describing the solute transport;

3. a rate equation for the kinetics of dissolution and/or precipitation at the solid/fluid interface

4. an equation describing the motion of the solid-fluid interface due to dissolution and/or precipitation.

This model is constrained to two dimensions, and the issue remains as to how to model the rate equations of dissolution and precipitation without easy access to experimental results.

An advanced physics-based cementation model was developed by Lander *et al.* (2008). This study employs a cellular automata approach to simulate quartz nucleation and a kinetic rate law to model the growth of cement in 2D. An essential aspect in this model is the difference between the euhedral and non-euhedral sites on the grain surface, as the rate of growth on the non-euhedral sites is around 20 times faster. Due to the fact that the overgrowth volume required to achieve a euhedral form, scales with the size of the seeding crystal, on average polycrystalline grains develop smaller volumes of cement than monocrystalline grains of the same size. The model of Lander reproduces this result. The strength of Lander's model is that it takes into account the crystallographic shape of quartz. However, the direction of the crystallographic axes of each grain is limited to only four directions: 0°, 45°, 90° and 135° with respect to the side of the 2D image.

1.7.3 Process-based models

Besides crystal growth, other processes that lead to a formation of solid rock and often modelled are deposition, compaction and cementation. Process-based models recognise that the statistics alone cannot reproduce a porous medium that is useful in predicting a wide range of properties, including permeability. One model focusing on modelling cement fabrics was introduced by Biswal *et al.* (2007) and its extensions by Biswal *et al.* (2009b,a). Realising the need to capture the multi-scale information regarding the morphology of the more complicated carbonate rocks, the authors altered an earlier model (Biswal *et al.*, 1999) to capture and correctly reproduce the resolution dependent porosity and

Table 1.4: Summary table of published process-based models indicating author, simulated processes, rock type of focus and whether or not flow was simulated in the resulting model output. 'LB' indicates that the flow simulation was performed using Lattice Boltzmann method.

Study	Simulated processes	Flow simulation	Rock type
Biswal *et al.* (2007, 2009b,a)	compaction, diagenesis (isopachous cement)	✓(LB)	**oolitic dolostone**
Latief *et al.* (2010)	compaction, diagenesis (syntaxial overgrowth)	✓(LB)	Fontainebleau sandstone
Bakke and Øren (1997); Øren *et al.* (1998); Øren and Bakke (2002, 2003)	deposition, compaction, cementation	✓	various sandstones, Bentheimer sandstone, Fontainebleau sandstone, Berea sandstone
Pilotti (1998)	deposition	✓	sandstone
Jin *et al.* (2003, 2004, 2012)	deposition, compaction, cementation	✓(LB)	unconsolidated sands and sandstones, Fontainebleau sandstone
Mousavi (2010); Mousavi *et al.* (2013)	deposition, compaction, cementation	✓	**carbonates**
Garcia *et al.* (2009)	deposition, compaction	✓(LB)	sands
Thompson *et al.* (2006)	deposition		granular materials
Sain (2010)	deposition, compaction, cementation	✓(LB)	sandstones

permeability scatter of oolitic dolostone, which is one of the most homogenous types of carbonate. The model mimics the growth of cement in a form of thin isopachous layers around ooids which contain dolomite cement grains with radii in the range of $5 - 25\mu m$. This model is not physics-based but rather object-based, and does not accurately simulate more involved diagenetic processes.

The model of Biswal et al. was modified by Latief *et al.* (2010) and applied to syntaxial overgrowth in Fontainebleau sandstone. Latief et al. employed the idea of decorating sediment grains with syntaxial overgrowths crystallites. The study concerned, therefore, quartz crystal geometries and only used a very uniform sediment size.

Bakke and Øren (1997) used a process-based model to recreate sandstones by simulation of the main sandstone-forming geological processes: sand deposition, compaction and diagenesis. They analysed thin section images and used this data as input in geological process simulation. The inputs consisted of the distribution of spherical grains, which was first simulated using a sphere packing model. Modelling of the sedimentation and compaction processes is object-based and followed by a voxelisation of the resulting geometry. Finally, diagenesis modelling is performed on the grid-based model.

Bakke and Øren (1997) focused on quartz overgrowths and subsequent clay coating of the free surface. Quartz overgrowth was simulated by uniformly increasing the radii of all the sand grains in the sand bed, and as such it did not take into account the crystal shape of quartz. The volume of cement was measured and allowed to be equal to the volume loss from the grain interpenetration due to compaction in order to obey the conservation of mass. Alternatively, the target cement could be independently specified with a cement thickness input parameter. The resulting transport and morphology predictions were shown to be in reasonable agreement with original samples. The main limitation of Bakke's model is the unphysical grain deposition modelling, which does not take into account grains deposition due to gravity. Additionally, the model is limited to only

spherical grains with a homogenous size distribution. Finally, the cementation model does not accurately reflect the geometries associated with quartz crystal.

Øren *et al.* (1998) applied Bakke's method to various sandstones and reported a good match between predicted permeabilities and formation factors of a reconstructed Fontainebleau sandstone with published data, as well as a good match between the predicted primary drainage and relative permeability curves for a water-wet Bentheimer sandstone and experimental data. Moreover, capillary pressures and oil relative permeabilities for a mixed-wet reservoir rock were simulated and a fair agreement with experimental measurements was found.

Similarly, Øren and Bakke (2002) applied the same model to reconstruct Fontainebleau sandstone. The results showed a good qualitative match between simulated permeability and experimental data. The study suffers, however, from limited flexibility in the cement growth model. In a subsequent study, Øren and Bakke (2003) demonstrated this model using a Berea sandstone and showed its predictive power in estimating permeability, conductivity, capillary pressure, and relative permeability. Computed two-phase and three-phase relative permeabilities for water wet conditions were in good agreement with experimental data.

A similar approach to modelling deposition can be found in the study by Pilotti (1998), who also developed a framework in order to generate synthetic granular porous media. The difference between the models of Pilotti and Bakke and Øren is that Pilotti simulates the depositional process of spherical grains under the conditions of a viscous fluid at rest, rather than a vacuum. Pilotti reported a good retrieval of the measured porosity and specific surface.

Again similarly to the work of Øren and Bakke, Jin *et al.* (2003) considered sphere packings to model sedimentation, compaction and cementation of conventional and unconventional sandstones, using Discrete Element Method in order to allow spheres to pack in a rectangular box. Additionally, the method accounts for the effects of gravity and contact forces. Syntaxial overgrowth on quartz grains was

simulated using an improved algorithm, based on the grain-growth algorithm by Schwartz and Kimminau (1987). Importantly however, Jin *et al.* (2003) take into account the effect of grain size on the rate of cement growth. Subsequently compaction of the fabric is performed by applying a uniaxial strain.

Jin *et al.* (2003) used Lattice Boltzmann simulations to quantify permeability in their model outputs. A good agreement between the permeability simulated in the synthetic rock with experimental data was reported. In a later study, Jin *et al.* (2012) used the model to demonstrate the impact of the rock forming processes on the evolution of permeability, again on Fontainebleau sandstone. In both studies, Jin et al. focused only on sandstones and only considered one type of cementation. Carbonates are known to be substantially more complex, as they consist of various types of skeletal and non-skeletal grains and can have a heavy diagenetic overprint, often including secondary-porosity features such as vugs and fractures.

Similar to other process-based models involving sphere packing groups, Mousavi (2010) and Mousavi *et al.* (2013) aimed to quantify the effect of rim cementation on pore space morphology and permeability. Unlike other models described so far, Mousavi focused on carbonates. Deposition is modelled through packing of grains and compaction is modelled through reshaping of the spherical grains into ellipsoids. Subsequently, rim cements are added either around all grains or only around disconnected groups of grains to create uniform or patchy cement fabrics respectively. Mousavi's predictions of resulting porosity of the cemented rock were in qualitative agreement with experimental trends.

In an effort to understand the effects of particle shape and polydispersity on permeability, rather than using only spherical elements for packing, Garcia *et al.* (2009) employed numerical simulations and measured the dependance of hydraulic permeability of granular materials on particle shape and grain size distribution. Several different synthetic sand deposits were generated by altering the grain sizes and simulating settling due to gravity with the presence of contact forces at play.

Subsequently, fluid flow in the resulting grain packs was simulated using a finite element method. The permeability of the model outputs proved to be a fair match with available experimental data. Interestingly, the results suggested that grain shape and size distribution have only a minor effect on the permeability for the systems studied. The authors demonstrated that packings of irregularly shaped grains do not differ substantially from close packings of spherical objects. A similar work focusing on cylindrical as well as spherical packings was undertaken by Thompson *et al.* (2006).

Among the most advanced cementation modelling efforts is the work of Sain (2010). Sain employed three schemes to model cementation in sandstones: rim cements, syntaxial overgrowths and a scheme where cementation depends on flow. The modelling does not simulate diagenetic processes physically, rather it attempts to emulate the effects of diagenesis on pore space using a process-based approach, which is the approach of this thesis as well.

The first cement type, rim cement, is modelled by adding cement at grain-pore boundaries. Sain implements this by increasing the radius of each grain in the deposited and compacted pack of spheres. The increment is modelled to be proportional to the initial grain radius. These packs are then transformed to regular grids.

The second cement type, nucleation cement, simulates the effects of nucleation and quartz overgrowth. This scheme uses a grain growth model proposed by Schwartz and Kimminau (1987). The approach is very similar to the implementation of cementation by Jin *et al.* (2004), with the distinction being that Jin et al. included initial grain-size dependence.

Finally, a contact cement scheme is implemented by simulating fluid flow and cementation in tandem. Keehm (2003) discussed this implementation for sandstone μCT scans. The scheme replicates geological scenarios where supersaturated pore fluids preferentially deposit cement at low flux zones. The Lattice

Boltzmann method was used for flow simulation, since it can handle complicated pore geometries and can replicate changes in flow due to small changes in pore microstructure (Chopard and Droz, 1998; Keehm, 2003). At every iteration of the contact cement scheme, low flux pore voxels are selected after the flow simulation. These pore voxels are then transformed into grain voxels. Further iterations are performed until either the porosity of the consolidated microstructure reaches zero or, conversely, the pore network loses pore connectivity and flow can not continue.

1.7.4 Modelling in this thesis

This thesis proposes a process-based and object-based model of calcite cementation with a stochastic initial condition. An implementation of this model is given in 2D as well as in 3D: Calcite2D and Calcite3D. The model does not incorporate compaction, dissolution or replacement of minerals and focuses on cementation. The 3D implementation also includes consideration of deposition. Cementation model assumes static conditions, i.e. a supersaturated solution with respect to calcium carbonate, and concentrates on the geometries of the two types of early calcite cement typical for carbonates: syntaxial and isopachous (see Section 1.6).

In the initial stage of the cementation model, mono- and polycrystallinity is assigned to grains at random as are the crystal axes directions of the monocrystalline grains (initial condition). Next a geometric approach is followed: syntaxial cement is modelled by circumscribing (or decorating) the grains with a shape of one of two rhombohedral forms of calcite ($01\bar{1}2$ or $40\bar{4}1$) and isopachous cement is modelled by adding a layer of constant thickness around the grains. In the 2D study the structure on which cement is grown is an image of a natural carbonate reservoir rock that has been stripped of cement. In the 3D study the statistics of grain size and shape distribution serve to generate a 3D structure in a process-based model that mimics deposition.

In the 3D implementation of the model, the sediment microstructure is created in a process mimicking deposition. The grains are modelled as rigid bodies falling due to gravity and settling on one another in a 3D box. To model the collision physics of the falling grains an, open-source Bullet Physics Library (Coumans, 2015) is employed in a Blender environment (http://www.blender.org). The model is flexible in terms of the shape and size distribution of grains, although in this application, the shapes are limited to convex ellipsoids.

The cementation modelling method introduced in this thesis is one of a few synthetic rock models that have been developed specifically to reconstruct carbonate rocks. Only about 20% of the studies reviewed in the previous sections focus on carbonates. The most notable of these are the process-based models of Biswal *et al.* (2007) and Mousavi (2010) and the statistical reconstructions of Liang *et al.* (2000b) and Okabe and Blunt (2004) as well as the application of the model of Wu *et al.* (2006) by van der Land *et al.* (2013).

The inspiration for the modelling work herein stems from Prism2D, a software simulating sandstone diagenesis developed by Lander *et al.* (2008). Theirs is the only other study so far to differentiate between monocrystalline and polycrystalline grains, to model accurate shapes of growing crystals (quartz) and to account for the effect of growing grains impinging on one another. Lander's model is physically-based as it employs a kinetic rate law to model the growth of cement, which is not the approach of this thesis. Instead a geometric approach is followed, which focuses on recreation of shapes characteristic to calcite cements (see Section 1.6). Prism2D models crystal growth on euhedral as well as on non-euhedral faces of the quartz crystal, while Calcite2D only models syntaxial cement on non-euhedral faces in the rapid epitaxial stage. Calcite2D, however, is fully flexible in terms of directionality of the crystal axes that monocrystalline grains can take, whereas Prism2D is limited to only four directions. Moreover, the model in this thesis is implemented in 3D (Calcite3D), as opposed to Prism2D, which enables better flow property prediction.

Additionally, this study is one of few that models more than one type of cement. Almost all studies focus on either modelling syntaxial overgrowths or fringe cements. The only other study that models more than one type of cement is that of Sain (2010).

Regarding the model of deposition in 3D, Calcite3D has significant flexibility in the shapes of grains as a full spectrum of ellipsoidal shapes can be modelled. The majority of models in the literature focus exclusively on spherical grains. The only exception in that regard among the reviewed studies is the work of Mousavi (2010) and of Garcia *et al.* (2009).

1.8 The Lattice Boltzmann method

After cemented synthetic samples are derived with the use of Calcite2D in the 2D study and Calcite3D in the 3D study, flow is simulated using the Lattice Boltzmann method in order to obtain absolute permeability.

Lattice Boltzmann (LB) simulation is one of the main methods used to predict flow through digital porous media (Chen and Doolen, 1998; Zhang *et al.*, 2002; Ma *et al.*, 2010; Kang *et al.*, 2010; Boek and Venturoli, 2010). Such simulations are often used to estimate particular quantities of interest concerning either the fluid flow or the porous medium. Amongst the most interesting flow properties in reservoir engineering (our current area of focus) is the permeability of porous subsurface rocks that host fluid, and estimating permeability is important in a wide variety of other fields such as biology (Grodzinsky, 2011; de Monte *et al.*, 2013; Khaled and Vafai, 2003; Sun *et al.*, 2007), medicine (Lorna J. Gibson, 2010; Sun *et al.*, 2007), hydrology (Zhang *et al.*, 2005), soil science (Patrick A. Domenico, 1997; Zhang *et al.*, 2005) and material science (Gibson *et al.*, 2001; Beavers and Joseph, 1967; Camargo *et al.*, 2012; Ghassemi and Pak, 2011).

In the field of geoscience, LB method is used for the simulation of oil and gas

behaviour in porous rock (Hazlett *et al.*, 1998; Coles *et al.*, 1996; Auzerais *et al.*, 1996; Jin *et al.*, 2004; Hao and Cheng, 2010). LB simulations of flow through pore geometries derived from real rocks have been used to estimate effective permeability (Gao *et al.*, 2012) or relative permeability (Ramstad *et al.*, 2010; Grader *et al.*, 2010), using microporous rocks (Jeong, 2010; Harland *et al.*, 2015), sandstones (White *et al.*, 2006), including the same Fontainebleau sandstone used in this thesis (Ferréol and Rothman, 1995), and carbonates (Grader *et al.*, 2010). Ever since computational power became sufficient to run LB on realistic synthetic rock samples, this method has been a popular alternative to the direct solution of the Stokes equation. This is particularly true for complex, multi-scale media: direct numerical simulations using gridded methods require extremely refined grids to capture the small scale complexities and the definition of boundary conditions becomes cumbersome due to the complexity of the geometry, both of which lead to a high computational cost of simulation.

The LB method simulates fluid flow by using the Boltzmann equation to dynamically update the fluid density as described by a set of interacting particles. LB methods represent the fluid as a large number of particles, and calculates the probability (density) of finding a given particle at a given position on a discrete lattice mesh. The algorithm consists of two steps: advection and collision. In the advection step the particles are propagated along their velocity vectors to adjacent lattice sites. In collision, the particles converging at each lattice site interact: they collide and are redistributed according to their velocities as follows. First the density (ρ) and the velocity vector (u) of the fluid at all points in the lattice are calculated. Then the average velocity and force terms are calculated and the equilibrium densities for each velocity vector are found. Finally collision takes place in which the particle densities are adjusted through the fundamental equation of the LB model (Sukop and Thorne, 2006):

$$f_i(x + v_i\Delta t, t + \Delta t) = f_i(x, t) - \frac{1}{\tau}(f_i(x, t) - f_i^{eq}(x, t)) \tag{1.3}$$

where i denotes the direction of momentum, f_i is the directional density (probability density function (PDF) per unit space of a particle traveling in direction i), f_i^{eq} is the equilibrium PDF, t is simulation time, Δt is the simulation time step, x is the location of the particle in the lattice, v_i is the velocity of the particle in direction i, and τ is the relaxation time parameter that is related to kinematic viscosity ν through the relation (Breitmoser *et al.*, 2012):

$$\nu = \frac{\tau - 0.5}{3} \tag{1.4}$$

The method relies on several parameters, some physics-based and some algorithmic, which must be calibrated before using LB to predict quantities of interest. The calibration of LB models has commonly been achieved by comparing the velocity of fluid flow simulated through a specific pore shape to one predicted analytically by the Hagen-Poiseuille equation (Narváez *et al.*, 2010). The LB parameters are chosen to minimise the discrepancy of the flow profile that develops in specific pore sizes to corresponding theoretically predicted values. The deficiency of that method is that in real media the permeabilities to be matched by LB come from laboratory experiments and the above theoretical value of τ does not include any experimental uncertainty, nor does it necessarily relate to real pore geometries which often contain a distribution of pore shapes and sizes with complicated network connectivity.

To remedy this issue this thesis develops a framework for calibration of the model parameters of LB. It is an attempt at applying Bayesian Uncertainty Quantification framework to assess the predictive envelope of LB.

1.8.1 Flow simulation in 2D vs 3D

This work aims to provide insight into the permeability of porous media through two approaches: a high resolution and large scale 2D study and a lower resolution and smaller scale 3D study.

Modelling permeability in 2D has limitations, the most significant of which is a loss of the impact that rock anisotropy has on permeability. This is not an issue in the work presented herein, as carbonate grainstones, which are the focus here, are isotropic. Another limitation of the 2D method is the loss of connectivity of pores in the 3^{rd} dimension, which affects permeability. As a result, some samples found in 2D to have no percolation might actually have pore connectivity in the 3^{rd} dimension and a non-zero permeability.

Despite the disadvantages, 2D permeability studies are still performed (Boek and Venturoli, 2010; Mahmoudi *et al.*, 2013). The advantage of 2D modelling is that samples of larger sizes and higher resolutions can be afforded. Cemented synthetic samples used in the 2D study in this thesis are 2000^2 pixels and have pixel size of $5\mu m$. This is effectively an order of magnitude higher than what is usually done in the 3D modelling. This size of sample allows modelling of a large number of grains and keeps the grains 'smooth' to the eye (non-pixelated). Also, it is large enough to allow for in-sample heterogeneity, e.g. the presence of areas with varying porosity within one sample.

A major disadvantage of modelling permeability in 3D is the limitation to the sample size and resolution, as the computational cost scales with it. So far 3D rock modelling that involves LB simulations is undertaken for samples of around 400^3 voxels (Ahrenholz *et al.*, 2008; Coon *et al.*, 2014; Harland *et al.*, 2015; Zhang *et al.*, 2013; Boek and Venturoli, 2010; Halisch, 2013; Zalzale, 2014). Synthetic samples used in a 3D study in this thesis have a computational size of 300^3 voxels and voxels $10\mu m$ in size. Samples of such resolution are limited to a relatively small number of grains as well as to the accuracy of the pixel representation of

the grains: in some cases thin pore throats are lost due to segmentation at a low resolution, which results in a loss of pore connectivity. All this influences the quality of permeability prediction.

1.9 Thesis Structure

Chapters 2 and 3 concern the 2D study. The details of the 2D implementation of the cementation model, Calcite2D, can be found in Chapter 2. Chapter 3 presents the results of porosity determination and permeability quantification obtained via Lattice Boltzmann simulation for cemented synthetic samples created based on a carbonate reservoir thin-section image stripped of cement.

Chapters 4 and 5 concern the 3D study. Chapter 4 presents the details of the 3D implementation of the model, Calcite3D, including the description of the procedure to generate a 3D sediment which serves as an input for the cementation model. The results of the 3D study follow in Chapter 5.

Chapter 6 presents a Bayesian framework for calibration of the relaxation parameter in the LB simulation as well as a case study of calibrating this parameter using the porosity and permeability data of Fontainebleau sandstone.

Finally, Chapter 7 includes a discussion and conclusions regarding the usefulness of the model in determining the impact of the monocrystalline to polycrystalline grains ratio in carbonate samples on cemented rock properties.

Chapter 2

Methodology of Cement Growth Model in 2D: Calcite2D

This chapter introduces **Calcite2D**, a Matlab implementation of the process-based cementation model in 2D focusing on early marine calcite cements: isopachous and syntaxial. Calcite2D has two stages: Stage 1 defines the sediment type in terms of the ratio of monocrystalline to polycrystalline grains and the directions of the crystal axes of the monocrystalline grains; Stage 2 implements cement growth on both types of grains in a stepwise fashion - 1 pixel layer every iteration. Stage 1 is not computationally intensive and can be undertaken on a personal computer. Stage 2 is much more intensive as it involves multiple iterations on a large matrix (the size of the porous medium) and was performed using the Edinburgh Compute and Data Facility ('Eddie') at University of Edinburgh.

The only process taken into account in the model is cementation. The process of compaction is not a part of the modelling as the focus herein is on *early* cements. Carbonate rocks with early cementation tend to be little affected by compaction, as the rock is lithified early and so it is more difficult to compact (Budd, 2002). The process of deposition is not modelled as the methodology utilises a back-stripped thin-section image of a natural reservoir carbonate.

As mentioned in Chapter 1, Section 1.7.4, this work is inspired by Prism2D, a 2D model of quartz overgrowth developed by Geocosm (Lander *et al.*, 2008). Similarly to Calcite2D, Prism2D differentiates between the polycrystalline grains and monocrystalline grains and it takes into account the accurate shape of crystal form of the modelled mineral. Besides the fact that Prism2D focuses on quartz, while Calcite2D on calcite, there are a few other notable differences between the two models. Prism2D is physics-inspired as it uses kinetic rate law to model the growth of cement, while Calcite2D takes a geometric approach and focuses on the recreation of shapes characteristic for calcite cementation. Prism2D models crystal growth on euhedral as well as on non-euhedral faces of the quartz crystal, while Calcite2D only models syntaxial cement on non-euhedral faces that occurs in the rapid epitaxial stage. However, Calcite2D does allow full flexibility in the directionality of the crystal axes of monocrystalline grains, which Prism2D does not.

This chapter presents the full methodology to create 2D calcite cement in a porous medium, starting form the treatment of the initial medium, the two stages of Calcite2D and finishing with a procedure to obtain the absolute permeability using Lattice Boltzmann simulations. This procedure is used to create thousands of cemented synthetic samples for various ratios of monocrystalline and polycrystalline cements and for two different calcite crystal forms. Due to the cost of a Lattice Boltzmann simulation, permeability is calculated only for a subset of all generated synthetic samples. Analysis of all results for the synthetic samples, including porosity (ϕ) and permeability (κ), is presented in Chapter 3. This chapter concludes with a discussion of the deficiencies of the 2D method, some of which are eliminated in the 3D version of the model introduced in Chapter 4.

Figure 2.1 shows the general steps in the methodology presented in this chapter. It starts with the segmentation and binarisation of a thin-section image that serves as an input to Calcite2D (a). In Stage 1 of Calcite2D, grains in the binary image are identified and a portion of them, chosen at random based on a model input, is labeled monocrystalline (b). For every monocrystalline grain, the crystal axis

(c-axis) is defined, also chosen at random from all possible 3D orientations. In Stage 2 of Calcite2D, the cement is grown on all of the grains (c). The type of cement is determined by grain type, with syntaxial growth on the monocrystalline grains and isopachous cement on the polycrystalline grains. The permeability of the cemented rock is then obtained via a Lattice Boltzmann simulation (d). The details of all steps of this methodology are given in the following sections.

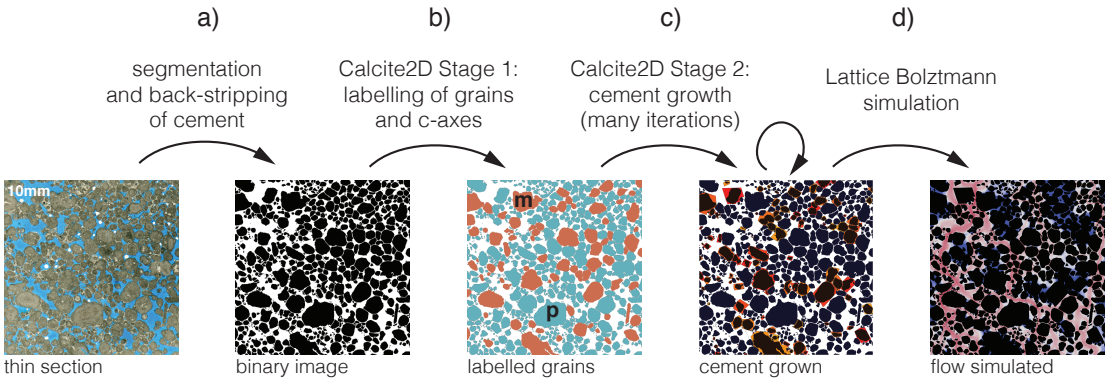

Figure 2.1: The methodology of the 2D cementation modelling; a) the thin-section image is segmented into pore, sediment and cement; cement is stripped and the image is binarised, b) Stage 1 of Calcite2D labels the grains as either monocrystalline (red, m) of polycrystalline (blue, p) and determines the directions of the crystal axes of the monocrystalline grains, c) Stage 2 of Calcite2D grows 1 pixel layer of cement every iteration until completion (reds - syntaxial cement, blues - isopachous cement), d) a Lattice Boltzmann simulation is performed on the final medium to obtain permeability.

2.1 Treatment of the 2D Porous Medium

To showcase the capabilities of Calcite2D a thin-section image of a real carbonate reservoir rock with early calcite cements is chosen (Figure 2.2a). The steps in the procedure that lead from the original colour thin-section image (Figure 2.2a) to the binary image that is used as an input to the cementation model (Figure 2.2c) are as follows:

1. first-pass automatic segmentation;
2. manual adjustment in a graphics package;
3. image resizing (from 3779^2 to 2000^2 pixels);
4. grain separation (post-processing step 1);
5. fine grains removal (post-processing step 2).

The details of these steps are given below.

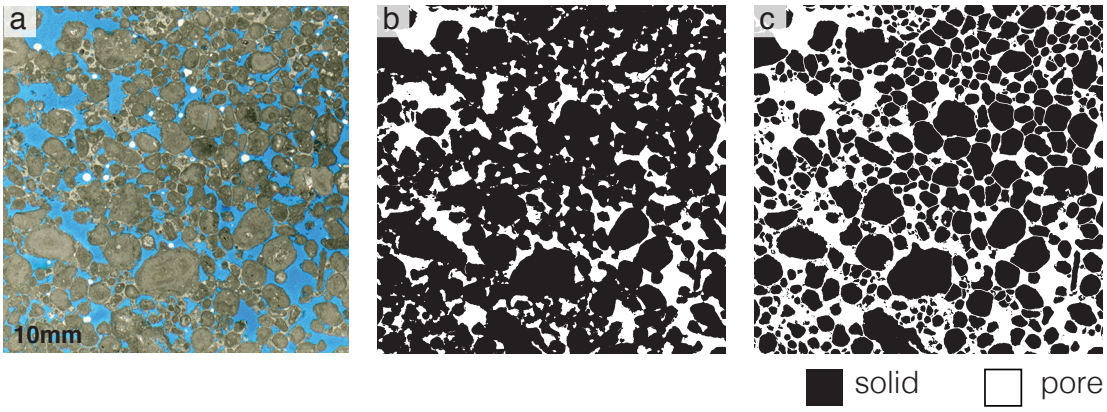

Figure 2.2: The porous medium used in the study; a) RBG thin-section image of a carbonate rock, b) manually segmented binary image of this thin-section differentiating between solid and pore (porosity 23.7%), c) the same image stripped of cement showing grains (black) and pore space (white) with manually inserted grain boundaries so that none of the grains are touching (porosity 36.3%) and with fine grains removed.

Since Calcite2D requires a binary image of carbonate *sediment*, the preparation of a thin-section must include segmentation that differentiates between grain, cement and pore as well as binarisation. Automatic methods for image segmentation did not work well for these purposes and significant amount of manual processing was necessary. This is because automatic methods do not differentiate well between grain and cement, which have very similar colour in the original image (Figure 2.2a). Cement tends to be slightly lighter than the rim of the grain, however

the same colour can be found in the grain interior or in other grains located elsewhere in the image. It is therefore impossible to specify a colour filter to target *exclusively* cement without also targeting a significant amount of grain pixels.

The first-pass automatic segmentation that is undertaken here, results in the segmentation of the original image (Figure 2.2a) into two classes that are essentially 'pores' and 'solids'. This segmentation is performed in Matlab on the original image, which has three colour channels: red, green and blue (RGB) and is based on filtering these three colour channels. The 'pore' class is observed to be either blue (high values of the blue channel) or white (high values of all channels), while the 'solid' class has much lower values of the blue channel and significantly higher values of the green and red channels.

After the initial automatic segmentation differentiating between the pores and solids in the original RGB image is performed, a significant amount of manual adjustment in a graphics package is undertaken to strip the cement off the grains. The resolution of the original colour image (Figure 2.2a) is 3779 pixels per $1cm$ ($2.65\mu m$) and manual segmentation is performed at that resolution. The resulting sediment image has 775 grains and both convex and concave grains are present.

Before the back-stripped binary image undergoes the two post-processing steps the image is resized to a more computationally manageable size of 2000 pixels per $1cm$. This is a good compromise between the resolution ($5\mu m$ is sufficient for the type of modelling in this thesis) and sample size that can be afforded computationally (see Section 2.4.1 for a discussion of resolution in Lattice Boltzmann simulations). Resizing results in a negligible change in porosity: the porosity of the 3779^2 pixel image is 36.15% and the porosity of the 2000^2 pixel image is 36.14%.

As the cementation methodology requires that all grains in the initial porous medium are disconnected, a manual intervention is required in a post-processing of

the back-stripped binary image. In the few instances that two grains are touching, a thin pore-throat is manually added to separate them. Such complete separation of grains is artificial as it does not occur in natural media, especially for those that underwent compaction. Shortly after deposition the grains in grainstone have just a few points of contact in 3D, which in a 2D section manifests as nearly all grains appearing to be disconnected and not touching. However, in the process of compaction the areas of contact between the grains increase, as the grains are pushed against each other. That is why some of the grains are observed to be touching in the thin-section image. However, due to the fact that the number of grain separations required is small, this artificial manual intervention has a negligible impact on porosity: an increase by 0.13% from 36.14% to 36.27%. The impact of grain separation on permeability is larger, but not dramatic: an increase by $640mD$ from $7080mD$ to $7720mD$ (9.0% change, see Table 2.1).

This post-processing step impacts the porosity and permeability results of the cemented model outputs presented in Chapters 3 and 5. It may artificially increase the porosity of the model outputs by up to 0.13% and the permeability by up to 9%. However, this is an issue mostly for the cemented model outputs with very little cement, as cement growth is very effective in closing the pore throats and making up for the material that was removed in this post-processing step. This is especially true for the isopachous cement, which renders all samples non-percolating after only three iterations, which is equivalent to a cement fringe 3 pixels or $15\mu m$ thick.

Table 2.1: Changes to the properties of the porous medium due to post-processing procedures.

Processing stage of the binary image	Porosity [%]	Permeability (LB) [mD]
back-stripped image	36.14	7080
step 1: grains separated	36.27	7720
step 2: fine grains removed	36.31	7940

As a further post-processing step, the connected solid pixels with an area smaller than 26 pixels ($650\mu m^2$) are removed from the image (the solid pixels are replaced with pore pixels). These fine 'grains' are mostly artefacts of the automatic segmentation and partly of the manual segmentation procedures and as such are not 'real' grains, thus a choice is made not to include them in the set of grains of the sample. There are 171 such 'grains' and their removal causes a reduction of the number of grains by 22% from 775 to 604 grains. These very fine 'grains' have a negligible effect on the porosity of the medium as after their removal it is increased merely by 0.04% from 36.27% to 36.31%. Permeability is increased by $220mD$ from $7720mD$ to $7940mD$ (2.8% change, see Table 2.1). The fine 'grain' removal makes the subsequent steps in the methodology (Calcite2D stages 1 and 2) less computationally expensive, as the run time of simulations scales with the number of grains. Moreover, the volume of syntaxial cement that would develop on such fine grains would be close to none, rendering the inclusion of these fine 'grains' in cement modelling moot.

Overall, this post-processing step impacts the porosity and permeability results of the cemented model outputs presented in Chapters 3 and 5 only slightly: the effect on porosity is negligible and the permeability may be artificially increased by up to 2.8%. Moreover, the fact that these fine 'grains' are mostly artefacts of the segmentation procedures justifies their removal from the image.

The unpublished laboratory data supplied by Petrobras associated with this reservoir rock type in 3D are $\phi = 24.4\%$ and $\kappa = 4700mD$. Due to the heterogeneity of carbonates, and the fact that a thin-section image carries only 2D information, the properties of the specific 2D rock image that is used in the modelling (Figure 2.2a) are expected to be different. The porosity of the segmented thin-section with natural cement (Figure 2.2b) is remarkably close to these data: 23.7%. The permeability, however, is dramatically different, as the naturally cemented medium is found to be not percolating, which is equivalent to $0mD$.

A *qualitative* assessment can be made that the naturally cemented medium (Figure 2.2b) has less pores and these are also smaller than in the back-stripped medium (Figure 2.2c). To *quantify* this observation, a method to determine the pore size distribution is used. This method consists of making a distance map of the pore space and multiplying it with the skeleton of the pore space. Implementation of this method involves the use of *bwdist* and *bwmorph* functions of the Image Processing Toolbox of Matlab. All non-zero entries of the resulting 2D matrix represent the pore width at a given pixel along the skeleton. This method gives the pore width at each point (pixel) along the skeleton. It is not biased towards the larger pores, as most pore size calculation methods are (Bhattacharya and Gubbins, 2006; Münster and Fabry, 2013; Rabbani *et al.*, 2014), as it represents very narrow pore throats as well.

To represent the impact of a group of pores of a given size on the properties of the rock better, the number of pores is multiplied within a given size interval (e.g. radius length between 20 and 22 pixels) by the mean of the interval (e.g. 21 pixels) to get the cumulative pore radius size distribution. Both curves in Figure 2.3, representing the back-stripped and the naturally cemented media, have significant peaks at small pore radius - around 10 pixel ($50\mu m$). This represents the narrow pore throats in both images. In case of the naturally cemented medium the peak at low radii lengths is much smaller compared to the back-stripped medium. Moreover, the tail for larger pore sizes shows decrease in number and volume of the larger pores. The difference between the two curves is greater for small pores than for large pores. The area between the two curves is proportional to the pore space volume (or area in the 2D case) lost in the process of cementation. This suggests that more pore space is lost in the smaller pores than the large pores.

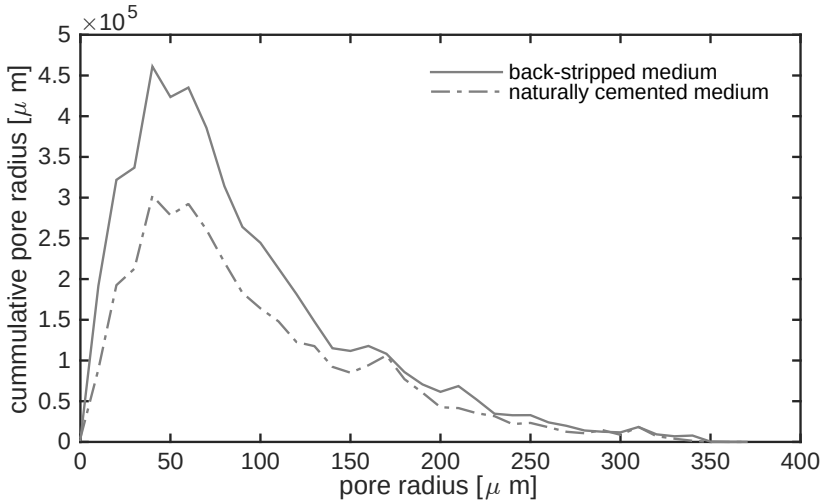

Figure 2.3: Cumulative pore size distribution for the back-stripped and naturally cemented media used in this study.

2.2 Calcite2D

The calcite cementation model presented herein is based on the premise that there are two basic types of carbonate sediment grains: polycrystalline and monocrystalline (see Introduction, Section 1.5). These two types of grains develop different types of early calcite cement that have different volumes and geometries and therefore have a different impact on cemented rock properties (Scoffin, 1987; Tucker and Wright, 1990). Polycrystalline grains have seeding sites on the grain boundary that develop cement growth with many different crystal axis directions. This results in a layer of nearly constant thickness developed round grains, an isopachous cement. The seeding sites on monocrystalline grains grow cement in optical continuity to the grain itself (the same crystal axis orientation), resulting in syntaxial cement (see Section 1.5).

Calcite2D has two stages, each of which takes one input parameter. The general steps of Calcite2D implementation are shown in Figure 2.4. Stage 1 involves grain identification and labelling as either polycrystalline of monocrystalline based on the input parameter α_0 (Figure 2.4a) as well as definition of crystal axes direction

and establishing of the polygonal bounds of epitaxial growth (Figure 2.4b). In the code, α_0 goes through a random number generator and the resulting portion of monocrystalline grains in the sample α_n may differ slightly from the input. Stage 2 of Calcite2D implements calcite growth and takes as the input parameter the target width of the isopachous cement that will coat all polycrystalline grains β (Figure 2.4c and d). The details of the implementation follow.

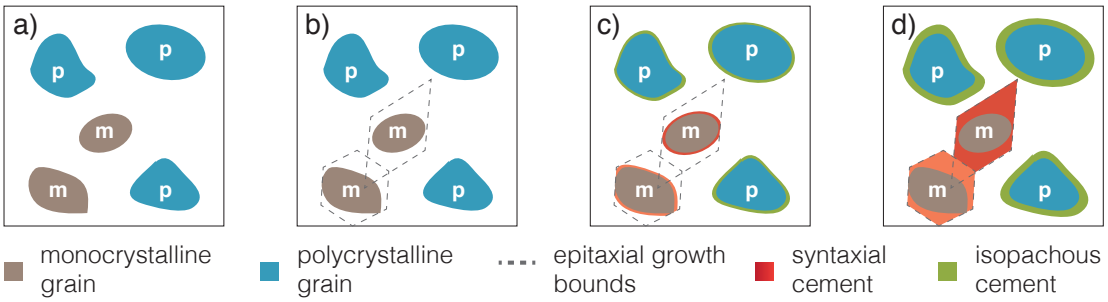

Figure 2.4: Steps of the Calcite2D implementation; a) detection of grains and labelling a portion of them monocrystalline based on the parameter α_0, b) establishing the outer bounds of the epitaxial growth for monocrystalline grains, c) growth of 1 pixel layer of cement around all grains; growth is prohibited outside of the epitaxial bounds, d) repetition of the addition of layers: for polycrystalline grains until the thickness of the isopachous cement fringes specified by the input parameter β is reached, for monocrystalline grains - until all bounding polygons are filled.

2.2.1 Stage 1: grain labelling and crystal axes definition

Grain properties

After the input porous medium is read, the grains are detected and a structure is created with the properties of each grain: the area in pixels, the position of the centroid, the convex hull area, the list of pixels belonging to the grain, and grain perimeter length. Another property calculated is the list of pixels on the outline of the grain (solid pixels 4-connected to at least one pore pixel).

Grain labelling

After the allocation of grain properties, grains are labelled as either monocrystalline or polycrystalline based on a random number generator that uses model input parameter α_0; the post-labelling ratio or monocrystalline to all grains α_n will differ slightly from that input. The grain type property is added to the grain structure when the labelling is completed and grain properties are used to calculate the ratio of the 'volume' (actually area) of monocrystalline grains in pixels to all grains α_v as well as the ratio of 'surface area' (actually perimeter length) of monocrystalline grains to all grains α_a.

Bounds of epitaxial cement

Once the monocrystalline grains are labelled, the bounding polygon that will be filled with cement must be determined. In the case of epitaxial growth, the cement is seeded on non-euhedral faces of the grain in optical continuity to the grain until all faces become euhedral. Due to the fact that calcite belongs to a hexagonal crystal system and the inherent crystal form of calcite is rhombohedral, the shape produced in this rapid growth on non-euhedral faces is a parallelepiped. A parallelepiped, just like a rhombohedron, consists of three pairs of parallel faces. While all faces of a rhombohedron are rhombs, the faces of a parallelepiped are parallelograms.

The reason for this implementation stems from calcite kinetics. Once a euhedral facet with the same orientation as the calcite rhombohedron is reached during the process of precipitation, epitaxial growth ceases (Dickson, 1983). As a result, only the region within a parallelepiped with three pairs of parallel faces, each of which is tangent to the grain, is created via the very rapid epitaxial growth. After the full shape of the epitaxial overgrowth is reached, mantle growth initiates at a much lower growth rate (Dickson, 1983; Lander *et al.*, 2008). Figure 2.5 demonstrates the resulting difference in volume between the full rhombohedral form (or rhomb

in 2D) and the form that grows epitaxially in the shape of a parallelepiped (or a parallelogram in 2D).

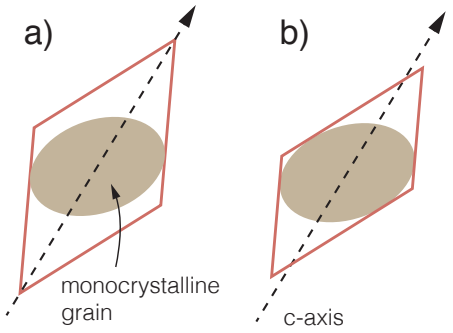

Figure 2.5: The difference in the volume between the full crystal form (a) and the form of the syntaxial cement that is developed around a grain in the epitaxial phase, as a result of a rapid growth on the non-euhedral faces (b).

Since the methodology presented in this chapter is in 2D, the bounding crystals are not in the form of 3D parallelepipeds, but in the form of 2D polygons that can take any possible shape of a *section* of a parallelepiped: a triangle, a tetragon, a pentagon or a hexagon. The approach to finding the shape of this bounding polygon is through a brief venture into the 3^{rd} dimension. For that purpose, a surrogate 3D grain is defined based on the 2D section of the grain as seen in the porous medium image. The smallest parallelepiped that can be circumscribed on this surrogate grain is found and the intersection of that parallelepiped with the plane of the image is determined.

Plane orientations of the chosen rhombohedral form

Two common rhombohedral forms of calcite are selected for modelling: $01\bar{1}2$ and $40\bar{4}1$ (see Section 1.6.6). The details of the implementation are presented on the example of the rhombohedral crystal form with Miller-Bravais index $01\bar{1}2$.

In the hexagonal system a plane has four Miller-Bravais indices $(hkil)$ which come from intersection of the plane with axes x, y, u and z. Axis u is coplanar with

axes x and y and at 60° to both of them (Kelly and Knowles, 2012). The plane with index $01\bar{1}2$ is parallel to the x-axis ($h = 0$), crosses y-axis at $y = b$ ($k = 1$) and z-axis at $z = \frac{1}{2} \cdot c$ ($l = 2$) (Figure 2.6). The following formula can be used to find the vector normal to this plane (Kelly and Knowles, 2012):

$$n = h\,\boldsymbol{a*} + k\,\boldsymbol{b*} + l\boldsymbol{c*} \tag{2.1}$$

where h, k and l are Miller-Bravais indices of the plane and

$$\boldsymbol{a*} = \frac{\boldsymbol{b} \times \boldsymbol{c}}{\boldsymbol{a} \cdot [\boldsymbol{b} \times \boldsymbol{c}]}, \boldsymbol{b*} = \frac{\boldsymbol{c} \times \boldsymbol{a}}{\boldsymbol{b} \cdot [\boldsymbol{c} \times \boldsymbol{a}]}, \boldsymbol{c*} = \frac{\boldsymbol{a} \times \boldsymbol{b}}{\boldsymbol{c} \cdot [\boldsymbol{a} \times \boldsymbol{b}]} \tag{2.2}$$

where $\boldsymbol{a}$, $\boldsymbol{b}$ and $\boldsymbol{c}$ are the vectors defining the unit cell.

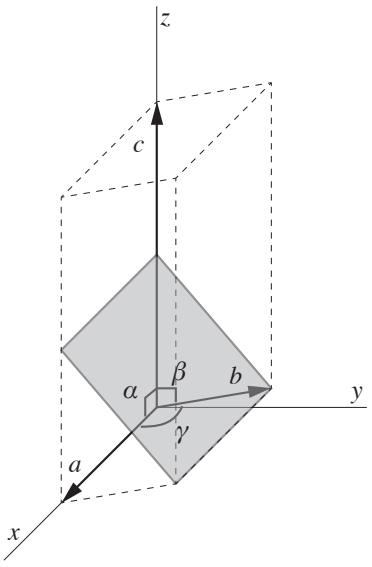

Figure 2.6: The unit cell of calcite with the $01\bar{1}2$ plane (shaded), $a = b = 4.991\mathring{A}$, $c = 17.062\mathring{A}$, $\alpha = \beta = 90°$, $\gamma = 120°$.

The vector normal to the plane with index $01\bar{1}2$ is found using $\boldsymbol{a} = \boldsymbol{b} = (4.991, 0, 0)$ and $\boldsymbol{c} = (0, 0, 17.062)$. The result is $\boldsymbol{n_1} = (0, 0.2314, 0.1172)$. Due to the 3-fold rotational symmetry of the hexagonal system about the z-axis the orientations of the remaining planes of the rhombohedral form can be determined by rotating the known plane by 120° and 240° degrees about the z-axis. For that

purpose, the Rodrigues' rotation formula can be used:

$$\boldsymbol{v_{rot}} = \boldsymbol{v}cos\theta + (\boldsymbol{k} \times \boldsymbol{v})sin\theta + \boldsymbol{k}(\boldsymbol{k} \cdot \boldsymbol{v})(1 - cos\theta) \tag{2.3}$$

where $\boldsymbol{v}$ is the vector to be rotated, $\boldsymbol{k}$ is the unit vector in the direction or the axis of rotation (in this case $\boldsymbol{k} = (0, 0, 1)$) and θ is the angle of rotation. Rotating $\boldsymbol{n_1}$ by 120° around the z-axis yields $\boldsymbol{n_2} = (-0.2004, -0.1157, 0.1172)$ and rotating by 240° yields $\boldsymbol{n_3} = (0.2004, -0.1157, 0.1172)$. A rhombohedron consists of three pairs of parallel faces, so these three vectors ($\boldsymbol{n_1}$, $\boldsymbol{n_2}$ and $\boldsymbol{n_3}$) are sufficient to describe the orientations of all the faces of the rhombohedron.

The three vectors $\boldsymbol{n_1} = (0, 0.2314, 0.1172)$, $\boldsymbol{n_2} = (-0.2004, -0.1157, 0.1172)$ and $\boldsymbol{n_3} = (0.2004, -0.1157, 0.1172)$ describe the angular relationships in the $01\bar{1}2$ rhombohedral form in the case where the crystal axis is parallel to the z-axis. In order to randomise the orientations of the crystals in the sample, all three vectors must be rotated by random angles about the x, y and z axes: θ_x, θ_y and θ_z. This can be achieved with the use of he rotation matrices:

$$R_x = \begin{pmatrix} 1 & 0 & 0 \\ 0 & cos\theta_x & -sin\theta_x \\ 0 & sin\theta_x & cos\theta_x \end{pmatrix}, R_y = \begin{pmatrix} cos\theta_y & 0 & sin\theta_y \\ 0 & 1 & 0 \\ -sin\theta_y & 0 & cos\theta_y \end{pmatrix}, R_z = \begin{pmatrix} cos\theta_z & -sin\theta_z & 0 \\ sin\theta_z & cos\theta_z & 0 \\ 0 & 0 & 1 \end{pmatrix} \tag{2.4}$$

according to the formula:

$$\boldsymbol{n_{rot}} = R_x R_y R_z \boldsymbol{n} \tag{2.5}$$

where $\boldsymbol{n}$ is the vector to be rotated and $\boldsymbol{n_{rot}}$ is the rotated vector.

Surrogate 3D grain

The remaining steps leading to the determination of the 2D bounding polygon are presented in Figure 2.7.

After the direction of the c-axis is determined with the use of the rotation matrices

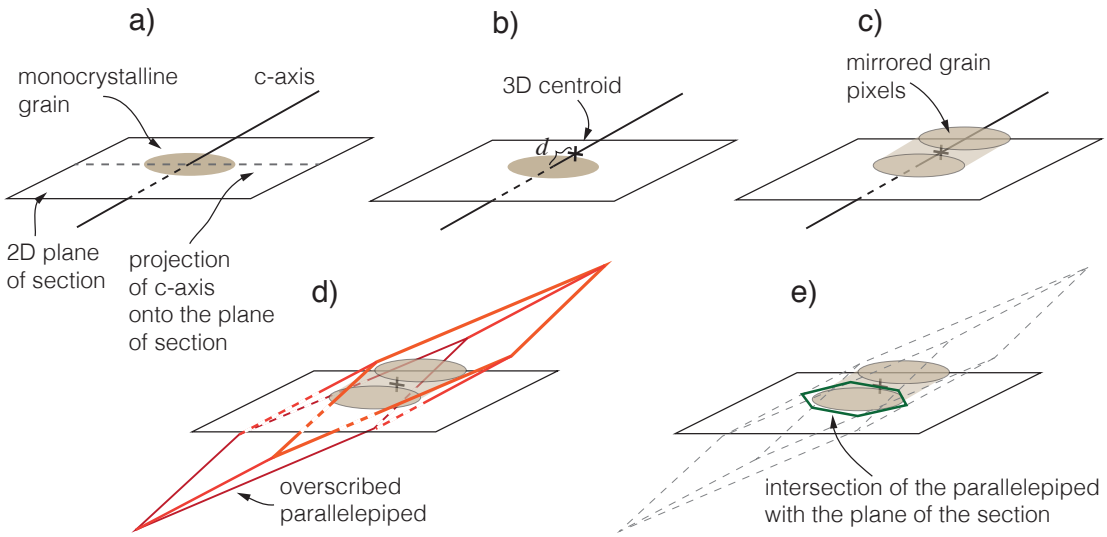

Figure 2.7: The procedure leading to the determination of the bounding polygon for syntaxial cement growth: a) the c-axis direction is defined; b) the 3D centroid is determined; c) the grain pixels are mirrored about the 3D centroid to yield the surrogate 3D grain; d) three pairs of tangential planes are found; they constitute the bounding parallelepiped in 3D; e) the intersection of the parallelepiped with the plane of the porous medium is found.

(Figure 2.7a), a 3D representation of the 2D grain is needed to find the three pairs of parallel planes of the bounding polyhedron. For that purpose a distance d is defined between the known centroid of the 2D grain and the unknown centroid of the surrogate 3D grain (Figure 2.7b). This distance is selected from a normal distribution $N(0, \frac{\sqrt{A}}{10})$, where A is the area of the grain in pixels. In other words, the distance is sampled from a normal distribution with standard deviation of $\sigma = 0.3r$, where r is a length equivalent to a radius of a circle with the same area as the grain. The choice of distribution is arbitrary, but it is made on an assumption that it is likely that the 3D centroid is in close proximity to the 2D centroid visible in the section (normal distribution). Moreover, this choice ensures that the distance between the 3D and 2D centroids are at most equal to the equivalent radius r ($\sigma = 0.3r$), which is a natural assumption.

Following the determination of the distance d for a given grain, the vector $\boldsymbol{cc}$ pointing from the 2D centroid to the 3D centroid is calculated by rotating the vector $(0, 0, d)$ using the rotation matrices (R_x, R_y and R_z). The grain pixels are then mirrored by the means of translation by the vector $2\boldsymbol{cc}$. Figure 2.7c shows the surrogate 3D grain which consists of the pixels of the original 2D grain and the mirrored pixels.

Tangent parallelepiped

The next step involves the determination of the bounding parallelepiped, which consists of three pairs of parallel faces tangential to the surrogate 3D grain (Figure 2.7d). The first pair of parallel planes is found using the vector $\boldsymbol{n_1}$ and a formula for a plane crossing a point: $\boldsymbol{n} \cdot (\boldsymbol{x} - \boldsymbol{p}) = 0$, where $\boldsymbol{n}$ is the vector normal to the plane and $\boldsymbol{p}$ is the directional vector of the point. Point $\boldsymbol{p}$ is the centroid of the surrogate 3D grain, so that the resulting plane $N_1^{\boldsymbol{cc}}$ crosses the 3D centroid. To derive planes parallel to $N_1^{\boldsymbol{cc}}$ that are tangential to the grain, we proceed to calculate the distances between all vertices of the convex hull of the surrogate 3D grain and the plane $N_1^{\boldsymbol{cc}}$. The vertex $\boldsymbol{v_1^1}$ with the maximum distance from plane

$N_1^{\boldsymbol{cc}}$ is the point that the first tangential plane $N_1^{\boldsymbol{v_1^1}}$ crosses. The coordinates of the vertex $\boldsymbol{v_1^1}$ and the normal vector $\boldsymbol{n_1}$ are used in the expression above to derive the equation of the tangential plane $N_1^{\boldsymbol{v_1^1}}$. We then proceed to calculate the distances between plane $N_1^{\boldsymbol{v_1^1}}$ and all of the vertices of the convex hull of the surrogate 3D grain. Again, vertex $\boldsymbol{v_1^2}$ with the maximum distance is the point crossed by the second tangential plane $N_1^{\boldsymbol{v_1^2}}$ and it is used to derive the equation of that plane.

This procedure is repeated for the remaining two pairs of parallel planes, using vector $\boldsymbol{n_2}$ to derive equations of planes $N_2^{\boldsymbol{v_2^1}}$ and $N_2^{\boldsymbol{v_2^2}}$ and vector $\boldsymbol{n_3}$ to derive planes $N_3^{\boldsymbol{v_3^1}}$ and $N_3^{\boldsymbol{v_3^2}}$. Finally, eight vertices of the parallelepiped are calculated as the points of intersection of eight combinations of three non-parallel planes using the formula:

$$\boldsymbol{x} = \frac{(\boldsymbol{x_1} \cdot \boldsymbol{n_1})(\boldsymbol{n_2} \times \boldsymbol{n_3}) + (\boldsymbol{x_2} \cdot \boldsymbol{n_2})(\boldsymbol{n_3} \times \boldsymbol{n_1}) + (\boldsymbol{x_3} \cdot \boldsymbol{n_3})(\boldsymbol{n_1} \times \boldsymbol{n_2})}{|\boldsymbol{n_1 n_2 n_3}|} \tag{2.6}$$

where $|\boldsymbol{n_1 n_2 n_3}|$ is the determinant of the matrix formed by the vectors normal to the planes and $\boldsymbol{x_1}, \boldsymbol{x_2}$ and $\boldsymbol{x_3}$ are the points that define the planes. These points are the set of vertices of the convex hull of the surrogate 3D grain found earlier in the procedure: $\boldsymbol{v_1^1}, \boldsymbol{v_1^2}, \boldsymbol{v_2^1}, \boldsymbol{v_2^2}, \boldsymbol{v_3^1}$ and $\boldsymbol{v_3^2}$.

2D bounding polygon

Finally, the bounding polygon (Figure 2.7e) is derived by intersecting the parallelepiped with the plane of the 2D medium (plane $z = 0$). The polygon is determined with the use of *intersectPlaneMesh* of the *geom3d-2014* toolbox (Legland, 20.05.2015). The intersection between the parallelepiped and the plane can have a minimum of three sides and a maximum of six sides. The polygon constitutes the maximum bounds within which epitaxial growth can occur and syntaxial cement in Calcite2D is prohibited outside these bounds. However, due

to obstacles encountered during growth in the form of impinging grains, only very rarely the full form of the polygon will develop.

To facilitate Stage 2 of the implementation (see Section 2.2.2), the vertices of the intersection polygon most distant from each other are determined and a line passing through then is saved as one of the properties of the grain. Stage 1 is completed after a structure with all grain properties is saved.

2.2.2 Stage 2: cement growth

Once polycrystalline and monocrystalline grains are defined and the associated polygonal outer bounds of the epitaxial growth are established, the cement growth algorithm of Stage 2 of Calcite2D can be applied. Stage 2 takes the target width of the isopachous cement fringes β as an input parameter.

After the input porous medium and the grain properties structure is read, the first step in the code is a verification whether the sample percolates or not. A percolation check is performed in both directions (x and y). This is followed by an iterative process of growing a layer of cement 1 pixel thick until no cement is produced anymore. In the case of the isopachous cement, that stopping point is determined by the input β to Stage 2 code. In this study values from 0 to 10 pixels are used. When the target width of isopachous cement fringes (β) is set to the maximum value used in this study: 10 pixels (an equivalent of $50\mu m$), 10 iterations of Stage 2 of Calcite2D are necessary to grow all of the isopachous cement.

The maximum possible extent of the syntaxial cement is determined by the bounding polygons, which are established in Stage 1. Although the outer bunds of syntaxial cement are determined in Stage 1, the *volume* of syntaxial cement cannot be determined before Stage 2 is completed. This is because the *hypothetical* extent of syntaxial cement delineated by the maximum bounds is often not achieved due

to the effect of grains impinging on one another. Syntaxial cement for a given grain stops growing either when the entire bounding polygon is filled, or when all seeding sites of the grain are blocked by impinging grains. Syntaxial growth in the entire medium ceases when all grains have reached that point. The amount of iterations necessary to achieve that point depends on the size of the bounding polygons, which is controlled by the size of the monocrystalline grains, and on the arrangement of the grains with respect to each other (the impinging potential). In general, Stage 2 takes a significant number of iterations until completion (in this study usually up to 100, but sometimes more than 200) and this number cannot be accurately determined before the simulation.

Isopachous cement growth

Firstly, 1 pixel layer of isopachous cement is grown around all polycrystalline grains, but only if the target width of the isopachous cement fringes β has not been achieved yet. The growth involves an iterative procedure on all outline pixels of each polycrystalline grain. For each of the outline pixels, the pixels in its 4-connected neighbourhood (north, south, east and west) are investigated in terms of their type (whether they are pore or solid). If a neighbouring pixel is found to be a pore pixel, it is turned into a solid (cement) pixel. If it is found to be a solid pixel, it means that an obstacle is encountered and that pixel is not available for cement growth for that grain. After this procedure is completed for all outline pixels of the grain, grain properties are updated with the new isopachous cement layer for that grain.

The iteration on all outline pixels is repeated for all of the polycrystalline grains and upon its completion the porous medium matrix is updated with the new layer of isopachous cement.

Syntaxial cement growth

The following steps and rules are followed for each monocrystalline grain in each iteration of Stage 2:

1. If a grain is monocrystalline and still active, i.e. it has grown cement in the previous iteration, steps 2 through 4 are followed for all outline pixels of that grain.

2. If an outline pixel is within the bounds of the current bounding polygon, investigate all 4-connected neighbouring pixels of that grain (north, south, east and west) in terms of their type (pore of solid).

3. If the neighbouring pixel is a pore and lies within the bounding polygon, it becomes a solid (cement).

4. If any of the neighbouring pixels is solid *and* belongs to another grain, implement 'impinging' effect to update the bounding polygon (details in a Section below).

5. After all outline pixels of a grain have undergone this procedure, update the grain properties with the new syntaxial cement.

6. If no new cement is added for a grain in a given iteration, deactivate the grain (implemented for runtime efficiency).

7. After iteration is completed for all monocrystalline grains, update the porous medium with the new cement.

Impinging grains and the 'shadow' effect

As mentioned in Chapter 1 (Section 1.6.5) the impinging effect, where grains create compromise boundaries and block each other's seeding sites, and the

'shadow' effect, where the cement behind an obstacle is not grown because non-euhedral seeding sites have been blocked, are observed in natural carbonate rocks (J.A.D Dickson, pers. comm). Calcite2D implements these effects by noting that every time an obstacle pixel is encountered, the area in its 'shadow' is of the form of a parallelogram with edges parallel to the two closest sides of the bounding polygon sides. The bounding polygon is adjusted by removal of that parallelogram. This is achieved by replacing the vertices of the bounding polygon that are in the 'shadow' with new points.

Figure 2.8 illustrates the intricacies of the 'shadow' effect implementation. Polygon vertices that are in the 'shadow' are found and replaced in a correct order with new points. First, all lines going through the outline point that encountered the obstacle (P_{fail}) and parallel to polygon edges are calculated as well as the points of intersection of these lines with the edges of the bounding polygon. For each of these lines only the intersection point closest to P_{fail} is considered (Figure 2.8a). The number of these points depends on the number of the edges of the bounding polygon and can vary from 2 to 3. All new vertices of the updated polygon are among these intersection points.

In order to aid the elimination of the points that are not to be the vertices of the updated bounding polygon from the set of the intersection points, a list of intersection points properties is made. This list includes: 1) the distances between the intersection point and P_{fail}, 2) the polygon edge number the point lies on and 3) the point coordinates. Following that, a line passing through P_{fail} and the grain centroid is calculated and the line perpendicular to it a small distance away from P_{fail} towards the grain centroid is determined (the 'perpendicular' line). The intersection points that lie on the opposite side of the perpendicular line to P_{fail} are eliminated from the list of potential new vertices of the updated polygon (Figure 2.8b).

This finalises the list of the new vertices. All that remains is the determination of the correct order in which they are to be inserted in the list of bounding polygon

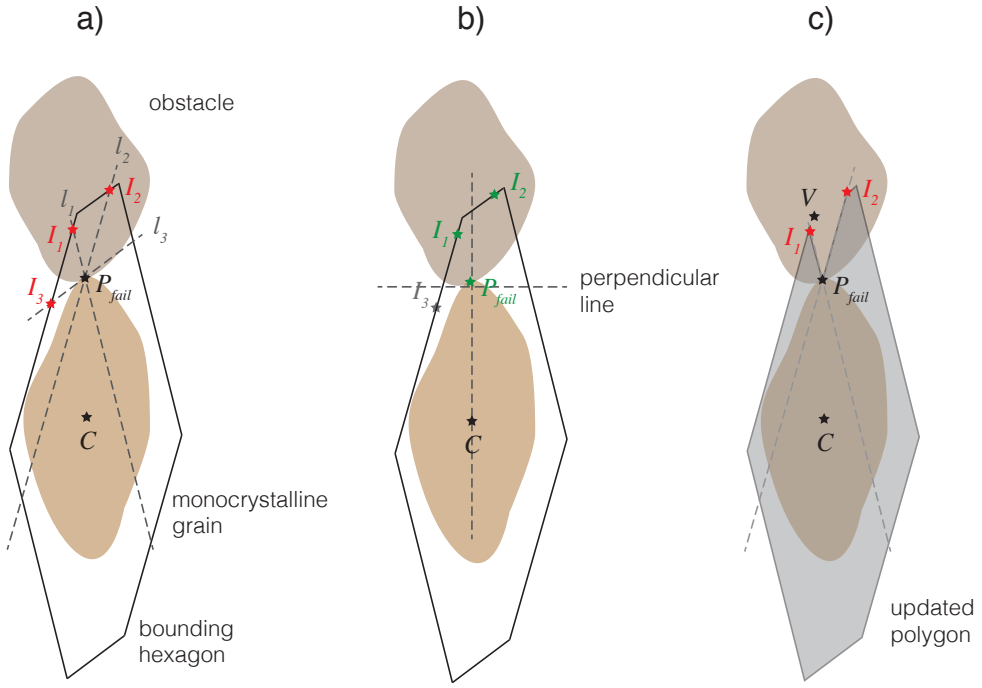

Figure 2.8: The steps in the implementation of the impinging and 'shadow' effects: a) the lines through the point that encounters the obstacle (P_{fail}) that are parallel to the edges of the bounding polygon, l_1, l_2 and l_3, intersect the sides pf the polygon at points I_1, I_2 and I_3 respectively (red); b) only the intersection points on the same side of the perpendicular line as P_{fail} (green) are considered; c) the remaining intersection points I_1 and I_2 (red) together with P_{fail} replace vertex V that lies in the 'shadow' zone to yield the updated bounding polygon.

vertices (a grain property), and the determination of the polygon vertices to be replaced by them, as they are in the 'shadow'. The list of eligible intersection points has a maximum of two points and there are several cases that need to be investigated. If both of these intersection points lie on the same edge of the current bounding polygon, it means that no current bounding polygon vertex is in the 'shadow' and no action is necessary. If the intersection points lie on two different edges, then at least one of the vertices of the current bounding polygon lies in the 'shadow' zone. Depending on the edges the intersection points lie on, i.e. whether they are two consecutive edges of the polygon or not, the current polygon vertices connecting these edges are replaced with three points: I_1, P_{fail}, I_2. This results in an updated bounding polygon (Figure 2.8c).

Figure 2.9 illustrates the result of the impinging and 'shadow' effect as implemented in Calcite2D. In a very simple synthetic porous medium with three monocrystalline grains two of them encounter obstacles during the growth. The bounding polygons are adjusted accordingly to accommodate the effect of the obstacles and the resulting cement volume is diminished by the volume denoted by green stars.

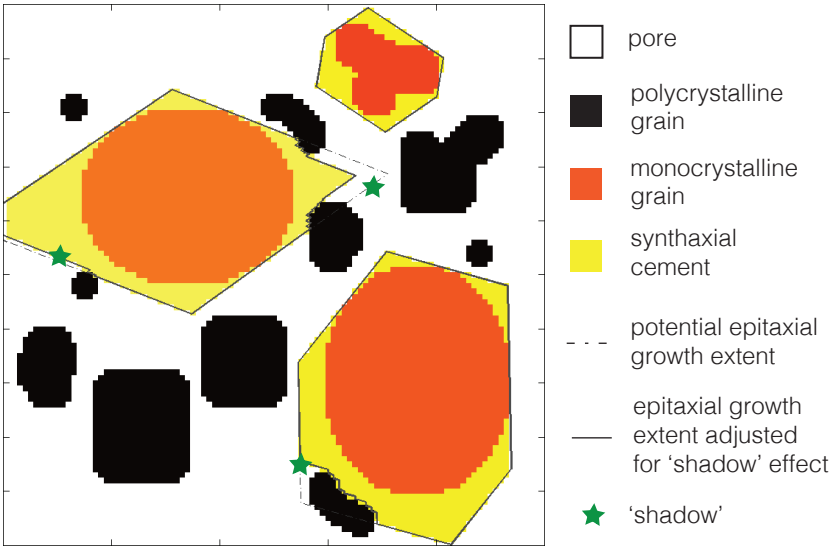

Figure 2.9: The 'shadow' effect implemented in Calcite2D illustrated in a simple synthetic medium of size 100^2 pixels.

Finishing steps

For runtime efficiency purposes, only the outlines of all grains are updated at the end of each cement growth iteration, i.e. the interiors of the grains are not considered. Before all outputs are saved, it is investigated whether the medium still percolates in both directions (x and y).

The entire procedure detailed in Section 2.2.2 is repeated until no cement is produced in an iteration.

2.2.3 Example model output of Calcite2D

Figure 2.10 illustrates two cemented synthetic samples that are grown on the 2000^2 pixel porous medium (Figure 2.2c), one using the crystal form $01\bar{1}2$ (a) and the other using the crystal form $40\bar{4}1$ (b). Both images exhibit textures realistic for calcite cementation. As mentioned in Chapter 1 (Section 1.6.6), crystal from $40\bar{4}1$ is more elongated. As a result, there are more elongated forms of syntaxial cement present in Figure 2.10b than in Figure 2.10a. The fact that the crystal form $40\bar{4}1$ leads to more elongated forms of syntaxial cement results in more iterations necessary for the completion of Stage 2 of Calcite2D. In the example shown, the synthetic sample with crystal from $01\bar{1}2$ (Figure 2.10a) required 109 iterations, while the synthetic sample with crystal from $40\bar{4}1$ required 194 iterations until completion.

2.3 Permeability Prediction Using the Lattice Boltzmann Method

In order to quantify the absolute permeability of the model outputs of Calcite2D, a 2D version of the Lattice Boltzmann code (D2Q9) DL_MESO is used to simulate

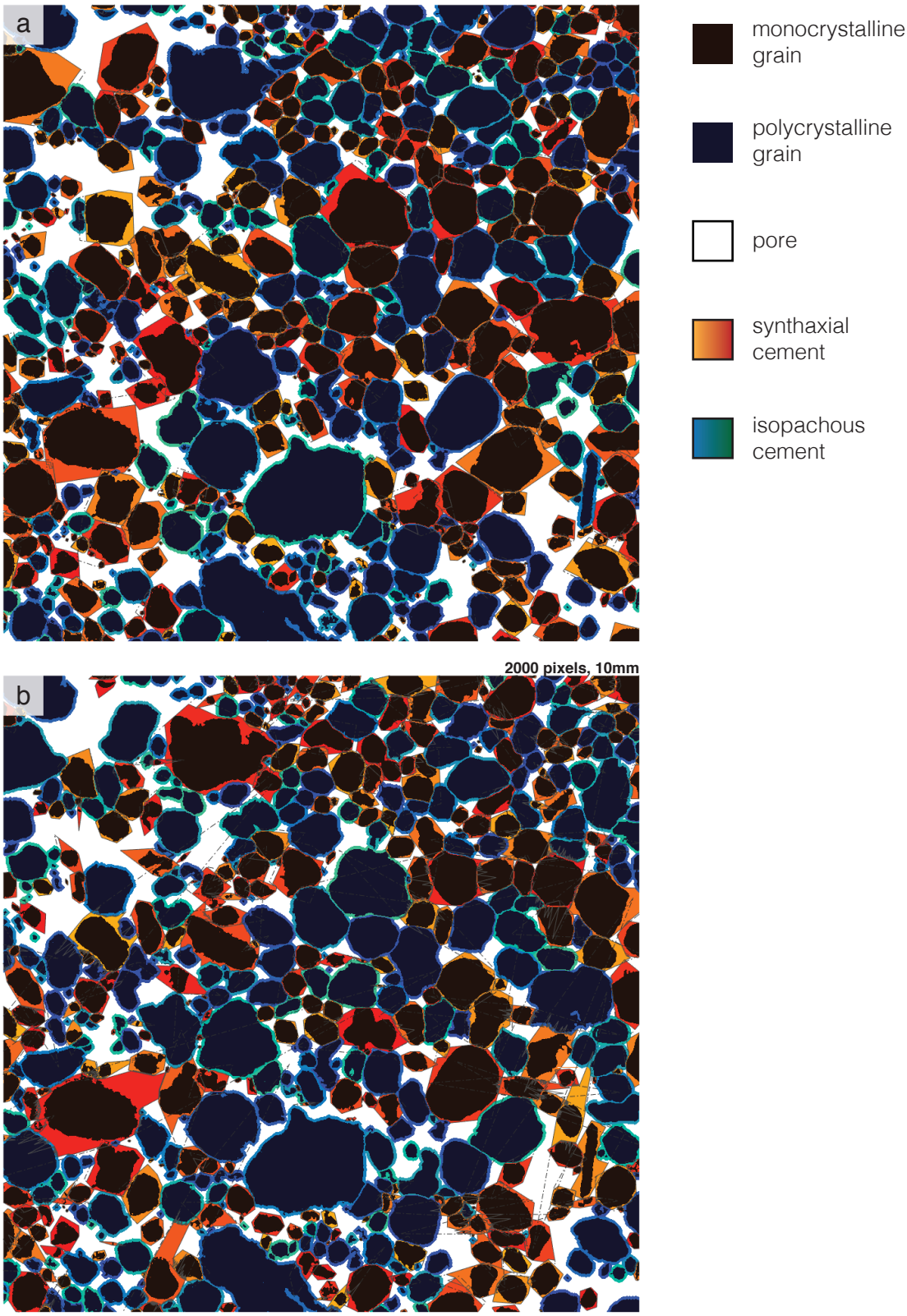

Figure 2.10: Model outputs of Calcite2D for both geometries of syntaxial cement with equal amounts of monocrystalline and polycrystalline grains in the sample ($\alpha_0 = 0.5$) and isopachous cement fringes of width $50\mu m$ ($\beta = 10 pixels$); a) crystal form $01\bar{1}2$, $\phi = 14.9\%$, b) crystal from $40\bar{4}1$, $\phi = 14.2\%$.

the flow through the synthetic media. DL_MESO was developed under the auspices of the Engineering and Physical Sciences Research Council (EPSRC) for the EPSRC's Collaborative Computational Project for the Computer Simulation of Condensed Phases (CCP5) (Seaton *et al.*, 2013).

2.3.1 Lattice Boltzmann simulation set-up

The boundary conditions applied to the porous media include the Zou-He pressure boundary (Zou and He, 1997) on the inlet and outlet sides of media, and a 'bounce-back' fully reflective boundary on the sides parallel to the direction of the pressure gradient. The Zou-He pressure boundary is chosen to minimise the computational cost of the simulation. An alternative to the Zou-He boundary is a periodic boundary, where the fluid exiting the outlet of the domain immediately re-enters the domain at the inlet and the fluid is forced by the application of velocity at the acceleration zone in the inlet. However, the use of a periodic boundary condition on the inlet and outlet of computational domain requires that the medium is either mirrored about the outlet, so that its length doubles (Harland *et al.*, 2015), or that a buffer zone is added on both sides of the medium (Narváez *et al.*, 2010). In both cases the computational domain is increased and so does the simulation time. The Zou-He pressure boundary condition was found to yield reliable prediction of permeability at a lower computational cost (Zou and He, 1997).

The choice of the 'bounce-back' boundary condition for the other sides of the domain was made due to two reasons. Firstly, this computational set-up mimics the experimental set-up for the measurement of permeability, where a core plug is enclosed from all sides except for the direction in which fluid is forced. Secondly, the alternative - a periodic boundary - works best if the pore and solid pixels across the boundary correspond to each other. This can be achieved e.g. by mirroring of the medium. However, if we were to mirror the medium in all three dimensions, it would increase the domain eight times, which would be

computationally prohibitive. Moreover, such mirroring of the sample would introduce correlation into the flow simulation, which would artificially increase flow and permeability prediction. Substituting buffer zones (as mentioned above) for mirror images of the computational domain is only a viable option on the faces perpendicular to the fluid flow. The introduction of such buffer zones on the faces of the medium parallel to the flow direction would result in almost all flow converging to these buffer zones and little of the fluid flowing through the actual sample. The outcome would be a useless result of a very high permeability.

Another alternative to mirroring of the computational domain is to design the medium in such a way that the pore spaces across the faces of the medium parallel to the pressure gradient correspond to one another exactly (Boek and Venturoli, 2010). However, manipulation of the cemented synthetic sample in order to force the inlet and outlet pores to correspond to one another would interfere with the integrity of the fabrics generated by Calcite2D, which is an undesired effect. On the other hand, if a periodic boundary condition is used across a boundary where pore and solid pixels do not match, unnatural pore geometries often occur leading to artefacts in the flow. The use of the 'bounce-back' boundary condition avoids these issues and is realistic for comparison of simulation with lab results.

The pressure difference between the inlet and outlet boundaries across the 2000^2 pixel sample was set to 0.1. This was determined through test-simulations to be a satisfactory compromise between the time to convergence (boosted by high pressure) and absence of turbulent flow and computational stability (promoted by low pressure). The relaxation parameter τ used in this study is 1, a value most commonly used in the literature (Narváez *et al.*, 2010). In the single-relaxation LB scheme, as the one used in this study, permeability calculation is known to depend on the relaxation parameter τ, which is discussed in more detail in Chapter 6.

2.3.2 Permeability calculation

Permeability is computed using the outputs for the density and the velocity of the fluid in the direction of the pressure gradient (fluid forcing direction) according to the formula (Zhang *et al.*, 2013; Boek and Venturoli, 2010):

$$\kappa_{LB} = \nu \frac{\langle U_x \rangle}{\bigtriangledown P} \tag{2.7}$$

where $\bigtriangledown P$ is the pressure gradient across the sample, calculated as the difference between the average density at the inlet pores and the average density at the outlet pores (0.1) divided by the size of the sample in grid units (2000); $\langle U_x \rangle$ is the average fluid velocity in the flow direction across the entire sample (pores as well as solids); ν is the kinematic viscosity of the sample and is equal to $\frac{\tau - 0.5}{3}$ in the D2Q9 implementation used in this study (Seaton *et al.*, 2013), where τ is the time relaxation parameter equal to 1 in all simulations. The relaxation parameter can be calibrated to achieve more accurate permeability predictions. Usually it is calibrated to the analytical Hagen-Poiseuille flow in a pipe (Narváez *et al.*, 2010). As this study focuses on the differences in permeability between various realisations of a synthetic cemented rock, careful calibration of the relaxation parameter is not employed, as an order of magnitude prediction of permeability is sufficient.

The conversion of κ_{LB} from lattice units to physical units is done according to the formula: $\kappa_{m^2} = \kappa_{LB} \cdot r^2$, where the r is the resolution of the porous medium used in the simulation ($5\mu m$). The resulting permeability in the units of m^2 is converted to the more common mD with the formula: $\kappa_{mD} = 1000 \cdot \frac{\kappa_{m^2}}{9.869233 \cdot 10^{-13}}$. The treatment of units is exactly the same in the 2D and 3D simulations, as the 2D sample is effectively treated as a 3D sample, where one of the dimensions (the depth) is equal to 1 lattice unit.

The amount of iterations of the LB simulation necessary to achieve a steady state (convergence) varies depending on the nature of the porous medium. Generally,

flow simulation in samples with high porosity tends to converge faster than in samples with low porosity. All simulations are run for 1,000,000 iterations and partial output is saved every 5,000 iterations, so that the convergence can be confirmed. Figure 2.11 illustrates a sample with porosity 30.5% for which Lattice Boltzmann simulation is run and Figure 2.12 shows that convergence has been achieved by the end of the simulation. In all simulations run in the 2D study the difference in permeability between the last two iterations with saved partial output (i.e. iteration 1,000,000 and 995,000) is less than 0.7%. As LB convergence for samples of low porosity (and generally low permeability) progresses slower than for the high porosity samples, that difference in permeability is smallest for high porosity/permeability samples and increases for lower permeability samples. The mean difference in permeability between iterations 1,000,000 and 995,000 for samples with κ higher than $1000mD$ is 0.005%, for samples with κ between 100 and $1000mD$ is 0.1%, and for samples with κ less than $100mD$ it is 0.13%. In order to obtain a more accurate permeability prediction, mostly for the benefit of the low porosity/permeability samples, an exponential convergence of permeability is assumed and permeability is extrapolated using a formula: $\kappa(t) = ae^{-bt} + c$, where t is the LB simulation time step, and the coefficient c gives the value of the permeability at infinite time.

2.4 Discussion

This Section discusses several aspects of the 2D cement and flow modelling. The choice of sample size and the effects that it might have for permeability simulation are examined in Section 2.4.1. The deficiencies of the 2D cementation modelling are discussed in Section 2.4.3.

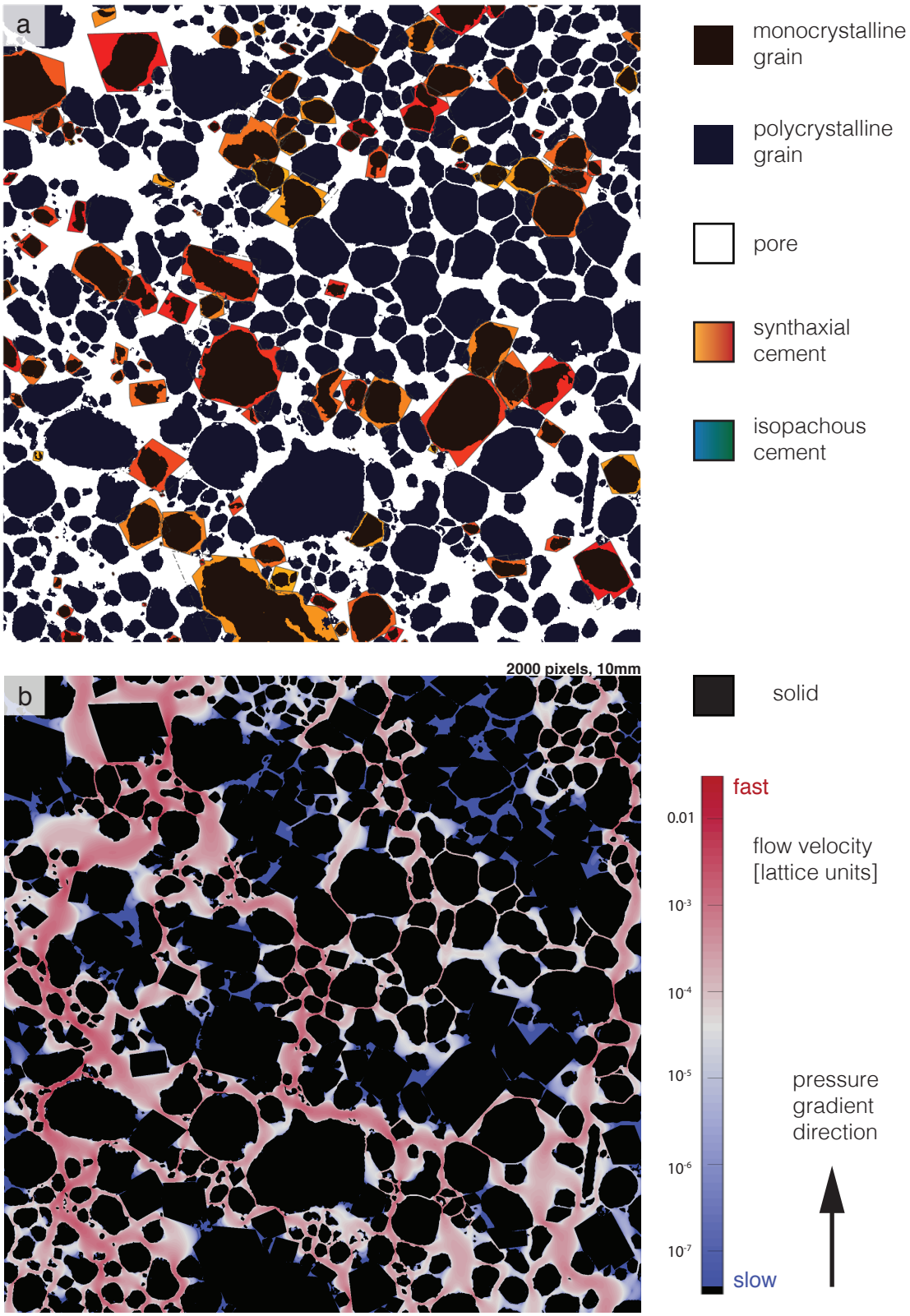

Figure 2.11: A model output of Calcite2D (a) with an associated result of the LB flow simulation (b); a) cemented synthetic sample with crystal form $01\bar{1}2$ obtained using model input parameters $\alpha_0 = 0.21$ and $\beta = 0$ pixels and a porosity $\phi = 30.5\%$, b) log of the magnitude of flow velocity for the same sample ($\kappa = 3200mD$).

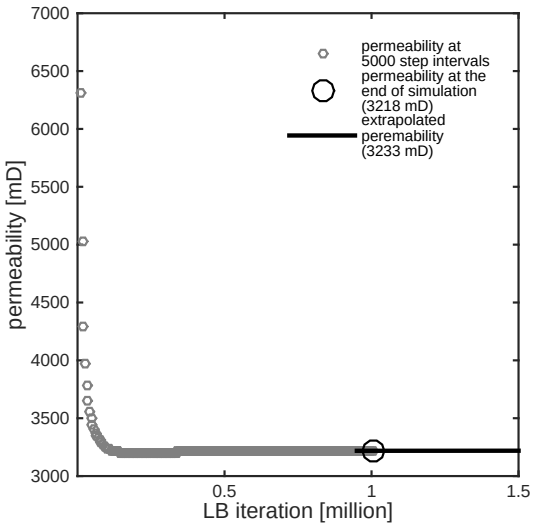

Figure 2.12: The convergence of permeability in a LB simulation in the sample shown in Figure 2.11. The simulation was performed for 1,000,000 iterations, saving output every 5,000 iterations. Five permeability values at the end of of the simulation (equivalent to 25,000 LB iterations) are fitted with a function $\kappa(t) = ae^{-bt} + c$, where t is the LB simulation time step. The value of the coefficient c $(3233mD)$ is used as the permeability of this synthetic sample at infinite simulation time.

2.4.1 Resolution of a sample in a Lattice Boltzmann simulation

When embarking on a study that utilises Lattice Boltzmann (LB) method, a choice must be made as to the size of the computational domain. Typically, the largest sample that is computationally possible is used. Some studies employ a correction for the resolution of the sample (Narváez *et al.*, 2010). Below we discuss the weaknesses of this practice. As a result this study does not introduce such corrections.

The permeability derived via LB simulation depends on the resolution of the sample. To illustrate this issue, the flow through the back-stripped 2D sample used in cementation modelling is simulated. The original image of the back-stripped carbonate (Figure 2.2c) has a size of 3779^2 pixels (sample $s3779$, pixel size $2.65\mu m$). LB simulation is performed on $s3779$ as well as on samples derived by reducing it to a size of 2000^2 pixels (sample $s2000$, pixel size $5\mu m$) and to a size of 1000^2 pixels (sample $s1000$, pixel size $10\mu m$).

Due to the resizing of the image, the pore space morphology differs slightly between these three samples ($s3779$, $s2000$ and $s1000$). The pore connectivity is typically lost when a sample is reduced in size, thus the differences in permeability between the samples are not only an effect of the difference in resolution, but also of the changes in pore connectivity. In order to investigate the effect of resolution alone, samples with equivalent pore space must be investigated. Such samples are derived by expanding $s1000$ by a factor of two and three to yield samples $s1000x2$ and $s1000x3$, respectively. These samples have porosity and pore topology exactly equivalent to $s1000$, but the pixel size differs and is $5\mu m$ and $3.33\mu m$ for $s1000x2$ and $s1000x3$, respectively. Additionally, sample $s2000$ is expanded by a factor of two to yield sample $s2000x2$ with pixel size of $2.5\mu m$. Table 2.2 presents the characteristics of all six samples used in the resolution study.

The three main controls on the permeability derived via the LB simulation are

Table 2.2: Characteristics of the six samples used in the resolution study.

Sample name	Pixel size [μm]	Porosity [%]	Permeability (LB) [mD]	Permeability (LB) extrapolated to pore size of $0\mu m$ [mD]
$s3779$	2.65	36.28	8050	7100
$s2000$	5	36.30	8320	8050
$s2000x2$	2.5	36.30	7420	-
$s1000$	10	36.34	9230	5710
$s1000x2$	5	36.34	7510	-
$s1000x3$	3.33	36.34	6860	-

porosity, pore connectivity (pore topology) and resolution of the sample (see Section 1.3). As all the samples in the resolution study have basically the same porosity (up to the 3^{rd} significant figure, see Table 2.2) the effect of the differences in porosity between the samples is ignored. The differences in permeability of the six samples (Figure 2.13) are assumed to be a combined effect of the differences in resolution and the differences in pore topology/connectivity resulting from image reduction. The nature of the impact of sample resolution and of pore connectivity on permeability are examined below.

Resolution effect

To analyse the resolution effect alone, samples of equivalent porosity and pore topology must be investigated (e.g. $s1000$, $s1000x2$ and $s1000x3$). In this group of samples permeability decreases linearly with pore size and can be fitted with a line: $\kappa(ps) = 3.52 \cdot 10^8 \cdot ps + 5.71 \cdot 10^3$, where κ is the permeability in mD and ps is the pore size in μm (Figure 2.13). The effect of a linear decrease in permeability as pore size in a sample is decreased (all other factors being constant) is documented in the literature (Narváez *et al.*, 2010). The linear relationship allows for an extrapolation of the line to the pore size of $0\mu m$, which is essentially equivalent to the resolution of the physical world. For the group of samples derived from $s1000$, this extrapolation yields a permeability of $5710mD$, which is a considerable

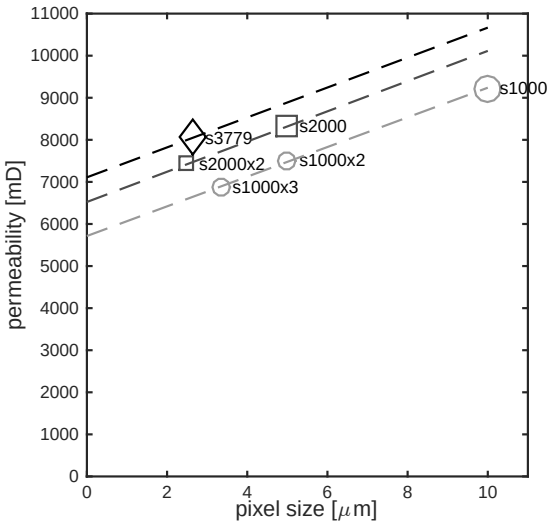

Figure 2.13: The permeability of the six samples investigated in the resolution study. The diamond denotes sample $s3779$, the squares denote samples derived form $s2000$, and the circles denote samples derived from $s1000$. Groups of samples with equivalent pore space morphology ($s3779$, $s2000$ and $s1000$) are fitted with linear fits.

departure from the permeability of $9230mD$ of sample $s1000$ (a change of 38%), although it is within the same order of magnitude.

The linear fit to samples $s2000$ and $s2000x2$ has a slope strikingly similar the slope of the fit to the group $s1000$, as the line equation is: $\kappa(ps) = 3.59 \cdot 10^8 ps + 6.52 \cdot 10^3$ (Figure 2.13). In the case of the group $s2000$, only two data points are available, but a linear relationship is assumed. The extrapolation of the permeability to a pore size of $0\mu m$ yields a permeability of $5280mD$, which is 21% smaller than the permeability of $8320mD$ of sample $s2000$.

The LB simulation on sample $s3779$ expanded by a factor of two was deemed too computationally costly. However, if a permeability-pore size relationship similar to the other sample groups is assumed, then it can be derived by averaging the slopes of the other two lines to derive: $\kappa(ps) = 3.55 \cdot 10^8 s + 7.10 \cdot 10^3$ (Figure 2.13).

The extrapolation of that line to a resolution of $0\mu m$ yields $5760mD$, which is 12% smaller than the permeability of $8050mD$ of sample $s3779$.

Pore connectivity effect

The effect of the differences in pore connectivity between samples can be analysed by an examination of samples with equal pore sizes. In this study there are only two such samples: $s2000$ and $s1000x2$. As the permeability of sample $s1000x2$ is smaller than that of $s2000$ it can be concluded that pore connectivity is *lost* in the process of image size reduction.

Essentially, the vertical spacing between the lines in Figure 2.13 is a result to the pore connectivity change due to image resizing. The spacing between the line for sample $s3779$ (black) and the line for the group of samples $s2000$ (grey) is smaller than the spacing between lines $s3779$ and $s1000$ (light grey). This can be explained as the more an image is reduced in size, the more pore connectivity is lost.

Modelled vs 'true' permeability

The two effects (resolution and pore connectivity) cancel each other to some extent. The technique aiming to improve the quality of permeability prediction by decreasing the pore size while maintaining the same pore space morphology, which can be achieved by extrapolating the permeability results to a pore size of $0\mu m$, tends to *decrease* permeability. However, the technique aiming to improve the quality of permeability prediction by acquiring an image at a higher resolution, which typically exhibits an increased pore connectivity, tends to *increase* permeability.

Even the highest resolution sample available in the study ($s3779$) does not have all the pore connectivity of the physical rock it is derived from, as the details are lost

in the process of image acquisition. In particular, microporosity, which can have a considerable impact on permeability (Harland *et al.*, 2015), is sub-resolution in most imaging techniques and therefore its impact is overlooked. For that reason, the extrapolation of the permeability for that sample to a pore size of $0\mu m$, will not reflect the 'true' permeability of the rock used to acquire the image.

The Lattice Boltzmann method is a model and as such it is only an approximation of the physical world. The wide use of this method however, proves that it is useful in predicting permeability of porous media. In order to improve predictive capability of LB, calibration of model parameters can be undertaken, particularly of the relaxation parameter τ. A Bayesian calibration of the Lattice Boltzmann method is presented in Chapter 6.

Sample size in this study

In this study a choice was made of a sample size of 2000^2 pixels. This size was deemed sufficient to resolve the details of most grains to a satisfactory degree. The permeability results are not corrected for the resolution effect, i.e. extrapolated to a pore size of $0\mu m$, as is done in some studies (Narváez *et al.*, 2010), due to the fact that such correction might artificially lower the result, as argued above.

As the computational time required to complete a given number of LB iterations is proportional to the amount of lattice points (pixels) (Figure 2.14), and because this study required a simulation on hundreds of samples, size 2000^2 was the largest sample that could be afforded. This size required about about 235 CPU hours for $500,000$ iterations, which was the duration of simulation for most samples. However, in some cases even 1.4 million iterations were necessary until a steady state was achieved.

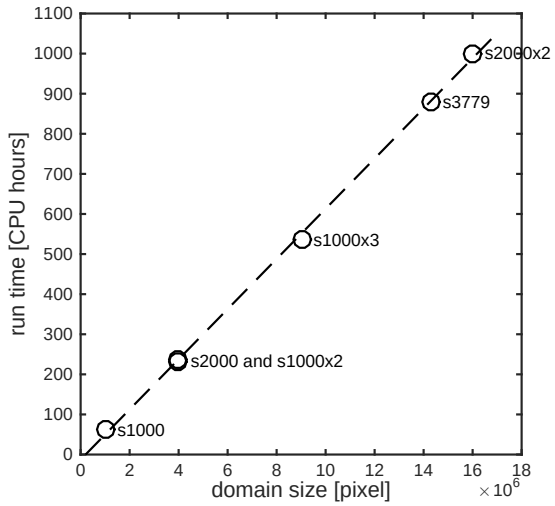

Figure 2.14: The runtime for 500k iteration of a LB simulation for all six samples in the resolution study. Runtime is directly proportional to the number of lattice points (pixels) and takes about 62.5 CPU hours per megapixel per 500k iterations.

2.4.2 Assumption of supersaturation

As noted in Chapter 1 (Section 1.7.4), the cementation model assumes constant supersaturation of the fluid filling the pore space. This means that there is an unlimited supply of calcite to be precipitated as cement. In a realistic scenario in natural carbonates supersaturation is unlikely to remain constant, or close to constant, for extended periods of geological time. However, as *early calcite cementation*, which is the focus of this thesis, occurs during a relatively short time at the beginning of diagenesis, the assumption of continuing supersaturation during that time is reasonable.

Furthermore, in the implementation of the model, cementation continues in pores even after they are cut off from the percolating pore space by growing cement. In a natural media, if such a situation occurs, the precipitation of cement stops as well, as it is impossible to bring any new solute into that pore. This might be considered a limitation of the cementation methodology. However, this limitation is somewhat mitigated by the fact that in realistic scenarios complete separation of

pores rarely happens as there is usually a *micro-scale* connection to the percolating pore space. As the resolution of the models presented in this thesis is quite coarse ($5\mu m$ in the 2D study) micro-scale pores or pore throats are sub-resolution. The decision to allow growth of cement even in pores are cut off is made to make the models more realistic. Moreover, in the case of the 2D model, the pores that are rendered cut off in the 2D almost always would have connectivity with the percolating pore space through the 3^{rd} dimension.

2.4.3 Deficiencies of the 2D methodology

All models are just an approximation of the physical world, but 2D models are automatically one step further away from the 'truth', as they are missing one dimension. Naturally, there are limitations inherent to the 2D modelling and some of such limitations present in Calcite2D are discussed below.

One of the caveats of the modelling methodology is that it requires two steps of manual intervention to the binarised porous medium: 1) introduction of thin pore throats to separate touching grains and 2) removal of very fine grains. Both these interventions result in a negligible increase of the porosity of the medium, as it is increased by a mere 0.17% from 36.14% to 36.31%. The effect of these interventions on permeability is larger, as it is increased by $860mD$ from $7080mD$ to $7940mD$ (12.1% change), but it is still relatively minor.

The permeability of the cemented synthetic samples obtained based on the post-processed medium will have higher permeabilities than the ones that would be derived from the pre-processed medium, but the difference is bound to be smaller than 12.1%. The goal of this study is the examination of the *trends* in permeability results of the cemented synthetic samples, rather than the accurate absolute values. An investigation of the trends in permeability results stemming from cementation is possible as long as cemented samples are grown from the same porous medium, regardless if it is post-processed or not.

In an effort to introduce a full flexibility in the directionality of the c-axes of monocrystalline grains in 3D, Stage 1 of Calcite2D involves a creation of a surrogate 3D grain, as discussed in Section 2.2.1. For that purpose a distance between the 2D centroid and the 3D centroid is modelled with a normal distribution that takes into account the size of the grain. This choice is somewhat arbitrary and it can be argued that other distributions would perform better in creating a realistic porous medium (e.g. a uniform distribution). However, this investigation is beyond the scope of this thesis.

In a 3D deposit, growing cement expands in all three dimensions. As a result, a 2D cross-section of a naturally cemented 3D sample will often exhibit cements grown by grains that lie outside of the plane of that section, i.e. the cement is present in the section but the grain is not. In the 2D cement model presented in this thesis, cement is only grown on the grains present in the initial porous medium. The possibility of other grains growing cement into the plane of the medium is not taken into account. This is another limitation inherent to the 2D model set-up.

Lastly, the most notorious limitation of the 2D rock modelling in terms of its usability in permeability prediction is the fact that the pore connectivity in the 3^{rd} dimension is lost. This leads to unrealistically low permeability predictions. For instance, the experimental permeability associated with the rock used in this study is $\kappa = 4700mD$, while the segmented and binarised 2D image of the same porous medium is not percolating (see Section 2.1). This stark difference in permeability highlights the limitation of modelling permeability in the 2D. The fact that there is no pore connectivity in a 2D cross-section of a 3D medium does not mean that there would be no connectivity in the equivalent 3D medium.

Another contribution to the difference in permeability between experimental data and the thin-section image comes from the heterogeneity of the rock. The fact that a sample of a given rock has a high permeability does not mean that another sample of the same rock must have the same, or even similar permeability.

All of the deficiencies inherent to the 2D modelling methodology discussed in Section 2.4.3 are eliminated in the 3D methodology presented in Chapter 4.

Chapter 3

Modelling of Early Calcite Cement Growth in 2D: Impact of Sediment Type on Porosity and Permeability

This thesis investigates whether the type of grains in carbonate deposit, specifically the fraction of monocrystalline grains in a sample, has an impact on the properties of rocks where early calcite cementation occurs. This chapter examines whether any useful insights to test this hypothesis can be gained in a 2D study, by exploring the impact on porosity and permeability from cemented synthetic samples generated using the methodology described in Chapter 2 (Calcite2D).

Section 3.1 presents relative cement volume and porosity results for synthetic samples produced using two rhombohedral forms of calcite: $01\bar{1}2$ and $40\bar{4}1$, while Section 3.2 presents the permeability results. The results are interpreted and discussed in Section 3.3 and conclusions follow in Section 3.4.

As discussed in Chapter 1, the type of grain in the sediment controls the type of

cement developed during early calcite cementation (see Sections 1.5 and 1.6). The volume of cement and its characteristic textures have an impact on the morphology of the pore space, which in turn has an impact on rock properties, such as porosity, capillary pressure and permeability. For example, cement that lines all pores with a thin layer but does not close any of the pore throats does not have an impact on the connectivity of pores or the tortuosity of flow. As such, its impact on permeability is relatively small. In contrast, if cement grows in a form of a crystal protruding into a pore and proceeds to block the flow in that pore, it might have significant implications for the permeability of the rock, especially in the case where the flow path through this pore is the highest flow velocity channel in the medium and the main contributor to flux.

The focus in this study is on two early calcite cement types specific to two grain types: isopachous cement, which develops on polycrystalline grains, and syntaxial cement, which is developed on monocrystalline grains (see Section and 1.6).

Quantities of interest

The results herein are presented in terms of several quantities of interest: three metrics of the content of monocrystalline grains in the sample: by number (α_n), by volume (α_v) and by area of the seeding surface (α_a). These are controlled by the model input parameter α_0. Another quantity of interest is the second model input parameter: the width of the isopachous cement fringes in pixels (β). Also of interest are the content of syntaxial cement in total volume of cement in the sample (γ_v), porosity (ϕ) and permeability (κ). The names of these quantities of interest and their units are summarised in Table 3.1.

Table 3.1: Quantities of interest.

Name	Definition	Unit
α_0	Stage 1 Calcite2D input parameter: the target content of monocrystalline grains in a synthetic sample	%
β	Stage 2 Calcite2D input parameter: the target width of the isopachous cement fringes	pixel ($5\mu m$)
α_n	content of monocrystalline grains by number of grains	%
α_v	content of monocrystalline grains by volume (actually the area of the grain cross-section in the 2D study)	%
α_a	content of monocrystalline grains by grain surface (actually the grain perimeter in the 2D study)	%
γ_v	content of syntaxial cement in overall volume of cement	%
ϕ	porosity	%
κ	permeability	mD

Generated synthetic samples

Calcite2D is used to generate multiple synthetic samples of varying content of monocrystalline grains (α_0) and varying width of the isopachous cement fringes (β). Two geometries of syntaxial cement are investigated: one that occurs if it is assumed that all monocrystalline grains develop a syntaxial cement of the rhombohedral the crystal form $01\bar{1}2$ and another one when the crystal form $40\bar{4}1$ is assumed. These two crystal forms are among the most common crystal forms of calcite observed in nature (see Section 1.6.6). For both crystal forms, a total of 6959 cemented synthetic samples are generated with input parameter values for the content of monocrystalline grains α_0 ranging from 0 to 100% and for the width of the isopachous cement fringes β ranging from 0 to 10 pixels (representing 0 to $50\mu m$) (Figure 3.1). In order to save simulation time and data storage space, each of the outputs of Stage 1 of Calcite2D (see Section 2.2.1) is used to produce 11 cemented synthetic samples, each one with a different input parameter for the

width of the isopachous cement fringes (β) in Stage 2 of Calcite2D (see Section 2.2.2).

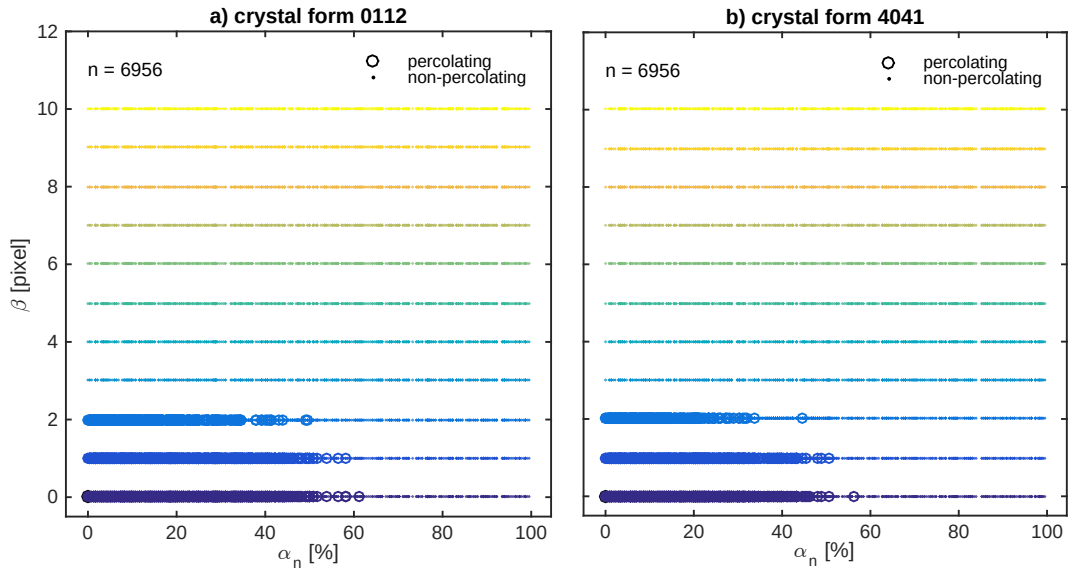

Figure 3.1: 6956 cemented synthetic samples generated for two crystal forms of calcite: a) $01\bar{1}2$ and b) $40\bar{4}1$, shown in the isopachous fringes width - monocrystalline grain content by number parameter space (β vs α_n). Circles denote percolating synthetic samples and dots - non-percolating synthetic samples.

The width of the isopachous cement fringes is constrained to discrete integer numbers ranging from 0 to 10, thus deriving the straight parallel lines in Figure 3.1. the monocrystalline grain content α_0 that is used as the input parameter in Stage 1 of Calcite2D cementation algorithm passes through a random number generator, and so the final the monocrystalline grain content in the sample by number of grains (α_n) may differ slightly from the input parameter α_0. The only percolating synthetic samples are generated for the width of the isopachous cement fringes smaller than 3 pixels (representing $15\mu m$) and the monocrystalline grains content less than 60% (Figure 3.1).

The best representation of the monocrystalline grains content in a sample

In order to obtain meaningful results of the impact of monocrystalline grains content on rock properties, the most suitable metric for the content of monocrystalline grains needs to be determined. Of the three possibilities: content by grain number (α_n), content by volume (α_v), and content by the surface area (α_a), the monocrystalline grain content by number (α_n) is perhaps the most natural parameter. However, it is the content by volume (α_v) that correlates best with porosity, and so with the volume of cement produced (Figure 3.2). Therefore monocrystalline grains content by volume (α_v) is used as a metric for the content of monocrystalline grains in all further analysis.

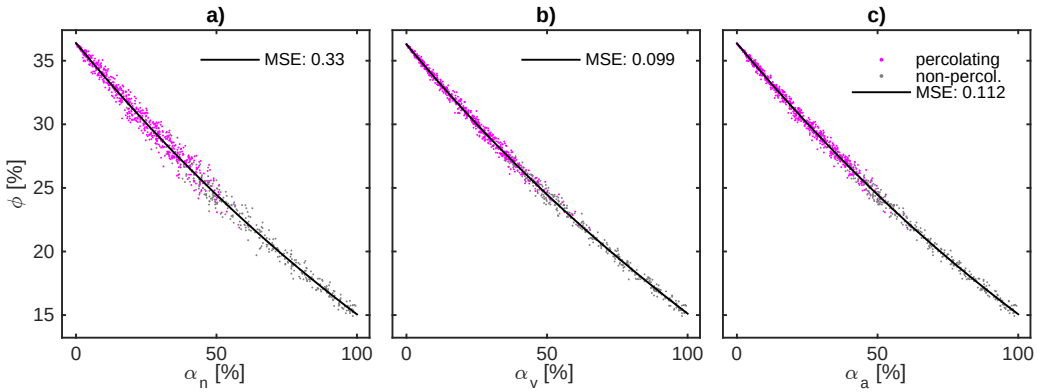

Figure 3.2: Comparison of the relationship of porosity ϕ with three different ways of defining the content of monocrystalline grains in the sample: a) by number of grains α_n, b) by volume α_v, c) by surface area of grains α_a. The results represent synthetic samples generated with the crystal form $01\bar{1}2$ and no isopachous cement ($\beta = 0$) and are fitted with an exponential curve of the form: $f(x) = ae^{bx} + ce^{dx}$.

This assessment is made based on the porosity results for synthetic samples generated with the crystal form $01\bar{1}2$ and no isopachous cement ($\beta = 0$) that are fitted with an exponential curve (Figure 3.2). The mean square error (MSE) represents the difference between the data points and the fit curve, and is used to determine the extent to which the model fits the data. A lower MSE signifies

a better fit to the data. The MSE is significantly lower in the case of the curve for the content by volume (0.099, Figure 3.2b) than in the content by number (0.33, Figure 3.2a) and slightly smaller than the content by surface area (0.112, Figure 3.2c), suggesting that the quantity of the monocrystalline grain content by volume is the most reliable control on the porosity of samples.

Figure 3.3 illustrates the outputs of Calcite2D where the difference between the two quantities, α_n and α_v, is considerable. In the top images (a, b), α_n is larger than α_v by 9.2%, which suggests that the mean size of monocrystalline grains is smaller than the mean grain size in the sample. In the bottom images (c, d), α_n is lower than α_v by 10.7%. The difference between α_n and α_v in the synthetic samples at the top (a, b) and at the bottom (c, d) leads to a difference in the porosity. Porosity is lower in samples where α_v is greater than α_n. In the absence of isopachous cement (a, c), the difference in porosity is 3.7%. The difference in porosity is reduced to 1.2% in synthetic samples where the isopachous cement fringes of a width of 10 pixels ($5\mu m$) are present (b, d).

Two crystal forms of calcite

The results are presented separately for the two rhombohedral crystal forms of calcite used: $01\bar{1}2$ and $40\bar{4}1$. This stems form the fact that the quantities of interest differ in the two cases. The porosity in the case of synthetic samples with the crystal form $01\bar{1}2$ is generally higher at the same monocrystalline grain content by volume (α_v) than in the case of $40\bar{4}1$ (Figure 3.4). The crystal form $40\bar{4}1$ produces synthetic samples with lower porosity, and the difference between the results associated with the crystal form $01\bar{1}2$ and $40\bar{4}1$ increases with an increasing content of monocrystalline grains.

This is further illustrated in Figure 3.5, which shows the model outputs generated using the crystal form $01\bar{1}2$ (a, b) and using the crystal form $40\bar{4}1$ (c, d). In these high monocrystalline content synthetic samples, the porosity of the samples with

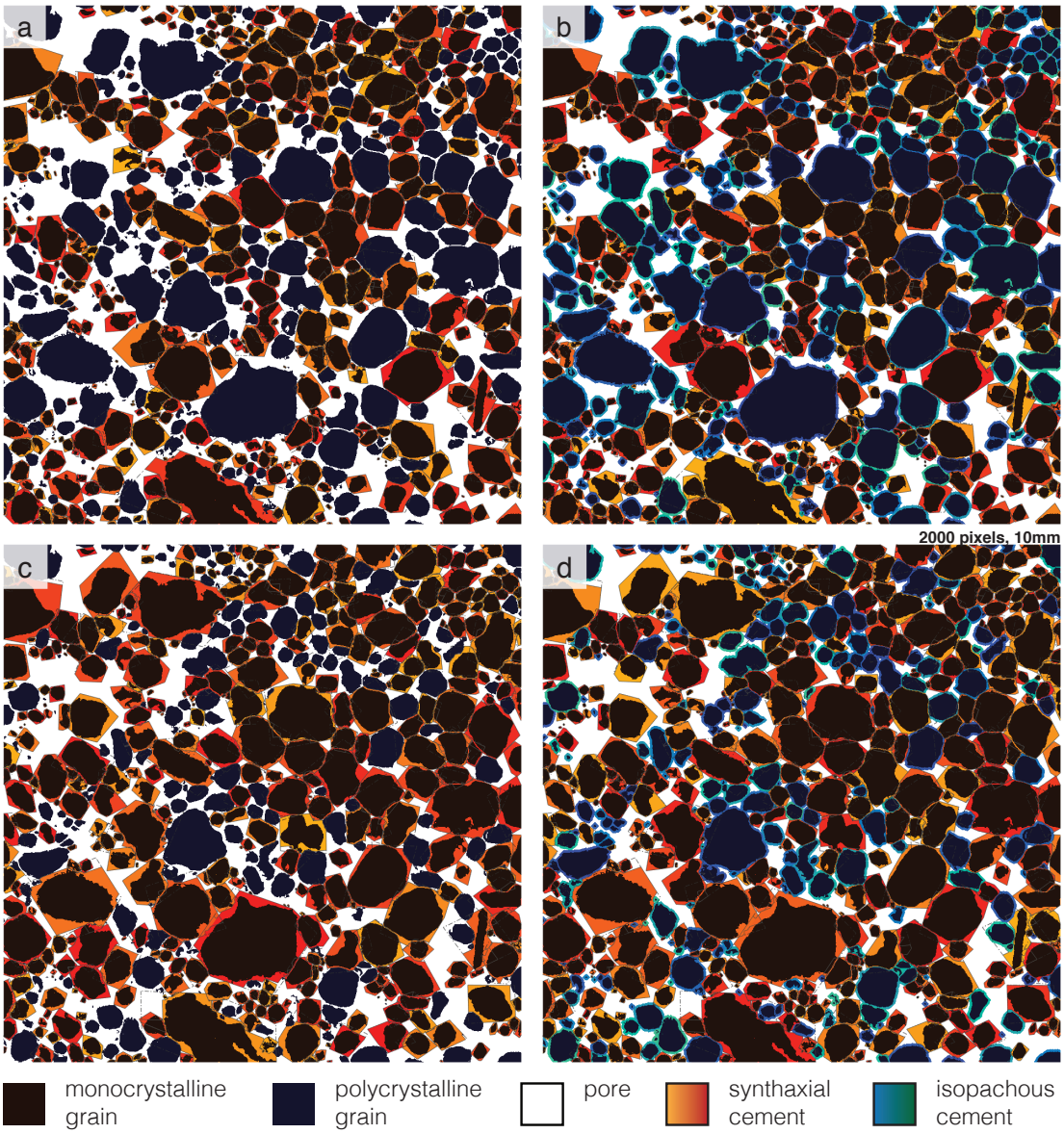

Figure 3.3: Cemented synthetic samples with the crystal form $01\bar{1}2$ and no isopachous cement (a, c) and 10 pixels ($50\mu m$) width of the isopachous cement fringes (b, d). In a) and b) α_n is considerably larger than α_v, while in c) and d) α_n is considerably smaller than α_v. The properties of each synthetic sample are as follows: a) $\phi = 23.4\%$, $\alpha_n = 62.7\%$, $\alpha_v = 53.5\%$; b) $\phi = 15.6\%$, $\alpha_n = 62.7\%$, $\alpha_v = 53.5\%$; c) $\phi = 19.7\%$, $\alpha_n = 64.2\%$, $\alpha_v = 74.9\%$; d) $\phi = 14.4\%$, $\alpha_n = 64.2\%$, $\alpha_v = 74.9\%$.

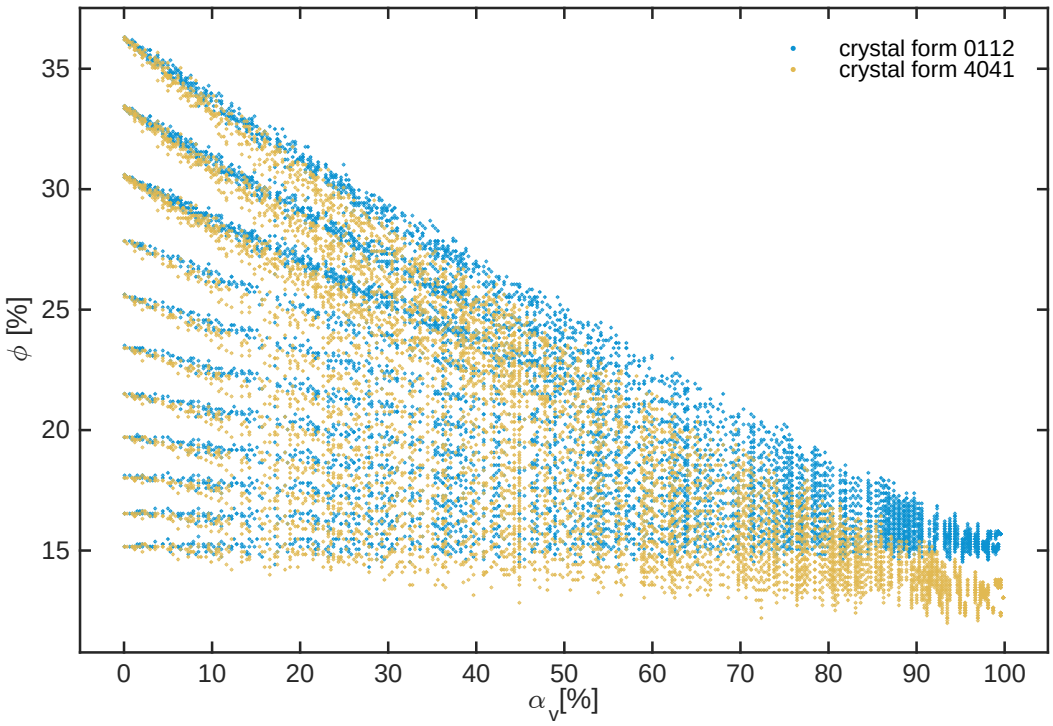

Figure 3.4: A comparison between the porosity of the synthetic samples produced with the crystal form $01\bar{1}2$ (blue) and $40\bar{4}1$ (yellow).

the crystal form $01\bar{1}2$ is around 15.5% and the porosity of the samples with the crystal form $40\bar{4}1$ is around 13.0%. Since there are so few polycrystalline grains, the width of the isopachous cement fringes does not significantly affect porosity.

Figure 3.5 also demonstrates that the crystal form $40\bar{4}1$ tends to produce more elongated shapes than crystal form $01\bar{1}2$. These elongated cements, depending on the orientation of the crystal axis and on the proximity and location of neighbouring grains, can sometimes protrude deep into the pore space, creating an above-average volume of cement for the grain and blocking the flow across large pores.

3.1 Impact of Monocrystalline Grains on Cement Growth and Porosity

The volume of cement and the porosity of the simulated synthetic sample cannot be accurately determined a priori, before the cement growth simulation is complete (Stage 2 of Calcite2D). This is because even if the extent of the bounding polygons is known (determined in Stage 1 of Calcite2D), the dynamics of impinging cements and the creation of the compromise boundaries in the course of cement growth can alter these otherwise pre-determined shapes. The following sections present the relationship between three quantities: the porosity (ϕ), the monocrystalline grains content by volume (α_v) and the ratio of the syntaxial cement to all cement (γ_v). The results are presented for all 6956 cemented synthetic samples generated for the two crystal forms: $01\bar{1}2$ and $40\bar{4}1$.

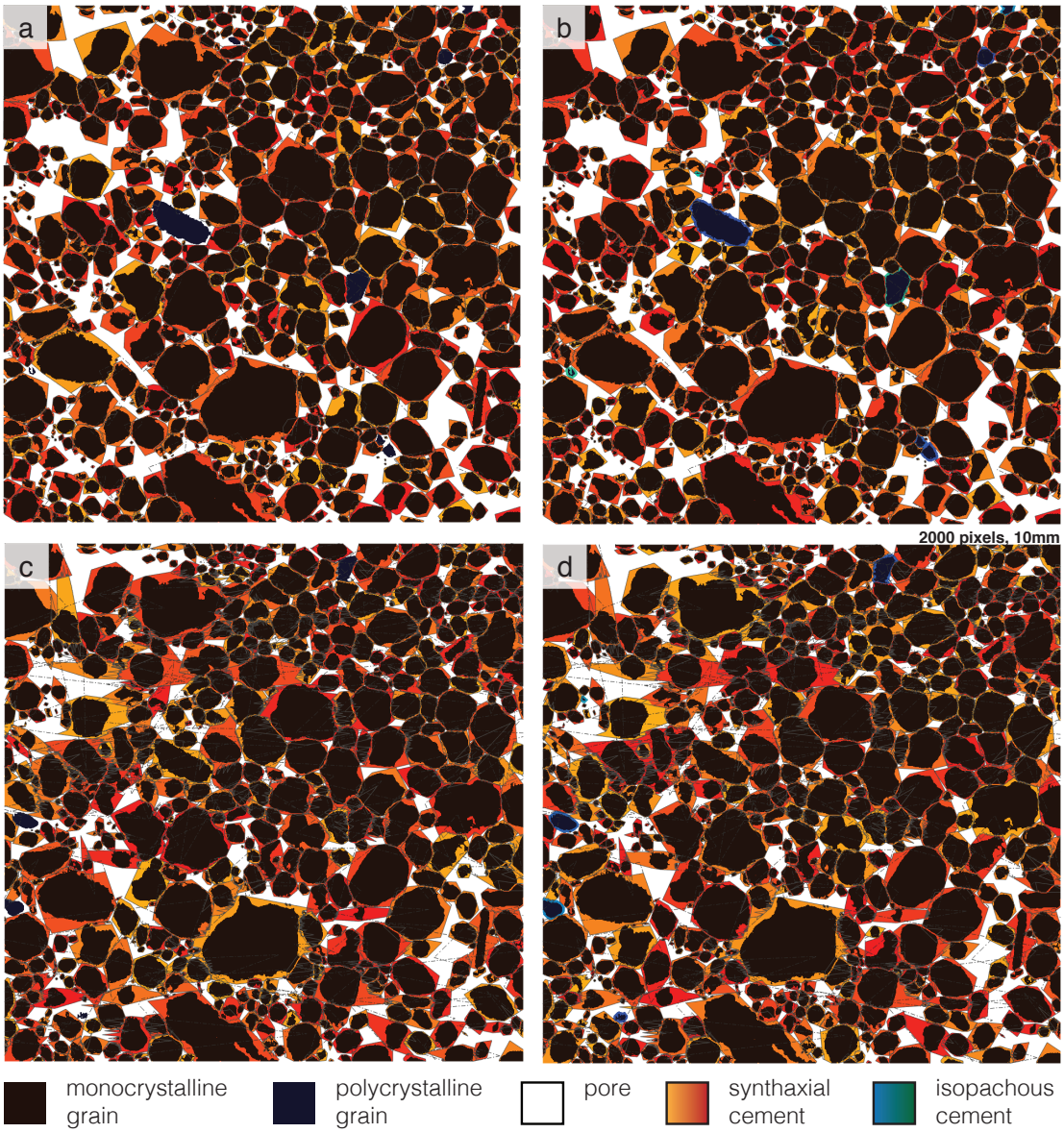

Figure 3.5: Calcite2D model outputs with a very high monocrystalline grain content for both crystal forms $01\bar{1}2$ (a, b) and $40\bar{4}1$ (c, d) with no isopachous cement (a, c) and 10 pixel ($50\mu m$) width of the isopachous cement fringes (b, d). The properties of each synthetic sample are as follows: a) $\phi = 15.8\%$, $\alpha_v = 98.5\%$; b) $\phi = 15.5\%$, $\alpha_v = 98.5\%$; c) $\phi = 13.1\%$, $\alpha_v = 99.9\%$; c) $\phi = 13.0\%$, $\alpha_v = 99.9\%$.

3.1.1 Impact on the relative volume of syntaxial cement (γ_v vs α_v)

Figure 3.6 shows the content of syntaxial cement in the overall volume of cement (γ_v) plotted against the content of monocrystalline grains in the sample (α_v) for all 6956 cemented synthetic samples for the two crystal forms modelled.

With the exception of the case of $\beta = 0$ (no isopachous cement), which has value of γ_v equal to 100%, regardless of the monocrystalline grain content, as syntaxial cement is the only cement in the sample, the results can be empirically fitted with a hyperbolic function (Figure 3.7). The slope of the curves decreases for larger values of α_v. The hyperbolic relationship becomes more linear, i.e. the change in the slopes along the curve decreases, the more isopachous cement there is.

The curves in both cases of the crystal form used are quite similar to each other, however the MSE is significantly smaller in the case of $01\bar{1}2$. In the case of crystal form $40\bar{4}1$ the hyperbolic shape of the curve is more pronounced, as the slopes along the curve change more dramatically than in the case of $01\bar{1}2$.

3.1.2 Impact on porosity (ϕ vs α_v)

Figure 3.8 shows the porosity of all generated synthetic samples as a function of the monocrystalline grain content. As in Figure 3.6, the gradient of colour in the direction parallel to the y-axis can be observed, suggesting that there is a strong dependence of the porosity on the amount of the isopachous cement in the sample.

The synthetic data for individual values of width of the isopachous cement fringes (β) can be fitted with an exponential curve of the form: $f(x) = ae^{bx}$ (Figure 3.9). The curve shape suggests that an addition of more monocrystalline grains to the synthetic sample has greater impact on the porosity in the case of samples where

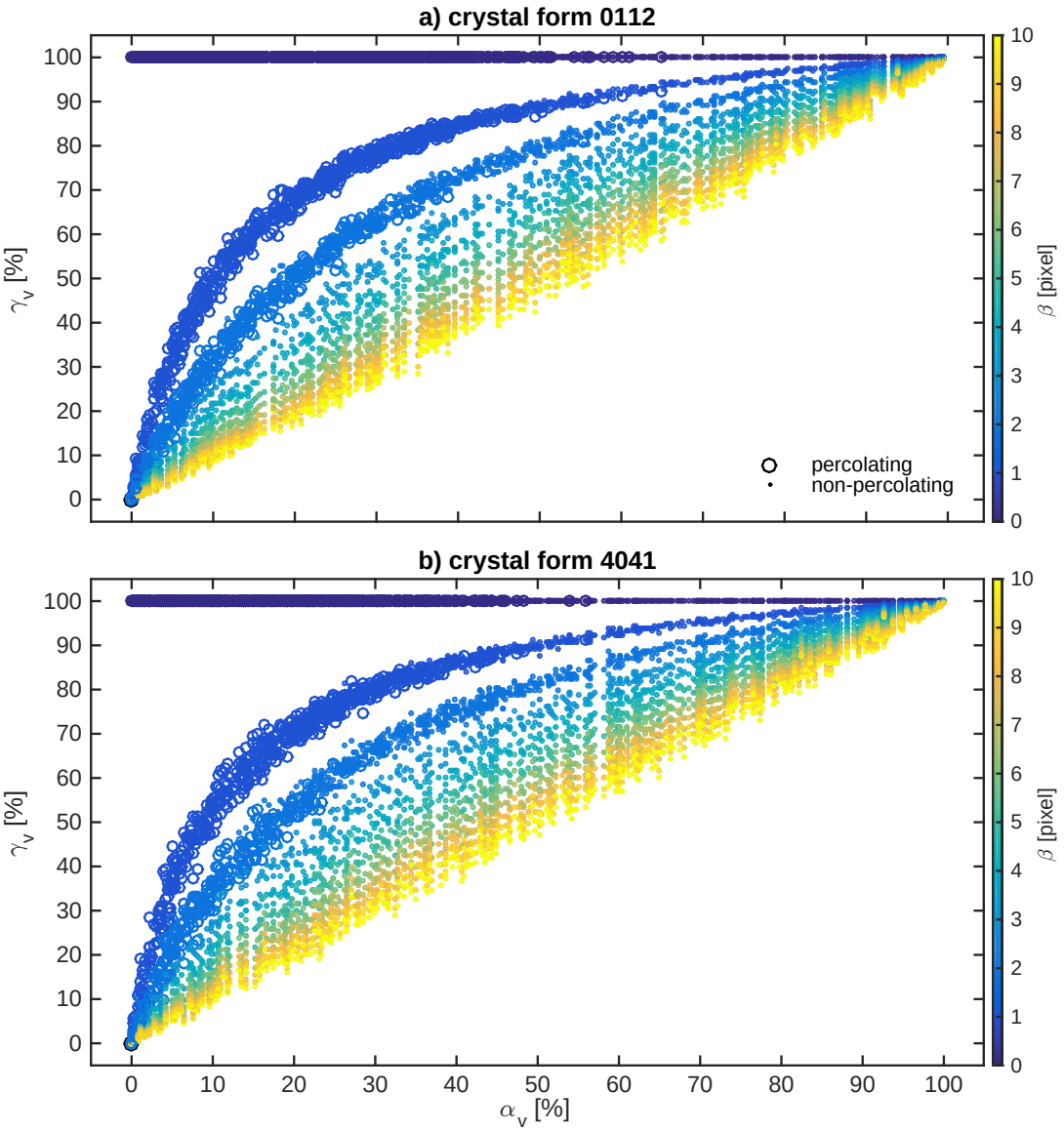

Figure 3.6: The content of syntaxial cement in the overall volume of cement γ_v vs the monocrystalline grain content in the sample by volume α_v for synthetic samples with the crystal form a) $01\bar{1}2$ and b) $40\bar{4}1$. The circles denote the percolating synthetic samples and the dots - non-percolating ones. The colours correspond to different values of the width of the isopachous cement fringes in the sample β: from blue (0 pixel) through to yellow (10 pixel or 50μm).

.

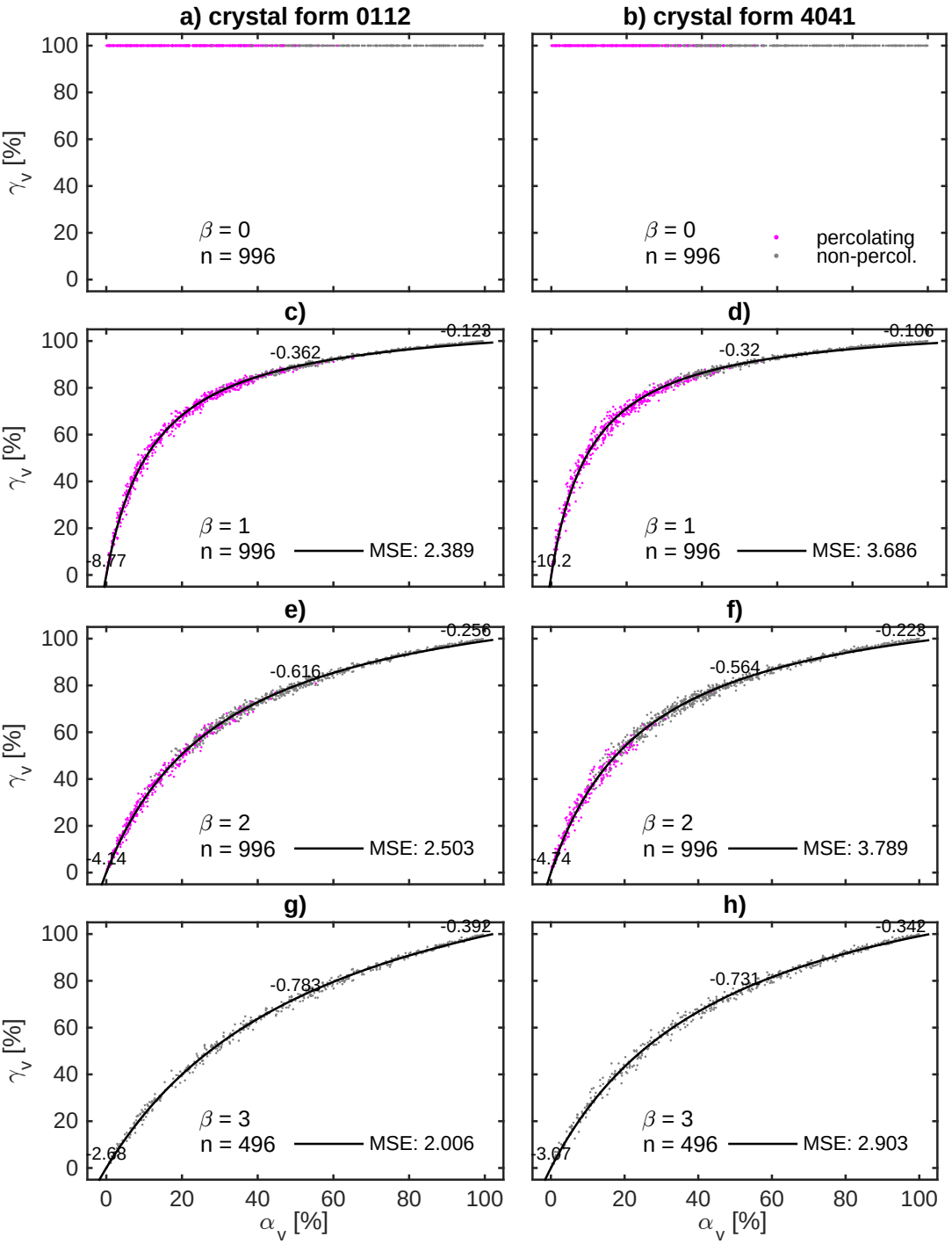

Figure 3.7: The content of syntaxial cement in the overall volume of cement (γ_v) vs the monocrystalline grain content by volume (α_v) for synthetic samples with the crystal form $01\bar{1}2$ (a, c, e, g) and $40\bar{4}1$ (b, d, f, h) for four values of the width of the isopachous cement fringes: 0 (a, b), 1 (c, d), 2 (e, f) and 3 pixels (g, h). The solid black line is the hyperbolic fit of the form: $f(x) = \frac{ax}{b+cx}$. The black numbers above each curve show the slope of the hyperbolic fit at α_v = 0, 50 and 95%.

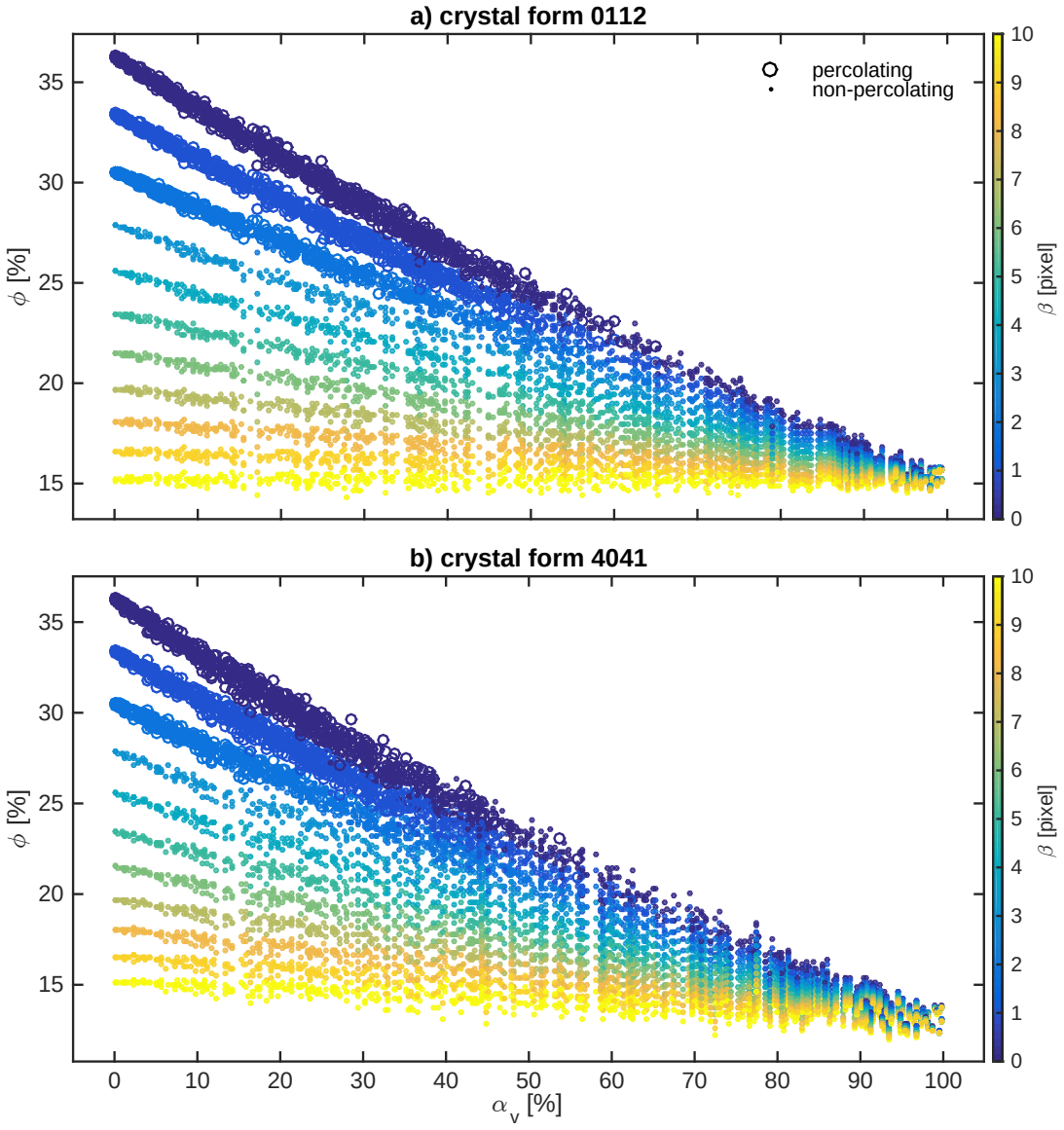

Figure 3.8: Porosity ϕ vs the monocrystalline grain content in the sample by volume α_v for synthetic samples with the crystal form a) $01\bar{1}2$ and b) $40\bar{4}1$. Symbols and colour scheme as in Figure 3.6.

the monocrystalline grain content is smaller. The slope of the exponential curve decreases and gets more uniform along the curve for higher values of the width of the isopachous cement fringes (β).

Here again it can be observed that the MSE is smaller in the synthetic samples with the crystal form $01\bar{1}2$. The slopes of the curve are higher in the case of $40\bar{4}1$, which suggests that the porosity decreases more rapidly with an increased content of monocrystalline grains in the sample.

Although the linear fit to the synthetic data is good, an exponential fit is preferred. This assessment is made with the use of a Bayesian information criterion (BIC) and a closely related to it Akaike information criterion (AIC). Both criteria are used for model selection among a finite set of models and are based on the likelihood functions. The model with the lowest BIC and the lowest AIC is preferred (Beck and Yuen, 2004a). In all but one of the plots in Figure 3.9 both the AIC and BIC are significantly smaller for the exponential fit (solid black line) than for the linear fit (dashed grey line).

The coefficients to the exponential fits to the $\phi - \alpha_v$ curves can be used to formulate the dependance of the porosity on parameters α_v and β. Coefficients a for curves representing synthetic samples with consecutive values of β can be fitted with an exponential function of the form $f(x) = a_1 e^{b_1 x + c_1}$. Coefficients b can be fitted with a linear function of the form $f(x) = a_2 x + b_2$ (Figure 3.10).

Using the exponential and linear fits derived in Figure 3.10 as the coefficients in the overarching exponential formula $f(x) = ae^{bx}$, an expression for the porosity in terms of α_v and β can be derived. For the crystal form $01\bar{1}2$ this phenomenological correlation takes the following form:

$$\phi = \left(37.1e^{-0.088\beta} - 0.272\right) e^{(0.00083\beta - 0.00842)\alpha_v} \tag{3.1}$$

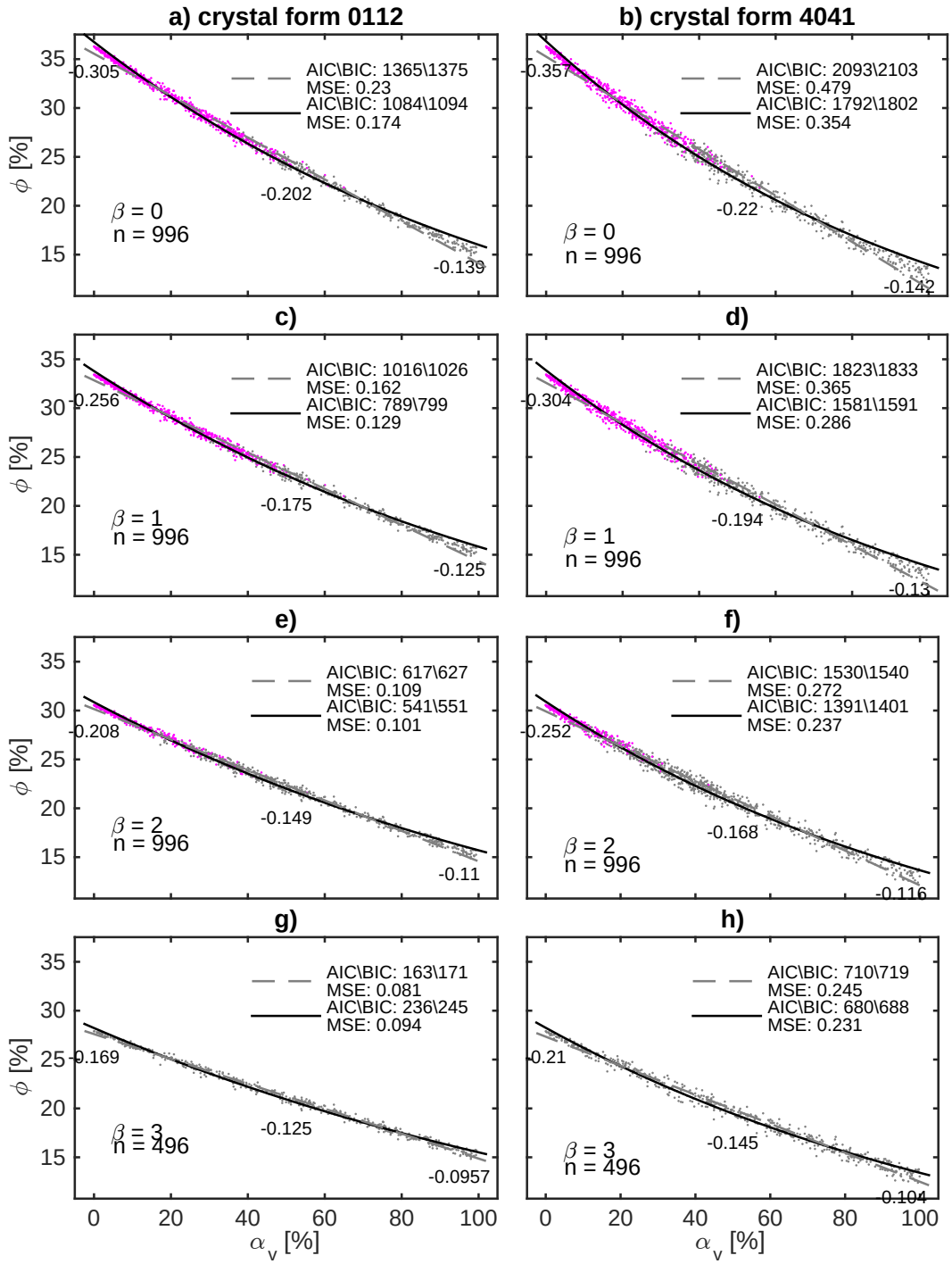

Figure 3.9: The porosity (ϕ) vs the monocrystalline grain content by volume (α_v) for synthetic samples with the crystal form $01\bar{1}2$ (a, c, e, g) and $40\bar{4}1$ (b, d, f, h) for four values of the width of the isopachous cement fringes: 0 (a, b), 1 (c, d), 2 (e, f) and 3 pixels (g, h). The grey dashed line is a linear fit to the synthetic data and the solid black line is the exponential fit of the form: $f(x) = ae^{bx}$. The black numbers above each curve show the slope of the exponential fit at α_v = 0, 50 and 95%.

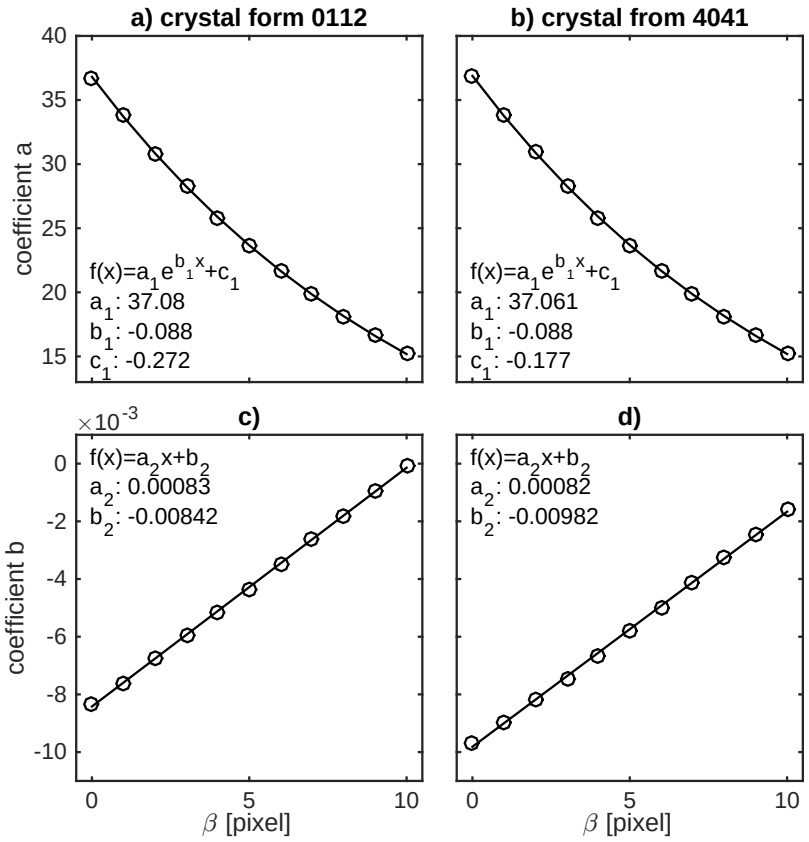

Figure 3.10: The coefficients of the exponential fits to the porosity ϕ vs the monocrystalline grain content by volume α_v for individual values of the width of the isopachous cement fringes β for the crystal form $01\bar{1}2$ (a, c) and $40\bar{4}1$ (b, d). For both crystal forms, coefficients a (a, b) and coefficients b (c, d) of the exponential fits can be fitted with an exponential function.

and for the crystal form $40\bar{4}1$ it takes a form:

$$\phi = \left(37.1e^{-0.088\beta} - 0.177\right) e^{(0.00082\beta - 0.00982)\alpha_v} \tag{3.2}$$

Upon an examination of these expressions it can be inferred that the impact of α_v on ϕ decreases for higher values of β, as the coefficient b is negative in the range of β values modelled. In the case of $01\bar{1}2$, coefficient b is less negative at any given value of β than in the case of $40\bar{4}1$, which suggests that the curves in the case of $40\bar{4}1$ are steeper. This in agreement with the results in Figure 3.8. Also, for higher values of β, coefficient b comes closer to 0 and the function approaches a straight line. This again finds a confirmation in the results, as the fit curves for increasing values of the width of the isopachous cement fringes (β) approach a straight line (the slopes are more uniform along the curve in Figure 3.8).

3.2 Impact on Permeability

This section presents the results of the last step in the methodology detailed in Chapter 2 (see Section 2.3) and shown in Figure 2.1: the Lattice Boltzmann simulation of flow in the cemented synthetic samples.

The choice of the cemented synthetic samples for the flow simulation is made from the pool of all percolating samples. This includes 1636 synthetic samples in the case of the samples with the crystal form $01\bar{1}2$ and 1331 samples in the case of $40\bar{4}1$. Only the samples with very thin isopachous cement fringes ($\beta = 0$, 1 and 2 pixels) are found percolating. Figure 3.11 shows the 195 samples selected in the case of $01\bar{1}2$ and 196 samples selected in the case of $40\bar{4}1$.

The primary strategy for selecting the synthetic samples for the LB simulation involves targeting samples at specific porosities. That way the impact of the monocrystalline grains content (α_v) on permeability (κ) for the synthetic samples

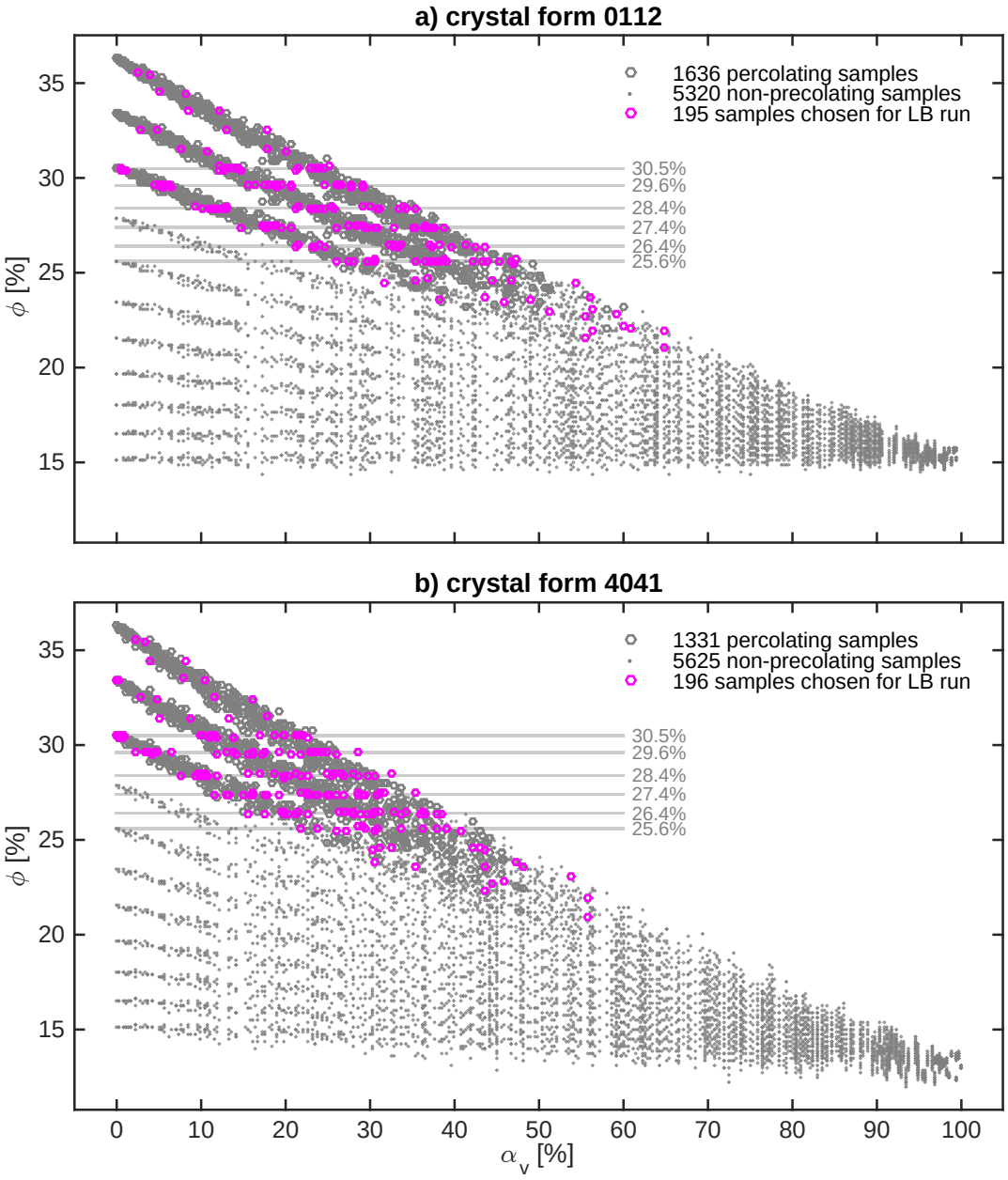

Figure 3.11: The samples selected for the LB simulation for the two crystal forms: $01\bar{1}2$ and $40\bar{4}1$.

of equal porosity (ϕ) can be investigated. For each of the targeted porosities, at least eight and preferably ten synthetic samples are selected from three groups of samples with a different width of the isopachous fringes (β = 0, 1 and 2 pixels).

The choice of the porosity values is made based on the availability of the synthetic samples within a 0.1% tolerance range of the targeted porosity, optimised for a uniform interval between the targeted porosities. The same six porosity values are targeted in both crystal form cases: 25.6, 26.4, 27.4, 28.4, 29.6 and 30.5%. Depending on the availability of synthetic samples, the number of the samples selected for the LB simulation for each of these porosities varies between 16 and 30 samples.

The secondary strategy for selecting the synthetic samples for the LB simulation involves the coverage of the full extent of the percolating synthetic dataset. For that purpose, porosities spaced every 1% are targeted and the samples with the highest and the lowest value of the monocrystalline content (α_v) are selected for the three values of β, for which percolating samples are available (0, 1 and 2 pixels). This way a maximum of six synthetic samples are picked for each targeted porosity.

3.2.1 Impact of porosity on permeability (κ vs ϕ)

A slight trend of the logarithmic permeability increasing with the porosity is observed in the poroperm data for the synthetic samples of both crystal forms of syntaxial cement (Figure 3.12), especially in the case of the samples with $\beta = 0$ (shaded yellow) and 1 (shaded green). Samples with $\beta = 2$ (shaded blue) are grouped in the low permeability zone. This illustrates the impact of isopachous cement on the permeability.

The gradient of colour in Figure 3.12, from blue in the bottom-right corner to yellow in the top-left corner of the plot, suggests a dependance of the permeability

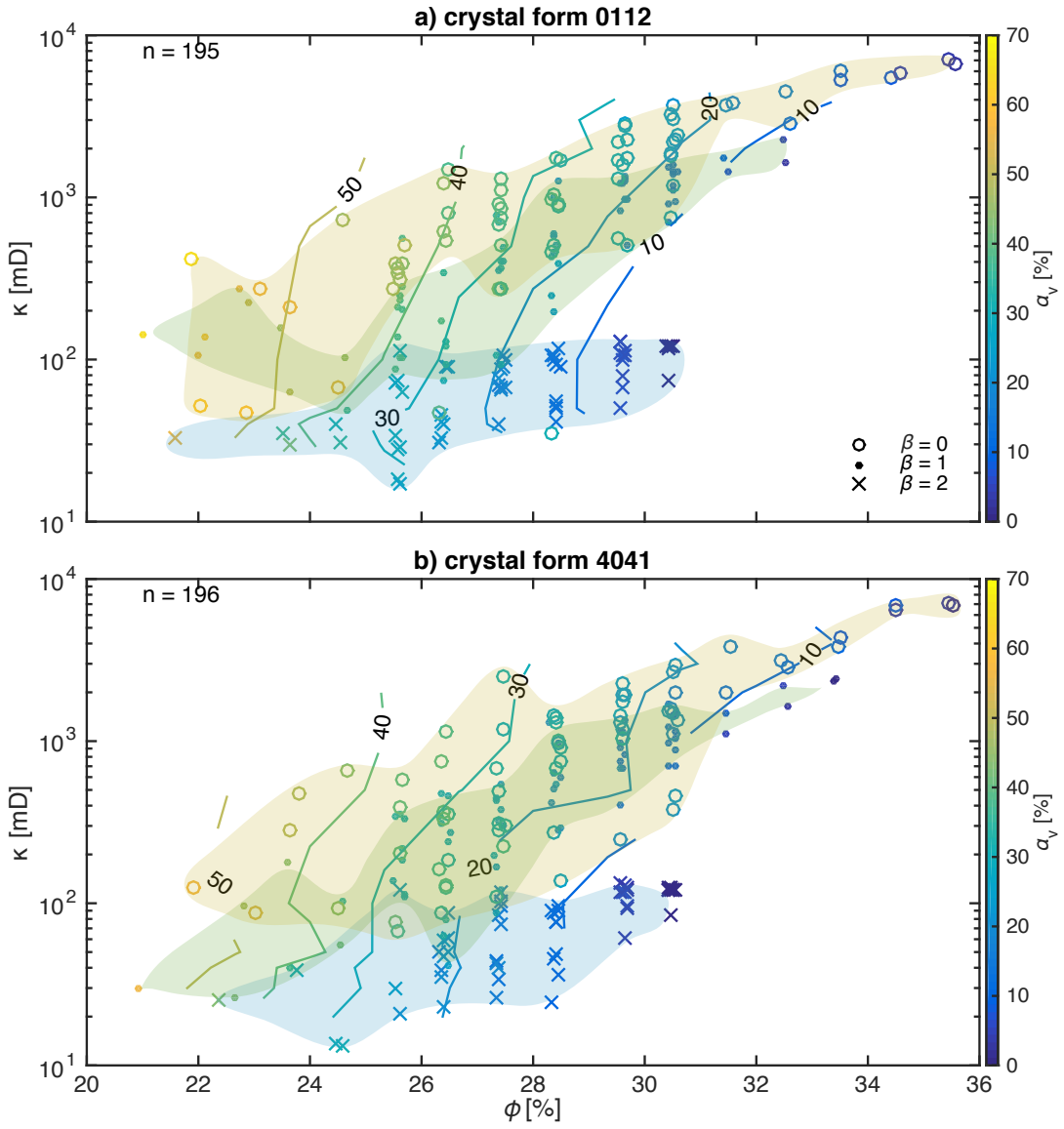

Figure 3.12: The permeability (κ) on a logarithmic scale vs the porosity (ϕ) for the synthetic samples with the crystal form a) $01\bar{1}2$ and b) $40\bar{4}1$. The circles denote the synthetic samples with no isopachous cement (shaded yellow), the dots - samples with 1 pixel ($5\mu m$) width of the isopachous cement fringes (shaded green), and x - samples with 2 pixels ($10\mu m$) width of the isopachous cement fringes (shaded blue). The synthetic data are coloured by the monocrystalline grains content by volume (α_v) from dark blue (low content) to yellow (high content).

on the monocrystalline grains content in the sample (α_v). In this figure, however, this effect is not easy to isolate as it is 'contaminated' by the effect that the porosity has on the permeability.

3.2.2 Impact of monocrystalline grains content on permeability (κ vs α_v)

Figure 3.13 illustrates the effect that the monocrystalline grains content (α_v) has on the permeability. The trend that can be observed is that the permeability decreases for a larger content of monocrystalline grains (α_v). This trend is particularly clear upon the inspection of the results with a different width of the isopachous cement fringes (β). The gradient of colour, from magenta in the top-left corner to light blue in the bottom-right corner of the plot, suggests a dependence of the permeability on the porosity.

In order to investigate the effect of the monocrystalline grains content on the permeability, the synthetic samples of different monocrystalline grain content but with the same porosity are considered. Figure 3.14 presents the permeability results for the six targeted porosities.

The linear fits to the synthetic data for each targeted porosity reveal that the slopes ($p1$) of the best fit lines are very similar for all porosities for both crystal forms, with the same mean equal to 0.053 in both crystal form cases (in the case of $40\bar{4}1$ the outlier at porosity 25.6% is excluded). The y-intercepts ($p2$) exhibit a strong linear dependance on porosity of the form $p2 = 0.44 \cdot \phi - 11.172$ in the case of $01\bar{1}2$, and $p2 = 0.345 \cdot \phi - 8.367$ in the case of $40\bar{4}1$. These findings allow a bivariate formulation of the dependance of the permeability on the monocrystalline grains content and the porosity in the case of $01\bar{1}2$ as a function:

$$log(\kappa) = 0.053 \cdot \alpha_v + 0.44 \cdot \phi - 11.172 \tag{3.3}$$

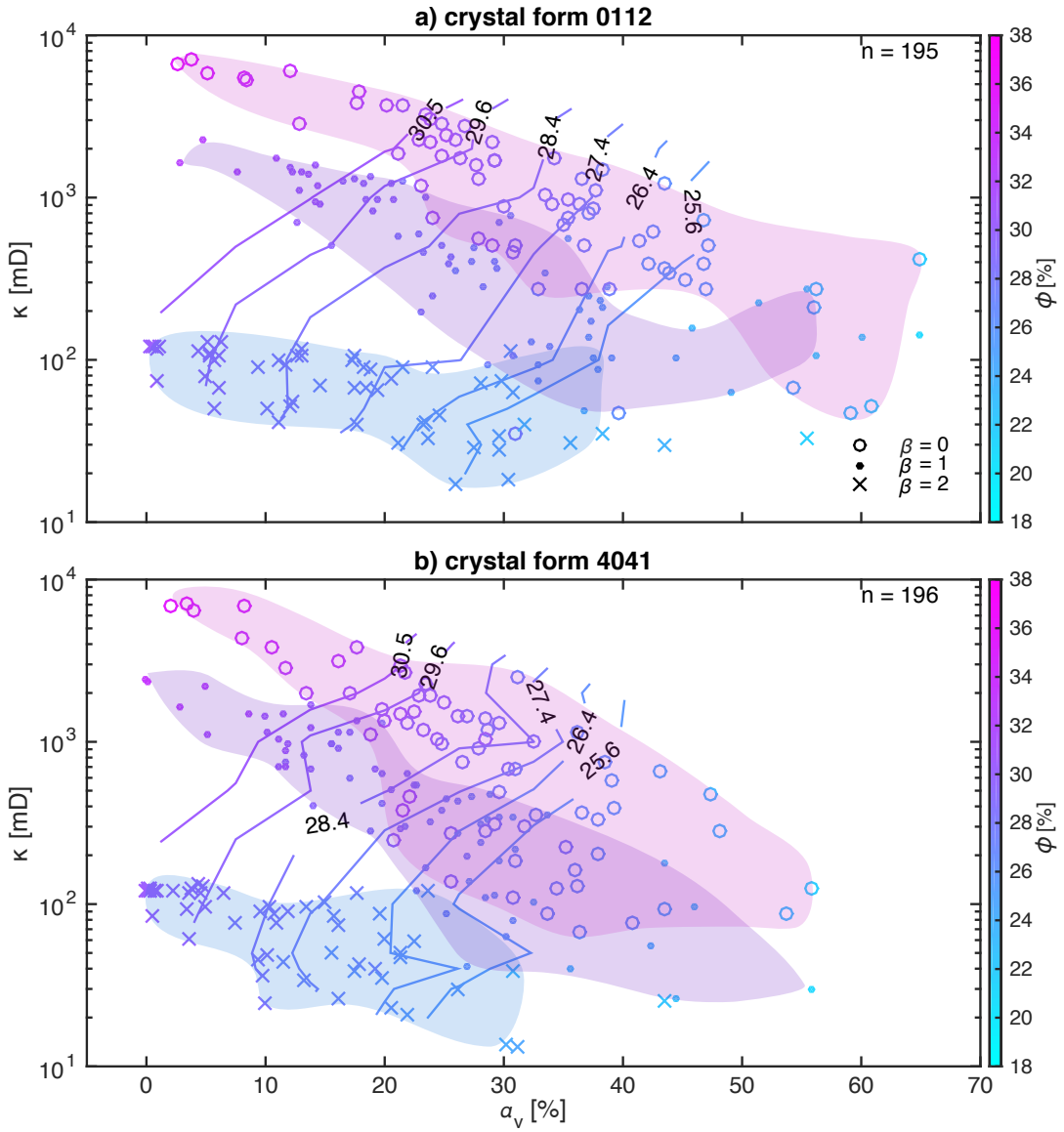

Figure 3.13: The permeability (κ) on a logarithmic scale vs the monocrystalline grain content by volume (α_v) for the synthetic samples with the crystal form a) $01\bar{1}2$ and b) $40\bar{4}1$. The circles denote the synthetic samples with no isopachous cement (shaded magenta), the dots - samples with 1 pixel width of the isopachous cement fringes (shaded violet), and x - samples with 2 pixels of the isopachous cement fringes (shaded blue). The synthetic data are coloured by porosity (ϕ), from light blue (low porosity) to magenta (high porosity).

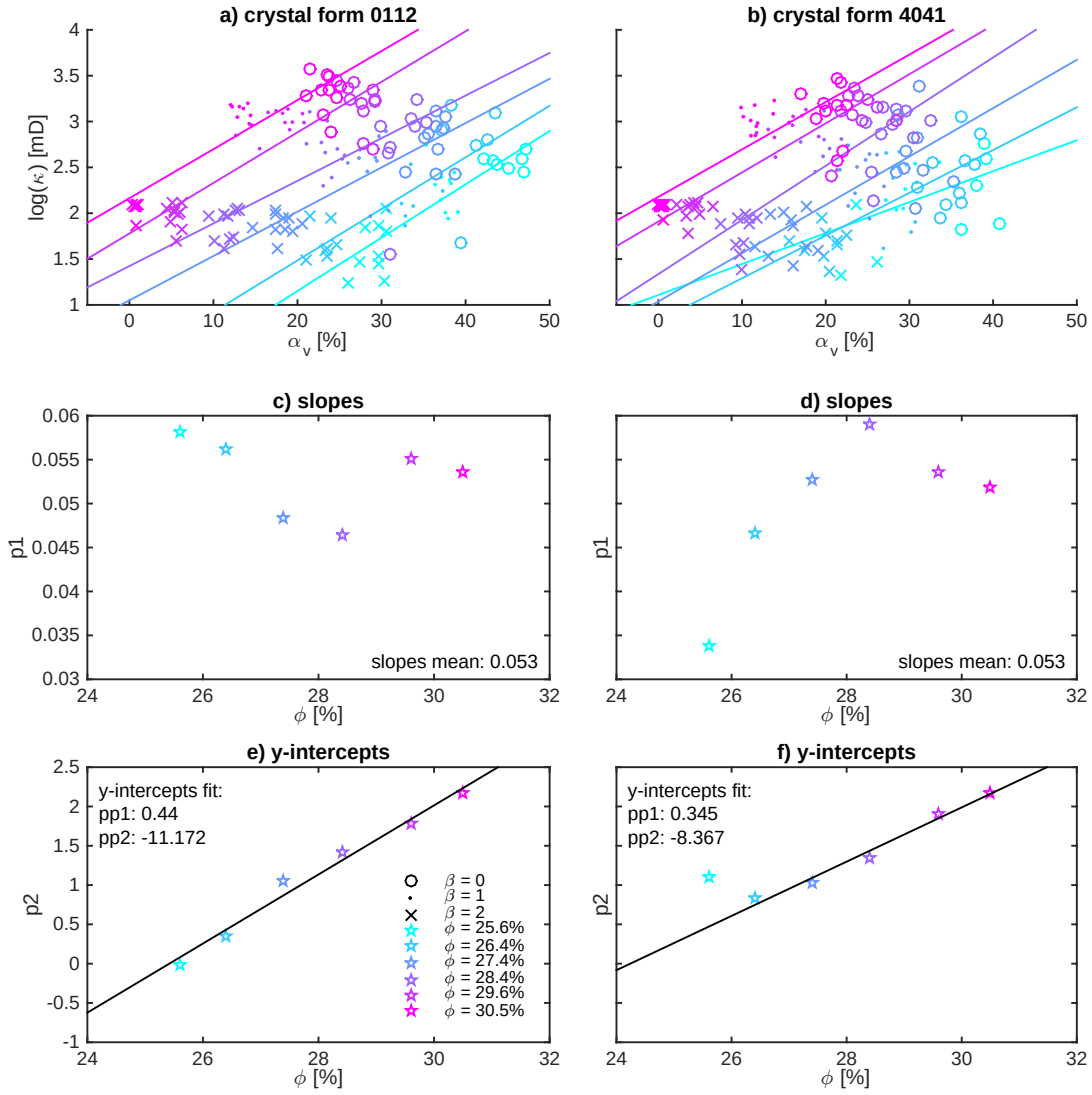

Figure 3.14: Top plots (a, b) show fits of $log(\kappa)$ vs monocrystalline grains content (α_v) for synthetic samples with the crystal form a) $01\bar{1}2$ and b) $40\bar{4}1$ at six investigated porosities: 25.6, 26.4, 27.4, 28.4, 29.6 and 30.5%. The points for each porosity are fitted with a straight line and the fit coefficients are plotted in the plots below: the slopes in c) and d) and the y-intercepts in e) and f). The synthetic data point representing synthetic samples with porosity 25.6% for the crystal form $40\bar{4}1$ is excluded from the analysis due to its anomalous nature.

and in the case of $40\bar{4}1$:

$$log(\kappa) = 0.053 \cdot \alpha_v + 0.345 \cdot \phi - 8.367 \tag{3.4}$$

where α_v and ϕ are the values for the monocrystalline grain content and the porosity in %, and κ is the permeability in mD.

The equations 3.3 and 3.4 formulate the dependance of the permeability on the monocrystalline grains content and on the porosity as linear, with the coefficient by the monocrystalline grains content 8 ($01\bar{1}2$) and 6.5 ($40\bar{4}1$) times smaller than the coefficient by the porosity, suggesting that the impact of the porosity on the permeability is stronger.

Figure 3.15 shows the variability of the point clouds for each case of the width of the isopachous cement fringes analysed in Figure 3.14. The standard deviation is generally greatest for the synthetic samples with no isopachous cement. In the case of $40\bar{4}1$, for samples with porosity 25.6%, the variability for $\beta = 2$ is anomalously big, therefore results for this porosity are excluded from the analysis presented in Figure 3.14.

3.3 Discussion

We proceed to interpret and discuss the results presented in the previous sections. The differences in porosity and permeability of the synthetic samples developed with the use of the two crystal forms ($01\bar{1}2$ and $40\bar{4}1$) are discussed in Section 3.3.1. The relative volumes of syntaxial and isopachous cements for the synthetic samples of a varying amount of monocrystalline grains are examined in Section 3.3.2. The trends in the results interpreted to be an effect of the competition of growing cements for pore space are explained in Section 3.3.3. Finally, Section 3.3.4 examines the permeability results.

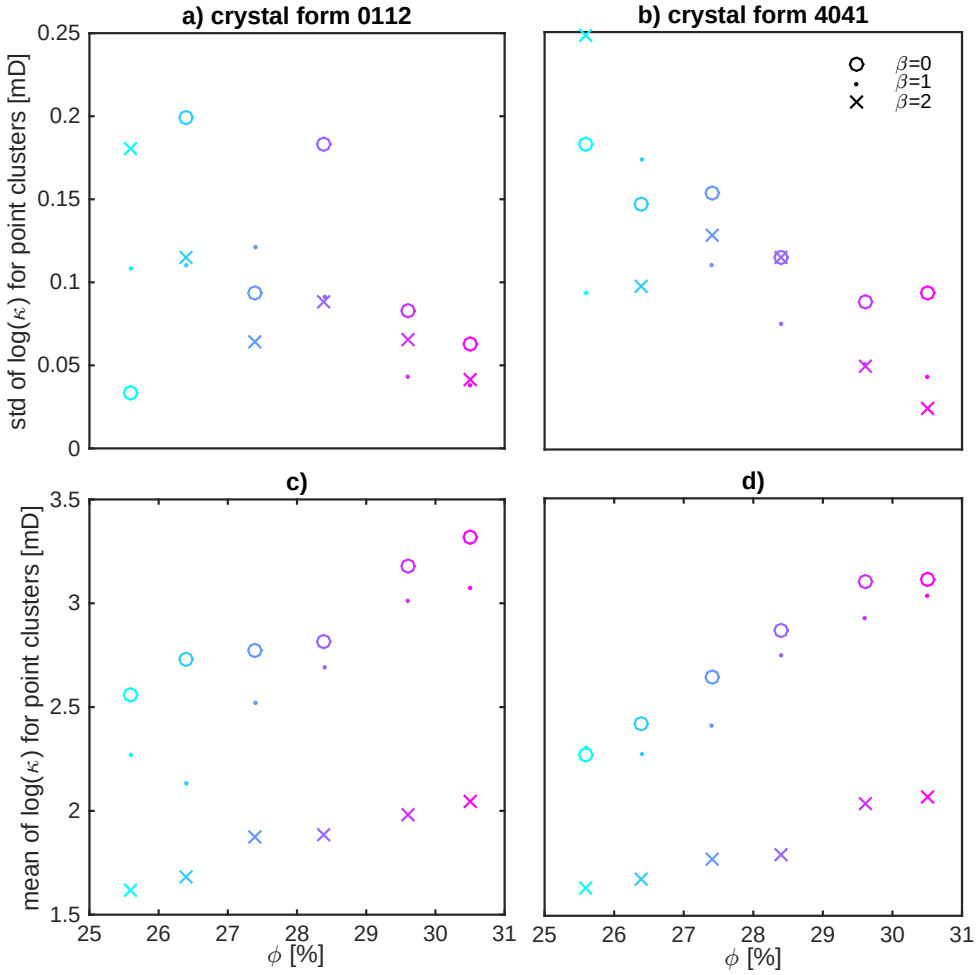

Figure 3.15: The statistics for the point groups for different values of the width of the isopachous cement fringes at the targeted porosities as depicted in the plots in Figure 3.14 for both crystal form cases: $01\bar{1}2$ (a, c) and $40\bar{4}1$ (b, d). For each of the six porosities, colour-coded as in Figure 3.14, the mean (c, d) and the standard deviation (a, b) is calculated separately for the synthetic samples with $\beta = \{0, 1, 2\}$ pixels. The standard deviation is normalised by the mean.

3.3.1 Differences in the results between crystal form $01\bar{1}2$ and $40\bar{4}1$

As the two crystal forms modelled differ in terms of shape and volume, the results for the synthetic samples produced using these crystal forms also differ. The sections below examine the differences in the volume of cement, the permeability, as well as in the variability in the synthetic data.

Cement volume

The crystal form $40\bar{4}1$ produces synthetic samples with a lower porosity than the crystal form $01\bar{1}2$ (Figure 3.4). This is because on an identical grain the crystal form $40\bar{4}1$ produces a *larger volume* of cement than $01\bar{1}2$. The volume of the epitaxial overgrowth developed on a spherical grain by a rhombohedral form $40\bar{4}1$ is 9.6 times bigger than the volume developed by the crystal form $01\bar{1}2$ (Figure 1.14). In a porous medium, however, syntaxial cement will hardly ever develop to its full shape, due to the effect of the impinging grains. That is why the difference in the porosity in the synthetic samples generated with the use of the two forms is not as stark as the difference in the volume of the two rhombohedral forms circumscribed on a spherical grain (5.8 times).

The difference in the cement volume can also be observed in Figure 3.5, where the porosity of the synthetic sample generated with the crystal form $40\bar{4}1$ is about 2.5% smaller than the porosity of the synthetic sample generated with the crystal form $01\bar{1}2$. Upon inspection of the images, it is noticeable that the elongated shape of calcite overgrowth generated with the crystal form $40\bar{4}1$ on average manages to claim more pore space than the more blocky crystal form $01\bar{1}2$.

Permeability

The permeability at equal porosities of the synthetic samples with the crystal form $40\bar{4}1$ is smaller than of the synthetic samples with the crystal form $01\bar{1}2$ (Figures 3.15c and d). Moreover, from equations 3.3 and 3.4 it can be inferred that for most porosities $log(\kappa)$ is bigger for synthetic samples with the crystal form $01\bar{1}2$, due to the factor by porosity (ϕ) in the expression being considerably larger than the factor in the equation for synthetic samples with the crystal form $40\bar{4}1$.

The difference in permeability is due to the difference in the *shape* of cements created with the two rhombohedral forms of calcite. Even at the same overall volume of cement in a synthetic sample, form $40\bar{4}1$ generates more elongated features that can reach further in the pore space to block it to the flow. This way the probability of closing the important flow pathways that are significantly contributing to the flow is greater and this is reflected by the permeability being on average lower.

Variability in the synthetic data

Moreover, the difference in the volume and the shape of the two rhombohedral forms gives rise to a difference in the variability in all presented results. In almost every plot presented in this chapter, the variability in the results is greater for synthetic samples with the rhombohedral form $40\bar{4}1$. It is perhaps best illustrated in Figures 3.7 and 3.9, which show that the MSE is considerably and consistently smaller for the results associated with the crystal form $01\bar{1}2$, which suggests that the crystal form $01\bar{1}2$ tends to produce more uniform porosities and volumes of syntaxial cement.

This is explained by the difference in the potential volume of cement that each monocrystalline grain is capable of producing. In case of the crystal form $40\bar{4}1$,

this potential volume is 9.6 greater than in the case of the crystal form $01\bar{1}2$. The extent to which this volume is realised in the course of the cement growth depends on the proximity of the neighbouring grains, the type of cement that the neighbouring grains develop and the orientation of the crystal axis of the grain in question. The *location* of the neighbouring grains is pre-determined as it is an input to the model in the form of the image of grain deposit. The cementation model has a limited control on changing the neighbourhood of any given grain, as it can only add cement around the existing grains. However, the *orientation* of the crystal axis of a grain is determined entirely at random in Stage 1 of Calcite2D. Therefore, it is mainly the orientation of the crystal axis that controls the amount of cement grown by a monocrystalline grain.

For an illustration of this effect please see Figure 3.5c and find the elongated form of the syntaxial cement visible in the top-left corner (coloured light orange). The crystal axis of this grain is oriented vertically in the image, which enables the cement growth into the large pore area above the grain. If the crystal axis was instead oriented horizontally, the cement growth would soon be blocked by the grains impinging on both sides, resulting in a much smaller volume of cement for that grain. The effect of the impingement by the neighbouring grains on limiting syntaxial cement growth can be observed e.g. for the largest grain in the sample (Figure 3.5c, centre bottom of image, light orange cement).

The monocrystalline grains that grow according to the crystal form $40\bar{4}1$ have the potential to grow a large volume of cement, but whether this potential is achieved depends on the direction of the crystal axis of the grain. Overall, the crystal form $40\bar{4}1$ can produce a wide range of cement volumes for a single grain. As a result, the variability in the porosity of the cemented synthetic samples is considerable. In contrast, the crystal form $01\bar{1}2$ produces blocky cement shapes, with a much smaller aspect ratio, and the random effect of the orientation of the crystal axes does not have such a great impact on the volume of cement produced.

For the same reasons, the difference in the variability of the results holds also

in the case of permeability. The standard deviation for the point groups for the synthetic samples with a different width of the isopachous cement fringes is generally greater for the synthetic samples associated with the crystal form $40\bar{4}1$ (Figures 3.15a and b). This once again shows that the crystal form $40\bar{4}1$ produces synthetic samples of a greater variability.

3.3.2 Syntaxial vs isopachous cement volumes

The curves of the porosity (ϕ) as a function of the monocrystalline grains content (α_v) are decreasing for almost all cases of the width of the isopachous cement fringes (β), with the exception of the curve for $\beta = 10$ pixels of the crystal form $01\bar{1}2$, which is nearly horizontal (Figures 3.8 and 3.9). The synthetic samples with no isopachous cement (dark blue) produce a curve with the steepest slope. As the width of the isopachous cement fringes increases, the slopes of the curves become more horizontal.

The decreasing nature of these curves suggests that the average volume of the isopachous cement produced by the polycrystalline grains is smaller than the average volume of the syntaxial cement produced by the monocrystalline grains. In the case of the synthetic samples of the crystal form $01\bar{1}2$ and $\beta = 10$, the average volume of the isopachous and syntaxial cement produced per grain are nearly equal, thus the curve is close to horizontal. If the cementation simulations were ran for a higher target width of the isopachous cement fringes ($\beta = 11$ and higher), the average volume of the isopachous cement per grain would surpass that of the syntaxial cement and the resulting curves would be increasing.

3.3.3 Competition for pore space

The slopes of the curves in Figures 3.8 and 3.9 are not constant, i.e. the linear fits to the synthetic data are inferior to the exponential fits (the AIC and BIC

analysis). The slopes of the exponential fits to the porosity in Figure 3.9 become more horizontal for larger values of α_v. Similarly, the slope of the curve of the content of the syntaxial cement in all cement (γ_v) as a function of the content of monocrystalline grains (α_v) decreases for larger values of α_v (Figure 3.7). These slope changes are in all cases most pronounced for the synthetic samples with no isopachous cement (Figures 3.7a, b and 3.9a, b).

The change of slope in the curves of the syntaxial cement volume (γ_v) and of the porosity as a function of the monocrystalline grains content is an effect of the competition between syntaxial cements for the available pore space (see Sections 1.6 and 2.2.2). The more monocrystalline grains there are in a sample, i.e. the larges α_v is, the smaller difference it makes for the final cement volume if more monocrystalline grains are added. This is because a smaller volume of the *potential* syntaxial cement can be actually grown, as there is less pore space available. The competition effect is found in other fields, such as the Langmuir adsorption model, where the molecules are competing for the adsorption sites (Helfferich, 1985). The Langmuir isotherm is described with a hyperbolic equation, just as the synthetic data for the content of the syntaxial cement in all cement (γ_v) as a function of the content of monocrystalline grains (α_v) shown in Figure 3.9.

The fact that the slopes in the above-mentioned Figures 3.9 and 3.7 are becoming increasingly more linear with the increasing width of the isopachous cement fringes (β), shows that the larger the width of the isopachous cement fringes (and the resulting average amount of the isopachous cement produced per grain), the smaller difference it makes if more monocrystalline grains are added. The thicker the isopachous cement is allowed to grow, the more aggressive competitor for the pore space it becomes for the syntaxial cement. As a result, the competition between the monocrystalline grains developing syntaxial cement has a smaller impact on the overall volume of cement, i.e. the monocrystalline grains have smaller impact in the synthetic samples with more isopachous cement.

Further insight into the effect of the competition for the pore space can be

gained upon the inspection of the cumulative pore size distribution curves for the synthetic samples of various content of monocrystalline grains (α_v) and various width of the isopachous cement fringes (β), as presented in Figure 3.16.

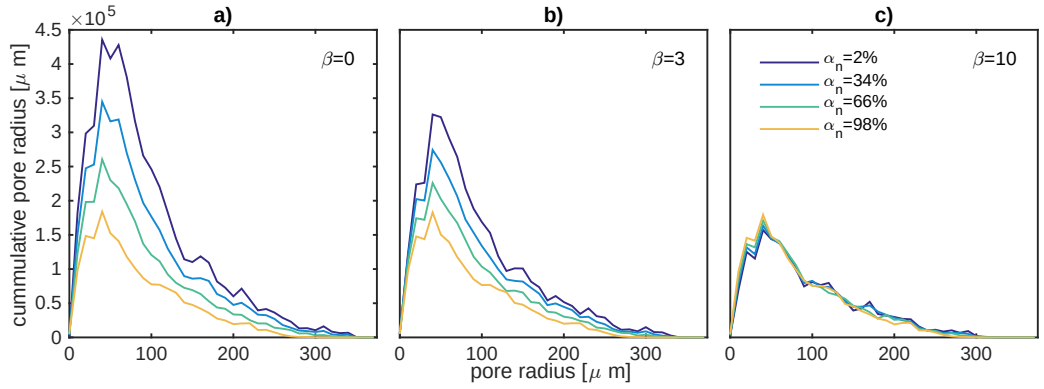

Figure 3.16: The cumulative pore size distributions derived in the same way as in Figure 2.3 in Chapter 2 for the synthetic samples with a different width of the isopachous cement fringes: a) 0 pixels, b) 3 pixels (15μm) and c) 10 pixels (50μm). Each curve is an average of several synthetic samples of similar content of the monocrystalline grains α_n =2, 34, 66 and 98%. In the case of the synthetic samples with β = 0 and 2 pixel, 15 samples are averaged, in other cases five samples are averaged.

In Figures 3.16a and b the peak at the pore radius of around 10 pixel is decreasing for the consecutive values of the monocrystalline grain content, however the differences get smaller for higher values of the monocrystalline grain content (the difference between the curve for $\alpha_n = 2\%$ and for 34% is greater than the difference between the curves for 34% and 66% and so on). This suggests that an increase of the number of the monocrystalline grains in the sample stimulates the competition for the pore space so that each monocrystalline grain on average has smaller effect on the total volume of syntaxial cement produced.

Note that as the width of the isopachous cement fringes (β) in increases, i.e. as we move from plot for $\beta = 0$ pixels to $\beta = 3$ pixels in Figure 3.16, the volume of the pore space, represented by the area under the curve, is reduced. Similarly, as

the content of the monocrystalline grains in the sample increases, the total pore space in the synthetic sample decreases.

3.3.4 Permeability

Here we examine the permeability results and discuss the effectiveness of the isopachous cement in closing pore-throats, the variability in the synthetic data and the context of poroperm data for grainstones in literature. Finally, the impact of the monocrystalline grains on the permeability is discussed.

The effect of isopachous cement on limiting permeability

The fact that there are no percolating cemented synthetic samples for the isopachous cement fringes width of $\beta = 3$ pixels ($15\mu m$) and higher (e.g. Figure 3.1), means that isopachous cement is very effective in closing off the pore-throats. Just a $15\mu m$-thick rim is enough to render a cemented synthetic sample impenetrable, regardless of the content of the monocrystalline grains. For example, a synthetic sample with $\beta = 3$ pixels and *no* monocrystalline grains does not percolate.

In the plots representing the dependence of the permeability on the porosity (Figure 3.12) and the monocrystalline grain content (Figure 3.13), the results for the synthetic samples for different values of the width of the isopachous cement fringes (β) are grouped together. In particular, the synthetic samples with $\beta = 2$ pixels form an isolated cluster in the low permeability zone. This clustering suggests that the amount of the isopachous cement is a strong control on the permeability.

This is further illustrated in Figure 3.17, which shows the velocity of flow for four samples: a back-stripped medium used as an input in Calcite2D and three

cemented synthetic samples with no or low monocrystalline grain content and $\beta = 0, 1$ and 2 pixels. Sample b) illustrates that at a low monocrystalline grain content ($\alpha_v = 12.2\%$), syntaxial cement lowers the permeability by excluding from the flow regions of the pore space by cutting them off with interlocking crystals (areas outlined with a green dashed line). The exclusion of these regions from flow results in a 23% reduction in the permeability compared to the back-stripped medium (a). This is not a dramatic change in the permeability.

However, when a comparable amount of the isopachous cement is introduced around all grains, as in the synthetic sample c), the change in the permeability is much greater: it is reduced by 70% in comparison to the back-stripped sample a). The isopachous cement fringes with a width of 1 pixel (representing $5\mu m$) have such a strong impact on the permeability because *all* pores are narrowed and thus the velocity of the flow through them decreases considerably. Increasing the width of the isopachous cement fringes even further to 2 pixel ($10\mu m$) in the synthetic sample d) results in a permeability reduction of 98% compared to the back-stripped sample. The majority of the narrow pore throats in the synthetic sample d) are closed off completely and the flow is possible only thanks to the high porosity pathway on the left side of the image.

Variability in the synthetic data

The permeability results span almost three orders of magnitude: from 10 to $10^4 mD$. This variability is partially due to the differences in the porosity of the synthetic samples. However, even upon the inspection of the synthetic samples at the same porosity, the differences in the permeability are vast and can span even two orders of magnitude (Figure 3.12). The synthetic data for cemented samples with the same width of the isopachous cement fringes (β) tend to be grouped together and the variability in these groups is much lower than in the entire synthetic dataset. The standard deviation of the point groups for each of the targeted porosities generally decreases with an increasing porosity (Figure

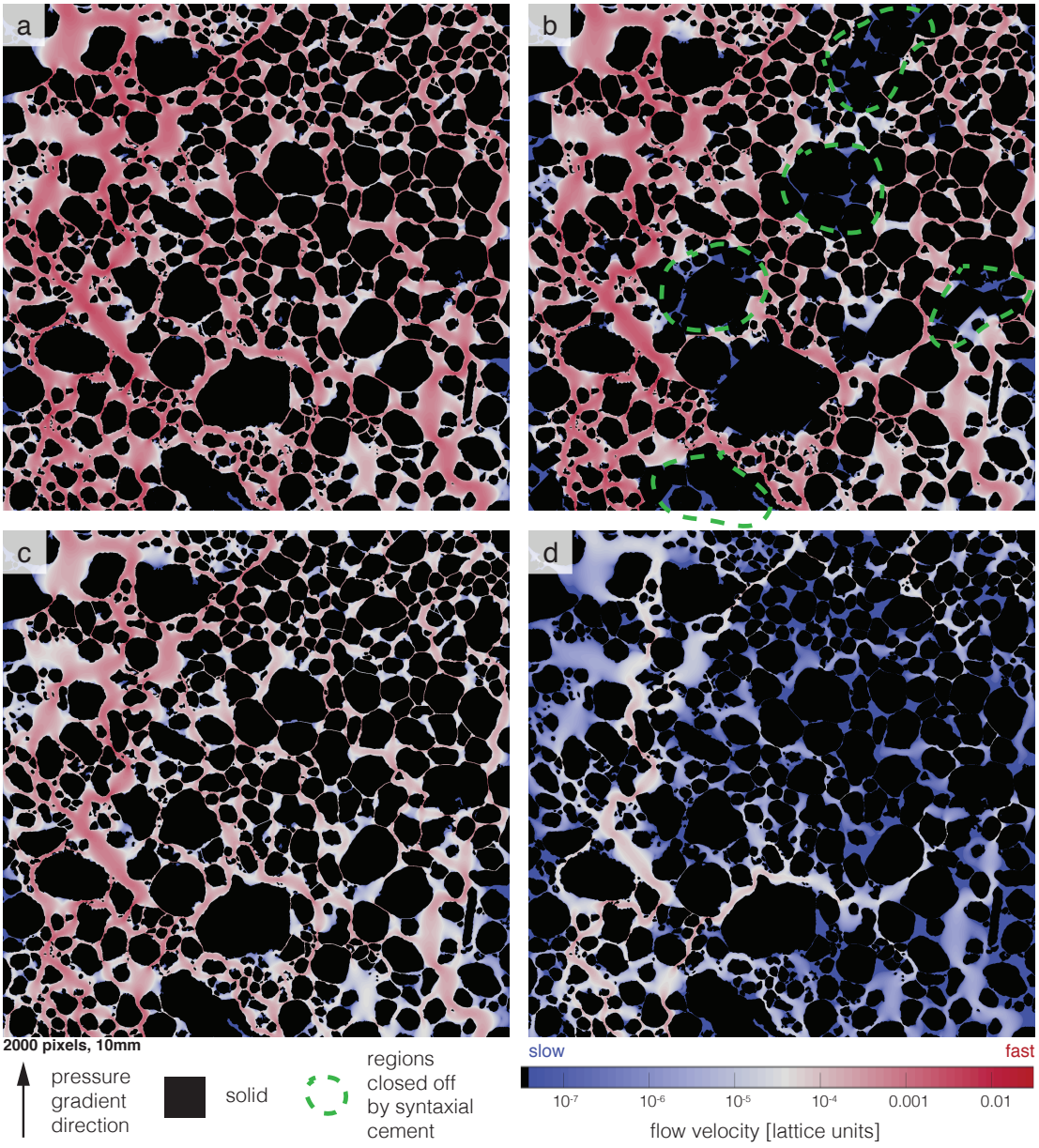

Figure 3.17: The log of magnitude of the flow velocity for the synthetic samples with none or low monocrystalline cement content and varying width of the isopachous cement fringes: a) the back-stripped sample ($\alpha_v = 0$, $\beta = 0$, $\phi = 36.3\%$, $\kappa = 7940mD$), b) a synthetic sample with no isopachous cement and a few monocrystalline grains ($\alpha_v = 12.2\%$, $\beta = 0$, $\phi = 33.5\%$, $\kappa = 6110mD$), c) a synthetic sample with $5\mu m$ width of the isopachous cement fringes and no monocrystalline grains ($\alpha_v = 0$, $\beta = 1$, $\phi = 33.4\%$, $\kappa = 2420mD$), d) a synthetic sample with $10\mu m$ width of the isopachous cement fringes and no monocrystalline grains ($\alpha_v = 0$, $\beta = 2$, $\phi = 30.6\%$, $\kappa = 130mD$).

3.15). The synthetic samples of low porosity tend to have a greater variability in $log(\kappa)$. Another trend observed in Figure 3.12 is that the variability in the results decreases the more isopachous cement there is in the synthetic sample, i.e. for higher β.

This can be explained by the fact that there is less randomness involved in the growth of the isopachous cement, as the only random step associated with the isopachous cement growth in the cementation model is determining whether a grain is to be treaded as polycrystalline or monocrystalline. After a grain is labelled polycrystalline in Stage 1 of Calcite2D, isopachous cement grows, pending adjustments due to the impinging grains, to a width determined by the input parameter in Stage 2. In the case of the monocrystalline grains, there is an additional random step of assigning the direction of the crystal axis of the grain, which (together with the arrangement of the neighbouring grains) has a great impact on the volume of the syntaxial cement produced per grain and its impact on flow (see Section 3.3.1).

In other words, the amount of the monocrystalline grains in a sample controls the variability in the permeability: the more monocrystalline grains there are, the larger is the variability in the permeability, as there are more possibilities in the random choice of the placement of the monocrystalline grains in the synthetic sample and in the directions of the crystal growth. Figure 3.13 illustrates this phenomenon, as the three shaded regions for synthetic data associated with the different widths of the isopachous cement fringes (β) increase in width from left (low variability at low monocrystalline grain content) to right (higher variability at high monocrystalline grain content).

The randomness in the location of the monocrystalline grains and the directions of their crystal axes can lead to very different permeabilities in samples of the same porosity (Figure 3.18). Both synthetic samples shown in Figure 3.18 are generated with the crystal form $40\bar{4}1$. Both of them have no isopachous cement and a porosity very close to 27.4%. These synthetic samples were selected as

two end-points of the synthetic data for $\beta = 0$ and $\phi = 27.4\%$ in Figure 3.12b: one with the highest and one with the lowest permeability. The parameters that characterise these synthetic samples (the width of the isopachous cement fringes, the monocrystalline grain content, and the porosity) are very similar, but the resulting permeability differs by an order of magnitude (22 times).

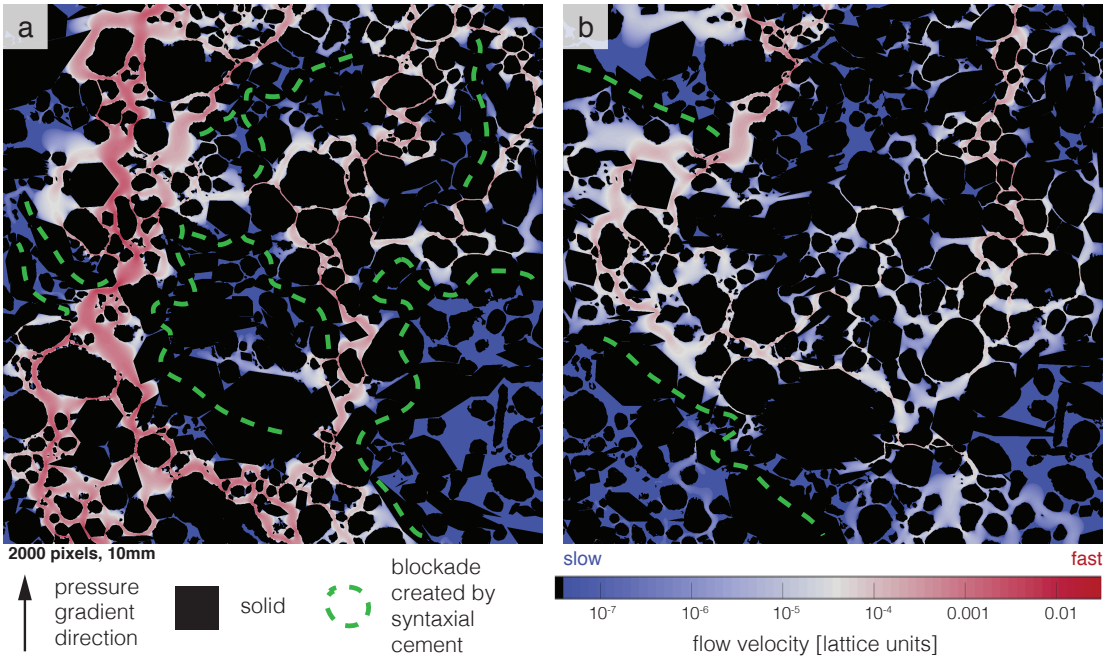

Figure 3.18: The impact of the randomness in the location of the monocrystalline grains in the synthetic sample and the orientations of their crystal axes on log of the flow velocity. From the group of the synthetic samples with no isopachous cement generated with the crystal form $40\bar{4}1$ and porosity of around 27.4%, two synthetic samples with the greatest difference in the permeability are shown: a) $\alpha_v = 31.2\%$, $\beta = 0$, $\phi = 27.5\%$, $\kappa = 2450mD$, b) $\alpha_v = 30.8$, $\beta = 0$, $\phi = 27.4\%$, $\kappa = 110mD$.

This stark contrast in the permeability is directly due to the randomness of the placement of the monocrystalline grains and the directions of the crystal axes. In the high permeability synthetic sample in Figure 3.18a, there is a high-velocity flow channel in the portion of the sample with higher porosity (left side), which remains open despite cementation and allows a fast flow of fluid though it. Monocrystalline grains are present in that high-velocity channel, but their crystal axes are oriented in such a way that the syntaxial cements do not interlock with

other grains, and so do not obstruct the flow. The situation is very different in the low permeability synthetic sample in Figure 3.18b, where syntaxial cements block off the flow at the top and at the bottom of that high-porosity channel (green lines), and so shut down the main highway for flow in the sample. The flow is therefore forced to continue in a convoluted way, which makes the flow path much more tortuous and significantly lowers the permeability.

Another factor that contributes towards the wide range of permeabilities for the synthetic samples at similar porosities is the dimensionality of the methodology. As discussed in Section 2.4.3, the synthetic samples that are percolating in 3D can have non-percolating 2D cross-sections. It is possible that the non-percolating 2D cemented synthetic samples in this study would be found percolating, if 3D pore connectivity was allowed. Similarly, some of the low permeability synthetic samples (e.g. the samples for $\beta = 2$) could have much greater permeability in 3D. The wide range of permeability might therefore be an artefact of the 2D methodology.

Data from the published studies and the plug data

There is no experimental dataset containing the porosity and the permeability data for natural samples with varying content of the monocrystalline grains in grainstones, which would be most useful in validating the results of this study. What does exist, however, is a few datasets of the porosity and the permeability for grainstones. Figure 3.19 presents the synthetic poroperm data for cemented samples generated in this study in the context of the published data for natural grainstones, as discussed in Chapter 1 (Section 1.4), as well as the plug data for several natural samples of the same rock type as is used as an input porous medium in this study (see Section 2.1).

None of the synthetic samples with a porosity less than 20% generated in this study are percolating and so the flow through them cannot be simulated. As a

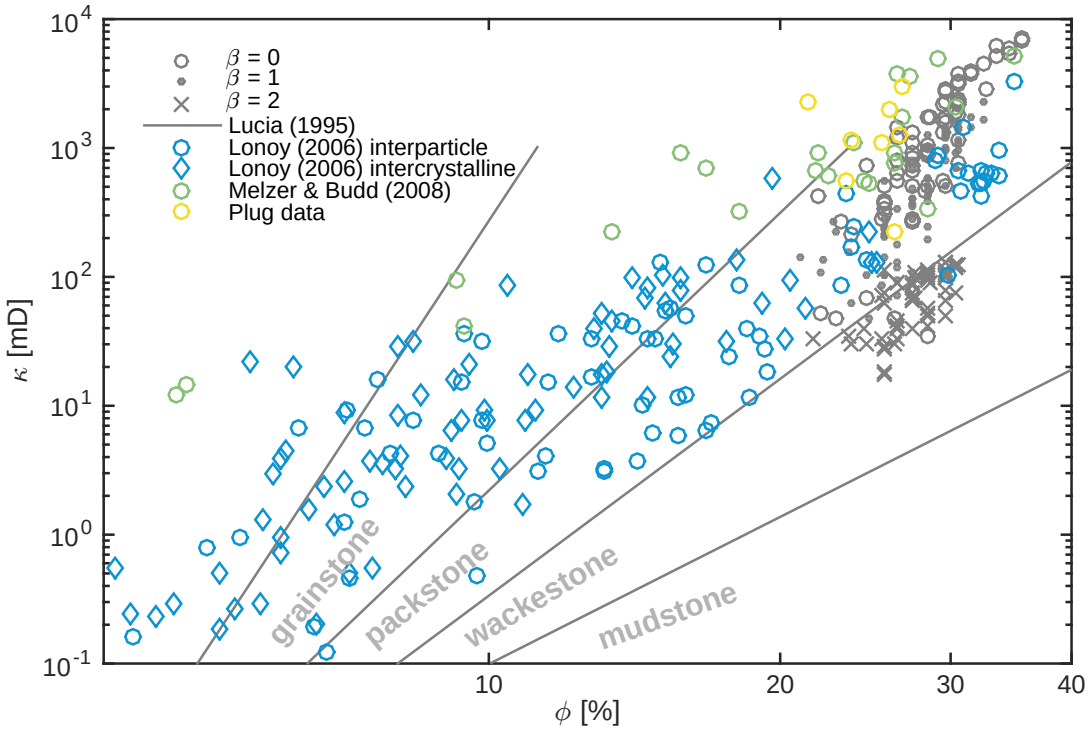

Figure 3.19: The synthetic poroperm data for cemented samples generated with the crystal form $01\bar{1}2$ (grey circles) and the data obtained from literature, including the rock-class divisions from the classification by Lucia (1995) (grey lines), the macroporosity data from Lønøy (2006) (blue) both for the interparticle (circles) and the intercrystalline porosity (diamonds), the data for grainstones from Melzer and Budd (2008) (green circles) and the plug data for the same rock type as is used as the input in the study (yellow circles).

result, all of the permeability results from this study are constrained to a relatively narrow porosity range of the poroperm plot, unlike any of the published poroperm data for grainstones. Moreover, the wide range of the permeability results for the available porosities might be an artefact resulting from the 2D methodology (see Section 2.4.3), as mentioned in the previous section. This should be taken into account when comparing poroperm results from this study with experimental data.

Moreover, recall that this cementation study is based on an initial porous medium which is derived through the segmentation of a thin-section image followed by two post-processing steps: firstly the separation of grains and then the removal of the fine grains. The post-processing steps have a negligible effect on the porosity of the sample, but the effect on the permeability can reach up to 12% (see Section 2.1). As a result, the permeability of the cemented samples generated in this study might be higher than if they were generated using the pre-processed image. The separation of grains affects the permeabilities of the samples with no isopachous cement the most, and so the permeability of these samples might be overestimated the most. The effect of the separation of grains is canceled by the growth of the isopachous cement, so the permeability of the samples with isopachous cement fringes is probably not significantly different than it would be if the pre-processed medium was used. Overall, if the pre-processed medium was used, the samples with $\beta = 0$ would have a permeability lower by up to 12%, while the permeability of the samples with $\beta = 2$ would not change by much. This would shift the high-permeability samples down in the poroperm plot so that the range of permeabilities exhibited by all cemented synthetic samples would be smaller.

The classification by Lucia (1995) places the synthetic samples generated in this study in the packstone sector of the poroperm (Figure 3.19), as the permeability is too low to place it in the grainstone sector. Note, however, that the permeability results obtained in this study might be artificially low due to the modelling of flow in the 2D, which might be causing the shift of the results down on the poroperm

plot, towards the packstone sector. Also, the permeability of the syntaxial samples with no isopachous cement ($\beta = 0$) might be overestimated due to the use of the post-processed image of the porous medium. The interparticle and the intercrystalline macroporosity data by Lønøy (2006) have a decent overlap with the synthetic data from this study, albeit the results in this study show more variability in the permeability. Some of the natural samples of the cement-dominated grainstones analysed by Melzer and Budd (2008) fall within the poroperm range as the synthetic samples generated in this study, particularly in the higher permeability portion. The same happens in the case of the plug data associated with the rock used in this study. Overall it can be concluded that Calcite2D produces synthetic samples with porosities and permeabilities that are more of less realistic for carbonates.

Dependence on the sediment type

One of the goals of this thesis is to investigate the dependence of the permeability on the content of monocrystalline grains in a sample. The results of the investigation in the 2D suggest that this dependence exists and can be formulated in the form of equations 3.3 and 3.4, which suggest that the dependance of the permeability on the monocrystalline grains content as well as on the porosity is linear, with the dependance on the content of monocrystalline grains several times weaker than the dependance on the porosity.

Thus, this 2D study confirms that the composition of deposit, i.e. the amount of the monocrystalline and polycrystalline grains in the sample, is one of the controls on the final permeability of the sample under early calcite cementation regimes investigated in this thesis.

3.4 Conclusions

The work presented herein aims to examine the impact of the composition of carbonate deposit, understood here as the ratio of the monocrystalline to polycrystalline grains, on the properties of rocks where early calcite cementation occurs. For that purpose a model is developed which implements the syntaxial cement growth on the monocrystalline grains and the isopachous cement growth on the polycrystalline grains. This model is used to generate cemented synthetic samples based on a real rock deposit following the methodology detailed in Chapter 2. The samples are generated for two common forms of calcite crystal. The generated synthetic samples are analysed with respect to several quantities of interest: the monocrystalline grain content, the relative volume of the syntaxial cement, the porosity and the permeability.

The results demonstrate the effect of the competition of growing grains for the available pore space: the more monocrystalline grains there are in the sample, the stronger the competition is and the smaller the impact of each individual grain on the resulting early calcite cement volume or porosity.

The synthetic samples with the syntaxial cements grown according to the more elongated crystal form $40\bar{4}1$ have lower porosity for the same monocrystalline grains content than synthetic samples grown according to the more blocky crystal form $01\bar{1}2$. Moreover, the permeability at constant porosity is smaller for the synthetic samples with the form $40\bar{4}1$. Additionally, the synthetic samples with the crystal form $40\bar{4}1$ exhibit greater variability in the results, as this rhombohedral form is more elongated and has the potential of producing a larger volume of cement.

The analysis of the permeability results as a function of the content of monocrystalline grains yields the following phenomenological correlation for the synthetic

samples with the crystal form $01\bar{1}2$:

$$log(\kappa) = 0.053 \cdot \alpha_v + 0.44 \cdot \phi - 11.172 \tag{3.5}$$

where κ is the permeability in mD, α_v is the content of monocrystalline grains in the sample by volume in % and ϕ is the porosity in %.

Admittedly, the above correlation is specific for the rock type investigated in this study, but it is likely that other rock types exhibit a similar dependence of the permeability on the monocrystalline grain content. It is therefore suggested that the composition of the carbonate deposit should be determined and used for a better prediction of the permeability alongside the porosity and other factors.

The poroperm results of the 2D modelling ($10 - 8000mD$) are in a reasonable agreement with the data reported for grainstones in the literature ($0.1 - 5000mD$) as well as for the plug data of the samples used in the modelling (porosity $22 - 27\%$, permeability $200 - 3000mD$), however the permeability results at any given porosity have a wide range due to the bias inherent to the 2D flow modelling and to the fact that a post-processed medium with separated grains was used in as a basis for the cement growth.

Limitations and the next steps

The advantage of working in the 2D is the higher resolution that can be afforded and the significantly lower computational cost. Simulating permeability in 2D, however, has limitations (see Section 2.4.3) and as a result of these limitations, the permeability results for some synthetic samples might be incorrect. This thesis addresses this issue with an implementation of an early calcite cementation model in the 3D, as detailed in Chapter 4.

Chapter 4

Methodology of Cement Growth Model in 3D: Calcite3D

This chapter introduces **Calcite3D**, a Matlab implementation of the process-based cementation model in 3D focusing on early marine calcite isopachous and syntaxial cements. The 3D methodology generates a synthetic 3D porous medium using characteristics observed in a 2D thin-section image, but otherwise the cement growing methodology presented here is very similar to the methodology in the 2D study (Chapter 2); hence the descriptions of these analogical elements are not detailed.

The two processes that are modelled here are the deposition and cementation. The process of compaction is not a part of the modelling as the focus herein is on the *early* cements. Early cemented carbonate rocks tend to be little affected by compaction, as the rock is lithified early and as such, it is more difficult to compact (Budd, 2002).

Similar to Calcite2D, Calcite3D has two stages: Stage 1 defines the sediment type in terms of the ratio of the monocrystalline to polycrystalline grains and the orientations of the crystal axes of the monocrystalline grains; Stage 2 implements

the cement growth on both types of grains in a stepwise fashion with a 1 pixel layer produced at every iteration. Stage 1 is not computationally intensive and can be undertaken on a personal computer. Stage 2 is much more intensive, as it involves multiple iterations on a large 3D matrix (the size of a synthetic sample) and requires a large number (as many as synthetic samples produced) of long runs on a single core (often exceeding 50h). Here, it was performed on the Eddie cluster at the University of Edinburgh.

This chapter presents the full methodology to create early calcite cement in a porous medium in 3D: starting from the analysis of a 2D thin-section to obtain a distribution of grain characteristics, to the generation of the 3D porous medium based on these characteristics, and finally the two stages of Calcite3D and finishing with the procedure to obtain the absolute permeability using Lattice Boltzmann method. This methodology is used to create a single synthetic grainstone deposit, which is then used to generate thousands of cemented synthetic samples for various Calcite3D model input parameters (the content of monocrystalline grains and the width of the isopachous cement fringes) and for two different calcite crystal forms (5946 cemented samples are generated using the crystal form $01\bar{1}2$ and 4086 samples are created using the crystal form $40\bar{4}1$).

Due to the computational cost of the Lattice Boltzmann simulation and because each run requires supercomputing power, the permeability is quantified only for a subset of all generated synthetic samples (457 samples or 4.5%). The flow simulations are performed on Archer, a UK National Supercomputing Service based around a Cray XC30 supercomputer. This chapter concludes with a discussion of the differences between the 2D and the 3D cementation modelling methodology, and the deficiencies of the 3D method. An analysis of the results for all the generated synthetic samples, including the porosity and the permeability, follows in Chapter 5.

Figure 4.1 shows the general steps in the cementation modelling methodology

in the 3D. This starts with the segmentation and the binarisation of a thin-section image and the extraction of a joint distribution of grain shapes and sizes. This distribution is used to create a packing of 3D grains in a process-based simulation that mimics the grains falling and setting due to gravity. The packing of grains is then cropped and voxelised to prepare as an input to the cementation model Calcite3D. In Stage 1 of Calcite3D, grains are randomly labelled as either monocrystalline or polycrystalline, based on a model input parameter. For every monocrystalline grain the crystal axis (c-axis) is defined, and chosen at random from all possible 3D orientations. In Stage 2 of Calcite3D, the cement is grown on all of the grains. As in Calcite2D, the type of cement is determined by the grain type, with the syntaxial cement growth on the monocrystalline grains and the isopachous cement growth on the polycrystalline grains. The permeability of the cemented rock is then obtained via the Lattice Boltzmann simulation. Below, the details of all the steps of this methodology are given.

4.1 Generation of a 3D Porous Medium

To make the cementation model more realistic and versatile, the initial structure of the carbonate sediment should be close to the real carbonate deposit. Current 3D imaging methods, e.g. microcomputed tomography (μCT), do not differentiate between the grain and the cement, which is necessary before one can segment the image and analyse the original deposit. To this end, a 2D thin-section image and the data extracted from it are used to generate a synthetic 3D deposit that serves as an input to the cementation model Calcite3D.

The proposed methodology is process-based and follows similar published models (see Section 1.7.3), such as the work of Bakke and Øren (1997). The grain size and the shape distributions are extracted from a thin-section image of a real carbonate reservoir rock and used to generate a distribution of grains that are simulated to fall and settle under gravity. The details of the methodology follow.

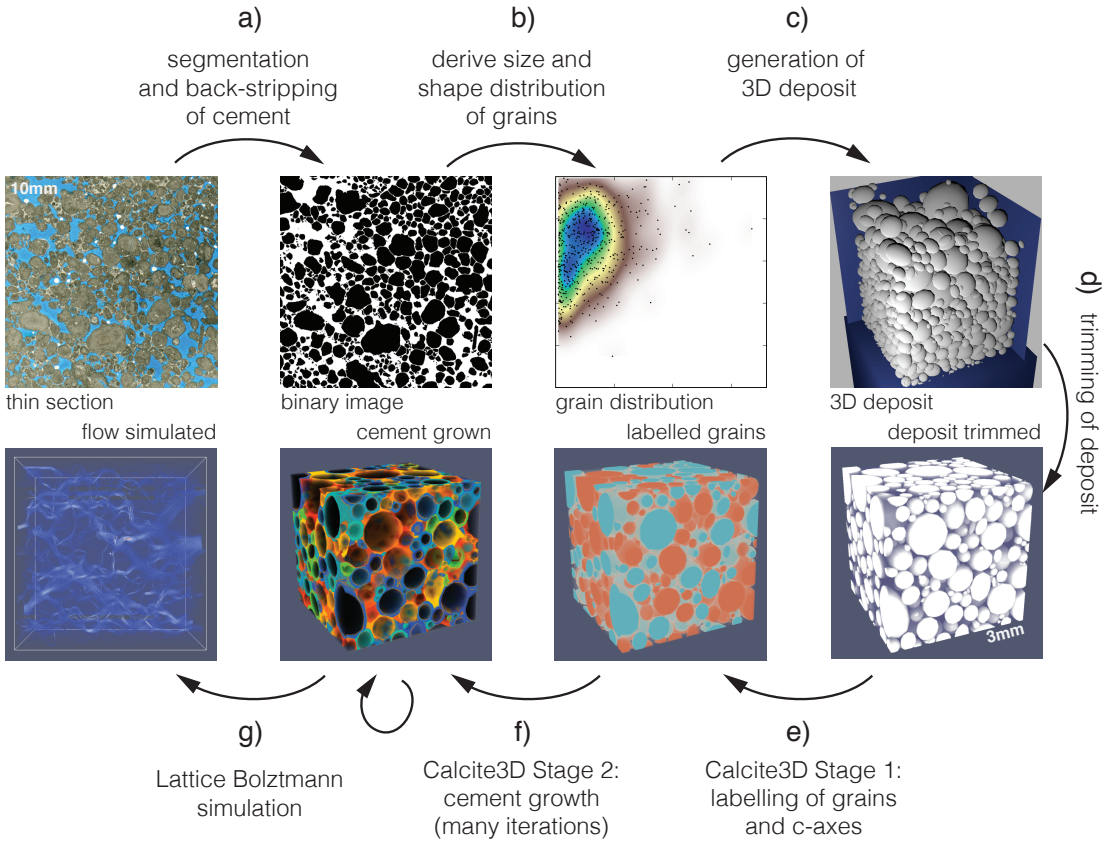

Figure 4.1: The general Calcite3D methodology: a) a thin-section image is segmented and stripped of cement, b) the joint distribution of grain size (the equivalent diameter) and shape (the aspect ratio of a fitted ellipse) is determined, c) the synthetic 3D deposit is generated based on that distribution, d) the synthetic deposit is cropped to avoid artefacts in grain arrangement due to box boundaries, e) Calcite3D, Stage 1: grains are labelled monocrystalline or polycrystalline and the crystal axes of the monocrystalline grains are determined, f) Calcite3D, Stage 2: the cement growth, g) the Lattice Boltzmann simulation of flow.

4.1.1 2D data from a segmented thin-section

The 3D deposition model aims to mimic the same carbonate rock type as is used in the 2D modelling, so the same thin-section image is used. The thin-section image (Figure 2.2a) is segmented and stripped of cement, following the methodology detailed in Section 2.1. The binary back-stripped image (Figure 2.2c) is then used to extract a joint distribution of grain shapes and sizes using Matlab's Image Processing Toolbox (function *regionprops*). Only the grains fully visible in the 2D image are considered. Inclusion of grains interrupted by the boundaries of the image could result in lowering of the average size of grain, and a shape distribution skewed towards the more elongated shapes. Excluding these incomplete grains avoids this bias. Of the 604 grains in the binary back-stripped image, 81 are incomplete, i.e. touching a boundary of the image, and 523 are completely visible.

The shape parameter is the aspect ratio of the grain. More specifically, it is the eccentricity of the ellipse with the same second-moments as the section of the grain visible within the plane of the image. The size parameter is the length equivalent to a diameter of a circle with an area equal to the area of the section of the grain (the equivalent diameter).

Figure 4.2a shows the shape and size data for the 523 complete grains visible in the binary back-stripped image as well as a probability density function of the two variables obtained with the use of the kernel density estimation (Silverman, 1986). The obtained probability density function is subsequently used to generate a sample of 6000 pairs of grain shape and size variables, as shown in Figure 4.2b. The generated sample has a probability distribution almost identical to the distribution of the grain shape and size parameters in the binary back-stripped image.

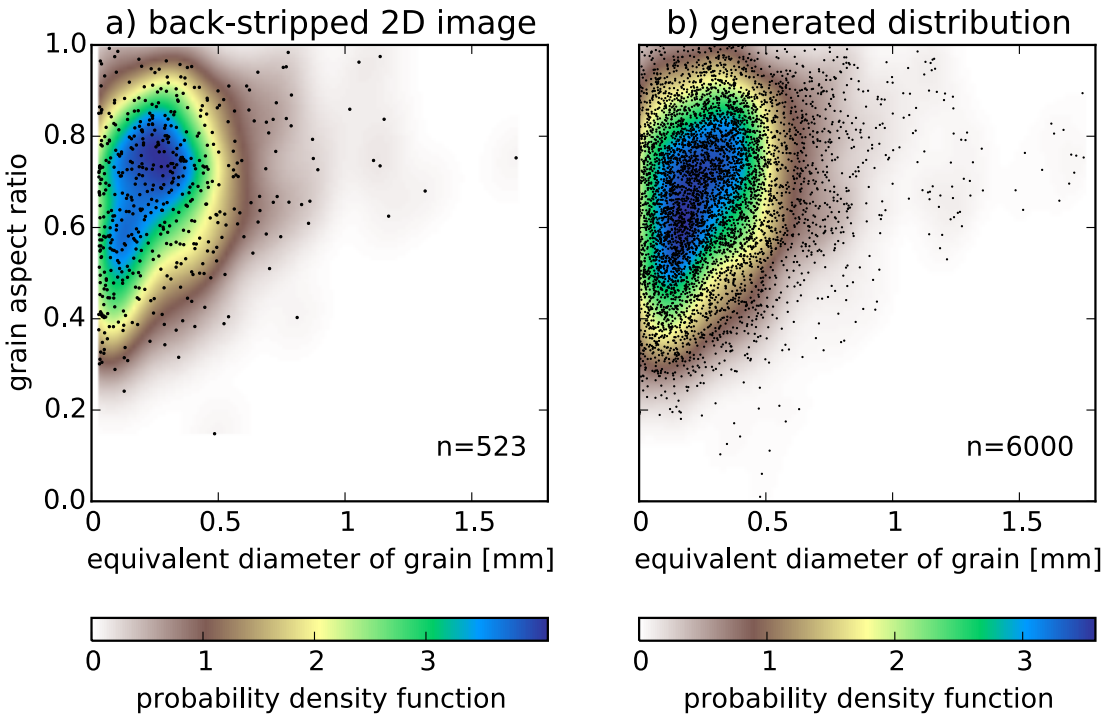

Figure 4.2: Joint distributions for grain size and shape for a) 523 complete grains visible in the binary back-stripped image, b) the sample generated using the kernel density estimation on the distribution in the back-stripped image. The grain shape parameter is the eccentricity of the ellipse that has the same second-moments as the section of the grain visible in the 2D plane. The grain size parameter is the equivalent diameter of a circle with the same area as the grain.

4.1.2 Deposition simulation

The generated sample of grain sizes and shapes is used to create a grainstone deposit. Grains are created and simulated in Blender, a free and open-source 3D creation suite (http://www.blender.org). The grains are initially created in the form of spherical meshes with 42 vertices and 80 triangular faces and a diameter specified by the size variable from the generated sample (the equivalent diameter). Their shape is subsequently modified by reducing two of the axes of the sphere so that the ratio of the two minor axes of the resulting ellipsoid to the major axis is equal to the shape parameter from the generated distribution (the eccentricity). Next, the grain meshes are randomly rotated, so that there is no bias arising form the pre-simulation orientations of the elongated grains.

In addition, an impenetrable static box is created with a base of 4×4mm and a height of 5mm, in which the grains will be deposited. 1904 grains are created and arranged in 119 layers of 4×4 grains directly above the box, spaced so that they do not intersect with each other.

The open-source Bullet Physics Engine (Coumans, 2015), incorporated in Blender, is then used for simulation of the physical interactions of grains falling and settling due to gravity. Bullet Physics implements gravity and collision physics and is a well established physics engine used for scientific modelling as well as game programming. For the purposes of the simulation, grains are treated as rigid bodies, which ensures that they do not deform when they collide with other objects. The friction coefficient is set high (0.9) so that the grains behave like natural grains, which seldom have smooth surfaces. A high damping coefficient (0.9) as well as a high rotation damping coefficient (0.9) are used to mimic the environment of deposition in a fluid, as opposed to deposition in air, which is characterised by a relatively small damping of movement. Lastly, a mass proportional to d^3, where d is the size parameter from the generated distribution (the equivalent diameter), is applied to each grain. This ensures that the grains

have a momentum proportional to their mass, thus larger grains have more impact in case of collision with smaller grains, just like in the physical world.

Figure 4.3a shows the state of the grains after the physics simulation in Blender is completed and 1904 grains have fallen and been deposited in the box of dimensions $4 \times 4 \times 5$mm. The output of the model is a mesh-based grain accumulation structure, i.e. the grains are described by a set of vertices and faces. The grains are subsequently saved in a Wavefront.obj format, which contains the coordinates of the vertices and faces of each grain.

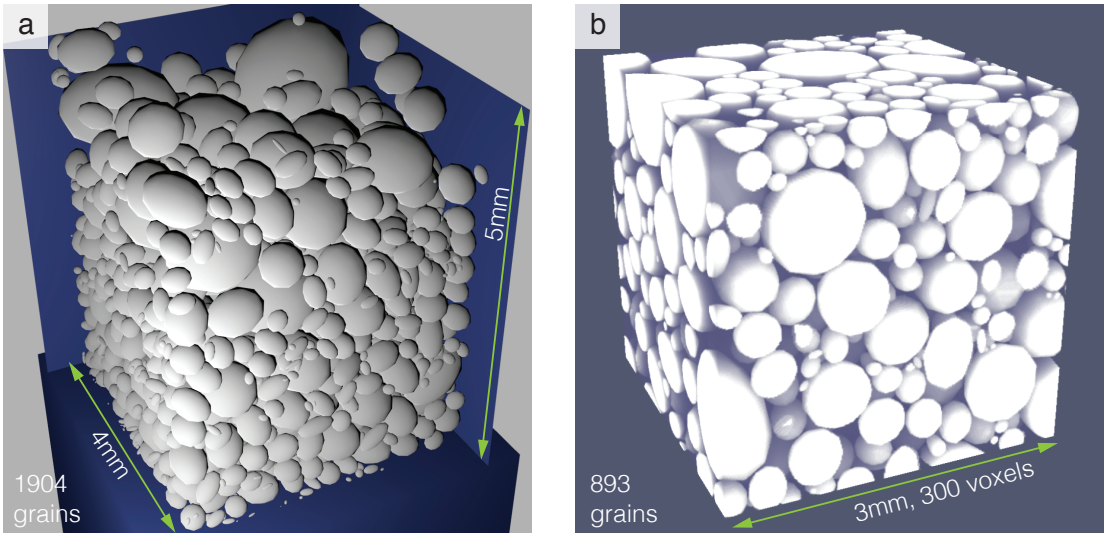

Figure 4.3: The model output of the deposition simulation: a) the end-state of the physics simulation using Bullet Physics Engine in Blender, 1904 grains (white) are deposited in a $4 \times 4 \times 5mm$ box (blue); b) post-processed synthetic deposit ready for cement simulation, grain packing in mesh representation is cropped to $3mm^3$ and voxelised to 300^3 voxels so that only 893 grains (white) remain.

4.1.3 Voxelised 3D porous medium

Before the product of the simulation of the settling grains can be used as an input in the cementation model, the grain packing needs to be post-processed. The procedure starts with reading the output of the grain deposit simulation in

the form of meshes (Figure 4.3a) into Matlab using a function *read_wobj* developed by Kroon (09.09.2011). A structure containing all grains is created, including the coordinates of 42 vertices and a list of 80 faces for each grain. The vertices and faces are retained as properties of each grain to be used in the cementation model.

In order to avoid artefacts in the arrangement of the grains arising from the proximity of the grains to the sides of the deposit box, the original deposit of dimensions $4 \times 4 \times 5$mm is cropped by 0.5mm from all sides except from the top, where it is cropped by 1.5mm. The deposit is cropped mainly from the top, because this area has a tendency to be uneven, as opposed to all the other sides, which are controlled by the sides of the deposit box. Cropping the top by 1.5mm ensures that no empty spots are captured. This procedure yields a porous medium of dimensions $3 \times 3 \times 3$mm and with a smaller number of grains.

Since both Calcite3D and the Lattice Boltzmann method require a voxelised medium as an input, the grains are then converted from a mesh to a voxel representation. The voxelisation of the mesh is achieved by choosing the number of voxels in each dimension. In this study the size of 300^3 voxels is chosen, which, combined with the porous medium of dimensions $3 \times 3 \times 3mm$, results in a voxel size of $10\mu m$. This is twice as big as the pixel size in the 2D study.

After all coordinates of vertices of grain meshes are converted from Blender units to grid units, each grain is voxelised. This is achieved by finding the extrema of the grain mesh in three dimensions so as to determine the smallest box with faces parallel to the faces of the 3D porous medium that can be circumscribed on the grain. Next, all grid points in the enclosing box are investigated as to whether they are located inside or outside of the grain mesh using function *inhull* by D'Errico (06.09.2012). The grid points inside the grain mesh are designated as solid voxels and the ones that are outside - as pore voxels. Figure 4.3b shows the cropped porous medium voxelised to a 300^3 voxel grid.

Comparison of the characteristics of the synthetic 3D deposit with the 2D thin-section

To allow comparison of the shapes and sizes of grains of the 3D medium with the original 2D data, 30 sections spaced every 10 voxel ($100\mu m$) are taken through the 300^3 voxel synthetic deposit. To avoid any bias in the shapes and sizes of grains due to image boundaries, only grains completely visible in these sections are considered, which amounts to 1412 grains. Figure 4.4b shows the resulting distribution and probability density function of these two variables.

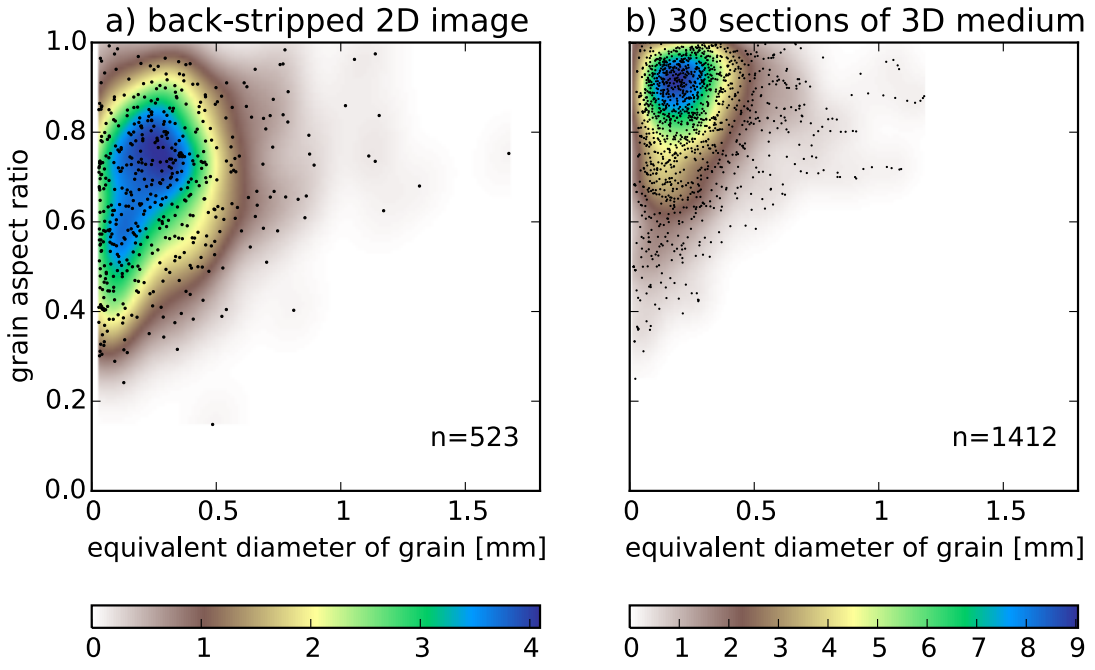

Figure 4.4: The joint distributions for grain size and shape for a) 523 complete grains visible in the binary back-stripped image, b) 1412 complete grains visible in 30 sections spaced every 10 voxels ($10\mu m$) though the 300^3 voxel synthetic deposit.

After analysing all possible 900 sections through the synthetic deposit in all three directions, the largest grain in the 3D medium was found to have a major axis 1.3mm long. Since the sections through the medium are taken at 0.1mm intervals, inevitably some of the bigger grains are considered more than once. This is manifesting in Figure 4.4b as the patterns of the trailing points in the large grain

range (around 1mm) in the centre of the image, which represent a single large grain appearing in multiple sections. Ideally each grain would be represented in the distribution only once. But to accomplish this, much fewer sections would need to be taken (no more than three), which would yield too few grains to be statistically sound.

The mean size of grain in the back-stripped medium is $286\mu m$, while the mean size in the 3D medium is $260\mu m$. The porosities of the two media are also very similar: the 2D medium has a porosity of 36.31% and the 3D medium has a slightly higher porosity of 37.91%. Thus it is concluded that this method of generating a 3D deposit is equally successful in reproducing grain sizes and porosity.

The method is less successful, however, in terms of the reproduction of grain shapes. Figure 4.4 shows that the joint distribution of shapes and sizes found in the 30 sections through the 3D medium (b) are not in good agreement in terms of the shape of the grains with the distribution derived from the 2D image (a). The mean eccentricity of grains in the 2D image is 0.67 while the mean eccentricity of the cross-sections of grains in the 30 sections of the 3D medium is 0.82. This difference suggests that there is a room for improvement in the methodology, as discussed further in Section 4.4.

4.2 Calcite3D

The cementation methodology implemented in Calcite3D is very similar to the one implemented in Calcite2D. The main difference is that here the bounding polyhedra of the potential syntaxial cement are represented in the voxel form, i.e. a set of voxels in the bounding polyhedron for each monocrystalline grain is retained as a grain property and modified along the course of the simulation due to impinging effects. This leads to greater memory requirements as well as to longer time-to-solution.

Since the algorithms of Stage 2 are voxel-based and multiple iterations on the voxels are required for all grains, the simulation of cement growth takes a significant amount of time. Simulation time for a high-monocrystalline content synthetic sample could take up to 60h on a single core. The time-to-solution depends on the number of monocrystalline grains. It cannot be accurately estimated before the simulation, as it depends on the impinging of grains and the modifications that arise in course of the run of the simulation. As the time limit for a job submitted on the Eddie cluster is 48h, the code is designed in such a way that it saves an input after every iteration (corresponding to a growth of 1 voxel layer of cement) and so it is possible to restart the code at the last iteration that was completed in case the nominal time on the cluster runs out.

Similar to Calcite2D, Calcite3D is based on the premise that there are two basic types of carbonate sediment grains: polycrystalline and monocrystalline (see Section 1.5). These two types of grains develop different types of cement that have different volumes and geometries and therefore have a different impact on the cemented rock properties (Scoffin, 1987; Tucker and Wright, 1990). Polycrystalline grains have seeding sites on the grain boundary that develop cement growth with many different crystal axis orientations. This results in a layer of nearly constant thickness developed around grains, an isopachous cement. The seeding sites on the monocrystalline grains grow cement in optical continuity to the grain itself (the same crystal axis orientation), resulting in syntaxial cement.

Calcite3D has two stages, each of which takes one model input parameter. The overall steps of Calcite3D implementation are equivalent to the stages of Calcite2D (Figure 2.4). Stage 1 involves the grain identification and labelling as either polycrystalline of monocrystalline based on the input parameter α_0 (Figure 2.4a) as well as the definition of the crystal axes orientations and establishing of the polyhedral bounds of the epitaxial growth (Figure 2.4b). Stage 2 of Calcite2D implements calcite growth and takes as the input parameter the target width of the isopachous cement fringes that will coat all polycrystalline grains β (Figure 2.4c and d). The details of the implementation follow.

4.2.1 Stage 1: grain labelling and crystal axes definition

The procedure starts with the reading of the inputs. This consists of a structure with grain properties including a mesh representation of a grain, i.e. the coordinates of vertices and the list of faces, and a set of voxels belonging to that grain as well as the voxelised 3D porous medium, which differentiates between pore and solid voxels.

Grain labelling

The grains are labelled either monocrystalline of polycrystalline, based on the input parameter α_0 and a random number generator, so that the final content of monocrystalline grains (α_n) might differ slightly from the model input parameter.

3D bounding polyhedron

For each monocrystalline grain the circumscribed crystal is determined. This is achieved following the methodology to find a tangent parallelepiped on a surrogate 3D grain described in Section 2.2.1. The difference is that instead of the surrogate grain, vertices of the mesh representation of the actual 3D grain are used. The technical details involved in this methodology are presented in Section 2.2.1 and what follows here is only a short description of the steps followed.

The orientation of the crystal axis of the monocrystalline grain is selected at random by rotating the planes associated with a rhombohedral form of calcite (either $01\bar{1}2$ or $40\bar{4}1$) in three directions using the rotation matrices. Afterwards, the six planes tangential to the grain are found. The intersections of the planes define the bounding parallelepiped which delineates the maximum potential extent of syntaxial cement growth for that grain, pending impinging effects.

Other grain properties

To facilitate Stage 2 of the cementation model, the grain properties are supplemented with a list of faces that bear a given vertex and a list of vectors normal to the faces of the grain (performed using the function *patchnormals* developed by Kroon (02.06.2009)). All grains are then given an 'active' label. The two most distant vertices (extrema) of the bounding polyhedron are found and retained as a pseudo c-axis of the grain. The extrema are used in the implementation of the impinging and the 'shadow' effects (details below).

Representations of the content of monocrystalline grains: α_n, α_v and α_a

After all grains are labelled, the number of the monocrystalline grains is calculated, which enables the derivation of the ratio of the number of monocrystalline grains to all grains (α_n). The volume of monocrystalline grains in voxels is also determined, so that the ratio of the volume of the monocrystalline grains to the volume of all grains (α_v) can be determined. Finally, the surface area of all grains is determined using the mesh representation of the grains and the package *geom3d* by Legland (20.05.2015), so that the ratio of the surface area of the monocrystalline grains to the surface area of all grains (α_a) can be calculated.

Outputs

The outputs saved at the end of Stage 1 of Calcite 3D include:

- A 3D porous medium matrix that differentiates between pores, monocrystalline and polycrystalline grains;
- A grain structure with grain properties common to both types of grains:

  - the coordinates of grain vertices and a list of faces;
  - a set of grain voxels;
  - a list of vectors normal to grain faces;
  - a list of faces which bear a given grain vertex;
  - an active/inactive label;
  - a monocrystalline/polycrystalline label;

- Grain properties exclusive to monocrystalline grains:
  - the coordinates of the centroid of the grain;
  - the plane orientations associated with the bounding parallelepiped;
  - the coordinates of of the vertices the bounding parallelepiped and a list of its faces;
  - the coordinates of the two most distant vertices (extrema) of the bounding parallelepiped.

Finally, all bounding parallelepipeds (crystals) are voxelised and saved as an output to be used in Stage 2 of Calcite3D. The voxelisation procedure is memory-intensive, as the voxel volume of all bounding polyhedra might many times exceed the volume of the 3D medium (300^3 voxels), particularly in the high-monocrystalline grain content cases (high α_0). However, this is implemented to accelerate Stage 2 and avoid many *inhull* calls, which are time-consuming.

4.2.2 Stage 2: cement growth

Once the polycrystalline and monocrystalline grains are defined and the associated polyhedral outer bounds of the epitaxial growth are assigned to them, the cement growth algorithm of Stage 2 of Calcite3D can be applied. Stage 2 takes the target width of the isopachous cement fringes (β) as an input parameter.

After the outputs of Stage 1 are loaded, the first step of Stage 2 determines whether the 3D porous medium percolates in all three directions. If the code is run for the first time, the simulation time is initialised to 0 and the current width of the isopachous cement fringes is set to 0. If the simulation is restarted, the current time step and the current width of the isopachous cement fringes are loaded from the last save point of Stage 2. The cement growth is then started, first with 1 voxel layer of isopachous cement growth on the polycrystalline grains, followed by a layer of syntaxial cement growth around the monocrystalline grains.

Similarly to Calcite2D, the isopachous cement growth stops as soon as the target width of isopachous cement fringes is reached, as set by an input β to Stage 2. In this study, values from 0 to 5 voxels are used, which means that a maximum of 5 iterations are necessary to grow the isopachous cement fringes to a thickness equivalent of 50 μm.

Note that the maximum possible volume of the syntaxial cement is determined by the bounding polyhedra found in Stage 1. The syntaxial cement for a given grain stops growing either when the entire bounding parallelepiped is filled, or when all seeding sites of the grain are blocked by impinging grains. The syntaxial cement growth in the entire medium ceases when all grains have reached that point. The amount of iterations necessary to achieve that point depends on the size of the bounding polyhedra, which are controlled by the size of the monocrystalline grains, and on the arrangement of the grains with respect to each other (the impinging potential). Stage 2 takes a significant number of iterations until completion (in this 3D study usually up to 100) and this number cannot be accurately determined before the simulation.

Isopachous cement growth

If the current width of the isopachous cement fringes is smaller than the target width specified by the input to Stage 2 of Calcite3D (β), the following steps are repeated for all polycrystalline grains:

1. Expand the mesh of the grain by translating all faces of the grain outward by 1 voxel (Figure 4.5a). This is achieved by translating each face along its normal (a grain property) by a length of 1 voxel and deriving the new plane using the equation of the plane passing through a point. The list of faces that each grain vertex is on (a grain property) is then used to determine the points of intersection of the expanded grain mesh. Grain properties are then updated with the new vertices.

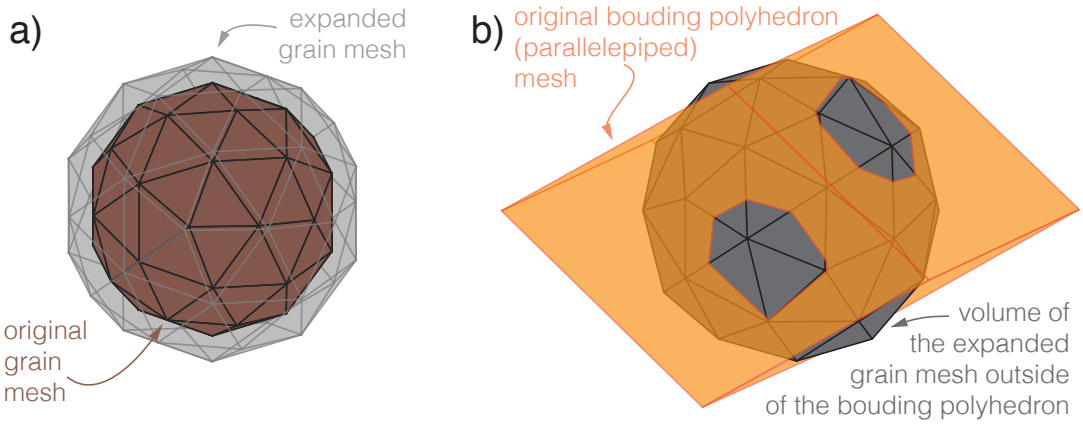

Figure 4.5: a) The grain mesh is expanded by translating all the faces outward by 1 voxel. b) The bounding polyhedron is circumscribed on a monocrystalline grain. New cement is added only in the intersection zone of the expanded grain and the bounding polyhedron.

2. If a grain is active, determine the set of voxels that are in the expanded grain, but not in the original grain - this set of voxels is the potential new isopachous cement. This is achieved by voxelising the expanded grain using

the same method as described earlier to voxelise each grain of the synthetic sample (see Section 4.1.3).

3. From the set of the voxels contained in the expanded grain, remove the voxels that are also contained in the original grain.

4. From the obtained set of voxels in a form of a 1-voxel-thick shell, remove the voxels that are already designated as solid, i.e. the voxels that belong either to another grain or to cement, as of the previous iteration of cement growth. The voxels that remain in that set are the new isopachous cement for that grain produced in that iteration.

5. If that set is empty, i.e. if no isopachous cement is produced for that grain in the current iteration, deactivate the grain.

6. Otherwise update the porous medium matrix with the new isopachous cement and update the properties of the grain to include the new cement.

After the procedure is repeated for all polycrystalline grains, the volume of isopachous cements found in this iteration is determined and the current width of the isopachous cement fringes is increased by 1.

Syntaxial cement growth

If there are any active monocrystalline grains left, i.e. if any monocrystalline grain produced a non-zero volume of the syntaxial cement in the previous iteration, repeat the following steps for all monocrystalline grains:

1. If a grain is active, expand the grain mesh, just like in the case of the isopachous cement growth (Figure 4.5a).

2. Voxelise the expanded grain and remove from that set voxels belonging to the original grain, so as to form 1-voxel-thick shell of voxels. Any new

syntaxial cement that is going to be produced for that grain in that iteration is in that set of voxels.

3. Remove from that set any voxels that lie outside of the bounding polyhedron (Figure 4.5b). This is achieved with the use of the *inhull* function.

4. For each of the voxels form the resulting set, verify whether they are already solid, i.e. are in another grain of cement as of the previous iteration. This is achieved by investigating the entries in the 3D porous medium matrix. The voxels that are found to be already solid are the 'obstacle' voxels and for each of them the following steps implementing the impinging effect are followed:

   (a) Find the 'extremum' of the bounding polyhedron of the grain (a grain property) that is closest to the 'obstacle' voxel.

   (b) Calculate *three* planes with orientations equivalent to the orientations of the faces of the bounding polyhedron (a grain property) and which are crossing the 'obstacle' point/voxel.

   (c) Determine the *three* planes of the bounding polyhedron that meet at the closer 'extremum' of the bounding polyhedron.

   (d) Intersect eight triplets of non-parallel planes of these *six* planes to obtain eight vertices of a parallelepiped (Figure 4.6a). This parallelepiped is the 'shadow' parallelepiped that is prohibited from growth by the fact that it is blocked by the 'obstacle' point.

   (e) From the set of voxels describing the current maximum extent of syntaxial cement growth, i.e. the current state of the bounding polyhedron modified by any previous impinging effects, remove the voxels that lie within the 'shadow' parallelepiped. This updates the maximum possible extent of the syntaxial cement growth for that grain.

5. From the set of the potential syntaxial cement voxels for that grain, remove the ones that are not in the set of the voxels belonging to the updated

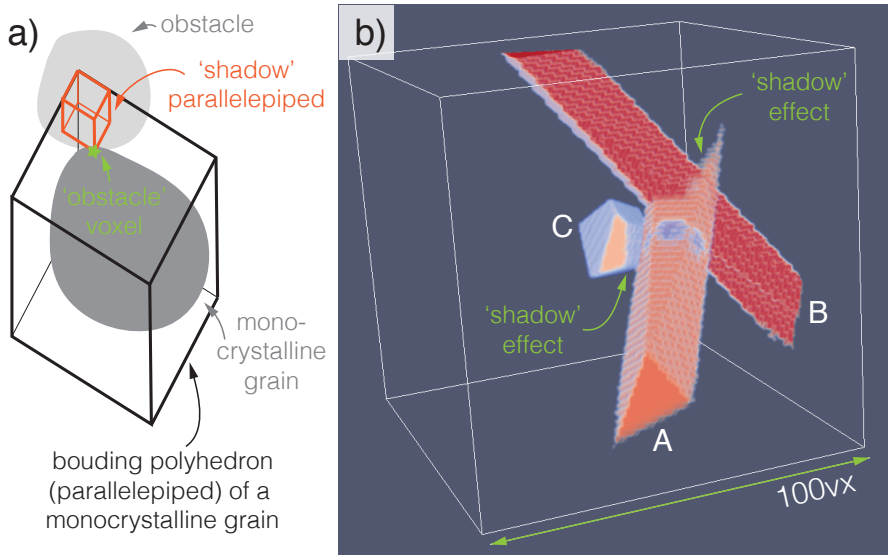

Figure 4.6: The impinging effect. a) Syntaxial cement growing around a monocrystalline grain encounters another grain at an 'obstacle' point (green star). As a result, the voxels inside of the 'shadow' parallelepiped (red) are removed from the list of the potential syntaxial cement voxels. b) The impinging and 'shadow' effects implemented in Calcite3D. Three monocrystalline grains, which developed syntaxial cement of the crystal form $40\bar{4}1$, are voxelised in a 100^3 voxel box. Syntaxial cement grown on these grains impinges on one another and the cement volume is limited.

bounding polyhedron. This completes the removals of voxels from that set as only the voxels that constitute the new syntaxial cement now remain.

6. If this set is empty, i.e. if no new syntaxial cement is produced for that grain in that iteration, deactivate the grain.

7. Otherwise update the 3D porous medium matrix with the new syntaxial cement and update the grain properties to include the new cement and the updated set of voxels of the bounding polyhedron.

After the procedure is repeated for all monocrystalline grains, the volume of syntaxial cements found in this iteration is determined.

Impinging grains and the 'shadow' effect

The idea behind the implementation of the impinging effect, as described in the previous section, is the same as in the case of the 2D model (see Section 2.2.2). It is based on an observation that when syntaxial cement encounters an obstacle during its growth, that 'obstacle' point is blocked and will not seed any more cement (Section 1.6.5). Thus a 'shadow' is created where no syntaxial cement can be produced by that grain. In the 2D case this 'shadow' takes a form of a parallelogram (Figure 2.8), while in the 3D case it takes a form of a parallelepiped (Figure 4.6a).

In the 2D model it is possible to retain the representation of the bounding polygon in a form of its vertices and edges and implement the impinging effect based on that representation. However, due to the increased complexity, in the 3D model it is not possible to implement the effect of impinging using the mesh representation of grains. This is the main reason why a voxel-based approach is chosen, even though memory and run time requirements are significantly larger.

Figure 4.6b shows a result of the implementation of the impinging effect on an

example of three monocrystalline grains with syntaxial cement of the crystal form $40\bar{4}1$ voxelised in a 100^3 voxel box. Grain B blocks grain A from growth (green arrow), so that only a small seeding area remains. Grain A impinges on grain C and reduces the volume of the syntaxial cement produced (green arrow).

Finishing steps

Once cement is grown for every active monocrystalline and polycrystalline grain, the updated porosity of the 3D porous medium due to the new isopachous and syntaxial cements produced in a given iteration is determined. The simulation time is increased by 1 and all outputs are saved, including the 3D porous medium matrix (which serves as the input for flow simulation), the current state of the grain properties (for the purposes of restarting the simulation in case it is interrupted) as well as the isopachous cement and the syntaxial cement volume produced in each iteration.

4.2.3 Example model output of Calcite3D

Overall, 5960 cemented synthetic samples were produced using the crystal form $01\bar{1}2$ and 4086 cemented samples were produced using the crystal form $40\bar{4}1$. While performed on a single core due to the sequential nature of the cement growth, the simulations required long time-to-solution and were performed on the Eddie cluster at the University of Edinburgh. In total, the simulations for the synthetic samples with the crystal form $01\bar{1}2$ took 24,500 CPU hours (4.12 CPU hours per sample) and the simulations for the samples with the crystal form $40\bar{4}1$ took 124,000 CPU hours (30.5 CPU hours per sample).

Figure 4.7 shows model outputs of Calcite3D. The simulation of the sample with the crystal form $01\bar{1}2$ (a) took 32 steps and 2.1h to complete, and the simulation with the crystal form $40\bar{4}1$ took 85 steps and 13.0h to complete. This

difference in the time-to-solution is because the crystal form $40\bar{4}1$ produces more elongated syntaxial cement forms, which can take more time steps to complete the simulation, especially if the cement growth is not blocked by impinging grains.

In both synthetic samples, cement is present that has grown into the plane of the section, even though the grain that seeded that cement is not present in that section. This applies to both isopachous (blue-green) and syntaxial (red-yellow) cements (Figure 4.7b). This is an improvement over the 2D model, where this phenomenon is not taken into account. 'Shadow' effects of impinging grains can also be observed in a couple of syntaxial cements present in the synthetic samples.

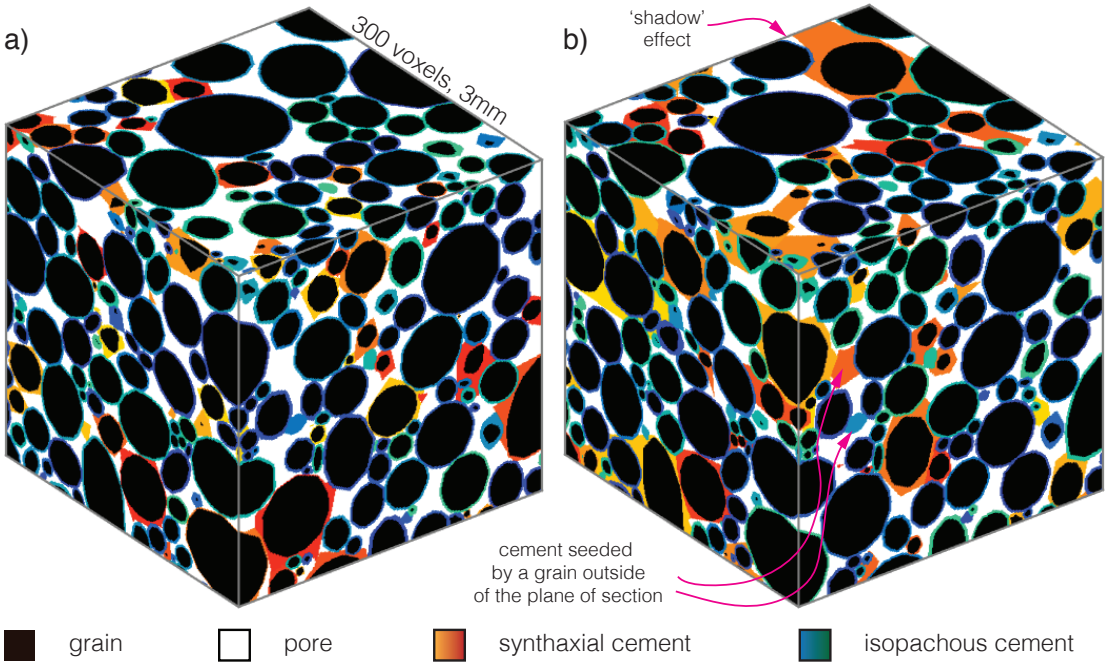

Figure 4.7: Model outputs of Calcite3D a) for the crystal form $01\bar{1}2$, $\alpha_v = 23.2\%$, $\beta = 2$ voxel, $\phi = 20.8\%$ b) for the crystal form $40\bar{4}1$, $\alpha_v = 18.7\%$, $\beta = 2$ voxel, $\phi = 16.2\%$.

4.3 Permeability Prediction Using Lattice Boltzmann Method

A 3D version of the Lattice Boltzmann code (D3Q27) DL_MESO is utilised. DL_MESO was developed under the auspices of the Engineering and Physical Sciences Research Council (EPSRC) for the EPSRC's Collaborative Computational Project for the Computer Simulation of Condensed Phases (CCP5) (Seaton *et al.*, 2013).

Due to the size of the synthetic samples (300^3 voxels) and the fact that Lattice Boltzmann is a computationally intensive method, supercomputing power was required to perform the simulations. Overall, 457 simulations were performed on Archer, a UK National Supercomputing Service based around a Cray XC30 supercomputer. This required a computing resource of about 2950 kAU, an equivalent of 196,000 CPU hours.

4.3.1 Lattice Boltzmann simulation set-up

As in the 2D study, the Zou-He pressure boundary (Zou and He, 1997) on the inlet and the outlet faces of the 3D porous medium and a bounce-back boundary on the faces parallel to the direction of the pressure gradient are used. The pressure difference chosen between the inlet and outlet boundaries is 0.1 across the 300^3 voxel medium. The relaxation parameter τ used in this study is 1, a value most commonly used in the literature (Narváez *et al.*, 2010). The justification for these choices is the same as in the case of the 2D study (see Section 2.3.1).

4.3.2 Permeability calculation

As in the 2D study, the permeability is computed using the outputs for the density and the velocity of the fluid in the direction of the pressure gradient (the fluid forcing direction) according to the formula (Zhang *et al.*, 2013; Boek and Venturoli, 2010):

$$\kappa_{LB} = \nu \frac{\langle U_x \rangle}{\bigtriangledown P} \tag{4.1}$$

where $\bigtriangledown P$ is the pressure gradient, calculated as the difference between the average density at the inlet pores and the average density at the outlet pores (0.1) divided by the size of the sample in grid units (300 voxels); $\langle U_x \rangle$ is the average fluid velocity in the flow direction across the entire sample (pores as well as solids); ν is the kinematic viscosity of the sample and is equal to $\frac{\tau - 0.5}{3}$ in the D3Q27 implementation of LB (Seaton *et al.*, 2013), where τ is the time relaxation parameter set to 1 in all simulations.

The conversion of κ_{LB} from the lattice units to the physical units is performed according to the formula: $\kappa_{m^2} = \kappa_{LB} \cdot r^2$, where the r is the resolution of the porous medium used in the simulation ($10\mu m$). The resulting permeability in the units of m^2 is converted to more the common mD with the formula: $\kappa_{mD} = 1000 \cdot \frac{\kappa_{m^2}}{9.869233 \cdot 10^{-}13}$.

The amount of iterations that each sample needs to reach a steady state varies. Generally, synthetic samples with high porosity tend to converge faster than the samples with low porosity. Samples with porosity of about 12% typically require about 100,000 iterations to achieve convergence, while samples with porosity of about 30% can reach convergence even after 20,000 iterations. Figure 4.8 illustrates a synthetic sample with porosity 12.4% for which Lattice Boltzmann simulation was run for 100,000 steps (about 570 CPU hours).

Similarly to the 2D study, in order to obtain a more accurate permeability prediction, an exponential relaxation of the estimated permeability is assumed

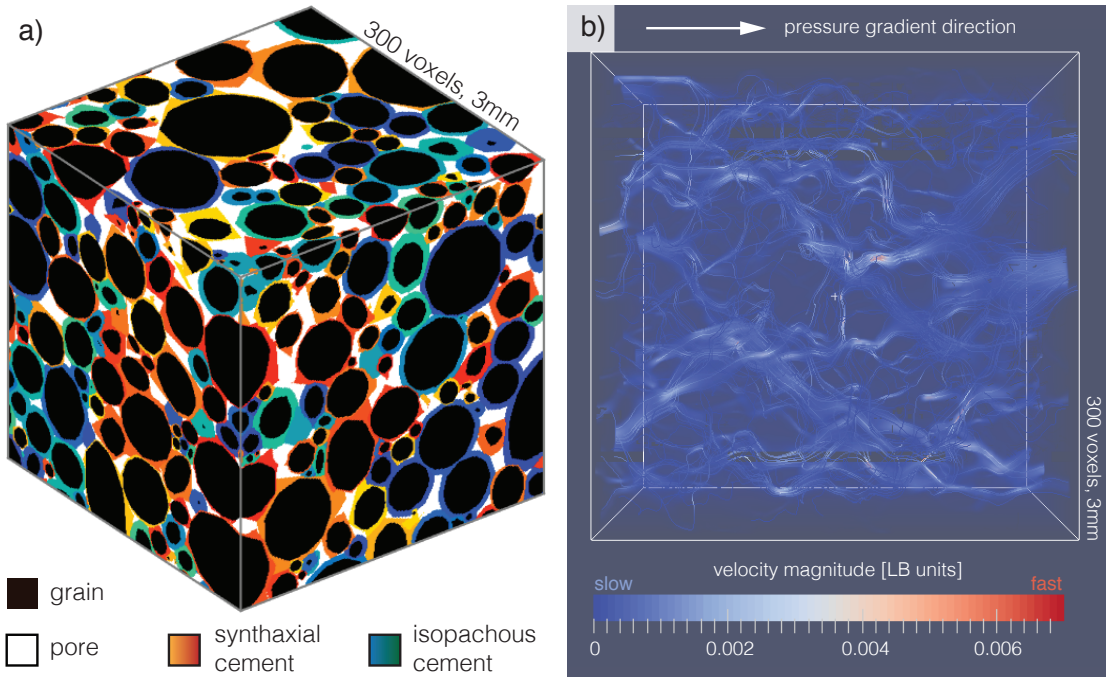

Figure 4.8: a) A model output of Calcite3D with the crystal form $01\bar{1}2$ ($\alpha_v = 66.3\%$, $\beta = 5$ voxel, $\phi = 12.4\%$); b) the magnitude of velocity is displayed along streamlines; the flow was simulated through the model output shown in (a) using the Lattice Boltzmann method and the resulting permeability is $\kappa = 850mD$.

as simulation progresses and, as such, the permeability is extrapolated using the formula: $\kappa(t) = ae^{-bt} + c$, where t is the LB simulation time step, and the coefficient c gives the value of the permeability at infinite time.

4.4 Discussion

In this section several aspects of the 3D cementation and flow modelling are discussed, including a comparison with the 2D modelling methodology and how the deficiencies of the 2D methodology are addressed in the 3D model (Section 4.4.1) as well as the modelling limitations inherent to the 3D methodology (Section 4.4.2).

4.4.1 Comparison with Calcite2D

All of the deficiencies inherent to the dimensionality of the 2D methodology, as discussed in Section 2.4.3, are eliminated in the 3D methodology. Modelling of the distance between the surrogate 3D grain and the 2D grain is not an issue as in the 3D methodology the *actual* 3D grains are used to find the bounding polyhedron. The cement grows in all three dimensions, and so certain sections of a cemented 3D porous medium exhibit cement associated with a grain that is not present in that section (Figure 4.7b). Modelling in 3D means that the connectivity of pores is maintained in all three dimensions, so there is no bias in the permeability modelling stemming from the lack of connectivity in the 3^{rd} dimension.

One aspect where the comparison of the two methodologies reflects unfavorably on the 3D model is the resolution and the sample size that can be afforded. Voxel size in the 3D study is twice as big as the pixel size in the 2D study ($10\mu m$ vs $5\mu m$). Sample size in the 3D study is 0.3 that of the size of the sample in the 2D

study (3mm vs 10mm, respectively). However, even though the synthetic sample is smaller in the 3D study, the number of grains modelled is almost 150% the number of grains considered in the 2D study (604 and 893 grains, respectively). Even though the sample is smaller, a larger representation of grains is considered in the 3D model.

4.4.2 Deficiencies of the grain deposition model

One step in the 3D methodology identified as a potential source of inaccuracies in the modelling is the methodology to create a 3D synthetic deposit based on statistics describing the size and shape distribution of grains observed in a 2D thin-section image (Section 4.1). While this method is successful in generating deposit with very similar *porosity* and *grain size* distribution to those observed in the 2D thin-section, the distribution of the grain *shapes* differs considerably. The current 3D method produces grains that are on average considerably more rounded than those observed in the 2D thin-section image (see Section 4.1.3).

The mismatch in grain shapes might arise from the way in which 2D statistics are used to define the shape of the 3D grain. The 3D grains are created in the form of ellipsoids with one major axis and the other two axes equal, so that the ratio of the length of the minor and the major axes is equal to the shape parameter (the eccentricity). All of the cross-sections in the direction parallel to the longest axis of such an ellipsoidal grain are circular. Since it is the longest axis of the grain, the number of cross-sections in a voxelised medium is also the largest in that direction. As a result, grain cross-sections that can be visible in a section of a 3D porous medium are more likely to be close to circular.

To address this issue several steps may be undertaken:

1. The shape and the size parameters derived from the 2D thin-section may be used in some other way, e.g. by applying the shape parameter as a ratio

of the length of the major and a minor axis of the ellipsoid and modelling the length of the third axis in some other way.

2. The library of shapes available can be extended to introduce more convex shapes, e.g. cylinders or cones, and perhaps even non-convex shapes.

3. Other variables describing the grains visible in the 2D thin-section can be explored, e.g. the equivalent diameter that is used as present as the size parameter could be substituted with the length of the major axis of the grain.

All of these possibilities could be investigated as a part of further work following this thesis.

Chapter 5

Modelling of Early Calcite Cement Growth in 3D: Impact of Sediment Type on Porosity and Permeability

This thesis investigates whether the type of grains in carbonate deposit, specifically the fraction of the monocrystalline grains in a sample, has an impact on the properties of rocks where early calcite cementation occurs. This chapter examines whether any useful insights to test this hypothesis can be gained from a 3D study, by exploring the impact on porosity and permeability from cemented synthetic samples generated using the methodology described in Chapter 4 (Calcite3D).

The structure of this chapter is the same as Chapter 3, which presents and discusses the results of the 2D study. Section 5.1 presents the relative cement volume and the porosity results for the synthetic samples produced using two rhombohedral forms of calcite: $01\bar{1}2$ and $40\bar{4}1$, while Section 5.2 presents the permeability results. Section 5.3 explores the specific surface of the pore/solid interface and the tortuosity (properties found in the Kozeny-Carman equation),

and how these vary depending on the type of deposit. Section 5.4 provides an interpretation and discussion of the results, including an examination of the differences in the results between the 2D and the 3D modelling.

Quantities of interest

The results in this chapter are presented in terms of the same quantities of interest as in Chapter 2 (see Table 3.1). In addition, two other quantities are discussed: the specific surface of the pore/solid interface in a sample (S, units of mm^2) and the tortuosity of the flow paths (T, dimensionless).

Generated synthetic samples

Calcite3D is used to generate multiple synthetic samples of varying content of the monocrystalline grains and varying width of the isopachous cement fringes. As in the 2D study, two geometries of the syntaxial cement are investigated: one that develops if it is assumed that all monocrystalline grains develop a syntaxial cement of the rhombohedral crystal form $01\bar{1}2$ and another one when the crystal form $40\bar{4}1$ is assumed. 5946 cemented synthetic samples are generated using the crystal form $01\bar{1}2$, with model input parameter values for the content of the monocrystalline grains (α_0) ranging from 0 to 100% and for the width of the isopachous cement fringes (β) ranging from 0 to 5 voxels (representing 0 to 50μm) (Figure 5.1). Due to significantly longer time-to-solution of the synthetic samples generated with the crystal form $40\bar{4}1$, than the synthetic samples with the crystal form $01\bar{1}2$ (see Section 4.2.3), fewer synthetic samples are generated using the crystal form $40\bar{4}1$ (4086). In order to reduce the computational cost and the data storage space, each of the outputs of Stage 1 of Calcite3D (see Section 4.2.1) is used to produce six cemented synthetic samples, each with a different input parameter for the width of the isopachous cement fringes (β) form 0 to 5, in Stage 2 of Calcite3D (see Section 4.2.2).

The synthetic samples generated for the two crystal forms are shown in the model input parameter space ($\beta - \alpha_0$) in Figure 5.1. All synthetic samples generated using the crystal form $01\bar{1}2$ are percolating and only 13 of the synthetic samples generated using the crystal form $40\bar{4}1$ are not percolating.

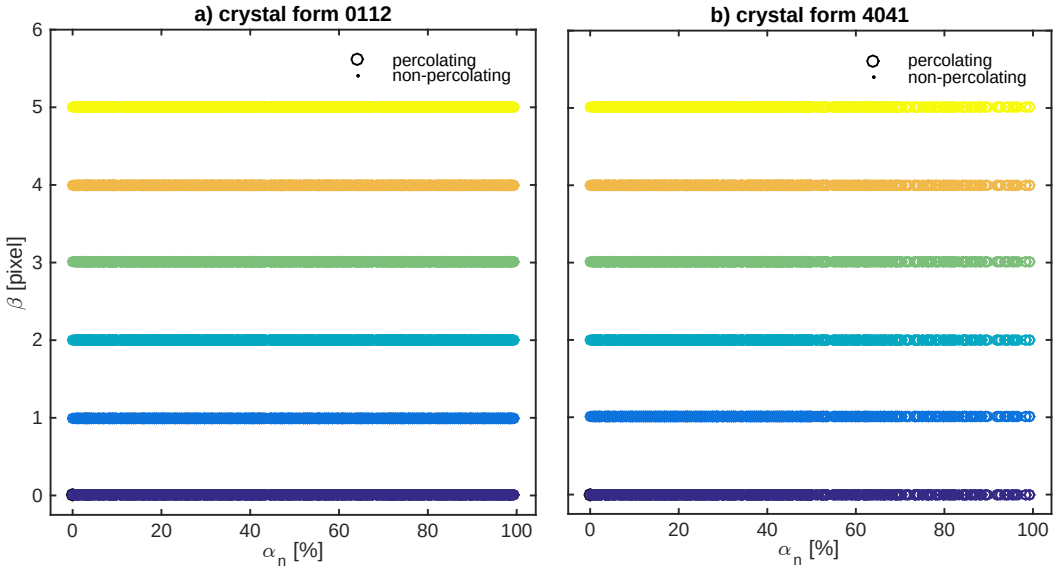

Figure 5.1: All cemented synthetic samples generated for two crystal forms of calcite: a) 5946 samples with the crystal form $01\bar{1}2$ and b) 4086 samples with the crystal form $40\bar{4}1$, shown in the isopachous fringes width (denoted by different colours) - the monocrystalline grain content by number parameter space ($\beta - \alpha_n$). The circles denote the percolating samples, and the dots - non-percolating samples. All samples with the crystal form $01\bar{1}2$ are percolating, only 13 samples with the crystal form $40\bar{4}1$ are not percolating.

The best representation of the monocrystalline grains content in a sample

The 2D study revealed that of the three possibilities (the content by grain number α_n, the content by volume α_v, or the content by the surface area α_a), it is the monocrystalline content by *volume* α_v that yields the best correlation with the porosity (see Figure 3.2). Interestingly, contrary to the 2D study, here it is the

monocrystalline grains content by the *surface area* α_a that has the strongest correlation with the porosity.

The mean square error (MSE) is significantly smaller in the case of the curve for the content by the surface area (MSE=0.111 for the crystal form $01\bar{1}2$ and 0.509 for $40\bar{4}1$) than in the content by number (MSE=0.303 for $01\bar{1}2$ and 1.362 for $40\bar{4}1$) or the content by volume (MSE=0.198 for $01\bar{1}2$ and 0.693 for $40\bar{4}1$), as illustrated in Figure 5.2. The MSE represents the difference between the estimator (fit curve) and what is estimated (data), and is used to determine the extent to which a model fits a dataset. A lower MSE signifies a better fit to the data. Even though this suggests that the monocrystalline grain content by the surface area is preferred, the monocrystalline grains content by volume α_v is used in all further analysis in order to maintain the consistency of presentation of the results with the 2D study.

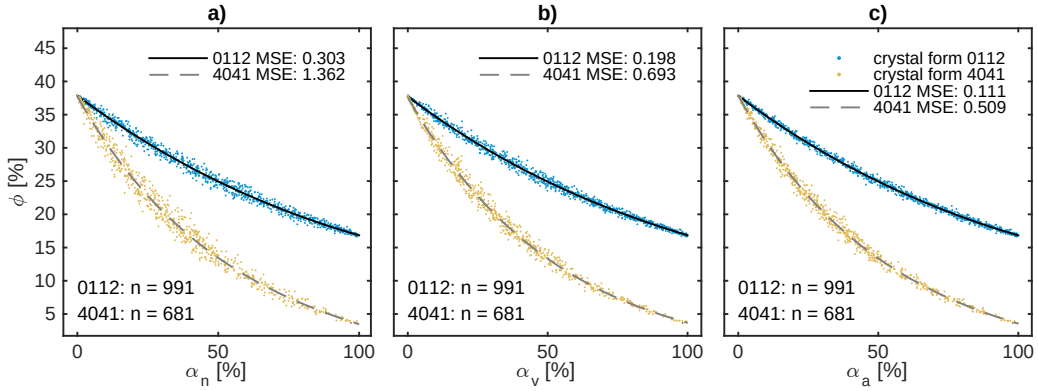

Figure 5.2: Comparison of the relationship of the porosity (ϕ) with three different ways of defining the content of monocrystalline grains in a sample: a) by number of grains α_n, b) by volume α_v, c) by the surface area of grains α_a for samples with no isopachous cement and two crystal forms: $01\bar{1}2$ (blue) and $40\bar{4}1$ (yellow). The results are fitted with an exponential curve of the form: $f(x) = ae^{bx} + ce^{dx}$.

Figure 5.3 shows synthetic samples where the difference between the two quantities α_n and α_v is considerable. In the top images (a, b), α_n is larger than α_v by 10.1%, which suggests that the mean size of the monocrystalline grains is smaller

than the mean size of all grains. In the bottom images (c, d), α_n is smaller than α_v by 11.1%. The difference between α_n and α_v in the synthetic samples at the top (a, b) compared to the samples at bottom (c, d) leads to a difference in the porosity. In the absence of isopachous cement, the porosity of the sample with a lower mean volume of monocrystalline grains (a) is *lower* by 1.4% than the porosity of the sample with a higher mean volume of monocrystalline grains (c). In the presence of the isopachous cement fringes of a width of 5 voxels ($50\mu m$), the porosity of the synthetic sample with a lower mean volume of the monocrystalline grains (b) is *higher* by 1.2% than the porosity of the sample with a higher mean volume of the monocrystalline grains (d).

Two crystal forms of calcite

As in the 2D study, the results are presented separately for the two rhombohedral crystal forms of calcite modelled: $01\bar{1}2$ and $40\bar{4}1$. This stems from the observation that the quantities of interest differ in the two cases. The porosity in the case of the crystal form $01\bar{1}2$ is generally higher for synthetic samples of the same monocrystalline grain content by volume (α_v) than in the case of $40\bar{4}1$ (Figure 5.4). The crystal form $40\bar{4}1$ produces synthetic samples with lower porosity, and the difference between the results associated with the crystal form $01\bar{1}2$ and $40\bar{4}1$ increases with increasing content of the monocrystalline grains. For high monocrystalline content samples, the porosity of the synthetic samples generated using the crystal form $01\bar{1}2$ converges to about 17% and the porosity of the synthetic samples generated using the crystal form $40\bar{4}1$ converges to about 4%.

This is further illustrated in Figure 5.5, which compares the synthetic samples generated using the geometry of the crystal form $01\bar{1}2$ (a, b) with the synthetic samples generated using the crystal form $40\bar{4}1$ (c, d). In these high monocrystalline content samples, the porosity of the samples with the crystal form $01\bar{1}2$ is around 17% and the porosity of the samples with the crystal form $40\bar{4}1$ is around 4%. Since there are so few polycrystalline grains, the width of the isopachous

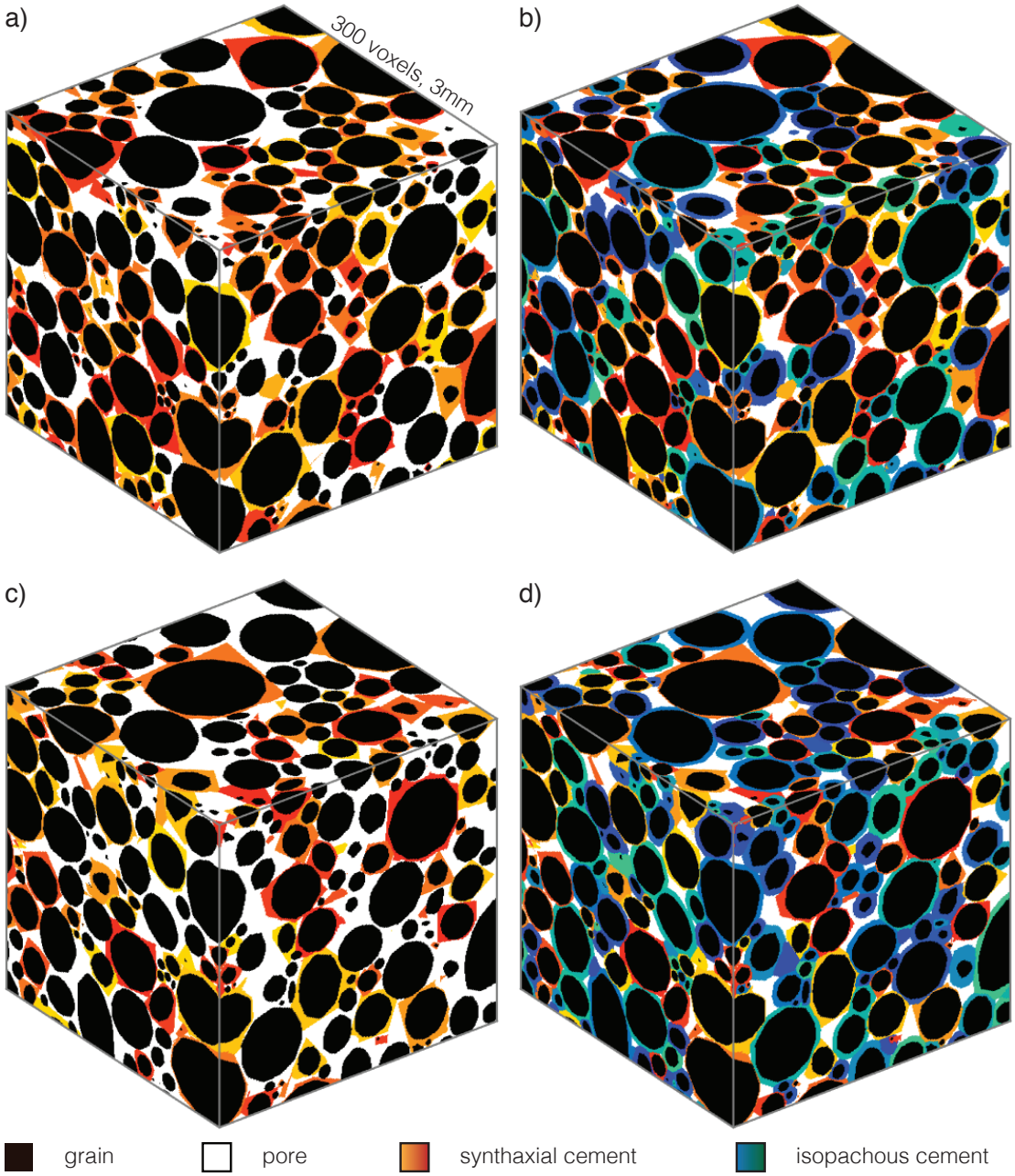

Figure 5.3: Cemented synthetic samples with the crystal form $01\bar{1}2$ and no isopachous cement (a, c) and 5 voxels ($50\mu m$) width of the isopachous cement fringes (b, d). In a) and b) α_n is considerably larger than α_v, while in c) and d) α_n is considerably smaller than α_v. The properties of each sample are as follows: a) $\phi = 24.0\%$, $\alpha_n = 61.2\%$, $\alpha_v = 51.1\%$; b) $\phi = 12.1\%$, $\alpha_n = 61.2\%$, $\alpha_v = 51.1\%$; c) $\phi = 25.4\%$, $\alpha_n = 40.9\%$, $\alpha_v = 52.0\%$; d) $\phi = 10.9\%$, $\alpha_n = 40.9\%$, $\alpha_v = 52.0\%$.

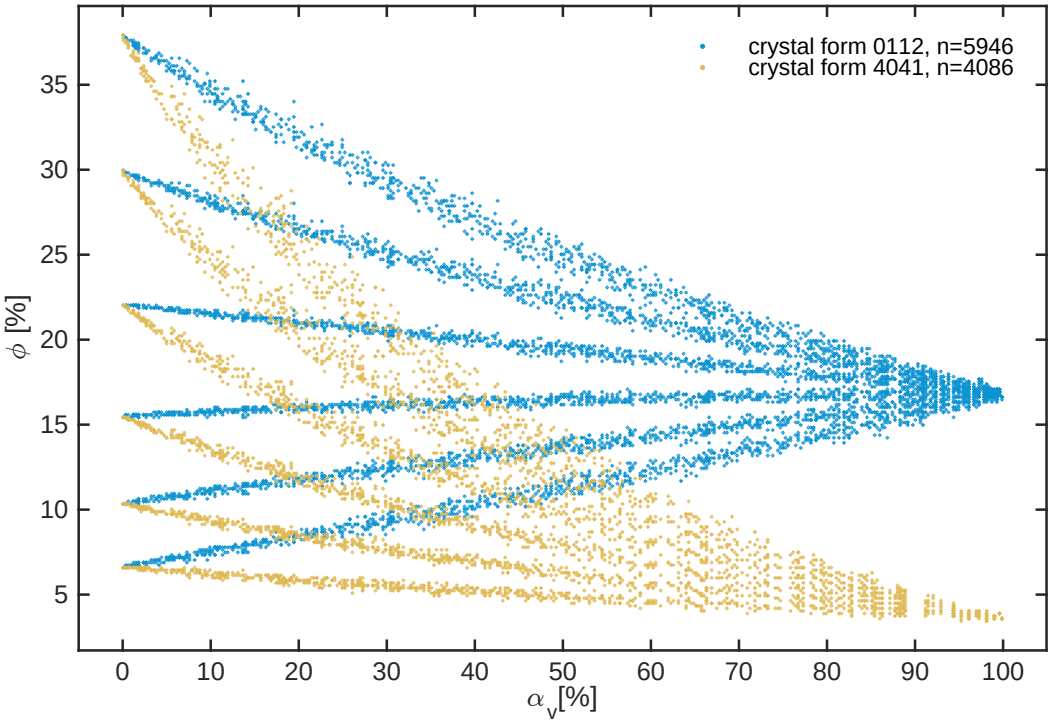

Figure 5.4: A comparison between the porosity of samples produced with the crystal form $01\bar{1}2$ (blue) and $40\bar{4}1$ (yellow).

cement fringes does not significantly affect porosity, and the introduction of the isopachous cement fringes of width 5 voxels ($50\mu m$) lowers the porosity by 1% in the case of $01\bar{1}2$ and by 0.4% in the case of $40\bar{4}1$.

Figure 5.5 also demonstrates that the crystal form $40\bar{4}1$ is much more effective in occluding the pore space than the crystal form $01\bar{1}2$. The elongated shape of the crystal form $40\bar{4}1$ causes syntaxial cement growth deep into the pore space, while the more blocky crystal form $01\bar{1}2$ produces a smaller volume of cement that occupies less pore volume.

5.1 Impact of Monocrystalline Grains on Cement Growth and Porosity

The volume of cement and the porosity of a synthetic sample cannot be accurately determined a priori, before the cement growth simulation is complete (Stage 2 of Calcite3D). This is because even if the shape of the bounding polyhedra is known, the dynamics of the impinging cements and the creation of the compromise boundaries in the course of the cement growth can alter these pre-determined shapes. The following sections present the relationship between three quantities: the porosity (ϕ), the monocrystalline grains content by volume (α_v) and the ratio of the syntaxial cement to all cement (γ_v.) All results are presented for cemented synthetic samples generated with the use of two rhombohedral forms of calcite: $01\bar{1}2$ and $40\bar{4}1$.

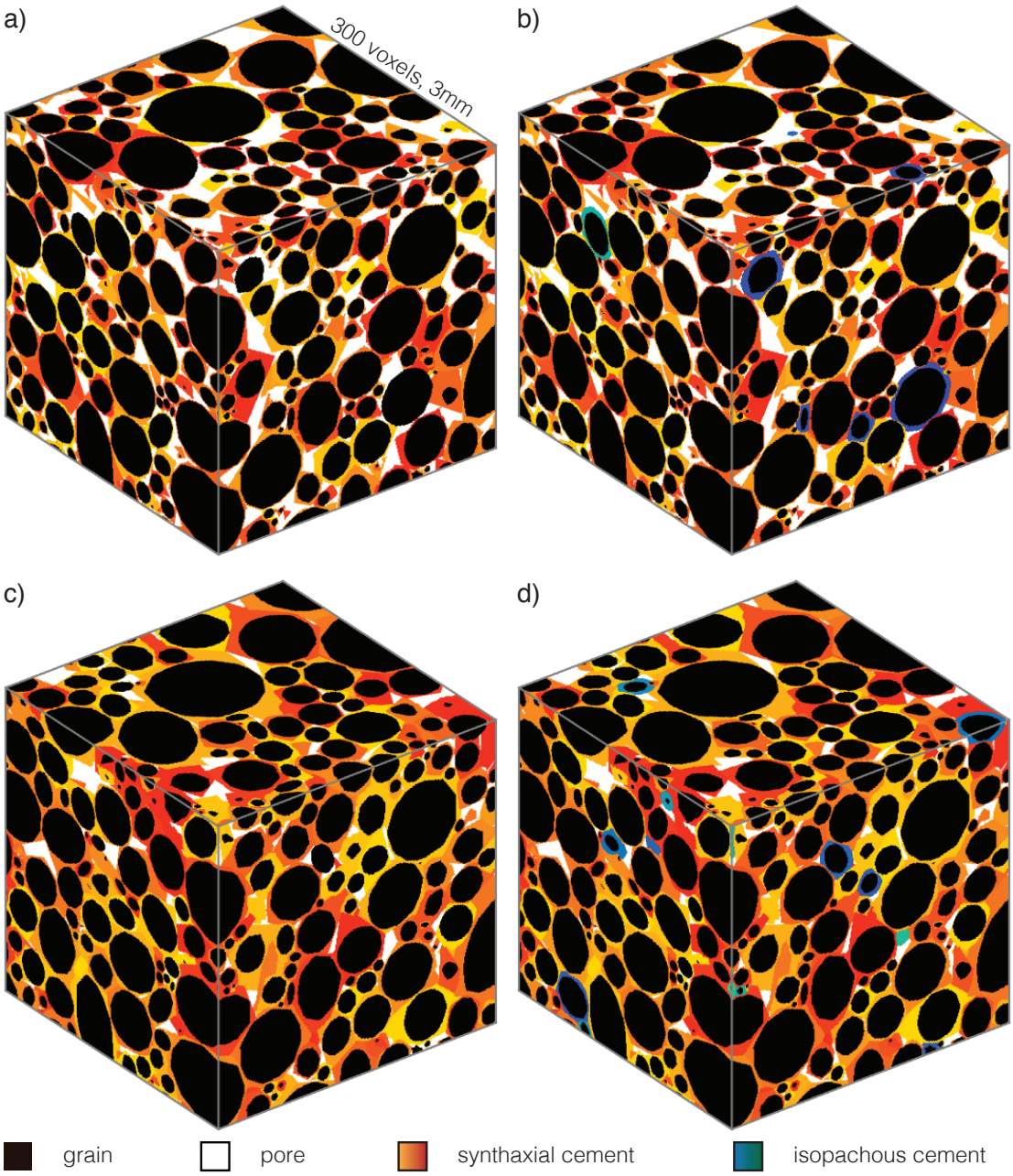

Figure 5.5: Very high monocrystalline grain content samples for both crystal forms $01\bar{1}2$ (a, b) and $40\bar{4}1$ (c, d) with no isopachous cement (a, c) and 5 voxel ($50\mu m$) width of the isopachous cement fringes (b, d). The properties of each sample are as follows: a) $\phi = 17.4\%$, $\alpha_v = 96.0\%$; b) $\phi = 16.4\%$, $\alpha_v = 96.0\%$; c) $\phi = 4.0\%$, $\alpha_v = 96.0\%$; c) $\phi = 3.6\%$, $\alpha_v = 96.0\%$.

5.1.1 Impact on the relative volume of syntaxial cement (γ_v vs α_v)

Figure 5.6 shows the content of the syntaxial cement in overall volume of cement (γ_v) plotted against the content of monocrystalline grains in the sample (α_v) for all cemented synthetic samples for the two crystal forms modelled. With the exception of the samples with $\beta = 0$ (no isopachous cement), which have a value of γ_v equal to 100% regardless of the monocrystalline grain content, as syntaxial cement is the only cement generated, the results can be fitted with a hyperbolic function as demonstrated in Figure 5.7.

Most curves in Figure 5.6 are concave downward, with the exception of curves for $\beta = 3$, 4 and 5 voxels in the case of $01\bar{1}2$, which are concave upward. This is in contrast to the results of the 2D study, where all curves are concave downward. The mean square error (MSE), which measures the mean deviation of the dataset from the fit curve, is significantly smaller in the case of $01\bar{1}2$, suggesting that results are less random, as noted in the 2D study. Moreover, the hyperbolic shape of the curve is more pronounced in the case of $40\bar{4}1$, as the slopes along the curve change more dramatically than in the case of $01\bar{1}2$.

5.1.2 Impact on porosity (ϕ vs α_v)

Figure 5.8 shows the porosity of all generated synthetic samples as a function of the monocrystalline grain content. As in Figure 5.6, there colour gradient in the direction parallel to the y-axis suggests that there is a strong dependence of the porosity on the amount of the isopachous cement in the sample. Figure 5.9 demonstrates that the results for the individual values of the width of the isopachous cement fringes (β) can be fitted with an exponential curve of the form: $f(x) = ae^{bx}$. This curve shape suggests that addition of more monocrystalline

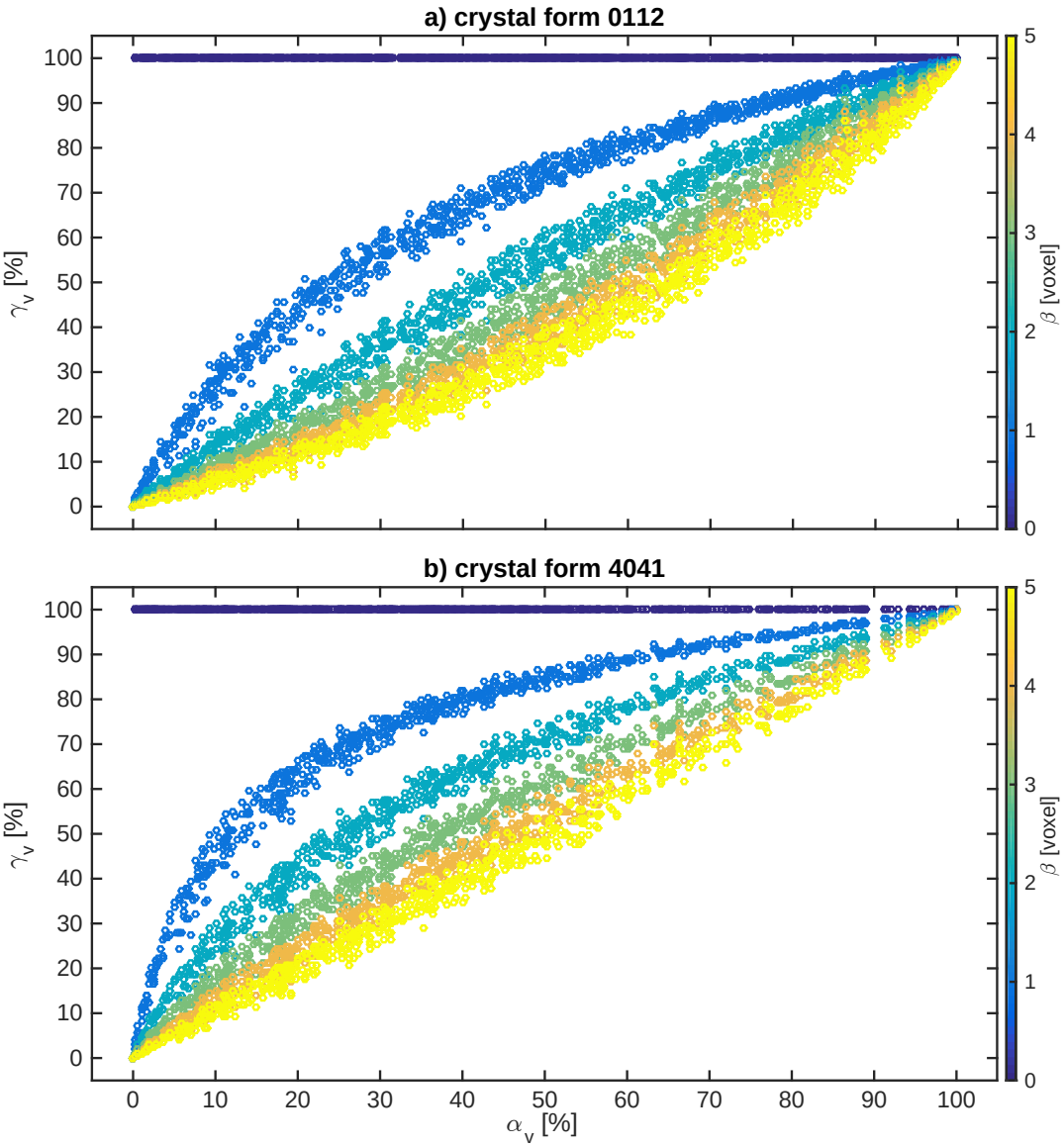

Figure 5.6: The content of the syntaxial cement in overall volume of cement (γ_v) vs the monocrystalline grain content in the sample by volume (α_v) for samples with the crystal form a) $01\bar{1}2$ and b) $40\bar{4}1$. The colours correspond to different values of the width of the isopachous cement fringes in the sample β: from blue (0 voxels) through to yellow (5 voxel or 50μm).

.

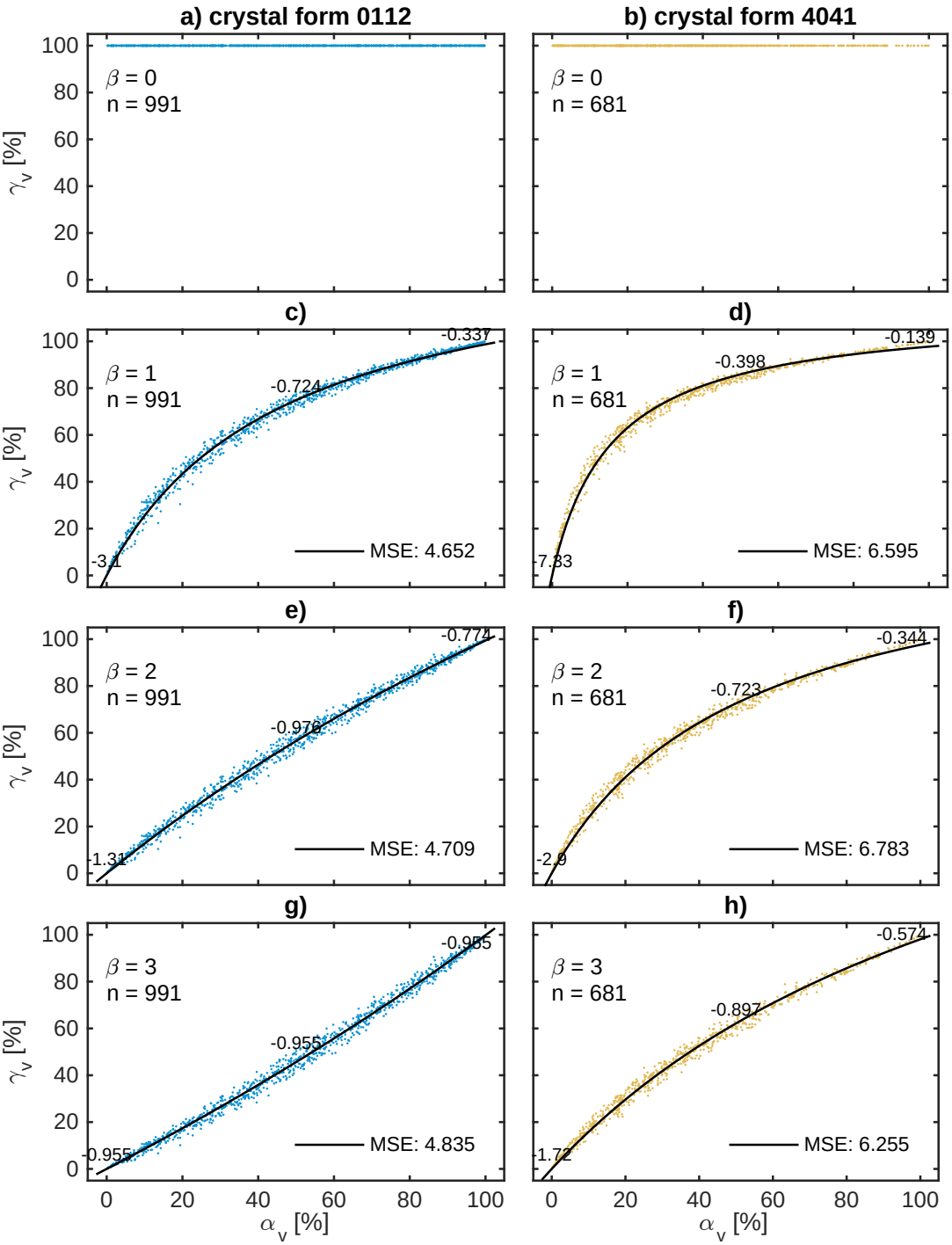

Figure 5.7: The content of the syntaxial cement in overall volume of cement (γ_v) vs the monocrystalline grain content by volume (α_v) for samples with the crystal form $01\bar{1}2$ (a, c, e, g) and $40\bar{4}1$ (b, d, f, h) for four values of the width of the isopachous cement fringes: 0 voxels (a, b), 1 voxel (c, d), 2 voxels (e, f) and 3 voxels (g, h). The solid black line is the hyperbolic fit of the form: $f(x) = \frac{ax}{b+cx}$. The black numbers above each curve show the slope of the hyperbolic fit at $\alpha_v = 0$, 50 and 95%.

grains to the sample has greater impact for samples where the monocrystalline grain content is smaller.

All curves in the case of $40\bar{4}1$ are decreasing and they become progressively more linear for larger β. Three decreasing curves in the case of $01\bar{1}2$, with $\beta = 0$, 1 and 2 voxels, are concave upward. It is notable that not all curves are decreasing for greater values of α_v, as is the case in the 2D study. The curves for $\beta = 3$, 4 and 5 voxels in the case of $01\bar{1}2$ are increasing and are concave downward.

The MSE is generally smaller for the exponential fits in the samples with the crystal form $01\bar{1}2$ (Figure 5.9). The slopes of the curve are higher in the case of $40\bar{4}1$, which suggests that the porosity decreases more rapidly with increased content of the monocrystalline grains in the sample.

The exponential fit curves can be used to formulate the dependance of porosity on parameters α_v and β. Upon inspection, the exponential fit coefficients (a and b) for the consecutive values of β can be fitted with an exponential function of the form: $f(x) = a_n e^{b_n x} + c_n$, where $n = 1$ for the fits to coefficient a and $n = 2$ for the fits to coefficient b (Figure 5.10).

Using the exponential fits derived in Figure 5.10 as the coefficients in the overarching exponential formula, an expression for the porosity in terms of α_v and β can be derived. For the crystal form $01\bar{1}2$ this phenomenological correlation takes a form:

$$\phi = (53.0e^{-0.176\beta} - 15.2)e^{(0.014e^{0.157\beta} - 0.021)\alpha_v} \tag{5.1}$$

and for the crystal form $40\bar{4}1$ it takes a form:

$$\phi = (55.7e^{-0.172\beta} - 17.3)e^{(0.009e^{0.194\beta} - 0.03)\alpha_v} \tag{5.2}$$

From these expressions it can be inferred that the impact on ϕ decreases for higher values of β, as coefficient b_1 by the first exponent is negative in both expressions

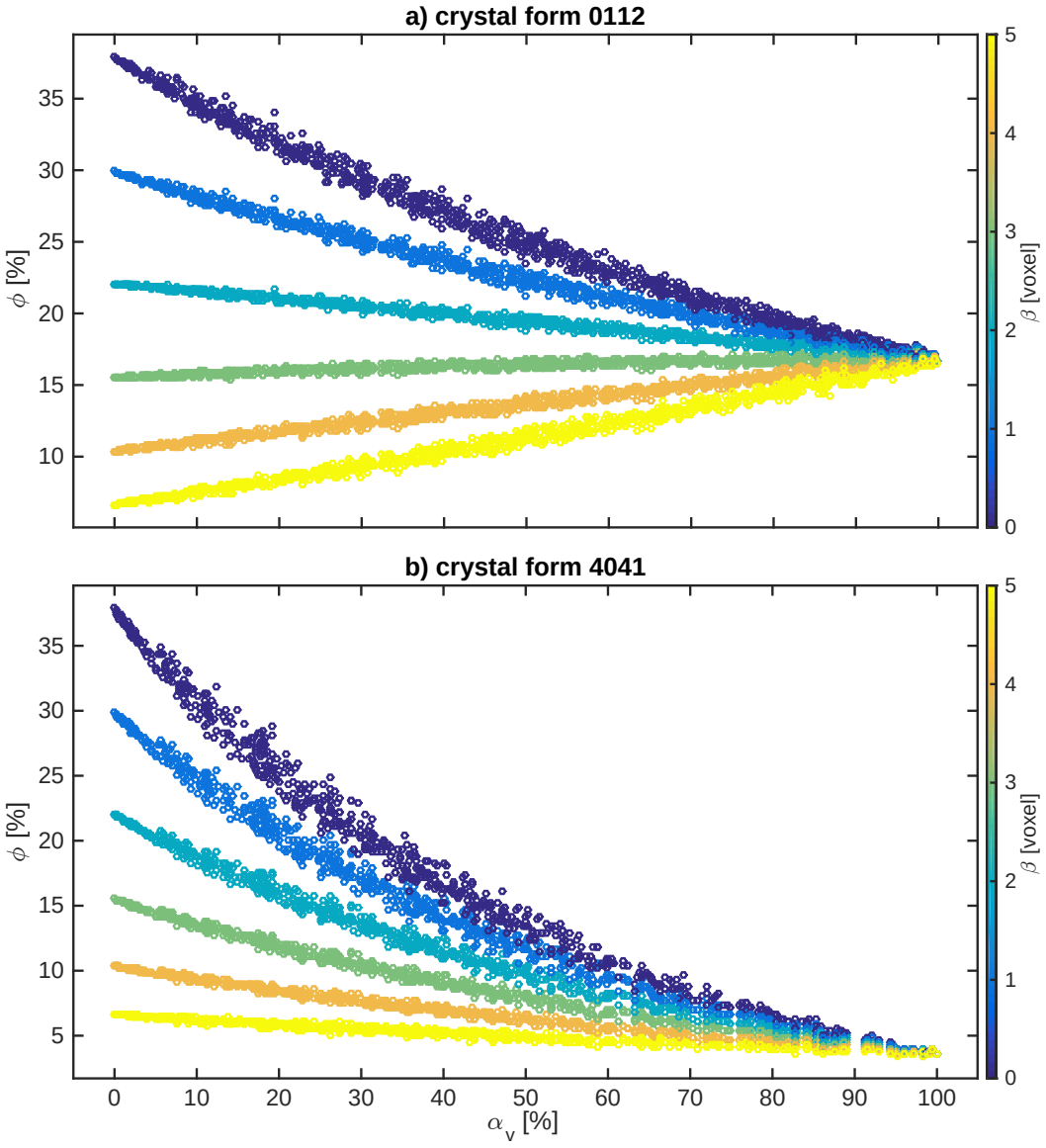

Figure 5.8: The porosity (ϕ) vs the monocrystalline grain content in the sample by volume (α_v) for samples with the crystal form a) $01\bar{1}2$ and b) $40\bar{4}1$. Colour scheme as in Figure 5.6.

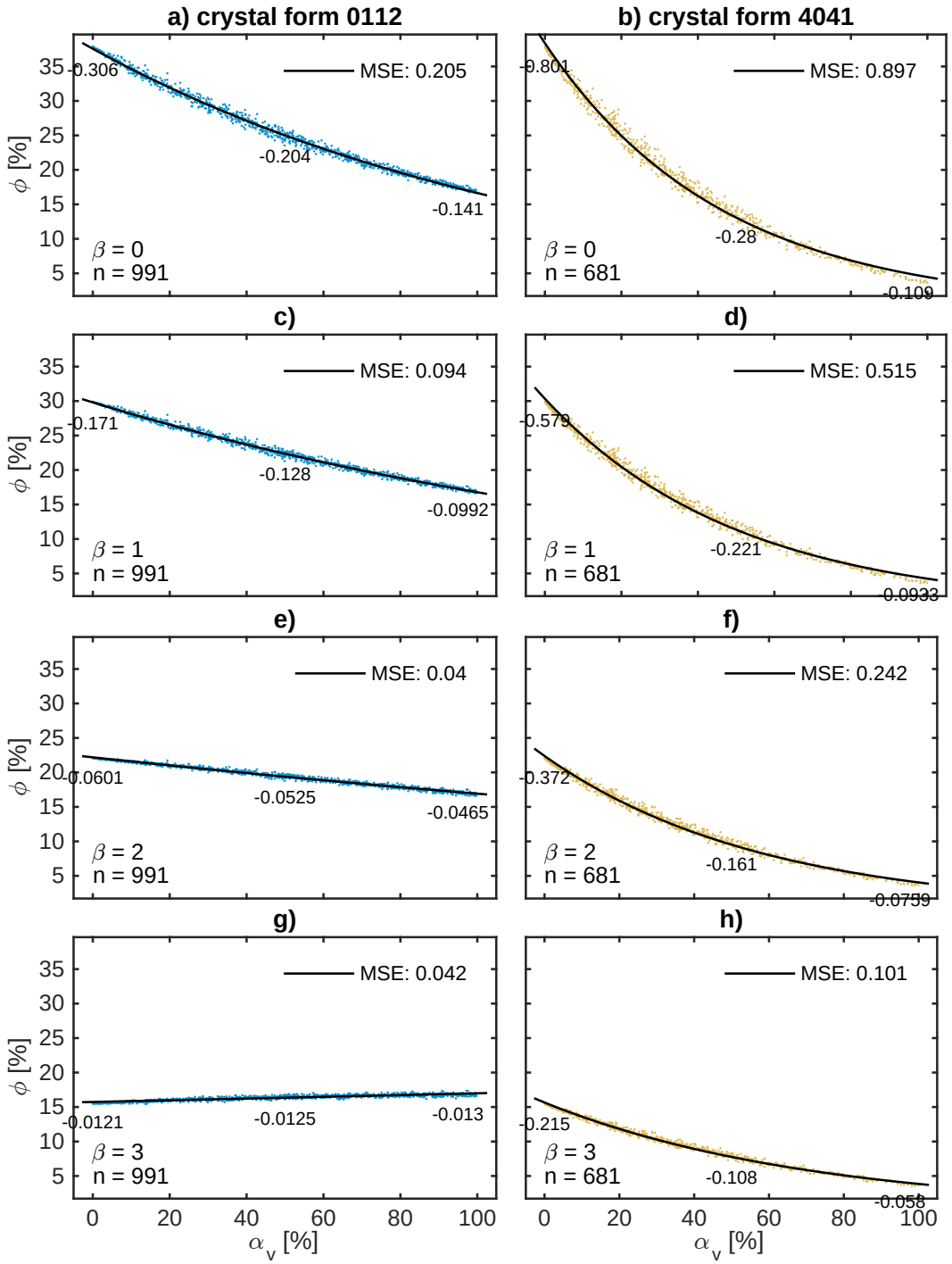

Figure 5.9: The porosity (ϕ) vs the monocrystalline grain content in the sample by volume (α_v) for samples with the crystal form $01\bar{1}2$ (a, c, e, g) and $40\bar{4}1$ (b, d, f, h) for four values of the width of the isopachous cement fringes: 0 voxels (a, b), 1 voxel (c, d), 2 voxels (e, f) and 3 voxels (g, h). The results are fitted with an exponential curve: $f(x) = ae^{bx}$. The black numbers above each curve show the slope of the exponential fit at $\alpha_v = 0$, 50 and 95%.

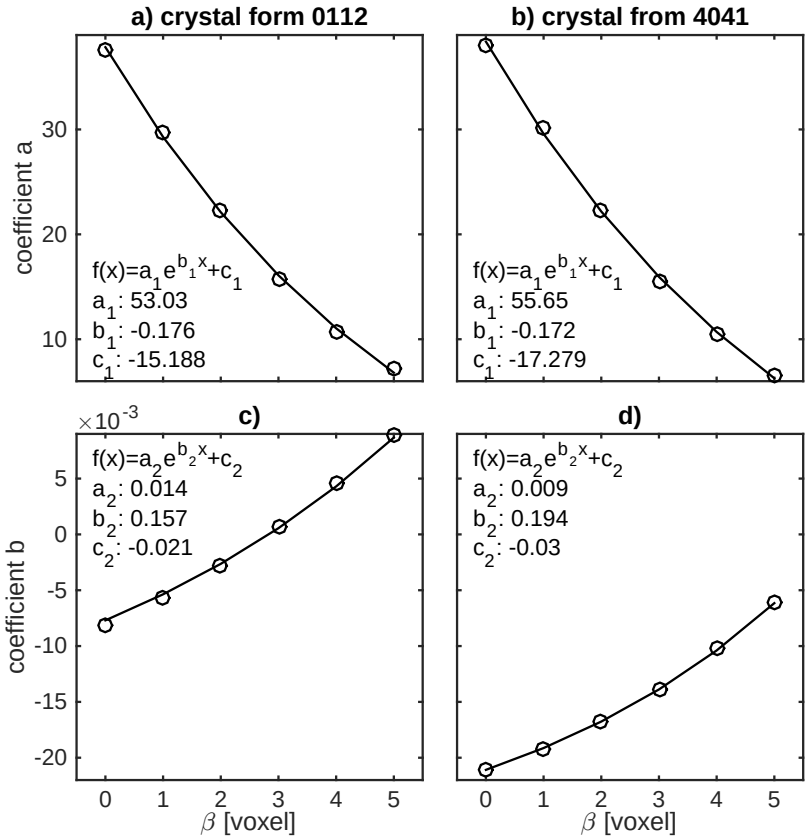

Figure 5.10: The coefficients of the exponential fits to the porosity (ϕ) vs the monocrystalline grain content by volume (α_v) for the individual values of the width of the isopachous cement fringes (β) for the crystal form $01\bar{1}2$ (a, c) and $40\bar{4}1$ (b, d). For both crystal forms, coefficients a (a, b) and coefficients b (c, d) of the exponential fits can be fitted with an exponential function of the form: $f(x) = a_n e^{b_n x} + c_n$.

(-0.176 and -0.172). The coefficient b_2 by the second exponent is smaller in the case of $01\bar{1}2$ than in the case of $40\bar{4}1$ (0.157 and 0.194 respectively), which suggests that the curves in the case of $40\bar{4}1$ are steeper. This in agreement with the results shown in Figure 5.8.

5.2 Impact on Permeability

This section presents the results of the last step in the methodology detailed in Chapter 4 (see Section 4.3) and shown in Figure 4.1: quantification of permeability in the model outputs of Calcite3D with the use of the Lattice Boltzmann method.

The choice of the cemented samples for the flow simulation is made from the pool of all percolating samples: all 5946 synthetic samples in the case of $01\bar{1}2$ and 4073 synthetic samples in the case of $40\bar{4}1$. Figure 5.11 shows 189 samples selected in the case of $01\bar{1}2$ and 268 samples selected in the case of $40\bar{4}1$.

As in the 2D study, the primary strategy for selecting samples for the LB simulation involves targeting synthetic samples at specific porosities. That way, the impact of the monocrystalline grains content (α_v) on the permeability (κ) for samples of equal porosity (ϕ) can be investigated. For each of the targeted porosities, at least eight and preferably ten samples are selected from groups of samples with different widths of isopachous fringes (β).

The choice of these porosity values is made based on the availability of samples within a 0.2% tolerance range of a targeted porosity optimised for a uniform interval between the targeted porosities. Six porosity values are targeted in the case of the crystal form $01\bar{1}2$: 12.3, 15.5, 17.1, 20.8, 24.7 and 28.2%. Since not enough synthetic samples with porosity 24.7% are available in the case of $40\bar{4}1$, this porosity value is substituted with 25.2%, so that the six porosities targeted in the case of the crystal form $40\bar{4}1$ are: 12.3, 15.5, 17.1, 20.8, 15.2 and 28.2%.

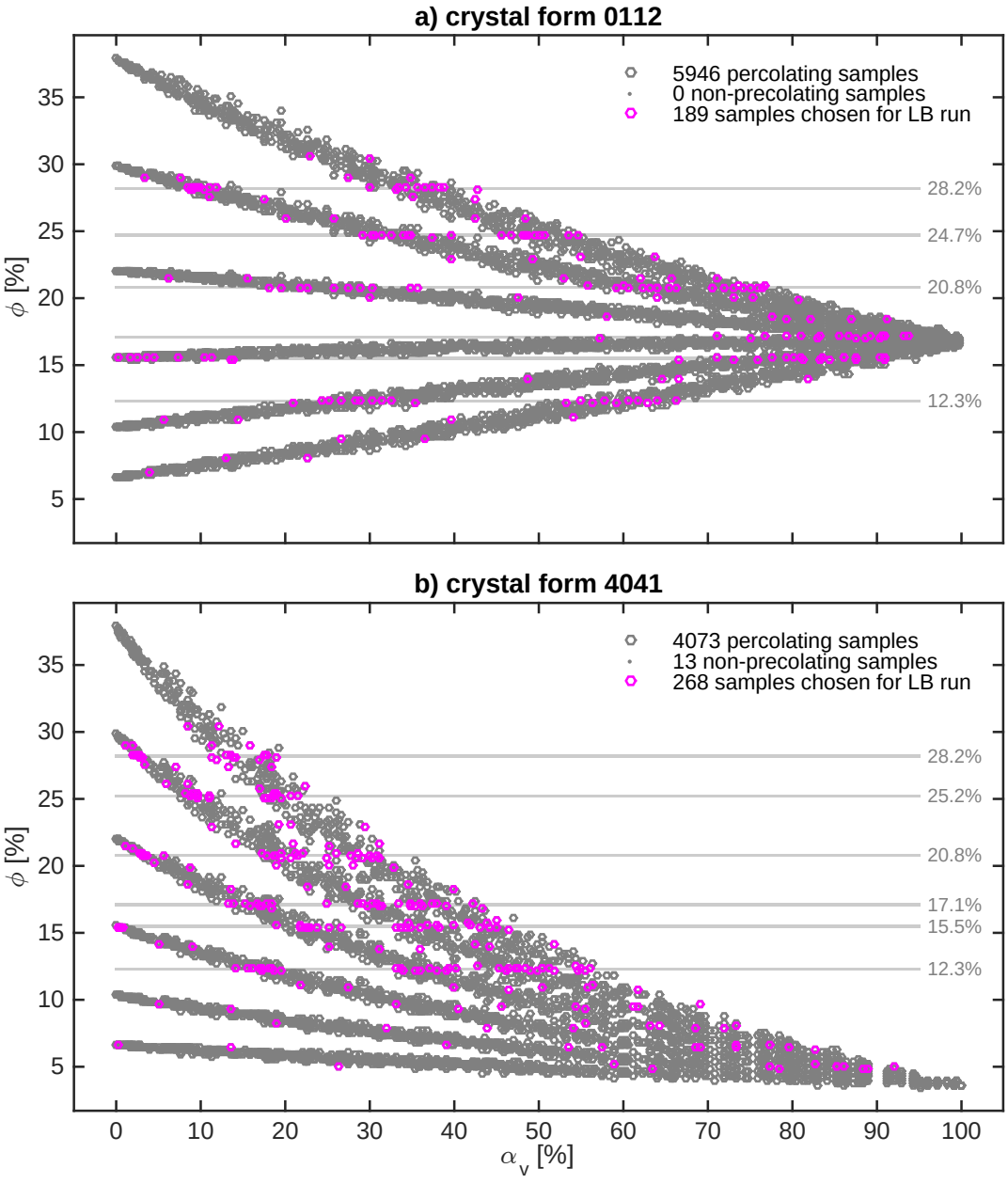

Figure 5.11: The cemented synthetic samples selected for the LB simulation for two crystal forms: $01\bar{1}2$ and $40\bar{4}1$.

Depending on availability, the number of synthetic samples selected for the LB simulation for each of these porosities varies between 20 and 40. In the case of $01\bar{1}2$, most of the targeted porosities offer only two groups with different width of the isopachous cement fringes, and only at porosities 15.5 and 20.8% three groups are available. In the case of $40\bar{4}1$, due to the decreasing nature of the ϕ-α_v curves, the number of available groups increases with decreasing porosity, from two groups at a porosity 28.2%, to four groups at a porosity 12.3%. The number of samples selected for the LB simulation in the case of $40\bar{4}1$ is larger due to the increased availability of samples.

The secondary motivation for selecting samples for the LB simulation is to cover the full range of the percolating synthetic dataset. For that purpose porosities from 5% to 30.5% spaced roughly every 1.5% are targeted and samples with the highest and the lowest value of the monocrystalline content (α_v) are selected from each group of the synthetic samples which have the same width of the isopachous cement fringes (β) available at any given porosity.

5.2.1 Impact of porosity on permeability (κ vs ϕ)

A clear trend of the permeability increasing with the porosity is observed for the synthetic samples of both crystal forms of syntaxial cement (Figure 5.12), and this can be fitted with an exponential function. In the case of $01\bar{1}2$ it takes the form:

$$\kappa = e^{3.98 \cdot log(\phi) - 3.32} \tag{5.3}$$

and in the case of $01\bar{1}2$ it takes the form:

$$\kappa = e^{3.22 \cdot log(\phi) - 0.67} \tag{5.4}$$

where κ is the permeability in mD and ϕ is the porosity in %. At lower porosities, the permeability is greater for the synthetic samples with the crystal form $40\bar{4}1$. This difference decreases for samples with higher porosities.

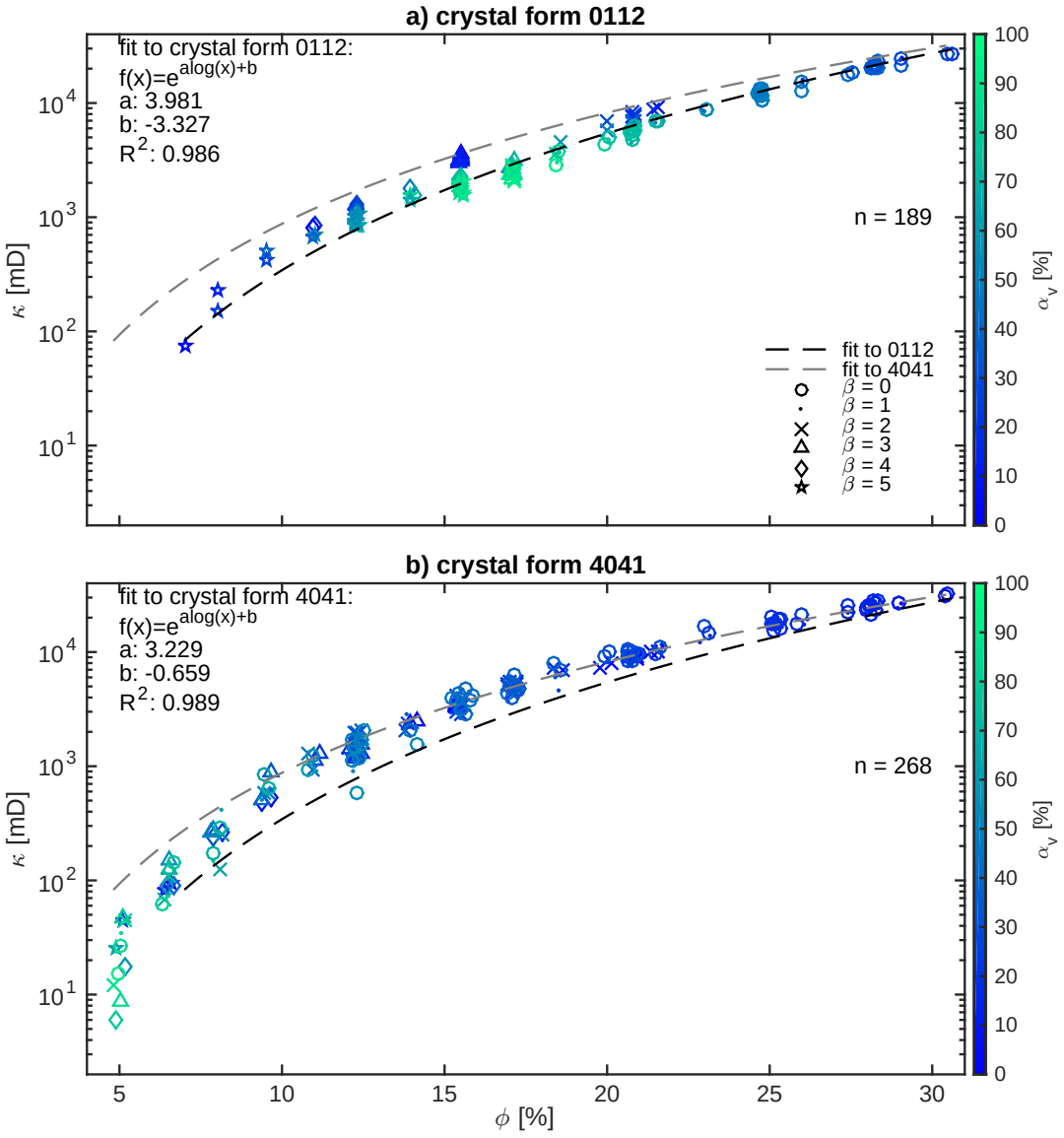

Figure 5.12: The permeability (κ) on a logarithmic scale vs the porosity (ϕ) for synthetic samples with the crystal form a) $01\bar{1}2$ and b) $40\bar{4}1$. Different symbols denote samples with a different width of the isopachous cement fringes: circles, dots, crosses, triangles, diamonds and stars represent samples with 0 voxels, 1 voxel ($10\mu m$), 2 voxels ($20\mu m$), 3 voxels ($30\mu m$), 4 voxels ($40\mu m$) and 5 voxels ($50\mu m$) width of the isopachous cement fringes, respectively. The synthetic data are coloured by the monocrystalline grains content in the sample by volume (α_v) from dark blue (low content) to green (high content). The results are fitted with a curve of the form: $\kappa(\phi) = e^{a \cdot log(\phi)+b}$.

In contrast to the 2D study, the permeability results at any given porosity, with the exception of very low porosities, are very close to each other, and so investigating trends in the dependance of the permeability on the monocrystalline grain content is difficult. Figure 5.13 shows a close-up of the results for each of the targeted porosities for the two crystal forms. Upon closer inspection, it is clear that in the case of $01\bar{1}2$ there is a gradient of colour parallel to the y-axis, and that samples with low a monocrystalline grain content (α_v) have generally higher permeabilities. The results in the case of $40\bar{4}1$ are inconclusive as there is no clear dependence of the permeability on the monocrystalline grain content.

5.2.2 Impact of monocrystalline grains content on permeability (κ vs α_v)

In the case of $01\bar{1}2$, the permeability decreases with the monocrystalline grains content (α_v) only for synthetic samples with a low content of isopachous cement, and increases for samples with a higher content of isopachous cement, e.g. where $\beta = 5$ (Figure 5.14). The permeability of the high monocrystalline content samples converges to a value of about $3000mD$.

In the case of $40\bar{4}1$, the permeability decreases for larger contents of monocrystalline grains (α_v). This trend is particularly clear in the results showing the impact of different widths of the isopachous cement fringes (β). The gradient of colour, from magenta in the top-left corner to light blue in the bottom-right corner of the plot, suggests dependence of the permeability on the porosity.

In order to investigate the effect of the monocrystalline grains content on the permeability, samples of different monocrystalline grain content but with the same porosity are considered for the six targeted porosities (Figure 5.15).

The linear fits to the results for each porosity (Figure 5.15) reveal that the slopes ($p1$) of the best fit lines are very similar for all targeted porosities, especially in the

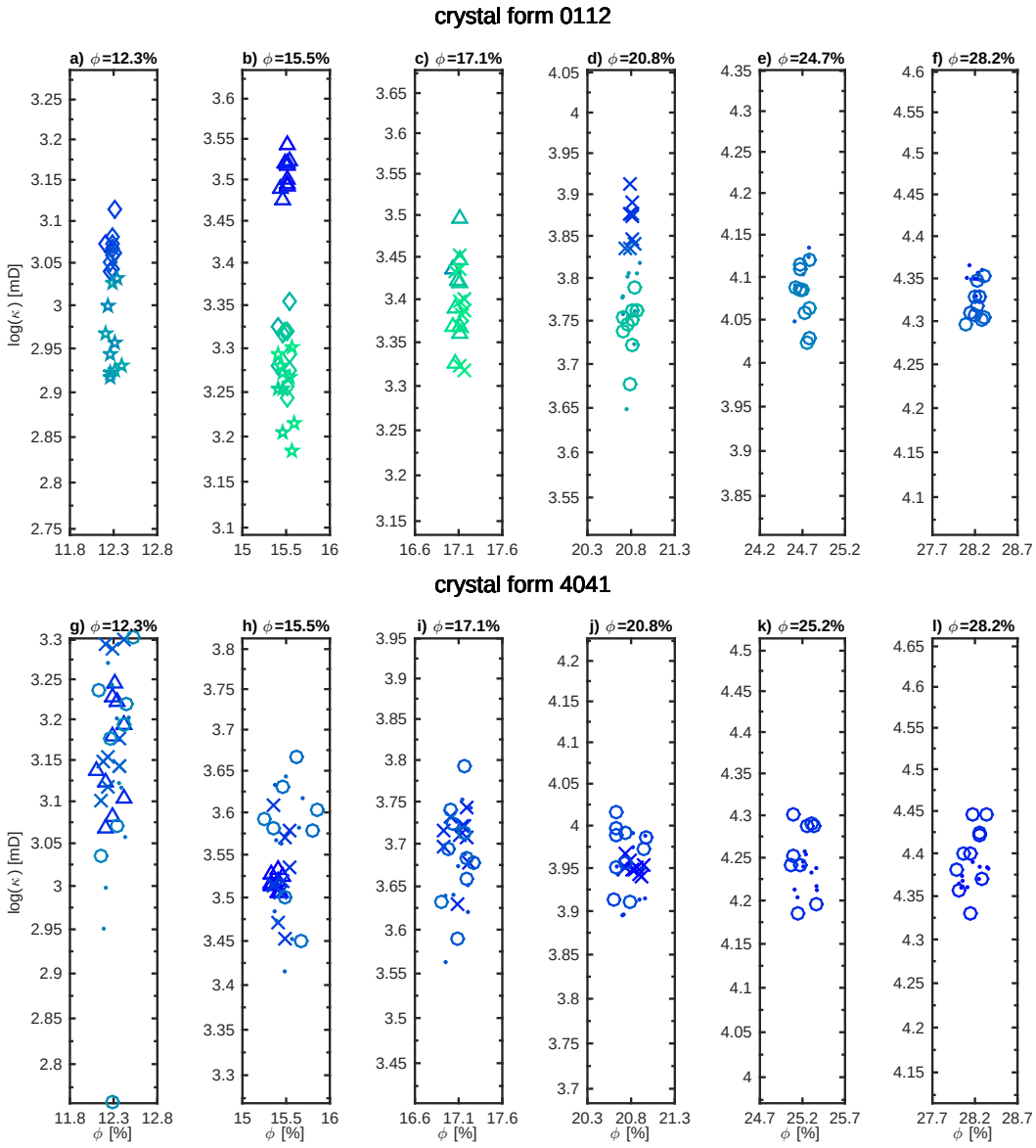

Figure 5.13: Detail of log permeability (κ) vs porosity (ϕ) for synthetic samples with the crystal form: $01\bar{1}2$ (a, b, c, d, e, f) and $40\bar{4}1$ (g, h, i, j, k, l) at the targeted porosities. All plots have the same range of both scales: $\phi = 1\%$ on the x-axis and $log(\kappa) = 0.54$ on the y-axis. The symbols and the colour scheme as in Figure 5.12.

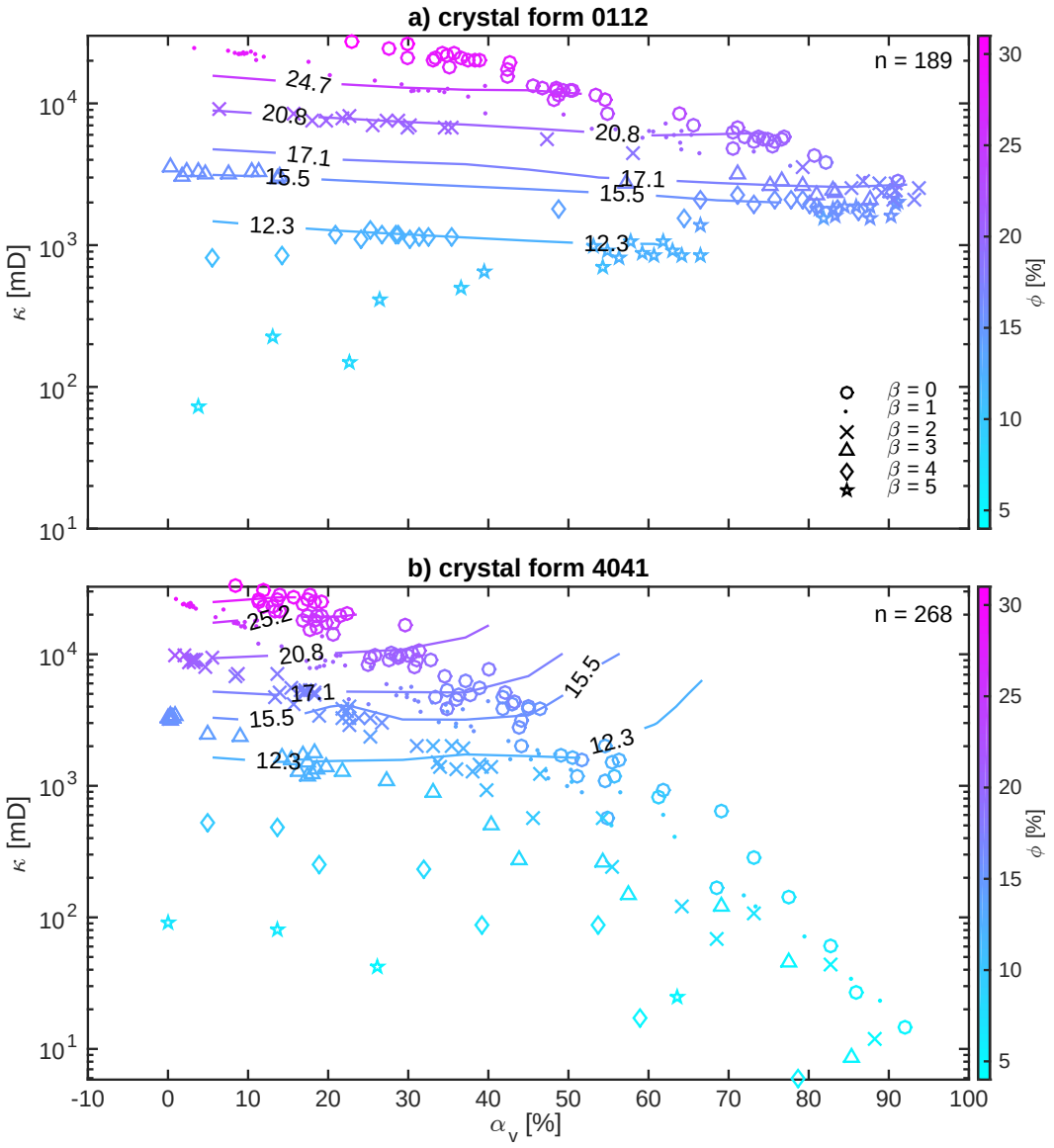

Figure 5.14: The permeability (κ) on a logarithmic scale vs the monocrystalline grain content by volume (α_v) for synthetic samples with the crystal form a) $01\bar{1}2$ and b) $40\bar{4}1$. Different symbols denote samples with different width of the isopachous cement fringes: circles, dots, crosses, triangles, diamonds and stars represent samples with 0 voxels, 1 voxel ($10\mu m$), 2 voxels ($20\mu m$), 3 voxels ($30\mu m$), 4 voxels ($40\mu m$) and 5 voxels ($50\mu m$) width of the isopachous cement fringes, respectively. The synthetic data points are coloured by the porosity (ϕ) from light blue (low porosity) to magenta (high porosity).

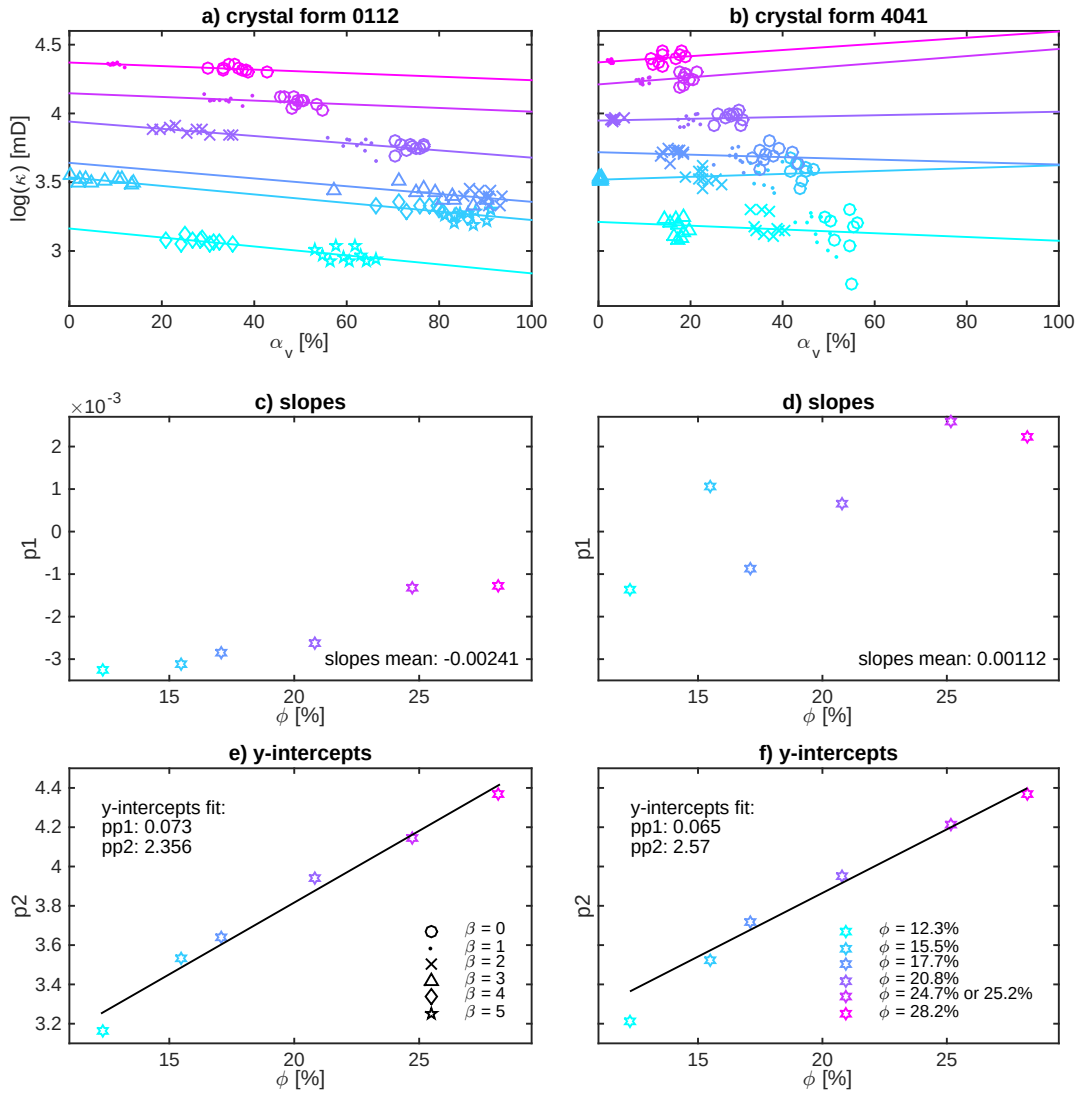

Figure 5.15: The top plots (a, b) show the fits to $log(\kappa)$ vs monocrystalline grains content α_v for synthetic samples with the crystal form a) $01\bar{1}2$ and b) $40\bar{4}1$ at six investigated porosities: 12.3, 15.5, 17.1, 20.8, 24.7 and 28.2% in the case of $01\bar{1}2$ and 12.3, 15.5, 17.1, 20.8, 25.2 and 28.2% in the case of $40\bar{4}1$. The points for each porosity are fitted with a straight line and the fit coefficients are plotted in the plots below: the slopes in c) and d) and the y-intercepts in e) and f).

case of $01\bar{1}2$ where the mean is equal to -0.00241. In the case of $40\bar{4}1$, the mean slope is 0.00111 but the results do not follow such a clear trend. The y-intercepts ($p2$) exhibit a strong linear dependance on porosity of the form $p2 = 0.073 \cdot \phi + 2.35$ in the case of $01\bar{1}2$, and $p2 = 0.065 \cdot \phi + 2.564$ in the case of $40\bar{4}1$. These findings allow for a formulation of the dependance of the permeability on the monocrystalline grains content and porosity in the case of $01\bar{1}2$ as a function:

$$log(\kappa) = -0.00241 \cdot \alpha_v + 0.073 \cdot \phi + 2.35 \tag{5.5}$$

and in the case of $40\bar{4}1$:

$$log(\kappa) = 0.00111 \cdot \alpha_v + 0.065 \cdot \phi + 2.564 \tag{5.6}$$

where α_v and ϕ are values for the monocrystalline grain content and the porosity in %, and κ is the permeability in mD. Equations 5.5 and 5.6 formulate a linear dependance of the logarithmic permeability on the monocrystalline grains and on the porosity, with the coefficient by the monocrystalline grains content 30 ($01\bar{1}2$) and 60 ($40\bar{4}1$) times smaller than the coefficient by the porosity.

The standard deviations for the point clouds for individual widths of the isopachous cement fringes analysed in Figure 5.15 are generally greatest for the synthetic samples with no isopachous cement and increase for samples with higher β (Figure 5.16). Low porosity samples generated using the crystal form $01\bar{1}2$ show an opposite trend. In the case of $40\bar{4}1$, for samples with low porosity, the variability in the results is considerable and this suggests that any trends observed in these results should be treated with caution.

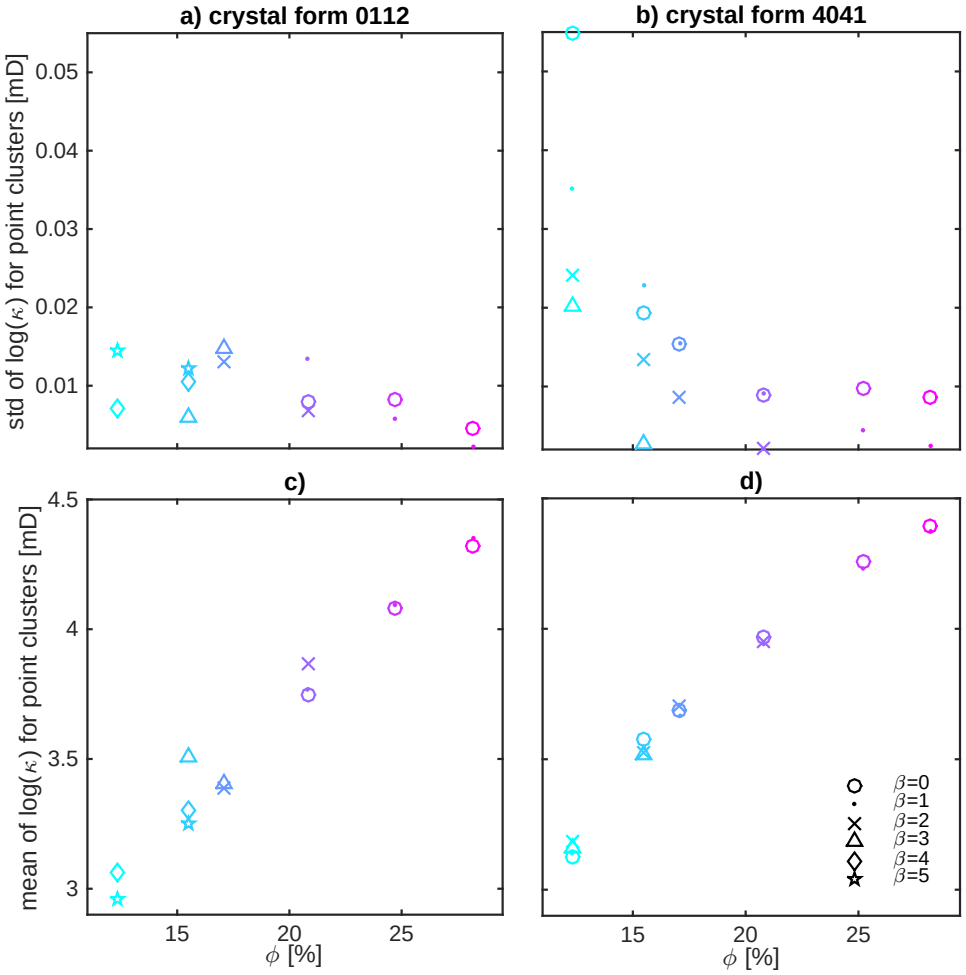

Figure 5.16: Statistics for the point groups for different values of the width of the isopachous cement fringes at the targeted porosities as depicted in plots in Figure 5.15 for both crystal form cases: $01\bar{1}2$ (a, c) and $40\bar{4}1$ (b, d). For each of the six porosities, colour-coded as in Figure 5.15, the mean (c, d) and the standard deviation (a, b) is calculated separately for samples with $\beta = \{0, 1, 2, 3, 4, 5\}$ voxels. The standard deviation is normalised by the mean.

5.3 Impact of Monocrystalline Grains on the Factors in the Kozeny-Carman Equation

Assuming that a porous bed can be regarded as a bundle of capillaries of equal length and constant cross-section, Kozeny and Carman proposed the following semi-empirical formula (Kozeny, 1927; Carman, 1937; Bear, 1972; Dullien, 1991):

$$\kappa = \frac{\phi^3}{\xi \cdot T^2 \cdot S^2} \tag{5.7}$$

which relates the permeability (κ) to four structural parameters: the porosity (ϕ), the specific surface area (S), the shape factor (ξ), and the hydraulic tortuosity (T).

This section examines two factors in the Kozeny-Carman formula: the tortuosity and the specific surface area with respect to the monocrystalline content (α_v) for two syntaxial cement geometries: $01\bar{1}2$ and$40\bar{4}1$.

5.3.1 Impact on specific surface (S vs α_v)

The specific surface of the solid/pore interface is derived for each synthetic sample by calculating the number of 6-connected solid voxels of every pore voxel. Figure 5.17 presents the results for 5946 synthetic samples generated with the use of the crystal form $01\bar{1}2$ and for 4086 synthetic samples generated with the use of the crystal form $40\bar{4}1$.

Figures 5.17a and b are coloured by the width of the isopachous cement fringes (β) and show that for synthetic samples with a low monocrystalline grains content, the specific surface is highest for samples with $\beta = 1$. In the case of $40\bar{4}1$, all curves are decreasing and converge to the surface area of about $100mm^2$ for the high monocrystalline grain content samples. In the case of $01\bar{1}2$, the curves converge

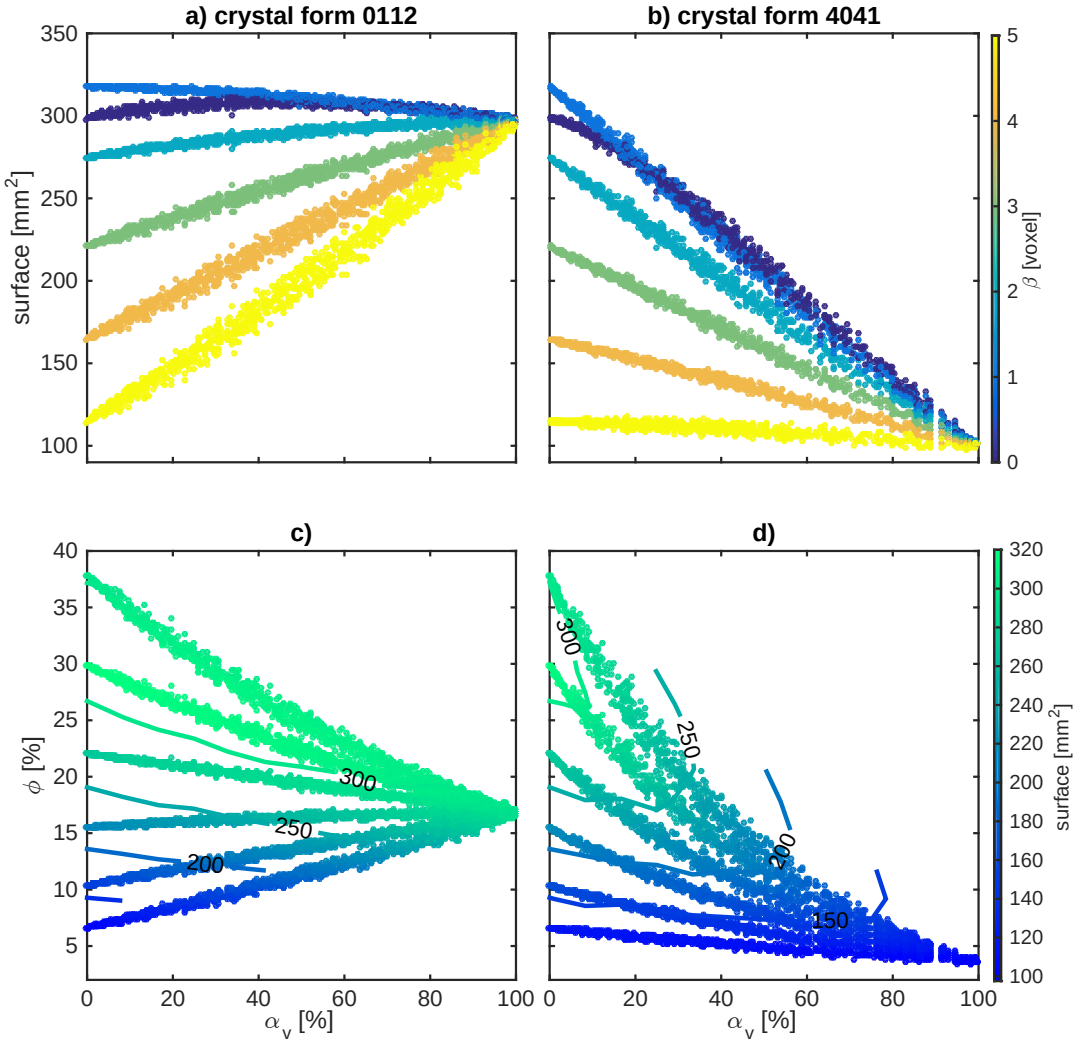

Figure 5.17: The specific surface of the pore/solid interface (S) as a function of the monocrystalline grain content in the sample by volume (α_v) (a, b) and its impact on the porosity (ϕ) (c, d) for samples with the crystal form $01\bar{1}2$ (a, c) and $40\bar{4}1$ (b, d). Plots of S vs α_v (a, b) are coloured by the width of the isopachous cement fringes (β), from 0 voxels (dark blue) to 5 voxels (yellow). Plots of ϕ vs α_v (c, d) are coloured by the specific surface area (S) from $100mm^2$ (dark blue) to $320mm^2$ (green).

to a surface area of about $300mm^2$ for the high monocrystalline grain content samples, and most of the curves are increasing. Only the curve for $\beta = 1$ is decreasing. The curve for $\beta = 0$ is increasing for small values of α_v, and changes to a decreasing curve after reaching a maximum at $\alpha_v = 40\%$.

Figures 5.17c and d are coloured by the specific surface of the pore/solid interface and illustrate that for samples of equal porosity the surface area is generally greater in the case of $01\bar{1}2$.

5.3.2 Impact on tortuosity (T vs α_v)

The tortuosity can be derived for the synthetic samples for which a Lattice Boltzmann simulation is performed, following the formula of Duda *et al.* (2011):

$$T = \frac{\langle U \rangle}{\langle U_x \rangle} \tag{5.8}$$

where $\langle U \rangle$ is the average magnitude of the intrinsic velocity over the entire sample volume and $\langle U_x \rangle$ is the volumetric average of its component parallel to the macroscopic flow direction. The tortuosity results for 189 synthetic samples with the crystal form $01\bar{1}2$ and for 268 synthetic samples with the crystal form $40\bar{4}1$ are shown in Figure 5.18.

Figures 5.18a and b are coloured by the width of the isopachous cement fringes (β) and show that in the case of $01\bar{1}2$ results converge to a tortuosity of about 1.2 for the high monocrystalline grain content samples, while similar convergence does not take place in the case of $40\bar{4}1$. In the case of $01\bar{1}2$, the curves for the low width of the isopachous cement fringes are increasing, while the curves for high β are decreasing. In contrast, all curves in the case of $40\bar{4}1$ are increasing. Generally, in both cases of the crystal form modelled, the tortuosity is greater for the synthetic samples with a greater width of the isopachous cement fringes. In

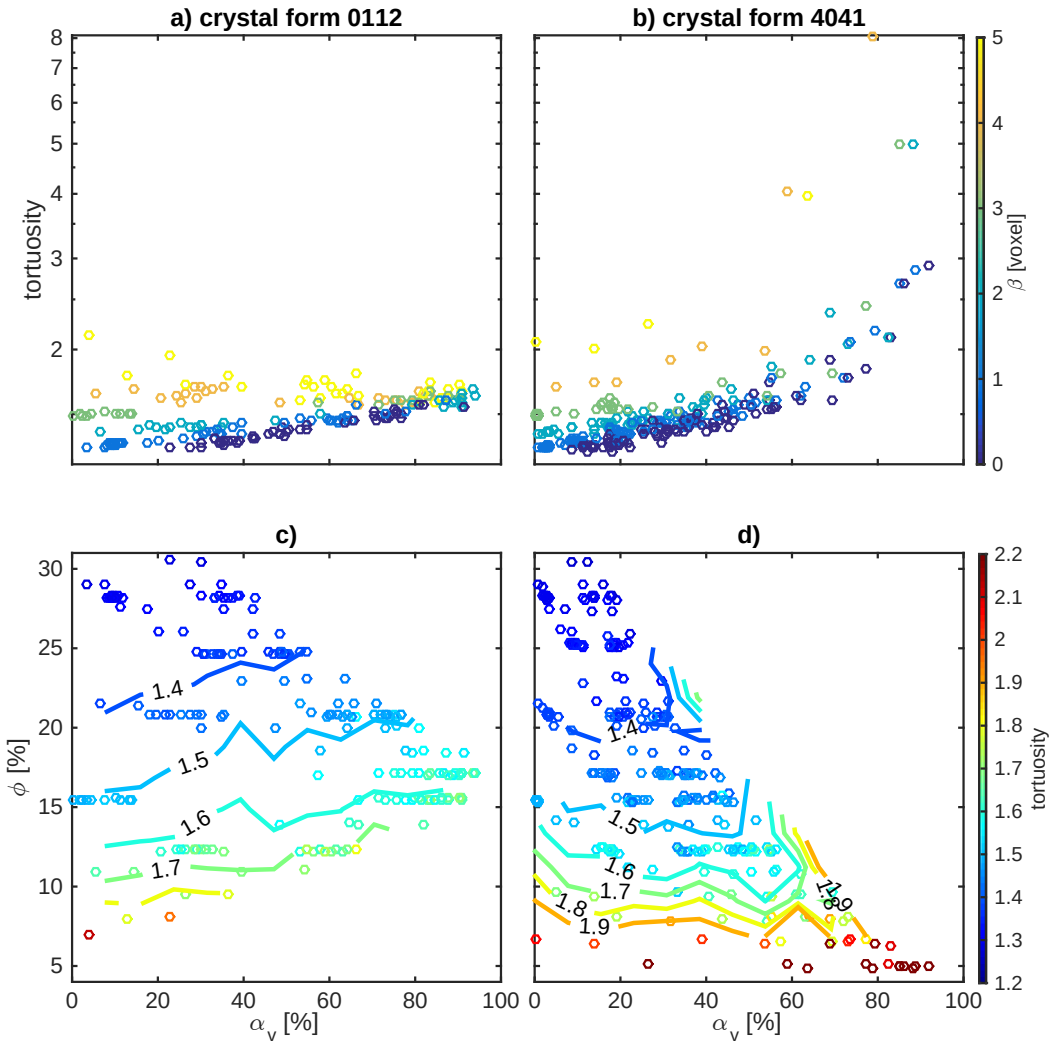

Figure 5.18: The tortuosity (T) as a function of the monocrystalline grain content in the sample by volume (α_v) (a, b) and its impact on the porosity (ϕ) (c, d) for synthetic samples with the crystal form $01\bar{1}2$ (a, c) and $40\bar{4}1$ (b, d). The plots of T vs α_v (a, b) are coloured by the width of the isopachous cement fringes (β), from 0 voxels (dark blue) to 5 voxels (yellow). The plots of ϕ vs α_v (c, d) are coloured by the tortuosity (T) from 1.2 (blue) to 2.2 and higher (red).

the case of $40\bar{4}1$, higher tortuosity can be reached (even up to 8) than in the case of $01\bar{1}2$, where the maximum tortuosity is around 2.2.

Figures 5.18c and d are coloured by the tortuosity and demonstrate that for synthetic samples of equal porosity, the tortuosity is generally greater in the case of the crystal form $01\bar{1}2$.

5.3.3 Kozeny-Carman equation

Figure 5.19 presents results of the permeability plotted against a factor involving three parameters present in the Kozeny-Carman equation that are quantified in this study: the porosity, the tortuosity and the specific surface area ($\frac{\phi^3}{S^2.T^2}$). The linear nature of the results suggests that the Kozeny-Carman equation holds for the synthetic samples generated in this study. The slope of the linear fit passing through the origin is the inverse of the geometric factor $\frac{1}{\xi}$. The polynomial coefficients of the fits are only slightly different for the two crystal forms modelled.

5.4 Discussion

We proceed to interpret and discuss the results presented in the previous sections, highlighting the similarities and differences to the results of the 2D modelling. The representation of the monocrystalline grains content in a sample that best explains cement volume produced in both the 2D and the 3D cementation models is explored in Section 5.4.1. The differences in the porosity and the permeability of synthetic samples generated with the use of the two crystal forms ($01\bar{1}2$ and $40\bar{4}1$) are discussed in Section 5.4.2. The relative volumes of the syntaxial and the isopachous cements for synthetic samples of varying amount of the monocrystalline grains are examined in Section 5.4.3. The trends in the results interpreted to be an effect of the competition of growing cements for the pore space

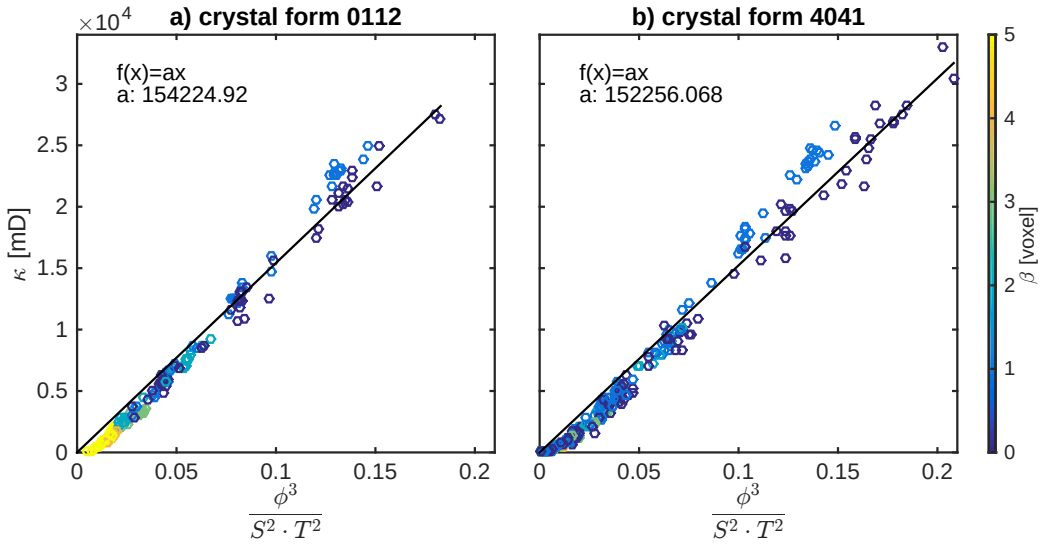

Figure 5.19: The permeability (κ) vs the factor $\frac{\phi^3}{S^2 \cdot T^2}$ from the Kozeny-Carman equation for synthetic samples with the crystal form a) $01\bar{1}2$ and b) $40\bar{4}1$. The slope of the linear fit to the synthetic data is the inverse of the geometric factor ξ from the Kozeny-Carman equation.

are explained in Section 5.4.4. Finally, the permeability results are discussed in Section 5.4.5.

5.4.1 Impact of convexity and shape of grains on the most accurate representation of the monocrystalline grains content

In the 2D study, the best fit to the porosity of synthetic samples as a function of the monocrystalline content (the lowest MSE) is achieved by the content by *'volume'* α_v (MSE=0.099), with the content by the 'surface area' α_a being a close second (MSE=0.112) (Figure 3.2). In the 3D study, however, it is the content by the *surface area* that exhibits the best fit with the porosity and the cement volume produced (MSE=0.111), as the content by volume exhibits a significantly higher variability in the results (MSE=0.198). The 'volume' of a grain is understood

here as a cross-section area in 2D and a volume in 3D, and the 'surface area' is understood as a perimeter in 2D and a surface area in 3D.

The above-mentioned results of the 3D modelling suggest that the grain surface area is a more reliable control than the grain volume on the porosity of the sample, and therefore on the cement volume developed by a grain. This can be explained by the fact that, as most monocrystalline grains develop a *layer* of cement around them, the volume of this is a function of the grain surface area.

The reason why the opposite trend is observed in the 2D study, i.e. smaller variability in the $\phi - \alpha_v$ results than in the $\phi - \alpha_a$ results, is because the distribution of the grain perimeters (which affects α_a, as it is defined as $\frac{\text{'surface area' of monocrystalline grains}}{\text{'surface area' of all grains}}$) is significantly more *heterogenous* than the distribution of the grain cross-section areas (which affects α_v, as it is defined as $\frac{\text{'volume' of monocrystalline grains}}{\text{'volume' of all grains}}$). This heterogeneity is responsible for the greater variability in the $\phi - \alpha_a$ results shown in Figure 3.2c (the MSE in that plot is slightly bigger) than in the case of the $\phi - \alpha_v$ results shown in Figure 3.2b.

To understand the sources of the heterogeneity in the distribution of the grain 'surface areas', we consider a set of grains with equal 'volumes'. The primary reason why a set of grains with equal 'volumes', results in a heterogenous distribution of grain 'surface areas' is due to the *heterogeneity* of the grain *convexities*. Two grains with different convexity will have very different 'surface area', with the more convex grains having a smaller 'surface area'. The grains in the 2D study are heterogenous in terms of the convexity (as defined by the ratio of the perimeter of the convex hull of a grain and the perimeter of the grain), as illustrated in Figure 5.20. By contrast, all the grains in the 3D study are convex, i.e. they have no heterogeneity. As a result, the heterogeneity of the grain convexities in the 2D medium is considerably greater than in the 3D medium.

The secondary reason why a set of grains with equal 'volumes' results in a

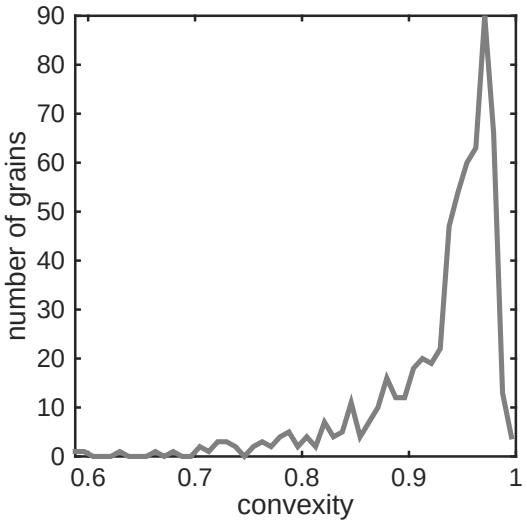

Figure 5.20: The convexity of 604 grains in the 2D porous medium. Convexity is defined as $\frac{\text{perimeter of the convex hull}}{\text{perimeter of the grain}}$.

heterogenous distribution of the grain 'surface areas' stems from the *heterogeneity* of the grain *shapes*. Two grains of the same 'volume' but with different shapes will have a different 'surface area'. Specifically, more elongated grains will have a greater 'surface area'. The heterogeneity of grain shapes is again greater in the 2D medium than in the 3D medium (Figure 4.4). The shape parameter in the 2D medium is spread out over a range of values, while in the 3D medium it is significantly more peaked.

To summarise, the heterogeneity in the distribution of the grain surface areas in the 3D study is affected *only* by the heterogeneity in the grain shapes, which is smaller in the 3D medium than in the 2D medium. By contrast, the heterogeneity in the distribution of the grain perimeters in the 2D study is affected *both* by the heterogeneity in the grain shapes and grain convexities. Moreover, the contrast in the heterogeneity of grain convexities between the 2D medium and the 3D medium is particularly stark, as all grains in the 3D medium are convex. These two factors (the heterogeneity in the grain shapes and convexities in the 2D medium) amplify the heterogeneity in the distribution of the grain perimeters and this results in a

greater variability of the results in the $\phi - \alpha_a$ space than in the $\phi - \alpha_v$ space in the 2D study (Figure 3.2).

5.4.2 Differences in the results between crystal form $01\bar{1}2$ and $40\bar{4}1$

The two crystal forms modelled differ in terms of shape and volume, so the results for synthetic samples produced using these crystal forms also differ. The sections below examine the differences in the syntaxial cement volume, the mean volume of isopachous and syntaxial cement per grain, the specific surface area of the pore/solid interface, the tortuosity, the permeability as well as in the variability in the results.

Porosity and syntaxial cement volume

Similar to the 2D study (see Section 3.3.1), the crystal form $40\bar{4}1$ produces samples with a lower porosity than the crystal form $01\bar{1}2$ (Figure 5.4), as the mean volume of the syntaxial cement developed by the crystal form $01\bar{1}2$ is lower than that of the crystal form $40\bar{4}1$. For the high monocrystalline content samples, the porosity converges to about 17% for the synthetic samples with the crystal form $01\bar{1}2$, and to about 4% for the synthetic samples with the crystal form $40\bar{4}1$. This difference in the porosity (about 13%) stands in contrast to the difference of about 3% in the 2D study, where the porosity of the high monocrystalline content samples converges to about 15% in the case of $01\bar{1}2$ and to about 13% in the case of $40\bar{4}1$.

This 4-fold difference in the porosity of the high monocrystalline samples in the 2D study and the 3D study stems essentially from the dimensionality of the two models. In the 3D model, the volume of the syntaxial cement produced is controlled by the *volume* of the bounding polyhedron reduced by the volume of the grain itself. As Figure 1.14 illustrates, the volume of the epitaxial overgrowth

developed in the absence of obstacles on a spherical grain by a rhombohedral form $40\bar{4}1$ is 9.6 times larger than the volume developed by the crystal form $01\bar{1}2$.

In the 2D methodology, however, the amount of the syntaxial cement is controlled by the cross-sectional *area* of a crystal form circumscribed on a monocrystalline grain reduced by the area of the grain itself. The 2D methodology assumes that the grain visible in the plane of the porous medium is cut close to its centroid (see Section 2.2.1). As the crystal axis of a monocrystalline grain can be oriented in any direction, the cross-section of the bounding polyhedron can take a range of shapes and its area will vary accordingly. A comparison between the mean cross-sectional area of the two crystal forms circumscribed on an identical spherical grain (which is achieved by rotating the rhombohedra by a full range of angles in the 3D) reveals that the mean amount of the syntaxial cement that would be produced in the absence of obstacles in the case of $01\bar{1}2$ is 5.5 times smaller than in the case of $40\bar{4}1$. This ratio is 1.7 times smaller than the ratio of volumes of the syntaxial cement produced on a spherical grain by the two rhombohedral forms in the 3D model (which is 9.6). The difference in the ratios between the 2D and the 3D model is the main reason for the difference in the porosity of the cemented synthetic samples.

It should be noted, however, that in a porous medium syntaxial cement will rarely develop to its full crystal form, due to the effect of the impinging grains. That is why the factor of 9.6 (in the 3D study) does not translate into the difference in the cement volume produced in the 3D cemented synthetic samples. In the absence of the isopachous cement ($\beta = 0$), the volume of the syntaxial cement in the high monocrystalline content samples ($\alpha_v > 90\%$) is about 21% in the case of $01\bar{1}2$ and about 34% in the case of $40\bar{4}1$. This yields a factor of 1.6, i.e. the crystal form $40\bar{4}1$ produces 1.6 times more cement than the crystal form $01\bar{1}2$. In the 2D study, in the synthetic samples with no isopachous cement, the amount of the syntaxial cement in the high monocrystalline content samples is about 21% in the case of $01\bar{1}2$ and about 24% in the case of $40\bar{4}1$. This yields a factor of 1.1.

This is again smaller than the ratio of the mean cross-sectional areas for the two crystal forms (which is 5.5).

In the absence of isopachous cement, the syntaxial cement in the high monocrystalline content samples in the case of $40\bar{4}1$ obscures 34% of the total sample volume compared to 21% in the case of $01\bar{1}2$. This stems from the fact that, due to its elongated shape, crystal form $40\bar{4}1$ can protrude deep into the pore space and often manages to bridge the pore space completely, which crystal form $01\bar{1}2$ achieves much less frequently, as illustrated in Figure 5.5.

Mean volume of the isopachous and syntaxial cement per grain

Since the mean volume of the syntaxial cement developed by the crystal form $01\bar{1}2$ is significantly smaller than that of in the case of $40\bar{4}1$, the behaviour of the $\beta - \alpha_v$ curves differs in the two cases. Figure 5.8 illustrates that all the curves in the case of $40\bar{4}1$ are decreasing, which suggests that at any monocrystalline grain content, the mean volume of the syntaxial cement per grain is greater than the mean volume of the isopachous cement per grain. In the case of $01\bar{1}2$, only the curves for the synthetic samples with low width of isopachous cement fringes ($\beta = 0$, 1 and 2 voxels) decrease. The synthetic samples with $\beta > 2$ produce increasing curves, as the mean volume of the isopachous cement exceeds that of the syntaxial cement as soon as isopachous cement fringes grown to a width of at least 3 voxels ($30\mu m$).

The same mechanism is at work in the case of the $\gamma_v - \alpha_v$ plots in Figure 5.6. The curves for the widths of the isopachous cement fringes which produce on average a smaller volume of cement per grain than the monocrystalline grains (all curves in the case of $40\bar{4}1$ and curves with $\beta = 0$, 1 and 2 voxels in the case of $01\bar{1}2$) are concave downward, whereas the curves where the mean volume of the isopachous cement is greater than the mean volume of the syntaxial cement per grain (the curves with $\beta = 3$, 4 and 5 voxels in the case of $01\bar{1}2$) are concave upward.

Surface area

The specific surface area of the solid/pore interface for the high monocrystalline samples converges to about $300mm^2$ in the case of $01\bar{1}2$ and to about $100mm^2$ in the case of $40\bar{4}1$ (Figures 5.17a and b). The specific surface area correlates with the porosity, which converges to about 17% in the case of $01\bar{1}2$ and to about 4% in the case of $40\bar{4}1$. Generally, the greater the porosity, the greater is the surface area of the pore space.

The difference in the specific surface in the synthetic samples generated with the use of these two crystal forms occurs as the crystal form $01\bar{1}2$ is much less effective in bridging across the pores and occluding them completely. Due to its blocky shape, this crystal form is much more likely to grow into the pore space but not come into contact with cement or grain from across a pore, and this way the solid/pore area remains high. In the synthetic samples with no isopachous cement, the specific surface area increases slightly, reaches a maximum at around 40% of monocrystalline grains, and then drops to $300mm^2$. For samples with wide isopachous cement fringes, the specific surface area increases significantly with the monocrystalline grains content. It is concluded that isopachous cement tends to bridge over pore space and thus eliminates the pore/solid interface.

Syntaxial cement of the form $40\bar{4}1$ is much more effective in bridging across the pores, eliminating the pore/solid interface and thus decreasing the specific surface area. As a result, all curves in Figure 5.17d are decreasing.

It is worth noting that the calculation of specific surface area on the voxelised model outputs has uncertainties. On one hand voxelisation introduces 'blocky' aspect to the synthetic sample that is not present in natural media, which are generally smoother on the scale of the resolution of the models in this thesis ($10\mu m$). The voxelisation effect can artificially *increase* specific surface area results. On the other hand, the interface between pore and solid in natural media is typically convoluted, indeed it sometimes can have a fractal nature, which can

yield very high surface areas. These non-convexities of the interface cannot be captured at the resolution of the models in this thesis. The effect of resolution in model outputs would artificially *decrease* the result for the specific surface area. Of the two effects with opposite impact on the specific surface area calculation: the voxelisation and the resolution, the latter is probably the stronger one. This would suggest that the results for specific surface area for the model outputs presented in this thesis are too low with respect to natural rocks.

Tortuosity

For the high monocrystalline grain content samples, the tortuosity converges to about 2.6 in the case of $01\bar{1}2$, however, no convergence takes place in in the case of $40\bar{4}1$ (Figures 5.18a and b). This can be explained by the differences in the porosity of the synthetic samples produced with the use of these two rhombohedral forms. The synthetic samples in the case of $01\bar{1}2$ have a significantly higher porosity (about 17%). The pore space of a higher volume is less susceptible to being perturbed by syntaxial cement. By contrast, the high monocrystalline content samples in the case of $40\bar{4}1$ have much lower porosity of about (4%). When the porosity is so small, it is likely that the sample is not percolating and if it does manage to percolate, this is often through a very convoluted (high tortuosity) pathway.

The tortuosity contours in Figure 5.18c generally increase with α_v, which suggests that tortuosity increases for synthetic samples at constant porosity in the case of $01\bar{1}2$. The samples with more monocrystalline grains have higher tortuosity because the form of syntaxial cement is blocky and so the topology of the pore space is largely maintained, while the grains become more angular (less hydrodynamic), which increases the angularity/tortuosity of the flow paths around them. The syntaxial cement of the form $01\bar{1}2$ tends to promote tortuosity to a greater degree than the isopachous cement. Even though isopachous cement is very effective in diminishing pore size, the topology of pore space is maintained

and grains remain rounded, which results in smoother flow paths and a smaller tortuosity.

A similar trend is not observed in the case of $40\bar{4}1$. The tortuosity contours in Figure 5.18d are essentially horizontal, suggesting that the tortuosity is independent of the monocrystalline grains content. The impact of the syntaxial cement in the case of $40\bar{4}1$ is very similar to the impact of the isopachous cement. The crystal form $40\bar{4}1$ produces elongated forms that tend to penetrate across the pores, which is indeed similar to the behaviour of the isopachous cement, especially when the thickness of isopachous cement fringes is high.

The combined effect of the tortuosity and the specific surface area on the permeability is explored in Figure 5.21. Two synthetic samples generated using the crystal form $01\bar{1}2$ and with the same porosity (15.5%) but different monocrystalline content are compared. The flow paths are less numerous (affected by the porosity and the specific surface area) and more angular (affected by the tortuosity difference), which leads to a significantly lower permeability in the sample with more monocrystalline grains (b).

Permeability

The permeability at equal porosities of synthetic samples with the crystal form $40\bar{4}1$ is bigger than of the synthetic samples with the crystal form $01\bar{1}2$ (Figures 5.12 and 5.16c and d). This is in contrast to the results of the 2D study and occurs because the monocrystalline grains content in the case of $40\bar{4}1$ in the 3D model has significantly stronger impact on the porosity than in the 2D model.

While in the 2D study the difference in the porosity of the synthetic samples with an equal content of the monocrystalline grains (α_v) and equal width of the isopachous cement fringes (β) reaches up to 3% for the high monocrystalline content samples, the difference in the 3D study is about 13%. The difference in

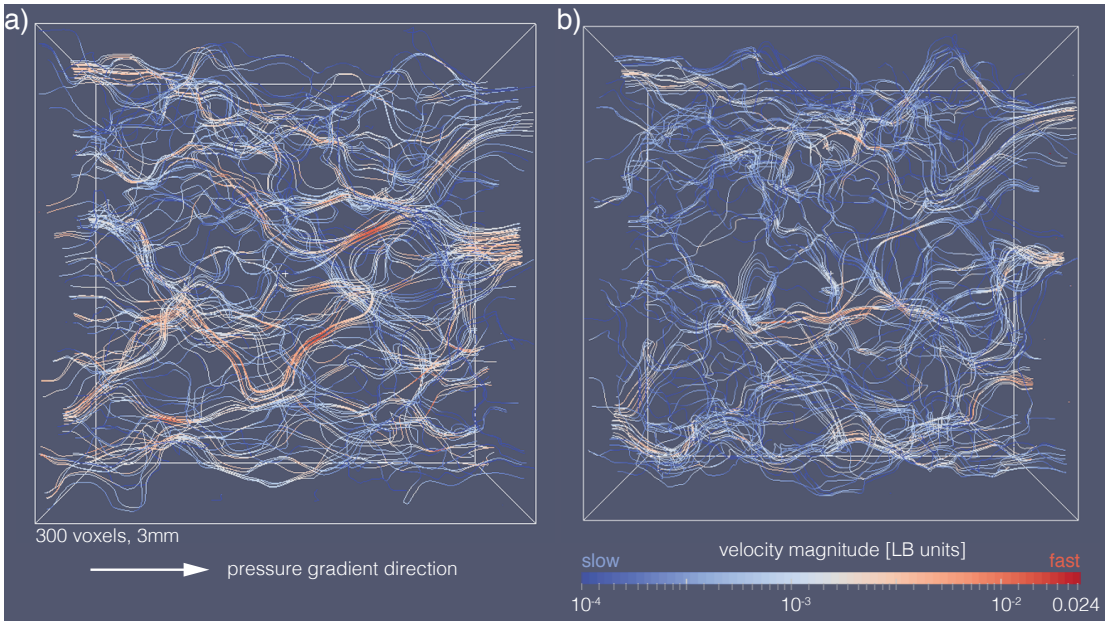

Figure 5.21: The magnitude of the flow velocity on a logarithmic scale displayed along the streamlines for samples generated using the crystal form $01\bar{1}2$ and with porosity $\phi = 15.5\%$, a) a low monocrystalline content sample ($\alpha_v = 7.4\%$, $\beta = 3$, $\phi = 15.51\%$, $\kappa = 3200mD$, $S = 225mm^2$, $T = 1.51$), b) a high monocrystalline content sample ($\alpha_v = 83.4$, $\beta = 5$, $\phi = 15.45\%$, $\kappa = 1620mD$, $S = 270mm^2$, $T = 1.73$).

the permeability is primarily an effect of the shape differences between the two rhombohedral forms of calcite modelled. At similar overall volume of cement in the sample, form $40\bar{4}1$ generates more elongated features that may reach further in the pore space, so blocking the flow paths. This way, the probability of closing the flow pathways that significantly contribute to the flow is greater, and this is reflected by the permeability being on average lower.

In the 3D modelling, the primary reason why the permeability of the synthetic samples of equal porosity is higher in the case of $40\bar{4}1$ than in $01\bar{1}2$ is because fewer monocrystalline grains are needed to produce an equal volume of cement. Fewer monocrystalline grains producing syntaxial cement of the crystal form $40\bar{4}1$ result in a patchy cement fabric in the sample and in a higher permeability, than the more uniform distribution of cement produced by more monocrystalline grains in the case of $01\bar{1}2$.

When we consider the synthetic samples with no isopachous cement, an observation can be made that slightly *more* monocrystalline grains are necessary to generate a sample of equal porosity in the 3D study than in the 2D study in the case of $01\bar{1}2$. However, in the case of $40\bar{4}1$, significantly *fewer* monocrystalline grains are necessary in the 3D study (see Figures 3.4 and 5.4). The fewer monocrystalline grains there are, the less likely it is that they close off pore space and, as such, reduce permeability.

For synthetic samples of equal porosity, the surface area is generally greater in the case of $01\bar{1}2$ (Figures 5.17c and d). In a similar fashion, the tortuosity is generally greater in the case of $01\bar{1}2$ (Figures 5.18c and d). Both properties (surface area and tortuosity) are in the denominator of the Kozeny-Carman equation, and so the permeability decreases with their increase (provided that the porosity is constant). This is in agreement with a lower permeability for samples of equal porosity in the case of $01\bar{1}2$ than in the case of $40\bar{4}1$ (Figure 5.12).

Variability in the synthetic data

As in the 2D study, the difference in the volume and shape of the two rhombohedral forms gives rise to a difference in the variability in all presented results. In almost every plot presented in this chapter there is greater variability, e.g. the MSE is higher, for the synthetic samples with the rhombohedral crystal form $40\bar{4}1$. This is perhaps best illustrated by Figures 5.7 and 5.9, which show that the MSE is considerably and consistently smaller for the results associated with the crystal form $01\bar{1}2$, as the crystal form $01\bar{1}2$ tends to produce more uniform porosities and relative syntaxial cement volumes. This reasoning has been explored in more detail in Section 3.3.1.

As in the 2D study, the trends in the variability of the results also hold in the case of the permeability. The standard deviation for the point groups for the synthetic samples with different widths of the isopachous cement fringes is generally greater for the synthetic samples associated with the crystal form $40\bar{4}1$ (Figures 5.16a and b). This illustrates that the crystal form $40\bar{4}1$ produces samples of greater variability.

5.4.3 Cement volume

The porosity of the synthetic samples is generally lower in the 3D study than in the 2D study, as the volume of cement produced is higher. The cement in the 3D model is grown in all three directions, and often reaches sections of the 3D medium in which the grain that produces this cement is not visible, as illustrated in Figure 4.7. The cement in the 2D model is seeded only by grains that are visible in the plane of the porous medium, and thus the final cemented medium lacks cement that could grow into that plane by grains that are not visible, and so leading to lower porosities.

Syntaxial cement

This section concerns the synthetic samples where only syntaxial cement is present ($\beta = 0$). Syntaxial cement volume developed by a monocrystalline grain depends on the shape of the grain, its size, the direction of the crystal axes, the proximity and the arrangement of the neighbouring grains, and the shape of the crystal form developed.

Let us consider a single grain of a diameter $250\mu m$ in both versions for the model: the 3D model where the porous medium has dimensions of $3 \times 3 \times 3mm$, and the 2D model where the porous medium has dimensions of $10 \times 10mm$. In the absence of any obstacles, the porosity occlusion by the syntaxial cement of the crystal form $01\bar{1}2$ growing on a spherical grain with diameter $250\mu m$ is 2.3 times greater in the 3D medium than in the 2D medium. An equivalent grain developing syntaxial cement of the crystal form $40\bar{4}1$ would obscure 3.9 times as much porosity in the 3D medium than in the 2D medium. The volume of cement in the 3D model is calculated here as the *volume* of the circumscribed polyhedron reduced by the volume of the grain. The 'volume' in the 2D model is the mean cross-sectional *area* of the bounding polyhedron with a plane passing through the centre of the grain, again reduced by the surface area of the grain.

Although the syntaxial cement volume in the synthetic samples with the crystal form $01\bar{1}2$ is very similar in the 2D and 3D studies (about 21% of the volume of the sample), the factor of 2.3 obtained above suggests that the porosity should be occluded more in the 3D modelling. In the case of $40\bar{4}1$, a significant difference in the cement volume produced is observed: 34% of the sample volume in 3D and 24% in 2D, but the ratio is still significantly smaller than the factor of 3.9 obtained above for a spherical grain in the absence of obstacles.

The reason why the difference in the porosity occlusion between the 3D and 2D models is not as high as the factor 2.3 in the case of $01\bar{1}2$ and the factor 3.9 in $40\bar{4}1$, is primarily due to the effect of the impinging grains. This results in that

the full volume of the bounding polyhedron that would develop in the absence of impinging grains can not realised at this stage of modelling.

An additional factor that curbs the ratio of the porosity occlusion in the 3D and the 2D models is the size of grains in the sample. The volume of the cement produced is controlled by the size of the grain. The mean grain size (equivalent diameter) is slightly smaller in the 3D study ($260\mu m$ compared to $285\mu m$ in the 2D study), which leads to a smaller cement volume per grain produced. Moreover, the grains size distribution in the 2D model is wider and the grains are on average larger than in the 3D medium, leading to a greater cement volume produced per grain in the 2D study.

Lastly, the difference in the complexity of grain shapes might influence the volume of cement produced by a grain. The grains in the 3D synthetic deposit are very regular and their 2D cross-sections show rounded convex shapes (Figure 4.3b). This is not the case in the 2D porous medium, which includes non-convex grains, often with a convoluted perimeter (Figures 2.2 and 5.20). The irregularity of the grain shapes leads to a greater occlusion of the porosity in the 2D model, particularly in the case of the syntaxial cement, as the cement needs to fill in these concave irregularities.

Isopachous cement

In the synthetic samples with no or few monocrystalline grains, increasing the width of the isopachous cement fringes (β) is very effective in decreasing porosity. This effect is even stronger in the 3D model results than in the 2D results: a width of $50\mu m$ in the 3D study (5 voxels) occludes the porosity of the synthetic samples by 31.2%, while the same width of $50\mu m$ in the 2D study (10 voxels) occludes the porosity by 21.2%.

The difference between the 2D and 3D model arises again from the dimensionality

of the two models. In the 2D model, all grains develop equal thickness of the isopachous cement fringes. In the 3D model, even though the *true* thickness remains the same for all grains, the *apparent* thickness of the isopachous cement fringes visible in the 2D sections of the 3D medium depends on the distance of the centroid of the grain to the plane of section. The larger this distance is, the larger the apparent thickness of the isopachous cement fringes. As the plane of section is unlikely to cut exactly through the center of the grain, the vast majority of the isopachous cement fringes observed in any given section have thicknesses appearing larger than the input to the cementation model (β). Overall, this leads to seemingly differing thickness of the isopachous cement fringes in 2D sections of any 3D cemented synthetic sample (Figures 5.3b and d).

The increased volume of the isopachous cement in the 3D study with respect to the 2D study in the case of $01\bar{1}2$, results in the mean isopachous cement volume produced per a polycrystalline grain being bigger than the mean syntaxial cement volume produced per a monocrystalline grain for $\beta > 20\mu m$. This is reflected in the concave-upward shape of the curves in Figure 5.6 and decreasing curves in Figure 5.8.

5.4.4 Competition for pore space

As in the 2D study, the exponential shape of the curves in Figure 5.8 and the hyperbolic shape in Figure 5.9 suggests a competition between the syntaxial and the isopachous cements for growth space. This has been discussed in detail in Section 3.3.3.

5.4.5 Permeability

Here we examine the permeability results and discuss the effectiveness of the isopachous cement in closing the pore-throats, the variability in the results, and

a comparison of the poroperm results derived here with data for grainstones noted in the literature. Finally, the impact of the monocrystalline grains on the permeability is discussed.

Effect of isopachous cement on limiting permeability

In this section, the synthetic samples with no monocrystalline grains are considered. In contrast to the 2D study, where the synthetic samples with the width of the isopachous cement fringes greater than $10\mu m$ are rendered non-percolating, in the 3D study almost all samples are percolating, even those where the width of the isopachous cement fringes reaches $50\mu m$.

Figure 5.22 illustrates flow velocity derived with a LB simulation in two model outputs of Calcite3D. Both synthetic samples consist only of polycrystalline grains. The synthetic deposit with no cement (Figure 5.22a) has a porosity of 37.8% and a permeability 59,800mD. The introduction of the isopachous cement fringes of width $50\mu m$ (Figure 5.22b) decreases the porosity to 6.6% and the permeability to $114mD$. Although the isopachous cement fringes occlude the vast majority of the pore space, the flow manages to continue due to the connectivity of pores in all three dimensions, unlike in a 2D medium.

Variability in the synthetic data

The permeability results span four orders of magnitude (Figure 5.12), but for the synthetic samples with similar porosity, the variability in the permeability does not go beyond $log(\kappa) = 0.54$ (Figure 5.13). The poroperm can be fitted with an exponential curve with a high coefficient of determination (R^2), demonstrating a clear pattern with little variation in the synthetic data.

This is in contrast to the 2D study, where the variability at any given porosity spans up to two orders of magnitude, as illustrated in Figure 3.12. The fact that

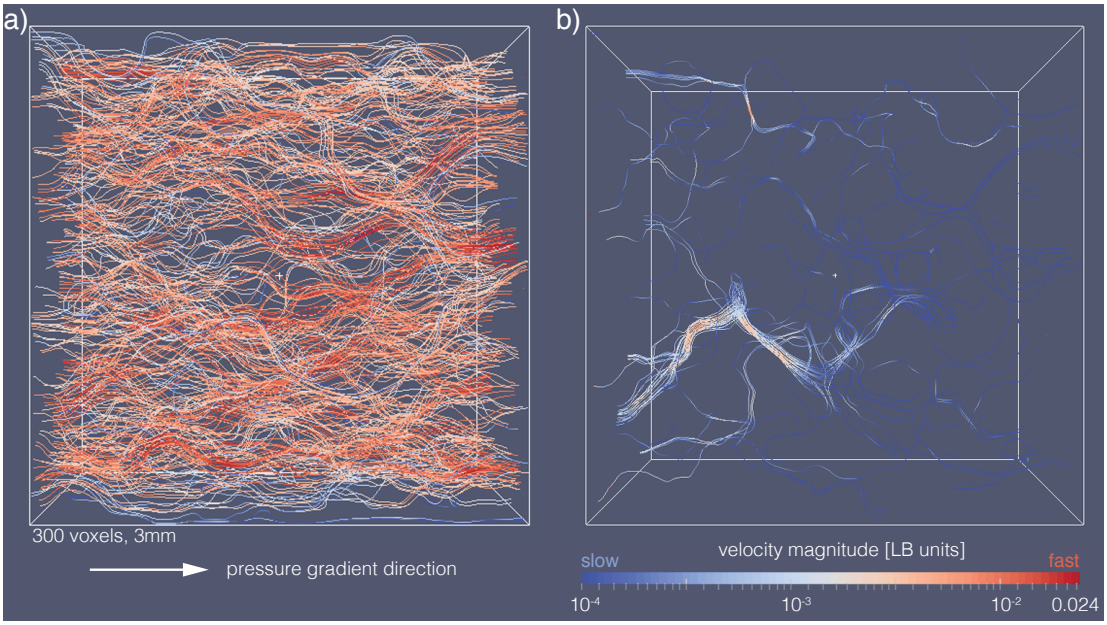

Figure 5.22: The magnitude of the flow velocity on a logarithmic scale displayed along the streamlines for samples with no monocrystalline grains content and different width of the isopachous cement fringes: a) a sample with no cement ($\alpha_v = 0$, $\beta = 0$, $\phi = 37.9\%$, $\kappa = 59800mD$, $S = 298mm^2$, $T = 1.22$), b) a sample with $50\mu m$ width of the isopachous cement fringes ($\alpha_v = 0$, $\beta = 5$, $\phi = 6.6\%$, $\kappa = 100mD$, $S = 114mm^2$, $T = 2.42$).

it is not the case in the 3D study is a result of the removal of the 2D bias in flow simulation. Flow simulated in 2D might lead to a bias in the permeability and skewing of the results towards smaller values, as the 2D media lack the pore connectivity in the 3^{rd} dimension (see Section 3.3.4). The clear trend in the poroperm data exhibited in the 3D results confirms this speculation: the pore connectivity is maintained in all three dimensions, and so the permeability results exhibit a much narrower range.

As in the 2D study, the results for the synthetic samples with the same width of the isopachous cement fringes (β) tend to be grouped together and the data variability in these groups is much smaller than of the entire synthetic dataset. The standard deviation of the point groups at each of the targeted porosities generally decreases with increasing porosity (Figure 5.16). The synthetic samples with low porosity tend to have greater variability in $log(\kappa)$.

Another trend observed is that the variability generally correlates with the monocrystalline grain content α_v (Figures 5.16 and 5.15a and b). The more monocrystalline grains there are in the sample, the greater is the variability in the permeability results in each group of samples with the same β. The only exceptions from this trend are the synthetic samples with $\beta = 3$ and $\phi = 17.7\%$ and the samples with $\beta = 1$ and $\phi = 20.8\%$ in the case of $01\bar{1}2$. This is explained by the direction of the crystal axes being assigned at random, as explored in Chapter 3 (see Section 3.3.4).

Figure 5.23 demonstrates how the randomness in the location of the monocrystalline grains and the directions of their crystal axes can lead to very different permeabilities at the same porosity. Both Calcite3D model outputs used to simulate the flow shown in Figure 5.23 are generated with the use of the crystal form $40\bar{4}1$, have no isopachous cement and porosity very close to 12.3%. These synthetic samples were selected as two end-points of the synthetic data for $\beta = 0$ and $\phi = 12.3\%$ in Figure 5.12b: one with the highest and one with the lowest permeability. The parameters that characterise these samples (the width of the

isopachous cement fringes, the monocrystalline grain content, and the porosity) are very similar, but the resulting permeability differs by a factor of 3.5.

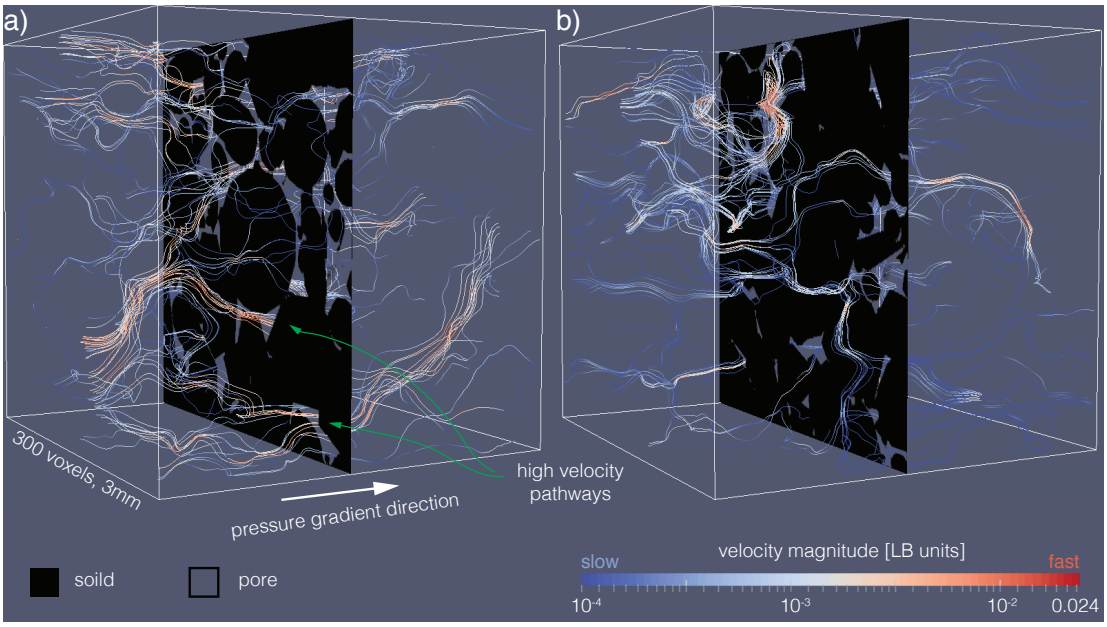

Figure 5.23: The impact of the randomness in the location of monocrystalline grains in the sample and the orientations of their crystal axes on the flow velocity (displayed along streamlines). From the group of samples with no isopachous cement generated with the crystal form $40\bar{4}1$ and with porosity of around 12.3%, two samples with the largest difference in the permeability were selected: a) $\alpha_v = 54.4\%$, $\beta = 0$, $\phi = 12.5\%$, $\kappa = 2030mD$, b) $\alpha_v = 54.9$, $\beta = 0$, $\phi = 12.3\%$, $\kappa = 580mD$.

This stark contrast in the permeability is directly due to the randomness of the placement of the monocrystalline grains and the directions of the crystal axes. In the high permeability synthetic sample (Figure 5.23a) there are multiple high-velocity flow pathways present because the large grain visible in the middle of the cross-section is polycrystalline and so has not developed any cement. In the low permeability synthetic sample (Figure 5.23b), this central grain has developed syntaxial cement, and as a result it blocked pathways through the middle of the porous medium. This in turn resulted in the majority of the flow concentrating in the top portion of the synthetic sample.

Kozeny-Carman equation

The synthetic samples generated with Calcite3D follow the behaviour described by the Kozeny-Carman equation (Figure 5.19). The linear fit coefficients are very similar (difference in the third significant figure) in the two cases of the crystal form modelled. It can be concluded that the Kozeny-Carman equation with a geometric factor $\xi = 6.5 \cdot 10^{-6}$ can be used to accurately describe the relationship between the permeability and the tortuosity, the specific surface of the pore/solid interface and the porosity in the synthetic samples in this study. It should be noted, however, that this expression cannot be used to predict permeability without simulating the flow, as flow velocity field is necessary for the tortuosity calculation.

Data from the published studies and the plug data

The permeability of the synthetic deposit, generated in this study with the use of the deposition model, is 59,800mD at porosity 37.9%. This is just short of being within the range of 15,800-56,600mD for Holocene grainstone sediment permeabilities as reported by Enos and Sawatsky (1981). However, the highest permeability grainstone samples in their study have porosities higher than the one used in this study (45.2-48.2%). For samples in the porosity range 40.1-42.0%, which is closer to the porosity of the synthetic deposit in this study, permeabilities in the range 24,900-31,900mD are reported. This is significantly lower than the permeability of the synthetic deposit produced by the depositional model used in this study.

This high permeability could be attributed to the approach taken to model the shapes of grains and the fact that these are rounded and convex. The ellipsoidal grains in the deposition model developed in this thesis have only few points of contact with the neighbouring grains, so that the narrowest portions of pore throats are effectively very short (Figure 4.3). The model thus results in the

creation of relatively large interstitial spaces, which allow for unobstructed fluid flow. The effect of pore spaces being too large, and grains touching only at few points of contact, is also due to the 3D modelling methodology not taking the mechanical compaction into account. In natural porous media, grains fit much closer together and narrow pore throats are common (Figure 2.2), leading to constriction of fluid flow and, as such, lower permeabilities.

Another reason for the increased permeability of the synthetic deposit may be the choice that is made in the treatment of the porous medium to remove the fine grains (Chapter 2, Section 2.1). The absence of fine grains is propagated from the 2D to the deposition model in the 3D (Chapter 4, Section 4.1.1). As the statistics of grain shape and size are an input to the grain generation model, the removal of fine grains results in very fine grains being absent from the 3D deposition model. On top of that, the pores and pore throats in the synthetic 3D deposit are unnaturally wide due to the perfect convexity and regularity of the grain shapes (as discussed above). This allows fine grains that are generated in the deposition model to fall freely through the wide pores to the bottom of the deposit, which is then cropped to avoid artefacts (Section 4.1.2). The result is that the finest grains are altogether removed from the synthetic sample. Figure 4.2 illustrates that a good number of fine grains are present in the 2D medium (on the left border of the image in Fig 4.2a) and the number of such small grains is significantly reduced in the 3D medium (Fig 4.2b). The absence of fine grains in the synthetic 3D deposit impacts its permeability by rendering the wide pores and pore throats even less obstructed for fluid flow. Moreover, their absence reduces the potential seeding sites for cement, resulting in higher permeability of the cemented model outputs.

As the permeability of the synthetic *deposit* is so high, the permeabilities of the *cemented* synthetic samples are higher than values reported for the natural carbonates and also higher than the samples of the same rock type as is used in this thesis to generate the synthetic deposit (Figure 5.24). Eight reservoir samples of the same rock type as the sample used in modelling (yellow circles in Figure

5.24) have a mean porosity of 24.9% and a mean permeability of $1450mD$, while this study predicts a permeability of $13{,}000mD$ at this porosity (see equation 5.3).

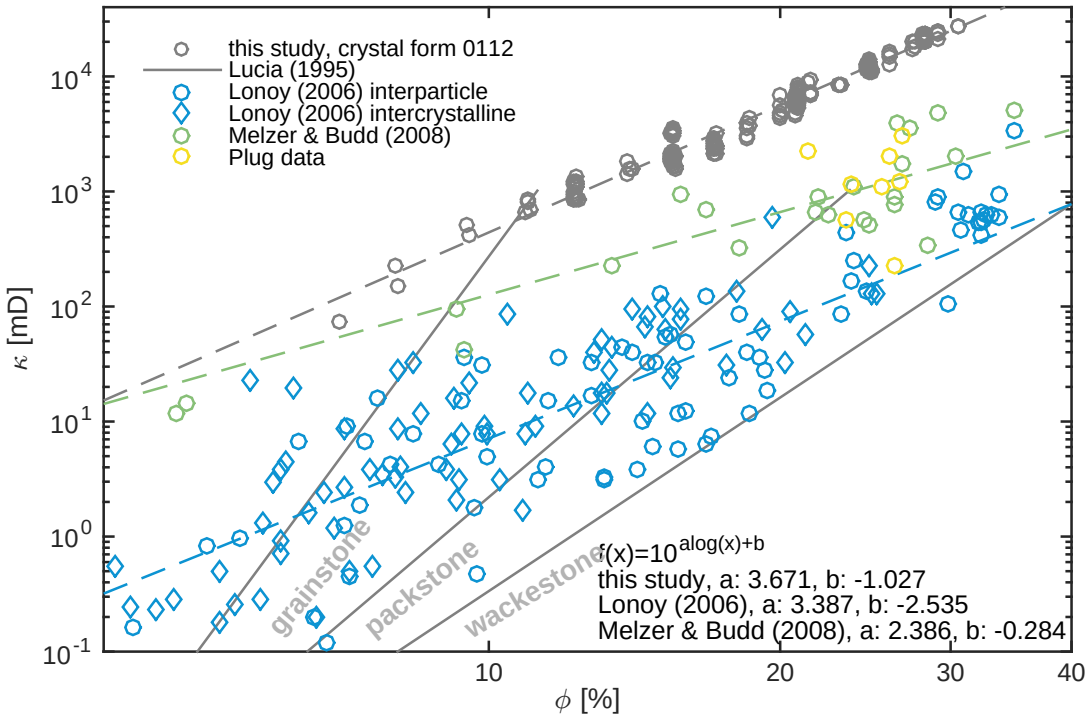

Figure 5.24: The synthetic poroperm data for the model outputs generated with the crystal form $01\bar{1}2$ (grey circles) and data obtained from literature: the divisions from the rock type classification by Lucia (1995) (grey lines), the macroporosity data from Lønøy (2006) (blue) both for the interparticle (circles) and the intercrystalline porosity (diamonds), the data for grainstones from Melzer and Budd (2008) (green circles) and the plug data derived for the same rock type as is used as the input in the study (yellow circles).

Another reason for the mismatch between the permeability of the cemented model outputs and the plug data is the difference in scale of the samples. The synthetic samples in the 3D modelling are $3mm^3$, while all the other data presented in Figure 5.24 are plug data derived for cm-scale samples (typically with a diameter of around $4cm$). There is an order of magnitude difference in these scales and, naturally, the larger scale samples have a potential of being more heterogenous. The synthetic samples generated here model a single highly permeable rock type.

It is not inconceivable that some *mm*-scale sub-samples of the plugs presented in Figure 5.24 are equally highly permeable and the fact that their permeability is much lower compared to model outputs is caused by the presence of less permeable layers in the plug. In short, plug samples capture more of the heterogeneity of the rock, including the less permeable layers, and this may be one of the reasons why the cementation model over-predicts the permeability of the plug data.

Upon the investigation of the *trend* in the poroperm results of the synthetic samples produced in this study, it can be concluded that their behaviour is very similar to the natural grainstones. The slope of the exponential fit to the interparticle and intercrystalline macroporosity data by Lønøy (2006) (blue line in Figure 5.24) is strikingly similar to the fit to the synthetic samples in this study (dashed grey line). The slope differs somewhat from the fit to the poroperm data for the cement-dominated grainstones analysed by Melzer and Budd (2008) (green line) but the classification by Lucia (1995) (grey lines) places the synthetic samples from this study in the grainstone sector of the poroperm.

It can be concluded that Calcite3D produces samples with permeabilities higher than in the typical natural media, which can be attributed mainly to the deficiencies of the *deposition* modelling methodology, which produced a synthetic deposit with unnaturally wide pores. However, the response of the synthetic deposit to cementation, which produces a similar poroperm trend as observed in the natural media, suggests that the *cementation* methodology is successful in modelling realistic *changes* in the cement volumes and in the pore space morphology.

Dependence on the sediment type

One goal of this study is to investigate the dependence of the permeability on the relative content of the monocrystalline grains. The 2D study suggests a strong dependence, as illustrated by a relatively high mean of slopes of the fit lines in

Figure 3.14 (0.053). However, the steepness of slopes is a result of a significant variability in the permeability for the synthetic samples of equal porosity, which in turn is an effect of the flow modelling in 2D.

In the 3D study, in the case of the crystal form $01\bar{1}2$, the dependence of the permeability on the monocrystalline grain content is subtle but clear, with the mean of the slopes equal to -0.00241 (Figure 5.15c). The mean of the slopes in the case of $40\bar{4}1$ is closer to horizontal (0.000111) and the synthetic data points are characterised by a much greater standard deviation of permeability, thus the dependence of the permeability on the monocrystalline grains content remains inconclusive.

Overall, the results of this study suggest that the composition of a carbonate deposit, i.e. the amount of the monocrystalline and polycrystalline grains in the sample, is a *weak* control on the final permeability of the sample under the early calcite cementation regimes investigated in this thesis. Additionally, the nature of the dependence of the permeability on the content of monocrystalline grins in a sample is controlled by the crystal form developed by syntaxial cement.

5.5 Conclusions

The work presented herein aims to examine the impact of the composition of a carbonate sediment, understood here as the ratio of the monocrystalline to polycrystalline grains, on the properties of rocks where early calcite cementation occurs. For that purpose a 3D model is developed which implements syntaxial cement growth on the monocrystalline grains and isopachous cement growth on the polycrystalline grains. This model is used to generate cemented samples based on a real rock deposit following the methodology detailed in Chapter 4. The synthetic samples are generated for two common crystal forms of calcite. The generated synthetic samples are analysed with respect to several quantities

of interest: the monocrystalline grain content, the relative volume of syntaxial cement, porosity, permeability, specific surface area and tortuosity.

The results demonstrate the effect of the competition of growing grains for the available pore space: the more monocrystalline grains there are in the sample, the stronger the competition is and the smaller the impact of each individual grain on the resulting early calcite cement volume or porosity.

The synthetic samples with syntaxial cements grown according to the more elongated crystal form $40\bar{4}1$ have porosity lower compared to the samples grown according to the more blocky crystal form $01\bar{1}2$ at the same monocrystalline grains content. The permeability at constant porosity is also higher for the synthetic samples with the crystal form $40\bar{4}1$. Additionally, samples with the crystal form $40\bar{4}1$ exhibit greater variability in the results due to the fact this rhombohedral form is more elongated and has a greater potential for producing larger volume of cement.

Concerning the synthetic samples produced using different crystal forms of calcite, the differences in the volume of the syntaxial cement and the porosity, arising from the difference in the shapes and volumes of the two crystal forms, are more pronounced in the 3D model results than in the 2D results. In the 3D model, the cements are 3-dimensional and their growth is not restricted to sections of the 3D medium where the grain seeding the cement is present.

The analysis of the permeability results as a function of the content of the monocrystalline grains yields the following phenomenological correlation for the synthetic samples with the crystal form $01\bar{1}2$:

$$log(\kappa) = -0.00241 \cdot \alpha_v + 0.073 \cdot \phi - 2.35 \tag{5.9}$$

where κ is the permeability in mD, α_v is the content of the monocrystalline grains in the sample by volume in %, and ϕ is the porosity in %. In the case of the synthetic samples generated with the use of the crystal form $40\bar{4}1$, the

dependence of the permeability on the monocrystalline grain content remains inconclusive.

The dependence of the permeability on the monocrystalline grains content is found weaker than in the 2D study. This may be attributed to the deficiencies of the 2D modelling methodology. The permeability results for some synthetic samples (particularly the low permeability ones) in the 2D study may be artificially low due to the modelling of the flow in the 2D. Additionally, the permeability of the synthetic samples with no isopachous cement or very thin isopachous cement fringes (which are typically high permeability) may be overestimated due to the fact that a post-processed porous medium with artificially separated grains is used. Both of these deficiencies lead to a higher range of permeabilities at any given porosity in the 2D modelling, and can lead to the dependence of the permeability on the sediment type being exaggerated.

The poroperm results in the 3D modelling ($10-30,000mD$) exhibit permeabilities above the range of these reported in the literature ($0.1-5000mD$) or the plug data of the samples used in modelling (porosity $22-27\%$, permeability $200-3000mD$), but the reason for that is the initial synthetic deposit, which has a very high permeability ($58,900mD$). However, the trend in the poroperm results closely resembles those reported in natural carbonate rocks.

Limitations and the next steps

Although we conclude that the *cementation* methodology is successful in modelling realistic changes in the cement volumes and in the pore space morphology, the *depositional* methodology is less successful in generating a synthetic deposit with realistic permeabilities. This will be addressed in further work, which will involve expanding the shape library used by the model to introduce less regular grain shapes. A methodology will be developed to optimise the parameters of the depositional model so that the 2D sections of the 3D medium more closely

resemble the characteristics of the 2D thin section images of the natural porous media.

Chapter 6

Calibrating Lattice Boltzmann Flow Simulations and Estimating Uncertainty in the Permeability of Complex Porous Media

Addressing the challenges in predictive computational modelling of rocks requires an interdisciplinary approach that blends scientific understanding and experimental data, fundamental theory, finely-honed algorithms (e.g. Lattice Boltzmann method), and high performance computing, such as the parallel implementation of the Lattice Boltzmann method on large scale architectures such as Cray XC30 of the UK National High Performance Computing Facility - Archer. Incorporating expert knowledge and experimental data, Bayesian inference stands amongst the prevalent uncertainty quantification and propagation techniques. It is used to quantify and calibrate uncertainty models in engineering simulations in order to achieve robust predictions of system performance and reliability.

Permeability results presented in Chapters 3 and 5 are produced via Lattice Boltzmann simulations and are used in order to gain intuition into the pore-scale

transport properties of rocks. The estimation of the impact of sediment type on permeability would benefit from quantifying the predictive envelope of the computational method. This chapter presents a framework, using state of the art methods of Bayesian inference, to obtain a predictive envelope on permeability predictions in cemented synthetic rocks. This framework is presented on the example of the Fontainebleau sandstone, as data for this rock are readily available.

6.1 Introduction

Lattice Boltzmann (LB) simulation is one of the main methods used to predict flow through porous materials (Chen and Doolen, 1998; Zhang *et al.*, 2002; Ma *et al.*, 2010; Kang *et al.*, 2010). Such simulations are often used to estimate particular quantities of interest concerning either the fluid flow or the porous medium. Amongst the most interesting flow properties in reservoir engineering (our current area of focus) is the permeability of porous subsurface rocks that contain fluid, and estimating permeability is important in a wide variety of other fields such as biology (Grodzinsky, 2011; de Monte *et al.*, 2013; Khaled and Vafai, 2003), medicine (Lorna J. Gibson, 2010; Sun *et al.*, 2007), soil science (Patrick A. Domenico, 1997; Zhang *et al.*, 2005) and material science (Gibson *et al.*, 2001; Beavers and Joseph, 1967; Camargo *et al.*, 2012; Ghassemi and Pak, 2011).

The LB method simulates fluid flow by using the Boltzmann equation to dynamically update the fluid density as described by a set of interacting particles. The method relies on several parameters, some physics-based and some algorithmic, which must be calibrated before using LB to predict quantities of interest. The calibration of LB models has commonly been achieved by comparing the velocity of fluid flow simulated through a specific pore shape to one predicted analytically by the Hagen-Poiseuille equation (Narváez *et al.*, 2010). The LB parameters are chosen to minimise the discrepancy of the flow profile that develops in specific pore sizes to corresponding theoretically predicted values. The deficiency of that

method is that in real media the permeabilities to be matched by LB come from laboratory experiments and the above theoretical value does not include any experimental uncertainty, nor does it necessarily relate to real pore geometries which often contain a distribution of pore shapes and sizes with complicated network connectivity.

This paper provides a more robust method to predict permeability in real porous media using LB. Our quantity of interest is the permeability of natural, complex porous media, and we show that the standard practice of calibrating LB to theoretical predictions for even an idealised, simple system results in significant uncertainties and model deficiencies. It appears that there has never been a thorough uncertainty quantification of the predictive accuracy of LB. We therefore perform a Bayesian calibration of the physical LB parameters as well as the model insufficiency parameters, using real permeability data in place of the standard theoretical velocities in an analytical pipe model. Our method of calibration is shown to provide more accurate simulations than the standard method for the real pore systems studied.

Herein we present a calibration framework for the most basic LB model that uses the Bhatnagar-Gross-Krook (BGK) collision model. It is known that the prediction of permeability using this single-relaxation-time LB model is sensitive to parameter τ. This is due to insufficient consideration of the boundary conditions (Pan *et al.*, 2006; Narváez *et al.*, 2010), as the bounce-back boundary rule imposes the location of the solid boundary which has a numerical error that depends on the parameter τ. Multiple-relaxation-time (MRT) or two-relaxation-time (TRT) LB models (Ginzburg, 2008; Ginzburg *et al.*, 2010; Hammou *et al.*, 2011) considerably reduce the dependence on parameter τ, but do not eliminate it completely (Pan *et al.*, 2006; Narváez *et al.*, 2010). We confirm the dependence of permeability on τ in flow simulations in natural porous media using the BGK-LB model. Rather than performing a purely model-based sensitivity study where the variability in the predictions based on the variation of the fluid viscosity via its numerical parameter τ would be investigated, we pursue a data-driven

approach using the full Bayesian framework. In further work we could apply the methodology developed here to the more complex TRT or MTR LB models.

We adopt a Bayesian framework for complex mechanical systems (Beck and Yuen, 2004b; Oden *et al.*, 2010; Yuen, 2010; Papadimitriou and Papadioti, 2013; Ma and Zabaras, 2011; Cheung *et al.*, 2011; Congedo *et al.*, 2012) to quantify and calibrate these parametric uncertainties based on experimental measurements of the pore size distribution in real samples and permeability measured in the same samples. Furthermore we propagate these uncertainties through LB simulations to make robust predictions of the relevant quantity of interest. We employ an enhanced parallel variant of the Transitional Markov Chain Monte Carlo (TMCMC) algorithm (Ching and Chen, 2007; Angelikopoulos *et al.*, 2012) to distribute the large number of LB runs in clusters with heterogeneous computer architectures (Hadjidoukas *et al.*, 2012). TMCMC is a parallel evolutionary sampling algorithm inspired by particle filtering that involves annealing and local Monte Carlo steps. Our results demonstrate the value of the Bayesian framework for LB simulations and provide credible uncertainty intervals for their predictions. We thus demonstrate that permeability predictions using current methods may suffer from significant, unquantified and unaccounted for uncertainties. We propose a semi-empirical way to calibrate BGK-LB parameters more robustly in future.

The paper is organised as follows: in Section 6.2 we outline the elements of LB simulation. Section 6.3 describes the real porous medium used, in this case a Fontainebleau sandstone. Section 6.4 presents a Bayesian framework in the context of our experimental and computational set-up. Results for the Bayesian calibration of LB parameters are given in Section 6.5. In Section 6.6 we elaborate on the significance of our results compared to existing methods and on the implications for the future use of LB. Our summary and conclusions are presented in Section 6.7.

6.2 Lattice Boltzmann (LB)

LB methods are a popular way to simulate fluid flow (Chen and Doolen, 1998; Zhang *et al.*, 2002; Ma *et al.*, 2010; Kang *et al.*, 2010; Boek and Venturoli, 2010) in many areas including material science (Ghassemi and Pak, 2011; Camargo *et al.*, 2012), hydrology (Zhang *et al.*, 2005), biology (Sun *et al.*, 2007) as well as the simulation of oil and gas behaviour in porous rock (Hazlett *et al.*, 1998; Coles *et al.*, 1996; Auzerais *et al.*, 1996; Jin *et al.*, 2004; Hao and Cheng, 2010). LB simulations of flow through pore geometries derived from real rocks have been used to estimate effective permeability (Gao *et al.*, 2012) or relative permeability (Ramstad *et al.*, 2010; Grader *et al.*, 2010), using microporous rocks (Jeong, 2010), sandstones (White *et al.*, 2006) (even the same Fontainebleau sandstone that we use in this study (Ferréol and Rothman, 1995)) and (typically with more complex porosity) carbonates (Grader *et al.*, 2010). Ever since computational power became sufficient to run LB on realistic simulations, this method has been a popular alternative to the direct solution of the Stokes equation. This is particularly true for complex, multi-scale media: direct numerical simulations using gridded methods require extremely refined grids to capture the small scale complexities and the definition of boundary conditions becomes cumbersome due to the complexity of the geometry, both of which lead to high computational cost of simulation.

LB methods represent the fluid as a large number of particles, and calculates the probability (density) of finding a given particle at a given position on a discrete lattice mesh. The algorithm consists of two steps: advection and collision. In the advection step the particles are propagated along their velocity vectors to adjacent lattice sites. In collision, the particles converging at each lattice site interact: they collide and are redistributed according to their velocities as follows. First the density ρ and the velocity vector u of the fluid at all points in the lattice are calculated. Then the average velocity and force terms are calculated and the equilibrium densities for each velocity vector are found. Finally collision

takes place in which the particle densities are adjusted through the fundamental equation of the BGK-LB model (Sukop and Thorne, 2006):

$$f_i(x + v_i\Delta t, t + \Delta t) = f_i(x, t) - \frac{1}{\tau}(f_i(x, t) - f_i^{eq}(x, t)) \tag{6.1}$$

where i denotes the direction of momentum, f_i is the directional density (probability density function (PDF) per unit space of a particle traveling in direction i), f_i^{eq} is the equilibrium PDF, t is simulation time, Δt is the simulation time step, x is the location of the particle in the lattice, v_i is the velocity of the particle in direction i, and τ is the relaxation time parameter that is related to kinematic viscosity ν through the relation (Breitmoser *et al.*, 2012)

$$\nu = \frac{\tau - 0.5}{3} \tag{6.2}$$

Although τ is linked to kinematic viscosity (Equation (6.2)) and thus may seem to be a model state, it is in fact a model parameter. Due to numerical stability issues, the value of τ which directly corresponds to the viscosity of the fluid of interest (e.g. water) cannot be used and a value for which computation is stable is used instead (Narváez *et al.*, 2010). Equation (6.2) then calculates permeability.

We perform LB simulations using the publicly available code LB3D v7.0, developed at University College London, University of Stuttgart and Eindhoven University of Technology (Breitmoser *et al.*, 2012). After Narváez *et al.* (2010) we use a computational domain composed of inlet (I), outlet (O) and the sample of interest (S), with a periodic boundary condition imposed on the inlet and outlet sides of the domain and bounce-back boundaries on the remaining sides (Figure 6.1). We investigate four cases of single phase flow: in Case 1 we aim to calibrate relaxation parameter τ to the Hagen-Poiseuille (HP) law using our Bayesian framework and the same simulation set-up as Narváez *et al.* (2010) with

pipe axes aligned in the z direction and varied widths $w = \{3, 4, 5, 6, 7, 12\}$. Domain dimensions in Figure 6.1 are defined as follows: $L_x = L_y = w + 2, L_S = 4w$, and $L_I = L_O = 3$. Case 2 takes into account the contribution of pores of different sizes to total error.

Cases 3 and 4 involve simulating flow through real rocks and calibration using real permeability data. In these cases we run the simulation on digital representations of cubic rock samples of dimension 100^3 lattice units (i.e. $L_x = L_y = L_S = 100$). We introduce inlet and outlet buffers of thickness $L_I = L_O = 10$, and forcing at the inlet cross section $C(1)$ (Figure 6.2). To avoid boundary issues we define the walls of the simulation domain that are parallel to the forcing direction to be solid. In each case we run LB simulations for 100000 time steps, at which point the properties of the simulations required to calculate permeability (velocity, density and pressure) become stable (Figure 6.3).

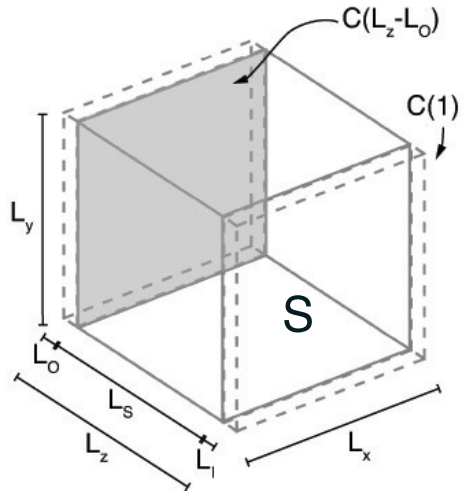

Figure 6.1: The computational domain of dimensions L_x, L_y and L_z consisting of the sample S (solid outline) of thickness L_S and inlet and outlet buffers (dashed outline) of thickness L_I and L_O. The buffers are introduced to avoid artefacts. The fluid is accelerated in the acceleration zone using body forces at the inlet cross section $C(1)$.

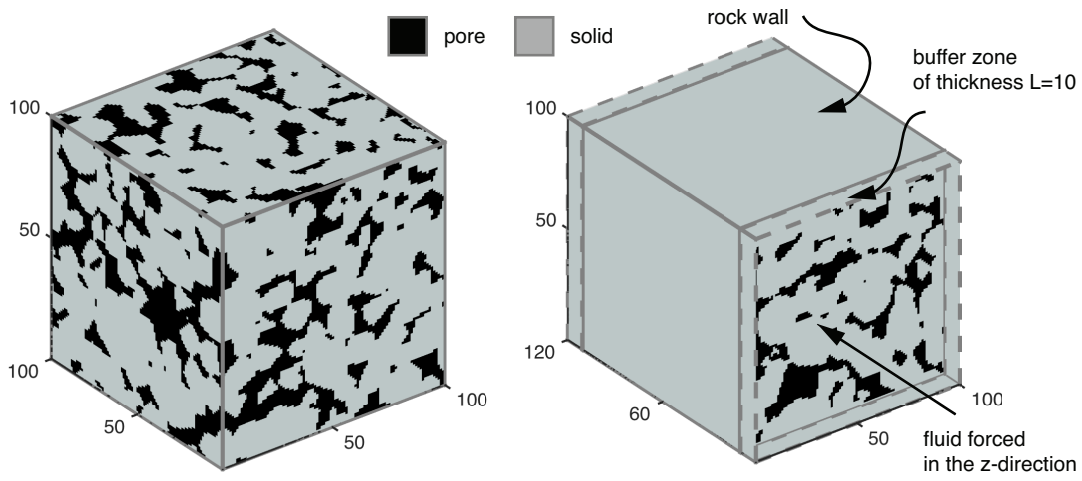

Figure 6.2: The computational domain in Cases 3 and 4. The Fontainebleau sandstone sample of dimensions 100^3 has buffer zones of thickness 10 attached to both walls perpendicular to the z-direction. The walls parallel to the fluid forcing direction are defined to be solid rock. The fluid is accelerated in the first layer ($z = 1$) of the inlet buffer.

The permeability κ is calculated using Darcy's law:

$$\kappa = -\eta \frac{\langle v_z \rangle_S}{\langle \nabla p_z \rangle_{P \cap S}} \tag{6.3}$$

where η is the dynamic viscosity, $\langle v_z \rangle_S$ is an average over the sample S of the components of the fluid velocity parallel to the overall flow direction, and $\langle \nabla p_z \rangle_{P \cap S}$ is the pressure gradient in the pore space P of sample S in the direction of the flow. The dynamic viscosity is $\eta = \nu \langle \rho \rangle_{P \cap S}$, where ν is as defined in Equation (6.2), and P is the set of pore grid points of the simulation domain, and $\langle \rho \rangle_{P \cap S}$ is the average density of the fluid in the volume of the pore space of the sample.

Following Narváez *et al.* (2010) we make an approximation of the average fluid density using just two cross sections through the sample. This is justified by the fact that after a long simulation the values of density fall uniformly across the

pores of the sample. We use an average of the values in the inlet cross section $C(L_I + 1)$ and the outlet cross section $C(L_z - L_O)$, so:

$$\langle \rho \rangle_{IO} \approx \frac{\langle \rho \rangle_{C(L_z - L_O) \cap P} + \langle \rho \rangle_{C(L_I + 1) \cap P}}{2} \tag{6.4}$$

where we define $IO = (C(L_z - L_O) \cup C(L_I + 1)) \cap P$ which is the pore space in the inlet and outlet cross-sections. Similarly, the average pressure drop across the sample is approximated using the same two cross sections:

$$\langle \nabla p_z \rangle_{IO} \approx \frac{\langle p_z \rangle_{C(L_z - L_O) \cap P} - \langle p_z \rangle_{C(L_I + 1) \cap P}}{(L_S - 1)} \tag{6.5}$$

Due to the fact that the velocity of fluid varies inside the sample and depends on pore geometry and topology, we calculate average velocity $\langle v_z \rangle_S$ by dividing the sum of all velocity components in the direction of the flow across the entire sample S by the volume of the sample.

6.3 Porous media

The porous medium we use for Cases 3 and 4 is derived from 3D micro computed tomography (microCT) of a sample of Fontainebleau sandstone obtained at the Institute for Computational Physics of the University of Stuttgart (http://www.icp.uni-stuttgart.de/microct/) (Hilfer and Zauner, 2011). We use a 100^3 sub-image of the full image with voxel resolution of $14.6 \mu m$.

Since the microCT images are monochromatic (in this case their voxel values are within a range between 0 and 216) as illustrated in Figure 6.4, we must binarise the images into either solid or void before we can use them for LB simulations. Binarisation defines all voxels with monochromatic value less than a threshold to be pore space or void, and the rest to be solid. Figure 6.4 illustrates how

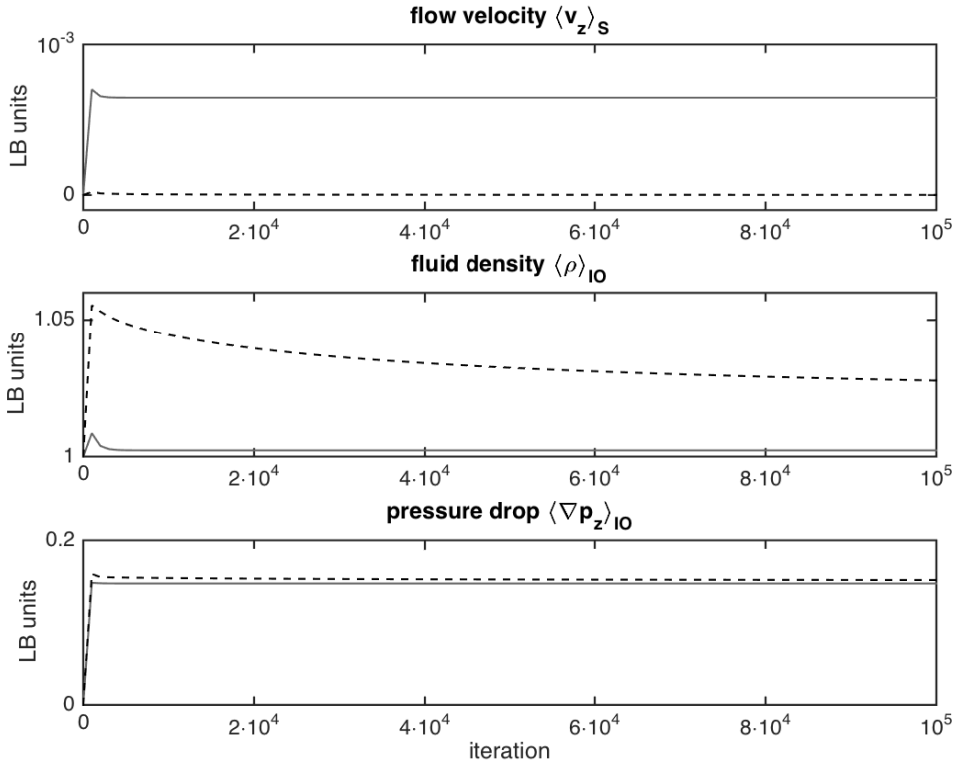

Figure 6.3: Outputs of the LB simulation used to calculate permeability shown throughout the run with $\tau = 0.6$ (100000 iterations): solid - high porosity (21.2%) sample, dashed - low porosity (6.2%) sample. From top to bottom we have average flow velocity in the direction of fluid forcing averaged over the volume of the entire sample - $\langle v_z \rangle_S$, the approximated average fluid density in the pores of the sample calculated using the inlet and outlet cross sections - $\langle \rho \rangle_{IO}$, and pressure difference between the inlet and outlet walls of the sample - $\langle \nabla p_z \rangle_{IO}$. All outputs are in dimensionless LB units.

choosing a higher threshold value results in a higher porosity sample than a lower threshold.

In our calibration method we investigate the porosity-permeability curve, so we need several samples of varied porosity. To obtain these we binarise the microCT image using eight different thresholds (6, 36, 66, 96, 126, 156, 186 and 216) to arrive at binarised representations with different porosities (6.2, 8.3, 9.8, 11.2, 12.7, 14.4, 16.4 and 21.2 percent, respectively). Figure 6.5 depicts these results, and Figure 6.6 illustrates that the corresponding porous media are complex and multiscaled as pore sizes range over an order of magnitude in all cases.

We are aware that the way we obtain samples of varying porosity by changing the binary threshold is not equivalent to obtaining samples in which differences in porosity arise from different stages of natural processes (i.e. diagenesis). However, the process of binarisation at different thresholds implemented here can be considered as a proxy for cementation. Greyscale values in the image change gradually from a grain (white, maximum pixel value of 216) to a pore (black, minimum pixel value of 0), therefore as the binarisation threshold is decreased the grains are progressively being 'overgrown' with more solid voxels (a proxy for cement). This results in overall porosity of the rock decreasing with the threshold of binarisation, e.g. threshold of 186 results in a porosity of about 17%, while threshold of 156 results in more 'cement' overgrown around the grains and a porosity of 15% (Figure 6.4). In this way the samples binarised at different thresholds maintain topologies similar to samples of Fontainebleau sandstone at different porosities.

6.4 Bayesian framework

We now present an overview of the Bayesian framework for model-based uncertainty quantification that we use herein. We start with the general formulation

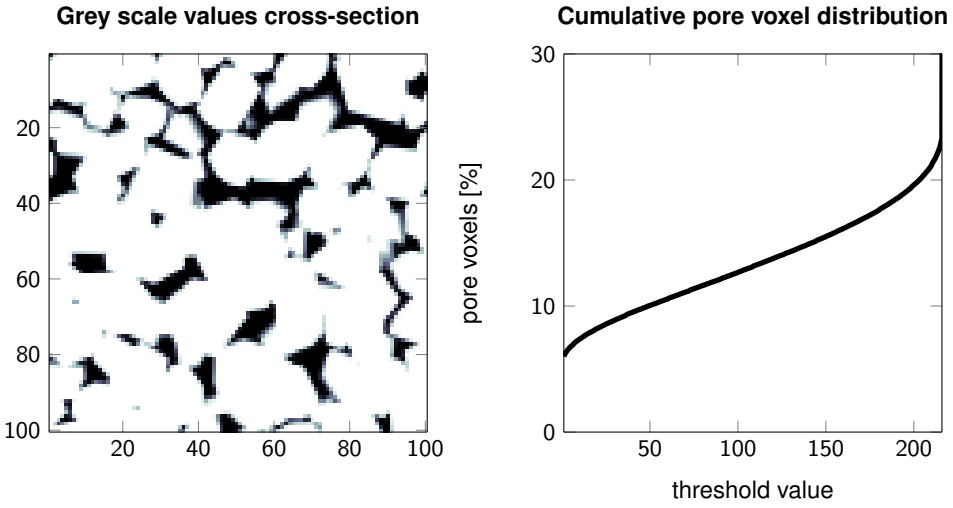

Figure 6.4: Slice through microCT image of Fontainebleau sandstone in grey scale (left). Cumulative percentage of pore voxels in a 3D sample of size 100^3 (right): the smaller the threshold we choose for binarisation (x-axis), the smaller the proportion of pore-voxels in the binarised medium (proportion of voxels on y-axis is equivalent to resultant porosity).

and continue with case-specific adaptations. Table 6.1 contains a summary of all variables.

6.4.1 General Bayesian formulation

Consider a class of models M which in our case will be the set of all LB models considered. Individual models within that class are assumed to differ due to variations in a set of parameters $\underline{\theta}$. Our goal is to use both data from empirical laboratory experiments or analytical calculations, and any other information available that is independent of the data (so-called *prior* information), to constrain appropriate values for $\underline{\theta}$.

In a Bayesian framework (Beck and Katafygiotis, 1998; Katafygiotis and Beck, 1998), the uncertainty in parameters $\underline{\theta}$ of model class M is quantified with a prior probability distribution function (PDF) $\pi(\underline{\theta}|M)$ which is updated with

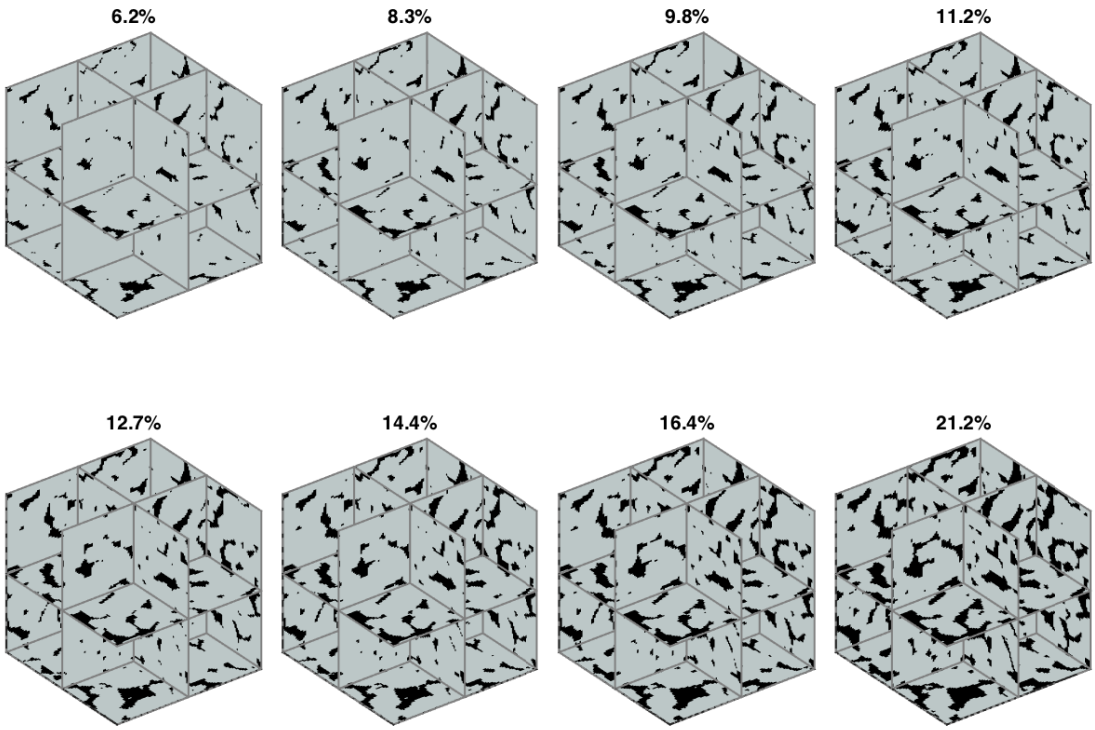

Figure 6.5: Slices through 3D microCT images of Fontainebleau sandstone of dimension 100^3 and resolution 14.6μm. The same sample binarised at eight different thresholds creates samples with eight different porosities: 6.2, 8.3, 9.8, 11.2, 12.7, 14.4, 16.4 and 21.2 percent. Dark indicates pore space and light grey indicates solid.

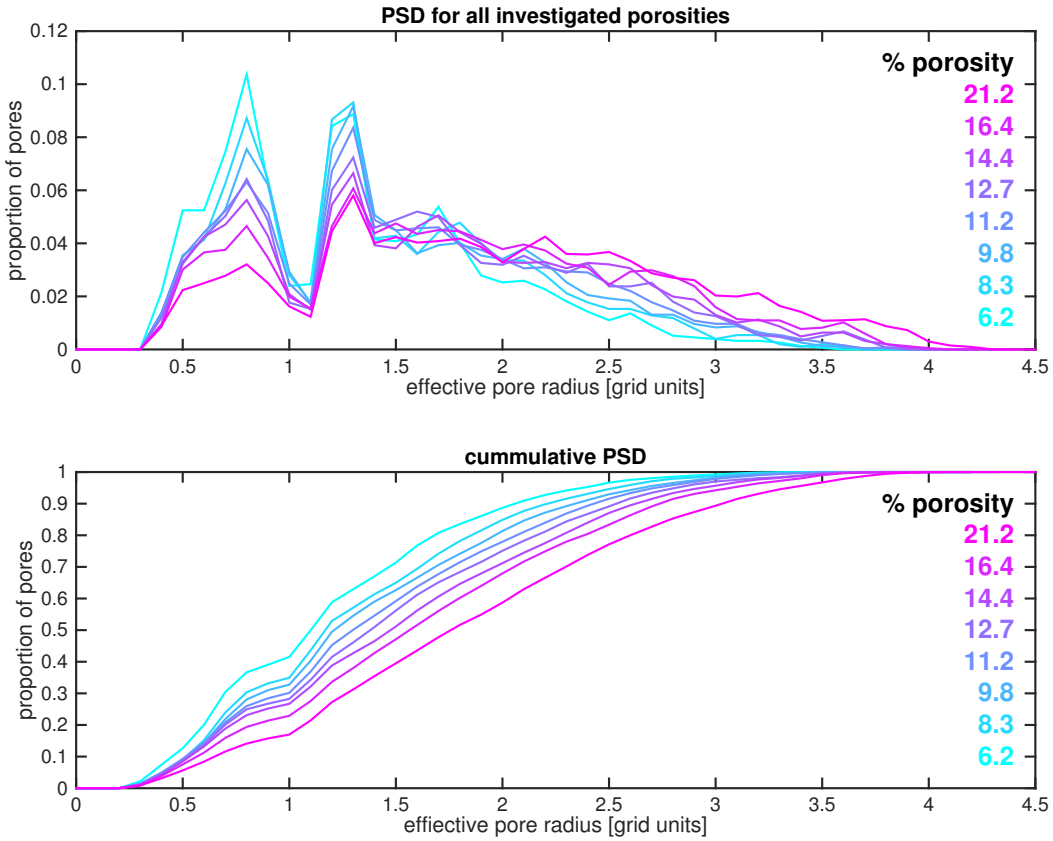

Figure 6.6: Effective pore size distribution (PSD) functions (top) and their cumulative distributions (bottom) for the microCT image of Fontainebleau sandstone binarised at eight different threshold values. The effective pore diameters, defined as the maximum diameter of a sphere that fits inside the pore, were calculated using the methods described in Bhattacharya and Gubbins (2006).

Table 6.1: Variables used in the Bayesian formulation.

General formulation

$\underline{\theta}$	Model parameter set
M	LB model class
$\pi(\cdot)$	Prior PDF
$p(\cdot)$	Posterior PDF
$\underline{D}$	Measured data
$\underline{f}$	Model predictions
$\underline{e}$	Prediction error
n	Number of observations (measurements)
$J(\cdot)$	Weighted measure of fit between the model predictions and measured data
Σ	Covariance matrix of the error term
Q	Quantity of interest
N	Number of TMCMC samples

Case-specific formulation

$\underline{\theta} \equiv \tau$	LB model temporal relaxation parameter
$Q \equiv \kappa$	Permeability (κ) is the quantity of interest in all cases
$\underline{f_\kappa}$	Model predictions: permeability predicted in LB simulation
$\underline{D_{\kappa,A}}$	Measured data: analytically obtained permeability of a pipe of square cross-section in Cases 1 and 2
$\underline{D_{\kappa,E}}$	Measured data: experimentally derived permeability of Fontainebleau sandstone in Cases 3 and 4
w	Pipe width (size) in Case 2
σ_w^2	Variance of uncertainty on pore size w in Case 2
$g(w)$	Functional form of the weight variance in Case 2
$d(w)$	Pore size distribution in Case 2
ϕ	Porosity

information from data $\underline{D}$ to give the so-called *posterior* PDF $p(\underline{\theta}|\underline{D}, M)$ according to Bayes rule:

$$p(\underline{\theta}|\underline{D}, M) = \frac{p(\underline{D}|\underline{\theta}, M)\ \pi(\underline{\theta}|M)}{p(\underline{D}|M)} \tag{6.6}$$

Here $p(\underline{D}|\underline{\theta}, M)$ is the *likelihood* of observing data $\underline{D}$ within the model class considered given a particular set of parameter values $\underline{\theta}$, and $p(\underline{D}|M)$ is the so-called *evidence* or estimate for the model class as a whole being appropriate to represent data $\underline{D}$. This evidence is given by the multi-dimensional marginal integral of the numerator over the space of all possible LB model parameter values:

$$p(\underline{D}|M) = \int_{\underline{\theta}} p(\underline{D}|\underline{\theta}, M)\pi(\underline{\theta}|M)d\underline{\theta} \tag{6.7}$$

The prior PDF $\pi(\underline{\theta}|M)$ of the model parameters incorporates all available information on the uncertainty of the model parameters before data $\underline{D}$ is taken into consideration. This may derive from previous experience in other modelling exercises, from mathematical knowledge (of convergence criteria of underlying equations, for example), or from any other relevant source. It could be obtained and parametrised by expert elicitation (O'Hagan *et al.*, 2006; Curtis and Wood, 2004), by literature surveys, or by conducting independent modelling tests.

Assuming that the model predictions $\underline{f}(\underline{\theta}|M)$ and the measurement data $\underline{D}$ satisfy the model prediction equation

$$\underline{D} = \underline{f}(\underline{\theta}|M) + \underline{e} \tag{6.8}$$

where the prediction error $\underline{e}$ (accounting for measurement, computational and modelling inadequacy) is normally distributed with zero mean and covariance matrix Σ, the likelihood $p(D|\underline{\theta}, M)$ is given as (Beck and Yuen, 2004b)

$$p(\underline{D}|\underline{\theta}, M) = \frac{|\Sigma(\underline{\theta})|^{-1/2}}{(2\pi)^{n/2}} \exp\left[-\frac{1}{2}J(\underline{\theta}; M)\right] \tag{6.9}$$

where

$$J(\underline{\theta}; M) = [\underline{D} - \underline{f}(\underline{\theta}|M)]^T \Sigma^{-1}(\underline{\theta})[\underline{D} - \underline{f}(\underline{\theta}|M)] \tag{6.10}$$

is the weighted measure of fit between the system model predictions and the measured data, $|\cdot|$ denotes determinant, and the parameter set $\underline{\theta}$ is augmented to include parameters that can be used to describe values of the covariance matrix Σ.

One of the key parameters to be identified within a BGK-LB simulation is the relaxation rate τ in Equation (6.1). In this work we concentrate on calibrating that parameter in four ways: Cases 1 and 2 use the Hagen-Poiseuille law, where data $\underline{D}$ is the analytically derived permeability $\underline{D_{\kappa,A}}$ in a pipe of square cross-section; Cases 3 and 4 both use experimental permeability data for Fontainebleau sandstone $\underline{D_{\kappa,E}}$, the distinction between them being that Case 3 is porosity-independent and Case 4 is porosity-dependent.

6.4.2 Bayesian formulation for calibration using Hagen-Poiseuille (HP) law (Cases 1 and 2)

When calibrating BGK-LB models using the Hagen-Poiseuille law we follow the steps of Narváez *et al.* (2010) and simulate the flow in a single open-ended pore of square cross-section (a pipe). We perform six LB simulations for pipes of various widths (3, 4, 5, 6, 7 and 12 lattice units). These widths are within the range of the pore widths typical for Fontainebleau sandstone. Figure 6.6 shows that the pore diameters range from 1 to 9 grid units for all investigated porosities. In each case the permeability derived from LB is compared with the analytically obtained permeability in a pipe of square cross-section calculated using the Hagen-Poiseuille law (Narváez *et al.*, 2010):

$$\underline{D_{\kappa,A}}(w) = \lim_{m\to\infty} \frac{w^2}{4}\left(\frac{1}{3} - \frac{64}{\pi^5}\sum_{n=0}^{m}\frac{tanh\left((2n+1)\frac{\pi}{2}\right)}{(2n+1)^5}\right) \tag{6.11}$$

In this calibration we treat the pore size w as a model state rather than a model parameter. In this case the prediction error equation (6.8) which quantifies the discrepancy between the LB predictions of the permeability for each state w has the functional form $\underline{f}(\underline{\theta}|M) \equiv \underline{f_\kappa}(\tau; w)$ and the theoretically calculated values $\underline{D} \equiv \underline{D_{\kappa,A}}$ are given by

$$\underline{D_{\kappa,A}} = \underline{f_\kappa}(\tau; w) + \underline{e} \tag{6.12}$$

where $e \sim N(0, \sigma_w^2)$ and the variance of the error is some function $\sigma_w^2 = g(w)$ of the width w of the pipe.

In general we identify three separate possible sources of uncertainty within the term $\underline{e}$: experimental uncertainty σ_{exp}^2, sampling uncertainty $\sigma_{time-sample}^2$ and model error σ_{model}^2. The overall uncertainty associated with each size w of the pore (Beck and Katafygiotis, 1998) is then

$$\sigma_w^2 = \sigma_{exp}^2 + \sigma_{time-sample}^2 + \sigma_{model}^2 \tag{6.13}$$

Recall that the values $\underline{D_{\kappa,A}}$ as dictated from Hagen-Poiseuille flow are analytically derived. Thus, in cases 1 and 2 there is no error associated with experimental measurements ($\sigma_{exp}^2 = 0$). Furthermore, the sampling uncertainty in the case of LB is negligible, as the model reaches a steady equilibrium with minute fluctuations at steady state after $O(10^5)$ steps. This can be viewed in Figure 6.3 which shows the convergence of the system properties throughout a typical LB run. Hence $\sigma_{time-sample}^2 \simeq 0$.

However, there is uncertainty associated with the inadequacy of the class M of BGK Lattice Boltzmann models to capture the theoretical values accurately (as LB is only a computational model). As a result of the first 2 components being negligible, the overall error for each width of the pipe σ_w^2 is the model error, that is $\sigma_w^2 \simeq \sigma_{model}^2$.

We investigate 2 ways of calculating the model error. The more straightforward

(Case 1) treats all six considered pore sizes (3, 4, 5, 6, 7 and 12) equally, and the error is described with the formula:

$$\sigma_w^2 = g(w) = \frac{1}{6}\sigma^2 \tag{6.14}$$

where σ is a constant that is to be estimated and $\frac{1}{6}$ is the weight normalising factor (introduced so that the sum of the weights for the six pore sizes is equal to 1).

The other approach (Case 2) is inspired by the fact that eventually we will apply the calibrated LB model to multi-scaled porous media and therefore we would like to allow that each pore size may contribute differently towards the final error estimate of the LB simulation. For example, smaller pores may be more poorly represented in cell-based discretisations such as those in Figure 6.5. Also, the rock is a collection of interconnected pores of multiple sizes (Figure 6.6) and it seems likely that a pore size that appears more frequently might contribute more towards errors in the model result than pore sizes that do not occur so frequently.

Let us consider a simple porous structure: a pipe with diameter 10 and length 100 lattice units. The pore size distribution of this structure consists of 100% of large pores and the permeability of such a structure is very high. On the other hand, consider the same pipe with a planar blockage of thickness 1 lattice unit across the end, but where that blockage has a single hole of width 1 through the middle of it. The pore size distribution by volume now includes 99.9% of large pores and 0.1% of small pores. We have changed the pore size distribution only slightly, but the permeability of the porous medium drops dramatically; the single small pore therefore has an impact on permeability much greater than could be inferred from its representation in the pore size distribution alone. The smaller the cross-sectional area of the small pore, the greater its curbing of permeability. Similarly, in a complex multiscale porous medium, fluid usually flows through multiple passages along any overall flow path and it is the cross-sectional area of the narrowest part of such passages that controls the passage flux.

Given the above physical arguments we expect the uncertainty associated with pores of width w to increase with the number of such pores and to decrease with increasing pore cross-sectional area. We therefore use the following ansatz for the uncertainty contribution from pores of width w:

$$\sigma_w^2 = g(w) = \frac{1}{\sum_w \frac{d(w)}{w^2}} \cdot \frac{d(w)}{w^2} \cdot \sigma^2 \tag{6.15}$$

where $d(w)$ is the normalised frequency of occurrence of pore size w in the porous medium. The weight normalising factor (first term on the right in Equation (6.15)) is equal to the reciprocal of the sum of weighting factors $\frac{d(w)}{w^2}$ for all considered pore sizes w.

The pore size frequency distribution is estimated using a publicly available code developed by Bhattacharya and Gubbins (2006). We calculate the effective pore size distribution (the maximum diameter of a spherical particle which fits inside the pore) in lattice units for all eight realisations of different porosity of the Fontainebleau sample (Figure 6.6) and use the average of the eight curves as $d(w)$. The weights we obtain for pore sizes 3, 4, 5, 6, 7 and 12 are 0.777, 0.133, 0.060, 0.022, 0.007 and 0.0003 respectively. The mismatch between permeability derived theoretically and permeability derived through LB simulation for most values of τ is greater for smaller pore sizes (Narváez *et al.*, 2010) so giving them largest weights will increase the resulting estimate of overall uncertainty of the prediction.

We define the covariance matrices Σ_1 and Σ_2 (the subscripts indicate case number) in Equation (6.10) to be diagonal matrices containing the entries of Equations (6.14) and (6.15) respectively on their diagonals, that is $\Sigma_{1,ii} = \frac{1}{6}\sigma_{w_i}^2$ and $\Sigma_{2,ii} = \frac{1}{\sum_{w_i} \frac{d(w_i)}{w_i^2}} \cdot \frac{d(w_i)}{w_i^2} \cdot \sigma_{w_i}^2$, where entry i on the diagonal corresponds to one of the six pipe widths w_i (3, 4, 5, 6, 7 or 12 lattice units).

6.4.3 Bayesian formulation for calibration using permeability data (Cases 3 and 4)

Cases 3 and 4 demonstrate Bayesian calibration of the LB model for flow in porous media given experimentally measured permeability data. The data $\underline{D} \equiv \underline{D_{\kappa,E}}$ used in these Case 3 is the porosity-permeability relationship of the Milly la Foret 'normal' Fontainebleau sandstones from Zinszner and Pellerin (2007) (shown in Figures 6.9 and 6.10). The covariance matrix Σ_3 that enters the likelihood formulation in Equation (6.10) then contains several contributions, some of which differ from those in Cases 1 and 2. The first contribution is the experimental uncertainty in the data (σ^2_{exp}): this consists of the uncertainty in the exact permeability of the rock sample given the experimental error involved in measuring permeability $\sigma^2_{measure}$, as well as the effect of anisotropy in the rock which results in differences in permeability depending on the flow direction $\sigma^2_{anisotropy}$ (Zinszner and Pellerin, 2007). Our source of experimental data provides only one permeability value per sample and does not explicitly take the direction of flow into account. We make an estimate of this anisotropy uncertainty of 10% of the nominal value of permeability: this is based on LB flow simulations using the three possible cube face pairs of the porous media sample as inflow and outflow boundaries, and comparison of the resulting permeabilities in the three directions.

A further component of the experimental error stems from the fact that, even though Fontainebleau sandstone is fairly homogenous, there is variability in the measured permeability depending on the sample of the rock that we extract. The variability stems both from the size of samples and from the location of samples in the bigger block of rock. LB simulations in this study are performed on cubic samples of edge length about 1.5mm. The permeability measurements were done on cylindrical plugs with a diameter 40mm and length 40-80mm (Zinszner and Pellerin, 2007). There is a discrepancy arising from the smaller scale of the sub-samples in which flow is simulated. We performed a test for sub-sample sizes from 60^3 to 280^3 voxels and confirmed that there is variability in permeability

depending on the sub-sample size. The other variability component comes from sub-sample location: different similarly sized sub-samples of a rock sample can have different permeability, even if their porosity happens to be the same or very similar. We combine both of these uncertainties into $\sigma_{rock-sample}$. Since our inference method relies on TMCMC sampling which in turn translates to numerous LB runs, we limit the sample size to control the computational cost to a size of 100^3 for which we estimate $\sigma_{rock-sample}$ of 10% based on our tests.

Similarly to Cases 1 and 2 we have $\sigma^2_{time-sample} \simeq 0$ and the final contribution encompasses the remaining unexplained model error. The overall uncertainty is then:

$$\Sigma_{3,ii} = diag(\sigma^2_{measure,i} + \sigma^2_{anisotropy,i} + \sigma^2_{rock-sample,i} + \sigma^2_{model}). \tag{6.16}$$

The final term pertaining to the model error is assumed to be constant for all permeabilities.

As an extension to the above, in Case 4 we make a porosity-dependent calibration where we include an independent $\tau(\phi_i)$ parameter for LB simulations on samples of different porosities. We couple them using the prediction error equation (6.8). In order to obtain a mean value and experimental uncertainty for each porosity we bin the measured values from Zinszner and Pellerin (2007) around the chosen porosities, which results in each having multiple measurements. Thus Case 4 augments the number of unknowns to nine, as the relaxation rates are different for each of the eight porosities (6.2, 8.3, 9.8, 11.2, 12.7, 14.4, 16.4 and 21.2 percent). That is, when data $D \equiv \underline{D_{\kappa,E}}$ is derived experimentally,

$$\underline{D_{\kappa,E}} = \underline{f_\kappa}(\tau_i|M) + \underline{e} \tag{6.17}$$

where $\underline{e} \sim N(0, \Sigma_4)$, and Σ_4 is defined in (6.16). The individual relaxation rates per porosity are now coupled via the prediction error $\underline{e}$ through Equation (6.8).

6.4.4 Priors on τ and σ

Regarding the priors for the model parameter τ, we assume a uniform prior truncated at bounds $\tau = 0.5$ and $\tau = 1.5$, where the simulation is known to be numerically unstable or computationally impractical. This distribution includes the value of 1.0, routinely used in BGK-LB simulations, as well as the value of 0.857 which is reported by Narváez *et al.* (2010) to yield the best result of permeability for Poiseuille flow in a quadratic pipe. We also assume uniform priors on σ, truncated at bounds $\sigma = 0.001$ and $\sigma = 10.0$.

6.4.5 Uncertainty propagation for robust posterior predictions

To obtain the marginal posteriors $p(\tau|\underline{D_{\kappa,A}})$ in Cases 1 and 2 and $p(\tau|\underline{D_{\kappa,E}})$ in Cases 3 and 4 we marginalise the joint posterior of the physical parameter τ with respect to the prediction error parameters. The marginalisation integrals are performed using kernel density estimates of the posterior samples, as produced from the last stage of the TMCMC algorithm (Ching and Chen, 2007; Angelikopoulos *et al.*, 2012).

Robust posterior prediction of the output quantity of interest Q (in our case it is the permeability κ) is obtained by taking into account the posterior uncertainties in the model parameters given the measured data D (Papadimitriou *et al.*, 2001). We define $F_Q(Q|\underline{\theta}, M)$ to be the conditional cumulative distribution of Q given the model parameters $\underline{\theta}$ and the BGK Lattice Boltzmann model M. The posterior estimate is generally formulated as follows (Angelikopoulos *et al.*, 2012; Papadimitriou *et al.*, 2001)

$$\bar{\mu}_Q \approx \frac{1}{N} \sum_{i=1}^{N} \mu_Q \left(\underline{\theta}^{(i)}; M \right) \tag{6.18}$$

(where N is the number of TMCMC samples) and the posterior variance

$$\bar{\sigma}_Q^2 \approx \frac{1}{N}\sum_{i=1}^{N}\sigma_Q^2(\underline{\theta}^{(i)};M) + \frac{1}{N}\sum_{i=1}^{N}\left[\mu_Q(\underline{\theta}^{(i)};M) - \bar{\mu}_Q\right]^2 \tag{6.19}$$

of the output Q, where $\underline{\theta}^{(i)}$ are taken from the posterior distribution of $\underline{\theta}$ given D. The posterior PDF in (6.6), the posterior mean in (6.18) and the posterior variance in (6.19) constitute robust measures of uncertainty of Q given the models and the data, taking into account the modelling and parametric uncertainties. The coefficient of variation $COV(Q)$, defined as the ratio of the standard deviation $\bar{\sigma}_Q$ to the posterior mean value $\bar{\mu}_Q$, constitutes an alternative measure of the uncertainty in Q.

6.5 Results

In Table 6.2 we summarise the three inference campaigns and some computational details. Each of the four TMCMC sampling campaigns had a significant computational cost. Each LB simulation for the eight samples that occurs in the posterior formulation has a time to solution of around 2 hours running on 64 cores. In order to make the sampling campaign feasible, a significant portion of the κ predictions was replaced by Kriging meta-models using the ideas described in Angelikopoulos *et al.* (2012). We ran simulations for several values of parameter τ for each sample and due to the smoothness of the $\kappa(\tau)$ curves (Figure 6.7) we were able to estimate the permeability prediction for τ values in-between the simulations we ran. This resulted in a substantial reduction in the computational cost (by 92%).

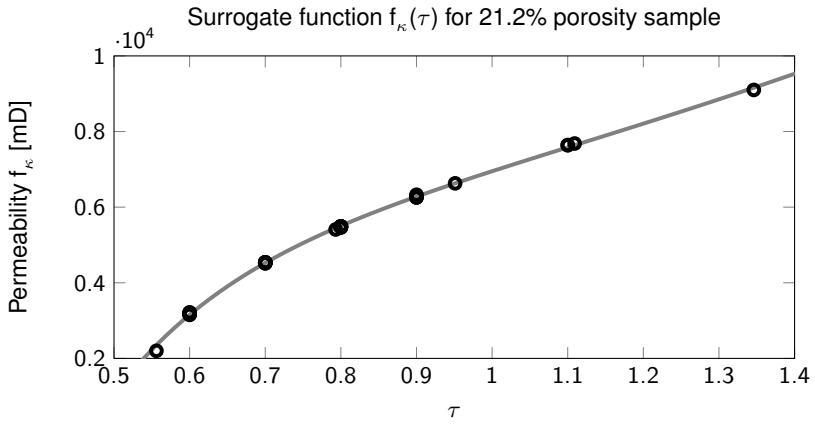

Figure 6.7: The circles represent the LB runs we performed for the sample of porosity 21.2% and the grey curve represents the best fit to the points that we have used as a surrogate meta-model to predict permeabilities of this sample for a large number of τ values without the computational cost of running the LB simulation.

Table 6.2: Summary of the four Bayesian inference campaigns presented in the results section.

Case	Data Source	Params	TMCMC Samples (N)	CPU-hrs [1]
1	HP permeability	(τ, σ^2)	30,000	120,000
2	HP permeability	(τ, σ_w^2)	30,000	120,000
3	Fontainebleau permeability	(τ, σ^2)	35,000	210,000
4	Fontainebleau permeability	$(\underline{\tau}, \sigma^2)$	35,000	250,000

[1] As recorded in simulations performed using the UK National Supercomputing Service Archer.

Table 6.3: Results of τ calibration for the four cases.

Case	Prior τ	Maximum-a-posteriori τ	Posterior mean τ	Coeff. of variation u
1	$C_1 \cdot U(0.5, 1.5)$[1]	0.949	0.947	3.5%
2	$C_2 \cdot U(0.5, 1.5)$	0.906	0.892	7.5%
3	$C_3 \cdot U(0.5, 1.5)$	0.661	0.667	5.3%
4	$C_4 \cdot U(0.5, 1.5)$	$\tau(\phi) = -1.047\phi + 0.804$	multiple	multiple

[1] C_1, C_2, C_3 and C_4 are normalising constants.

6.5.1 Uncertainty quantification and propagation using HP (Cases 1 and 2)

In Cases 1 and 2 we use the theoretical formulation of the HP flow through a narrow pipe to infer the posterior PDF of the τ parameter of LB, and we propagate this uncertainty to permeability predictions. We use 5000 samples per TMCMC stage, for a total of 30000 samples, following six stages until convergence.

To compare the two models we determine the Bayes factor $K = \frac{p(D|M_2)}{p(D|M_1)}$, where $p(D|M_i)$ is the posterior probability of observed data D given model M_i, or model evidence; M_1 is the error model in Case 1 and M_2 is the error model in Case 2. The model evidence in Cases 1 and 2 is 0.72 and 19.48 respectively, which gives a Bayes factor of 27.0 and points to M_2 being significantly more strongly supported by the data than M_1 (Beck and Yuen, 2004b).

The posterior PDF $p(\tau|\underline{D_{\kappa,A}})$ in each case is estimated using kernel density estimates from the 5000 samples of the last sampling stage, and is presented in Figure 6.8 (solid curves). The most probable value of τ in Case 1 is 0.949 and in Case 2 it is 0.906 (Table 6.3). Both are somewhat higher than the value of 0.857 suggested in the literature (Narváez *et al.*, 2010). The associated

coefficient of variation (standard deviation divided by mean) of τ are 3.5% and 7.5% respectively. The distribution in Case 1 has a well pronounced symmetrical peak and in Case 2 is skewed slightly towards higher values with a tail towards lower values to accommodate predictions of all pore sizes.

Using the final 5000 samples we predict the permeability using Equations (6.18) and (6.19). We propagate the results using porous media in Figure 6.5 in order to test whether the so-calibrated LB model can accurately predict permeability for different porosities. The results for Case 1 are summarised in Figure 6.9 and for Case 2 in Figure 6.10.

The predictions of permeability are quite similar for the two HP cases. The 95% and 50% credibility intervals (shaded areas), defined as ranges of values with 95% and 50% probability respectively of the predicted value falling within the interval, are considerably wider in Case 2. This reflects the fact that this model endeavours to capture a range of pore sizes.

Our result in Case 1 suggests that the BGK-LB model cannot quantitatively capture the experimental permeability values. The result in Case 2 suggests that the LB model can capture the experimental permeability only for low porosities (< 0.12). For higher values predicted permeability lies well outside of the 95% credibility interval, demonstrating the model deficiency in this porosity regime. This over-estimation of the permeability in the LB simulation for even these relatively simple naturally porous sandstones is alarming, as it throws into question the method's applicability to realistic media.

6.5.2 Uncertainty quantification and propagation using permeability data

In order to reconcile the prediction and experimental discrepancy, we proceed to calibrate our LB model parameter with experimental permeability data.

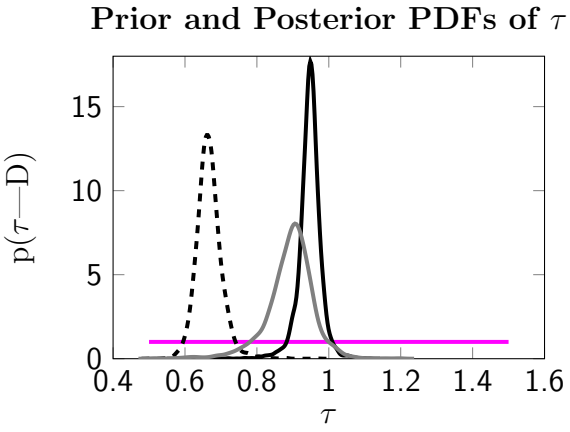

Figure 6.8: Solid black - calibration using the Hagen-Poiseuille law (Case 1), maximum-a-posteriori (MAP) value at $\hat{\tau} = 0.949$; solid grey - calibration using the Hagen-Poiseuille law using a model that takes pore size and abundance into account (Case 2), MAP value at $\hat{\tau} = 0.906$, dashed - calibration using permeability data (Case 3), MAP value at $\hat{\tau} = 0.661$.

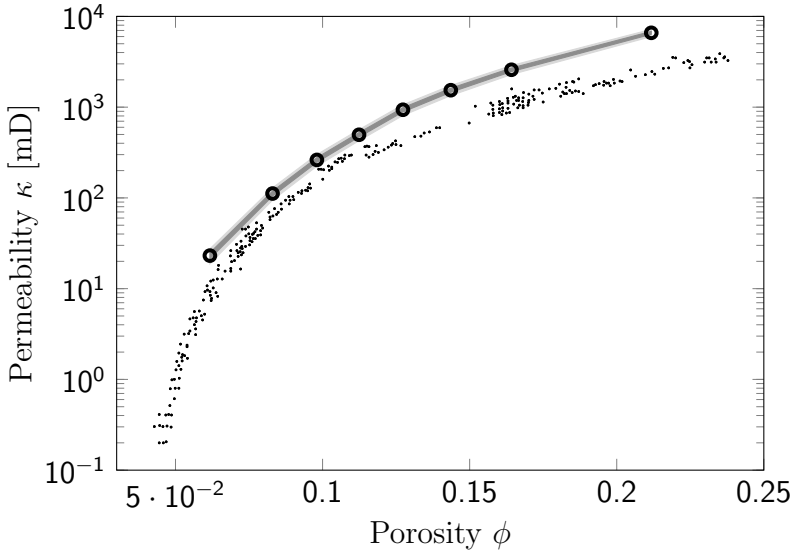

Figure 6.9: Prediction using the Hagen-Poiseuille law calibration (Case 1). Small dots - experimental data of the permeability of Fontainebleau sandstone ($\underline{D_{\kappa,E}}$) from Zinszner and Pellerin (2007); light and dark grey shading - 50% and 95% Bayesian credibility intervals; large circles - permeability predictions $\underline{f_\kappa}$ using the MAP $\hat{\tau}$.

Porosity-independent relaxation parameter (Case 3)

We again employ the TMCMC with 5000 samples per stage, for a total of 35000 samples, following seven stages until the convergence criteria have been satisfied.

The posterior PDF $p(\tau|\kappa)$ is estimated using kernel density estimates from the 5000 samples of the last sampling stage, and is presented in Figure 6.8 (dashed curve). A comparison between the three posterior PDFs in Cases 1, 2 and 3 in Figure 6.8 indicates that the PDF in Case 3 is almost disjoint from the PDFs in Cases 1 and 2. The mode of the posterior PDF using the permeability information is at $\tau = 0.661$, whereas its associated uncertainty is smaller at 5.3%. This significantly smaller than the value of 1.0 typically used in BGK-LB simulations.

Propagation of the TMCMC samples with the calibrated τ value yields results presented in Figure 6.11. It is clear that our prediction is significantly better compared to Case 1 or Case 2. We capture a greater range of porosities within

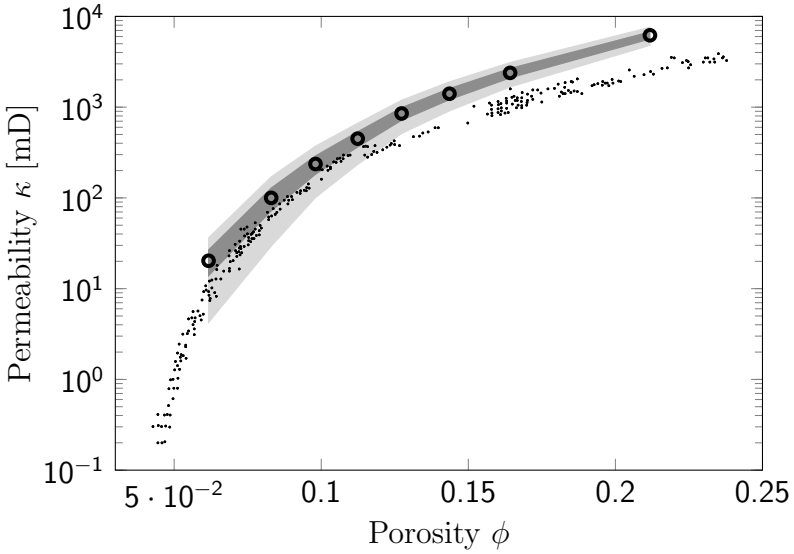

Figure 6.10: Prediction using the Hagen-Poiseuille law calibration in Case 2. Small dots - experimental data of the permeability of Fontainebleau sandstone ($\underline{D_{\kappa,E}}$) from Zinszner and Pellerin (2007); light and dark grey shading - 50% and 95% Bayesian credibility intervals; large circles - permeability predictions $\underline{f_\kappa}$ using the MAP $\hat{\tau}$.

the modelling uncertainty. We can predict values with porosities larger than 0.16 compared to 0.12 in Cases 1 or 2. For larger values of porosity, however, we still do not manage to recreate the experimental observations.

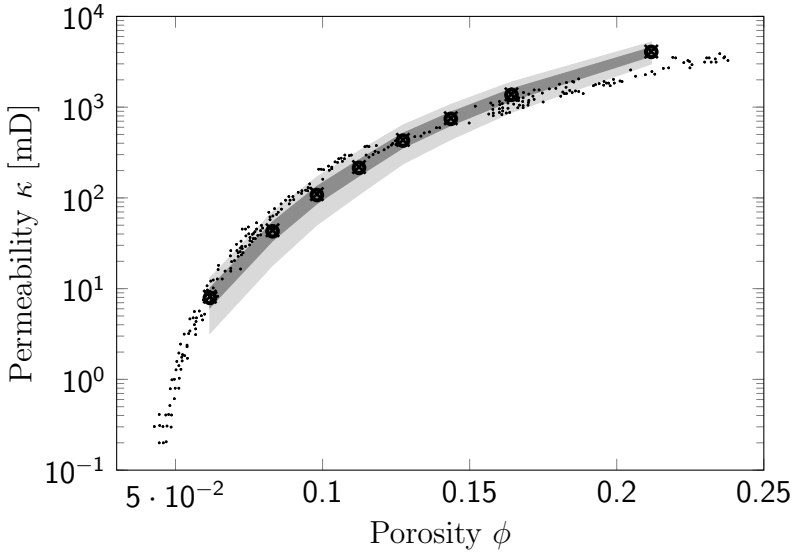

Figure 6.11: Robust prediction using permeability data (Case 3). Circles indicate predictions using posterior mean τ; crosses indicate predictions using MAP τ; small dots - experimental data of the permeability of Fontainebleau sandstone ($\underline{D_{\kappa,E}}$) from Zinszner and Pellerin (2007); light and dark grey shading - 50% and 95% Bayesian credibility intervals; large circles - permeability predictions $\underline{f_\kappa}$ using the MAP $\hat{\tau}$.

The large difference in the predicted values of τ in the HP cases (1 and 2) and Case 3, as well as the persisting discrepancy for over-estimating the permeability for higher-porosity samples, suggests the need to refine the LB model to allow for porosity-dependent relaxation rates.

Porosity-dependent relaxation rate (Case 4)

We repeat the sampling campaign in order to estimate the posterior distribution function of $p(\underline{\tau}|\kappa)$, where now we allow for the relaxation rates to be porosity dependent. We split the data into eight disjoint regimes of porosity, where we

assume that the prediction error within each regime is the same. The marginal τ distributions for all eight porosities are shown in Figure 6.12.

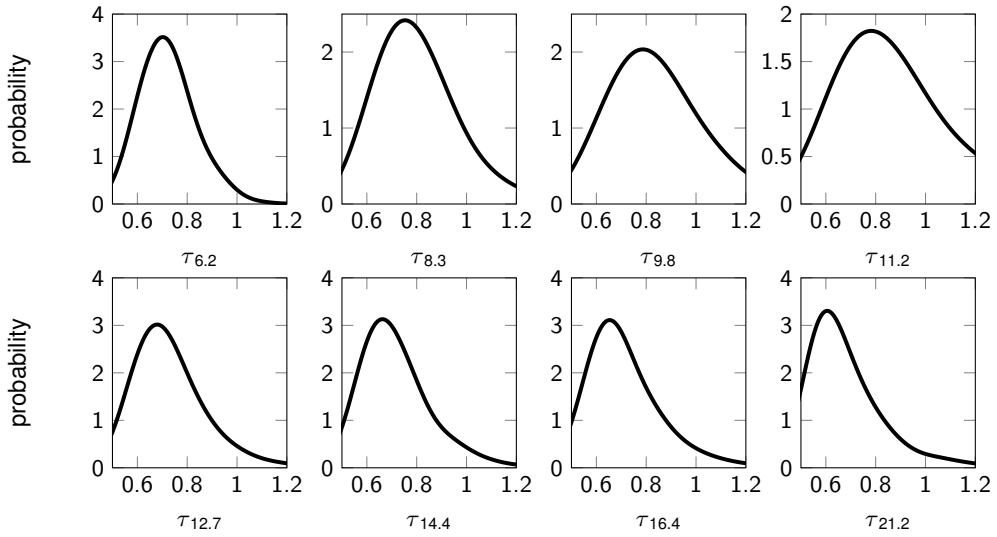

Figure 6.12: Inference of τ from permeability data using the porosity-dependent model (Case 4). Marginals of the joint posterior PDFs for the eight τ parameters for each analysed porosity (6.2% though 21.2%) are obtained via kernel densities.

Figure 6.13 shows that the MAP values of $\hat{\tau}_{\phi_i}$ fit well with the experimental data and interestingly in this case there is clearly a long tail in each posterior PDF towards lower permeability values. We also fit these MAP values of τ with a linear function in order to suggest which value of parameter τ should be used in simulations on rocks of porosities that we did not model explicitly. Figure 6.14 presents the resulting MAP relaxation rates as identified for each porosity.

6.6 Discussion

Our Bayesian calibration of the BGK-LB parameter τ using permeability data and a porosity-independent formulation (Case 3) results in the MAP value $\tau = 0.661$. This value is considerably smaller than the value found when using the Hagen-Poiseuille law for calibration, and it leads to significantly more accurate

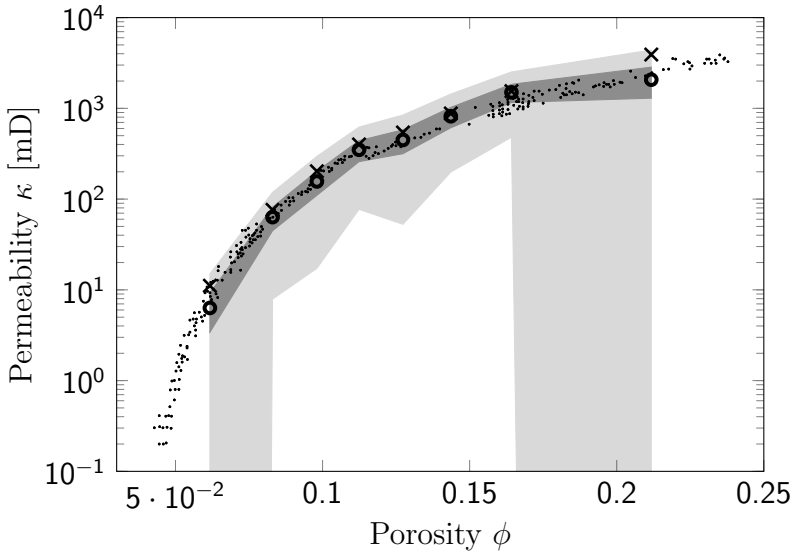

Figure 6.13: Prediction using permeability data in the porosity-dependent mode (Case 4). Circles indicate predictions using posterior mean τ; crosses indicate predictions using MAP τ; small dots - experimental data of the permeability of Fontainebleau sandstone ($\underline{D_{\kappa,E}}$) from Zinszner and Pellerin (2007); light and dark grey shading - 50% and 95% Bayesian credibility intervals; large circles - permeability predictions $\underline{f_\kappa}$ using the MAP $\hat{\tau}$.

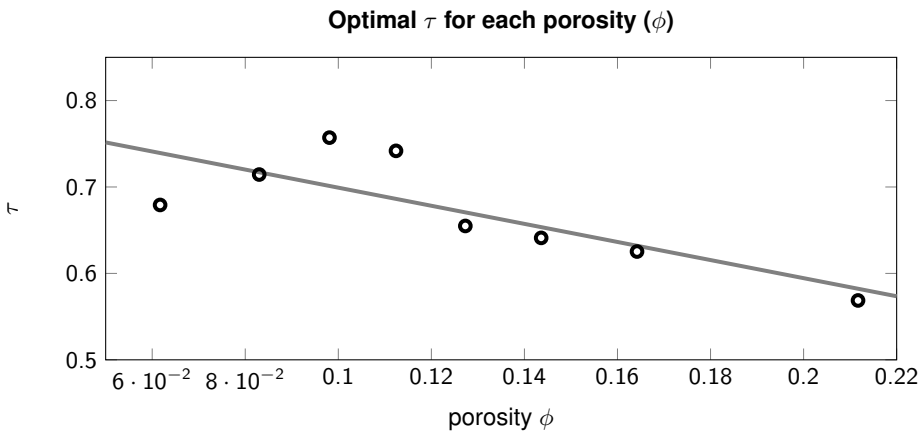

Figure 6.14: Black circles are the MAP τ for investigated porosities and the grey line is a linear fit of the form $\tau(\phi) = p_1 \cdot \phi + p_2$, where $p_1 = -1.047$, $p_2 = 0.804$.

permeability predictions (Figure 6.11). This value, however, is close to the value of $\tau = 0.688$, which is reported by Narváez *et al.* (2010) as resulting in permeability values that are in good agreement with experimental data for Fontainebleau sandstone. Routine calibration of LB parameters in the literature to-date have depended upon theoretical values for channel flow or similar theoretical cases that are used as test-beds. Results of such calibration fail to predict the experimental values of permeabilities in porous media, even under uncertainty. In the case of a Hagen-Poiseuille calibration the estimated posterior PDF of τ is of limited value for predicting permeability values. This is due to the different nature of the geometry and flow inside porous media, containing contributions from a range of pore sizes and their complex patterns of interconnections.

When we calibrate τ using all permeability data in a porosity-independent mode (Case 3) the permeability predictions improve overall, but still contain significant discrepancies for samples of higher porosities. This inspired us to assume a porosity-dependent mathematical formulation for the relaxation parameter τ (Case 4). This calibration yields a result where the MAP parameter τ is approximately a function of the total porosity ϕ of a complex medium: $\tau(\phi) = -1.047 \cdot \phi + 0.804$ (Figure 6.14). This new semi-empirical model for choosing the time relaxation parameter provides significantly more accurate predictions (Figure 6.13) compared to the porosity-independent case (Figure 6.11). The superiority of porosity-dependent calibration can be quantified by using Bayesian model prediction and the Bayes ratio between the porosity-independent model evidence and porosity-dependent model evidence in the permeability-based calibration of τ (Beck and Yuen, 2004b). This ratio is equal to 12.3, which according to Jeffreys (1961) is a *strong* evidence that the porosity-dependent model is significantly more plausible given our experimental data.

This empirical model provides a new modus-operandi regarding permeability predictions. To illustrate the predictive power of our model we selected two independent samples of Fontainebleau sandstone. From the collection of microCT

images of Fontainebleau sandstone made available by the Institute for Computational Physics of the University of Stuttgart (Hilfer and Zauner, 2011) we select two images different from the image used so far: one of resolution $14.6\mu m$ and the other $29.2\mu m$ (Figure 6.15). Following the procedure detailed in Section 6.3 we obtain several binary variants of each of the two greyscale microCT images, each with a different porosity: for the $14.6\mu m$ image we generate eight binarisations and for the $29.2\mu m$ image we generate six binarisations (Table 6.4). We perform two sets of predictions of permeability, one with the value of $\tau = 0.661$ calibrated for the porosity-independent case, and the other using τ according to our semi-empirical model $\tau(\phi) = -1.047 \cdot \phi + 0.804$ (Table 6.4). The results of the LB simulation for the porosity-independent case (Figure 6.16) yield permeabilities that fall within the credibility intervals of our propagation for the analysed sample. In the porosity-dependent case (Figure 6.17) the permeabilities of the independent samples again fall within the credibility intervals, but this time they are also much closer to the experimental data for Fontainebleau sandstone.

Table 6.4: Parameters τ for the independent samples calculated using the model in Figure 6.14.

$14.6\mu m$ sample		$29.2\mu m$ sample	
Porosity [%]	τ	Porosity [%]	τ
6.1	0.740	5.3	0.748
8.2	0.718	7.6	0.725
9.6	0.703	10.0	0.699
11.1	0.688	12.6	0.672
12.5	0.673	15.9	0.638
14.2	0.655	20.2	0.593
16.3	0.634		
20.1	0.584		

We would like to stress that LB parameterisation methods, especially for more complex LB models of for example two-phase flows, should be approached with

great caution. Depending on the quantity of interest and the experimental set-up we want to simulate, we must carefully assess the relevance of previously published values from literature. Here we present a study for a rock type with published experimental permeability data. In the absence of data for a specific rock formation we suggest that porosity-permeability data at least from a similar rock-type are used. A more involved hierarchical Bayesian approach to calibration involving different types of rocks and theoretical expressions could also be advantageous in this LB calibration method.

Our findings also have significant ramifications for more advanced LB models, including multi-phase, multi-species examples. The usual method of calibration in those systems includes experimental set-ups using contact angle simulations. In future work we will investigate how this calibration compares to calibration with real relative permeability data in the above Bayesian framework. We seek to resolve this matter in two-phase LB simulations (oil and water), which is of notable interest to petroleum engineering.

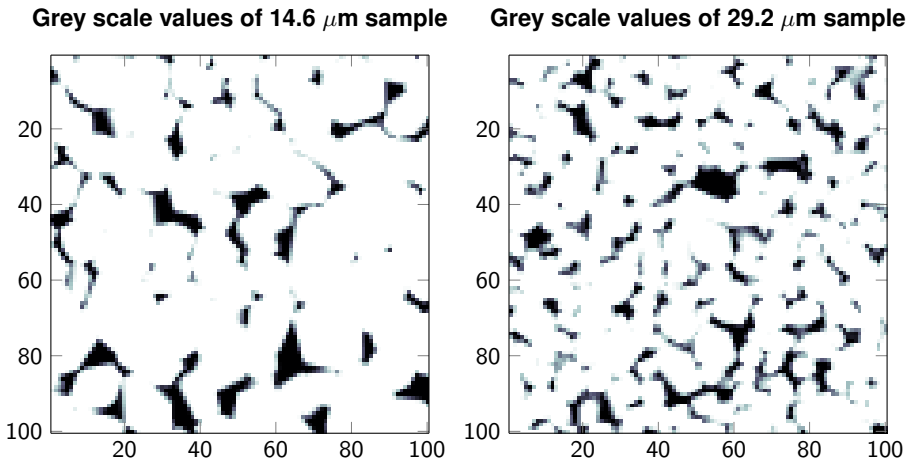

Figure 6.15: Images of the independent samples used in calibration validation. Slices through microCT image of Fontainebleau sandstone in grey scale.

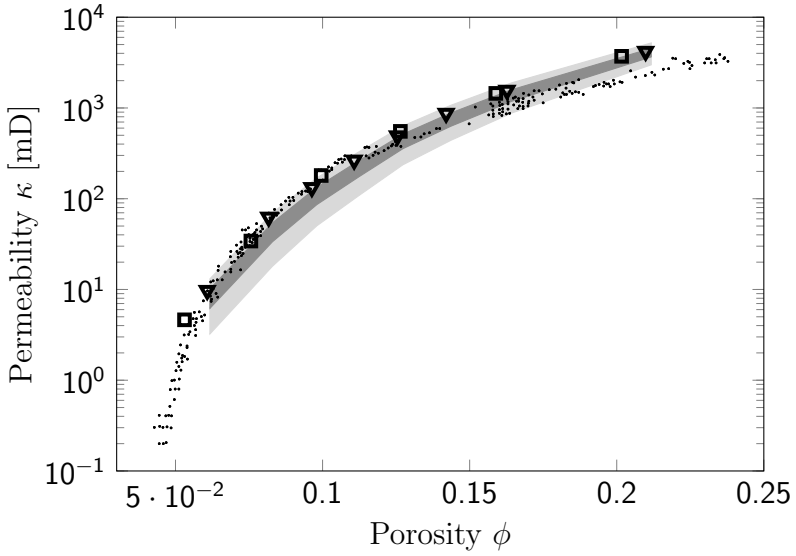

Figure 6.16: Permeabilities of independent samples calculated using $\tau = 0.661$ in the context of prediction using permeability data (Case 3). Triangles - permeabilities for the $14.6\mu m$ sample; squares - permeabilities of the $29.2\mu m$ sample; small dots - experimental data of the permeability of Fontainebleau sandstone ($\underline{D_{\kappa,E}}$) from Zinszner and Pellerin (2007); light and dark grey shading - 50% and 95% Bayesian credibility intervals; large circles - permeability predictions $\underline{f_\kappa}$ using the MAP $\hat{\tau}$.

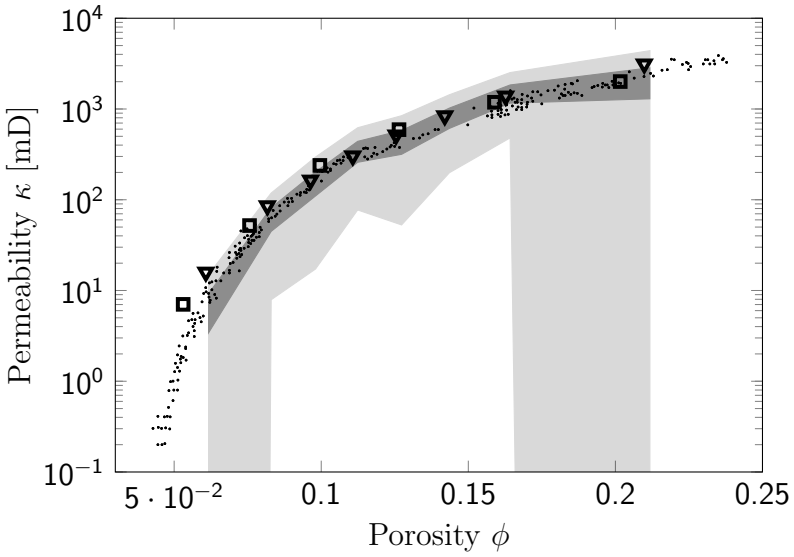

Figure 6.17: Permeabilities of independent samples calculated using porosity-dependent τ as in Table 6.4 in the context of prediction using experimental data in the porosity-dependent mode (Case 4). Triangles - permeabilities for the $14.6\mu m$ sample; squares - permeabilities of the $29.2\mu m$ sample; small dots - experimental data of the permeability of Fontainebleau sandstone ($\underline{D_{\kappa,E}}$) from Zinszner and Pellerin (2007); light and dark grey shading - 50% and 95% Bayesian credibility intervals; large circles - permeability predictions $\underline{f_\kappa}$ using the MAP $\hat{\tau}$.

6.7 Conclusions

We develop a Bayesian inference framework to analyse the power of single-relaxation-time Bhatnagar-Gross-Krook (BGK) Lattice-Boltzmann (LB) models to predict permeability of porous media. The framework enables systematic parameter estimation of LB model parameters (in the scope of this work, the relaxation parameter τ), for the currently used calibrations of LB based on Hagen-Poiseuille law. Our prediction of permeability using the Hagen-Poiseuille calibration suggests that this method for calibration is not optimal and in fact leads to substantial discrepancies with experimental measurements, especially for highly porous complex media.

We proceed to re-calibrate the LB model using permeability data from porous media, which results in a substantially different value of the maximum-a-posteriori (MAP) τ parameter than those proposed previously (0.661 here compared to 1.0 typically used in BGK-LB simulations or 0.857 resulting from the calibration for the 3D Poiseuille flow in a quadratic pipe by Narváez *et al.* (2010)). We augment our model introducing porosity-dependence, where we find that the MAP value for τ decreases for samples of higher porosity. In this new semi-empirical model one first identifies the porosity of the given medium, and on that basis choses an appropriate LB relaxation parameter from the relation in Figure 6.14. These two approaches result in permeability predictions much closer to the experimental permeability data, with the porosity-dependent case being the better of the two. Validation of this calibration method with independent samples of the same rock type yields permeability predictions that fall close to the experimental data (Figure 6.16), and again the porosity-dependent model provides better results (Figure 6.17). We thus conclude that our calibration model is a powerful tool for accurate prediction of complex porous media permeability.

Note that the optimal (MAP) τ is adjusted specifically for the pore geometries

and size distribution of Fontainebleau sandstone. Rock types with a significantly different pore space character should undergo an adjustment of their own.

The intention of this work is to present a sophisticated calibration method and showcase the instability of the LB relaxation parameter. While we have used the simple BGK collision model to illustrate this method, it can also be applied to more advanced Multiple Relaxation Time (MRT) scheme. We do not promote the use of BGK-LB over MRT-LB scheme. This work serves to highlight the instability of the BGK-LB relaxation parameter, which is of importance to future users of the BGK-LB scheme when modelling complex media.

6.7.1 Other applications

The Bayesian uncertainty quantification framework and its associated algorithms described in this chapter can be used to calibrate and quantify the predictive envelope of other models presented in this thesis. For example, it could be used to calibrate the shape and size parameters of grains and the way they are used in the depositional model so that the characteristics of the 3D synthetic deposit most closely resemble the characteristics observed in 2D thin section images.

Another application of the Bayesian framework could come in robust prediction of permeability for different sediment types. This would be particularly valuable, as it would greatly improve the quality of fluid flow prediction upscaled to reservoir-scale, as discussed in Chapter 7.

Chapter 7

Conclusions, Discussion and Outlook

This Chapter discusses the conclusions of the modelling undertaken in this thesis (Section 7.1), the importance of pore-scale modelling and explores how the results might be used in reservoir modelling (Section 7.2). Also considered are datasets that would be useful to validate or otherwise improve modelling (Section 7.3) and finally an outline of how this work might be extended in the future (Section 7.4).

7.1 Conclusions of the Thesis

In Chapter 1 three hypotheses were proposed regarding the impact of calcite cement in carbonates on the resultant properties (porosity and permeability) of early cemented carbonate rocks (see Section 1.1):

1. Early cements exert a major control on the porosity and permeability in carbonate grainstones;

2. Grainstone sediment type, understood as the ratio of monocrystalline to polycrystalline grains, controls the properties of early cemented grainstones;

3. Crystal form of syntaxial cement controls the properties of early cemented grainstones.

This thesis has sought to test these hypotheses through the use of 2D (Chapters 2 and 3) as well as 3D (Chapters 4 and 5) models of early calcite cementation.

These models assume the existence of two grain types: polycrystalline and monocrystalline, and two early calcite cement types specific to these grain types: isopachous and syntaxial, respectively. Of the many possible crystal forms that syntaxial cement can take, this thesis focuses on two common rhombohedral forms: a blocky form $01\bar{1}2$ and an elongated form $40\bar{4}1$.

As the modelling depends heavily on the use of Lattice Boltzmann method (flow simulation to obtain permeability results), the importance of calibrating the model parameters of this method were recognised and addressed in Chapter 6 using a Bayesian uncertainty quantification approach.

Sections below reiterate the conclusions of the work undertaken in the thesis.

7.1.1 Conclusions of the cementation modelling

The results demonstrate the effect of the competition of growing grains for the available pore space: the more monocrystalline grains there are in the sample, the stronger the competition is and the smaller the impact of each individual grain on the resulting early calcite cement volume or porosity.

The synthetic samples with syntaxial cements grown according to the more elongated crystal form $40\bar{4}1$ have lower porosity for the same monocrystalline grains content than the synthetic samples grown according to the more blocky

crystal form $01\bar{1}2$. Moreover, the permeability at constant porosity is smaller for the synthetic samples with the form $40\bar{4}1$. Additionally, the synthetic samples with the crystal form $40\bar{4}1$ exhibit greater variability in the synthetic data, as this rhombohedral form is more elongated and has a potential of producing larger volume of cement.

2D modelling

The analysis of the permeability results as a function of the content of monocrystalline grains yields the following phenomenological correlation for the synthetic samples with the crystal from $01\bar{1}2$:

$$log(\kappa) = 0.053 \cdot \alpha_v + 0.44 \cdot \phi - 11.172 \tag{7.1}$$

where κ is the permeability in mD, α_v is the content of monocrystalline grains in the sample by volume in % and ϕ is the porosity in %.

Admittedly, the above correlation is specific for the rock type investigated in this study, but it is likely that other rock types exhibit a similar dependence of the permeability on the monocrystalline grain content. It is therefore suggested that the composition of the carbonate deposit should be determined and used for a better prediction of the permeability alongside the porosity and other factors.

The poroperm results of the 2D modelling ($10 - 8000mD$) are in a reasonable agreement with the data reported for grainstones in the literature ($0.1 - 5000mD$) as well as for the plug data of the samples used in the modelling (porosity $22 - 27\%$, permeability $200 - 3000mD$), however the permeability results at any given porosity have a wide range due to the bias inherent to the 2D flow modelling and to the fact that a post-processed medium with separated grains was used in as a basis for the cement growth.

The advantage of working in the 2D is the higher resolution that can be afforded

and the significantly lower computational cost. Simulating permeability in 2D, however, has limitations (see Section 2.4.3) and as a result of these limitations, the permeability results for some synthetic samples might be incorrect.

3D modelling

Concerning the synthetic samples produced using different crystal forms of calcite, the differences in the volume of the syntaxial cement and the porosity, arising from the difference in the shapes and volumes of the two crystal forms, are more pronounced in the 3D model results than in the 2D results. In the 3D model, the cements are 3-dimensional and their growth is not restricted to sections of the 3D medium where the grain seeding the cement is present.

The analysis of the permeability results as a function of the content of the monocrystalline grains yields the following phenomenological correlation for the synthetic samples with the crystal form $01\bar{1}2$:

$$log(\kappa) = -0.00241 \cdot \alpha_v + 0.073 \cdot \phi - 2.35 \tag{7.2}$$

where κ is the permeability in mD, α_v is the content of the monocrystalline grains in the sample by volume in %, and ϕ is the porosity in %. In the case of the synthetic samples generated with the use of the crystal form $40\bar{4}1$, the dependence of the permeability on the monocrystalline grain content remains inconclusive.

The dependence of the permeability on the monocrystalline grains content is found weaker than in the 2D study. This may be attributed to the deficiencies of the 2D modelling methodology. The permeability results for some synthetic samples (particularly the low permeability ones) in the 2D study may be artificially low due to the modelling of the flow in the 2D. Additionally, the permeability of the synthetic samples with no isopachous cement or very thin isopachous cement

fringes (which are typically high permeability) may be overestimated due to the fact that a post-processed porous medium with artificially separated grains is used. Both of these deficiencies lead to a higher range of permeabilities at any given porosity in the 2D modelling, and can lead to the dependence of the permeability on the sediment type being exaggerated.

The poroperm results in the 3D modelling ($10-30,000mD$) exhibit permeabilities above the range of these reported in the literature ($0.1-5000mD$) or the plug data of the samples used in modelling (porosity $22-27\%$, permeability $200-3000mD$), but the reason for that is the initial synthetic deposit, which has a very high permeability ($58,900mD$). However, the trend in the poroperm results closely resembles those reported in natural carbonate rocks.

Although we conclude that the *cementation* methodology is successful in modelling realistic changes in the cement volumes and in the pore space morphology, the *depositional* methodology is less successful in generating a synthetic deposit with realistic permeabilities. This will be addressed in further work, which will involve expanding the shape library used by the model to introduce less regular grain shapes. A methodology will be developed to optimise the parameters of the depositional model so that the 2D sections of the 3D medium more closely resemble the characteristics of the 2D thin section images of the natural porous media.

7.1.2 Conclusions of calibration of Lattice Boltzmann model

We developed a Bayesian inference framework to analyse the power of Lattice-Boltzmann (LB) models to predict permeability of porous media. The framework enables systematic parameter estimation of LB model parameters (in the scope of this work, the relaxation parameter τ), for the currently used calibrations of LB

based on Hagen-Poiseuille law. Our prediction of permeability using the Hagen-Poiseuille calibration suggests that this method for calibration is not optimal and in fact leads to substantial discrepancies with experimental measurements, especially for highly porous complex media.

We proceeded to re-calibrate the LB model using permeability data from porous media, which results in a substantially different value of the optimal τ parameter than those proposed by Narváez *et al.* (2010) (0.654 here compared to 0.857). We augmented our model introducing porosity-dependence, where we found that the optimal value for τ decreases for samples of higher porosity. In this new semi-empirical model one first identifies the porosity of the given medium, and on that basis choses an appropriate LB relaxation parameter from the relation in Figure 6.14. These two approaches result in permeability predictions much closer to the experimental permeability data, with the porosity-dependent case being the better of the two. Validation of this calibration method with independent samples of the same rock type yielded permeability predictions that fall close to the experimental data (Figure 6.16), and again the porosity-dependent model provided better results (Figure 6.17). We thus conclude that our model is a powerful tool for accurate prediction of complex porous media permeability.

7.2 Importance and Challenges of Pore-Scale Modelling

In the context of reservoir quality a question often arises on the merit of pore-scale models. What can modelling work at such a small scale bring into practical applications, which are larger scale (e.g. oil extraction from a reservoir)? This question is particularly valid in the case of carbonates, which are very heterogenous.

As far as *pore-scale* research is concerned, it is worthwhile as reservoir displacements and indeed cement growth ultimately occurs pore-by-pore and thus understanding mechanisms at the pore-scale is of fundamental importance. The advantage of *modelling* is that compared to lab experiments it is relatively cheap. Models can also be used to explain mechanisms and predict properties.

Rock properties derived in pore-scale modelling may be used to populate a reservoir model. A reservoir model represents the physical space of the reservoir by an array of discrete cells, delineated by a grid (regular or irregular). Each cell has associated properties such as porosity and permeability. If a sediment type, understood as the ratio of monocrystalline to polycrystalline grains, of a cell in a reservoir model is known, porosity and permeability of this sediment type, as derived through modelling in this thesis, can be applied to that grid cell. Reservoir-scale simulation of fluid flow can then be performed with the use of these sediment-type-specific results.

Figure 7.1 shows how cementation modelling in this thesis can be used to generate synthetic data to populate a reservoir model. Once the characteristics of a carbonate sediment are established for a given grid cell of the reservoir model, i.e. grain size and shape distribution and the content of the monocrystalline grains vs polycrystalline grains, a synthetic 3D model can be generated (a). A cementation model is used to simulate early cement growth on that deposit (b) and the *porosity* of the final cemented rock is derived. Next, the flow is simulated on the final cemented synthetic rock (c) and the *permeability* is quantified. The porosity and permeability results can then be used to populate the properties of the cell in a reservoir model associated with the sediment characteristics that were used in the first step of the methodology (a).

The use of Bayesian techniques for permeability studies of reservoir rocks is quite common (Seiler *et al.*, 2010; Subbey *et al.*, 2004), but in the specific context of the thesis, the following computational procedure can be followed: the uncertainty quantification and propagation framework described in Chapter

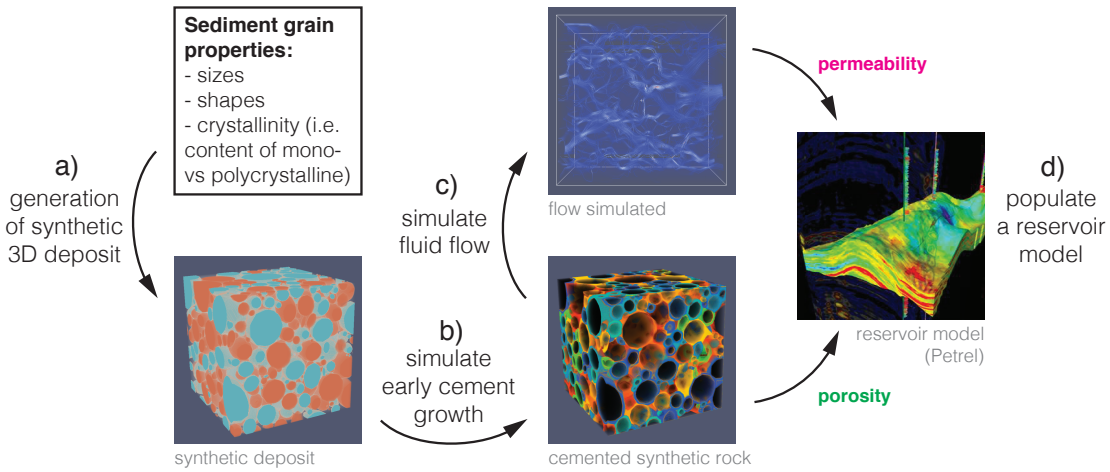

Figure 7.1: A proposed methodology leading to population of a reservoir model with the results of the cementation modelling developed in this thesis; a) a synthetic deposit is generated based on the sediment grain characteristics for a given grid cell in the reservoir model (grain size and shape distribution, crystallinity); b) early cement growth is simulated (porosity is obtained); c) the flow through the final cemented synthetic medium is simulated (permeability is quantified); d) a cell in a reservoir model is updated with the porosity and permeability of the final early cemented synthetic rock. Source of the reservoir model image: *http://www.software.slb.com*.

6 can be used to obtain a robust prediction of porosity and permeability of mm-scale samples. This would provide essentially a uncertain material property which can be used for solving the partial differential equation multi-physics system on a reservoir scale (e.g. in Petrel). The reservoir model of sediment type could be then populated with the porosity and permeability derived through cementation modelling including the predictive envelope. The permeability uncertainty would be then propagated at each location to the reservoir-scale, where the described Bayesian framework would be used to obtain a final *robust* prediction of fluid flow behaviour.

7.2.1 Model output size and resolution

Choosing a representative size for a sample is a challenge. This is especially true for carbonates, which are notorious for their heterogeneity. Blunt *et al.* (2013) recommend a sample size of about $5mm^3$ for carbonate rocks. In this thesis, the size of the 2D model outputs is $10mm^2$ (resolution of $5\mu m$) and the size of the 3D models outputs is $3mm^3$ (resolution of $10\mu m$). The size of the 3D synthetic samples is somewhat smaller than what is recommended for carbonates, however, as the model focuses on grainstones, which are relatively homogenous, this compromise of the sample size for the sake of resolution is not unreasonable. Still, when comparing the permeability results of the cemented model outputs to plug data, which are derived for samples and an order of magnitude larger, there is a significant mismatch, as the models cannot capture all different ranges of variability in the rock. Ideally, the size of the 3D model outputs would be larger, but this could not be computationally afforded in this study due to the large number of models generated and processed (including the LB simulation). The size of $3mm^3$ was maximum of what could be reasonably afforded and a compromise between sample size and resolution.

Due to computational constraints, the size of the sample can be only increased at the cost of the resolution. However, compromising resolution comes with

its own challenges, most important of which is the issue of microporosity. In carbonates there is often significant connected porosity with pore sizes down to about $0.1\mu m$ (Blunt *et al.*, 2013). Capturing micropores is especially important is cases where the meso or macropores are disconnected from each other on a meso/macro scale and only connected via micro-pore throats. Including microporosity in the analysis is particularly important in the multiphase flow simulation. However, capturing microporosity requires a resolution of at least $0.1\mu m$ and, if we also assume the recommended representative size for a carbonate sample ($5mm^3$), this translates to a computational domain size of $50,000^3$ cells, which is computationally impossible to achieve now or in the near future. To overcome this challenge one needs to settle on identifying the key porosity, the one that contributes most to the overall flow, and ignore the details. This way *useful*, albeit approximate, predictions of single and multiphase flow properties can be derived.

7.3 Dataset Wish List

The work presented in this thesis would benefit from an access to further data. The sections below list three datasets that are of the highest interest and details as to how they might improve the modelling work.

7.3.1 Data to validate the cementation model

In order to verify if the cementation model produces synthetic samples with realistic cement volumes for a given sediment type a dataset is necessary that includes:

1. the volume of sediment (grains);
2. the volume of monocrystalline grains;

3. the volume of *only* the early calcite cements;

4. the permeability of the rock at the stage in the diagenesis when only the early cements were present.

The volume of sediment, monocrystalline grains and early calcite cement can be determined from thin-section analysis if a dataset of samples with a wide range of monocrystalline grain content is obtained.

The permeability data is more problematic. Since removal of later cements in natural samples for the purposes of measuring the permeability at the stage of diagenesis where only early cement were present is impossible, obtaining such dataset would require samples where only early cements are present. However, if such a dataset were acquired, it could be used to verify and calibrate (using the Bayesian approach) the models presented in this thesis.

7.3.2 Orientations of crystal axes of monocrystalline grains

In both the 2D and the 3D modelling methodologies an assumption is made that the monocrystalline grains in a sample are oriented at random. To verify this, a dataset including grainstones with significant amount of monocrystalline grains could be used. Electron backscatter diffraction (EBSD) can be used to find the crystal orientation of the material. The cementation models in this thesis would then be modified accordingly.

7.3.3 Crystal form of syntaxial calcite cements in natural media

To the best of our knowledge, there are no studies on the abundance of the different crystal forms in the cement of natural carbonates (J.A.D. Dickson, pers. comm.). Therefore, modelling presented in this thesis focuses on two rhombohedral crystal forms of calcite that are reported to be common in literature. Moreover, due to lack of reports to the otherwise, the models assume that only one crystal form is developed by all monocrystalline grains in a sample.

The modelling work in this thesis would therefore benefit from a systematic study regarding the relative abundance of various crystal forms of calcite in syntaxial cement in carbonates. The models in this thesis could then be easily modified to allow other crystal forms or a variety of crystal forms in one synthetic sample.

7.4 Further Work

The models presented in this thesis would benefit form additional work, both in *modification* of the present models as well as from *extensions* to the models. If appropriate datasets are acquired, the Bayesian framework could also be used to quantify a robust predictive envelope of the models.

7.4.1 Improvement of the depositional model

The depositional modelling is the main weakness of the 3D modelling methodology. Although it succeeds in producing a 3D medium with porosity and mean size of grains very similar to the medium upon which it is modelled (a 2D thin-section image), the grain shape distribution is considerably different. This also results in a permeability which is too high compared to natural grainstones.

To address this issue several steps may be undertaken:

1. The grain shape library may be extended, to include greater variability of shapes, possibly including non-convex shapes.
2. The way the size and shape parameters derived from the 2D thin-sections are used to generate the 3D grains may be modified, e.g. by substituting the currently used equivalent diameter with another size parameter (e.g. the length of the major axis of a grain).
3. Mechanical compaction may be implemented, which would result both in porosity decrease as well as in modification to the shape of grains.

Bayesian techniques may aid in model selection when deciding on the size and shape parameters that result in 3D porous medium that most closely resembles the 2D data. Once these parameters are selected, their values may be estimated under uncertainty.

7.4.2 Improvement of the existing cementation model

At present, the directions of the crystal axes of the monocrystalline grains are assigned at random. However, it could be easily changed if a dataset (EBSD) was acquired that would suggest otherwise.

In the present implementation of the models, the assigning of grain type is grain-shape-independent. However, polycrystalline grains are more likely to be rounded (e.g. ooids, pellets), while monocrystalline grains, which are mostly skeletal, can have complex shapes and are typically more likely to be elongated (e.g. sea urchin fragments). Also, it may be possible to make the cement type grain-type-dependent: e.g. elongated grains are more likely to be monocrystalline. Modifying Stage 1 of the cementation model (both Calcite2D and Calcite3D) so that the grains with an aspect ratio greater than a given threshold are labeled

monocrystalline, regardless of the input α_0, would render this modelling more realistic.

The 2D modelling methodology would also benefit from taking into account the *apparent* thickness of the isopachous cement fringes visible in a section, as this differs from the *true* thickness, as can be observed in the synthetic samples produced with the 3D model. Moreover, nucleation of a new cement could be introduced, which would reflect the fact that it is possible that cement grows into the plane of the section by grains that lie outside that plane. This would make the 2D modelling more similar to the 3D modelling, and so create more realistic results.

7.4.3 Further development of the cementation model

Further development of the cementation model could involve addition of other cement fabrics, such as meniscus cement or pendant cements, which are formed during diagenesis in the vadose zone above the water table. The modelling can be expanded beyond just the early cements and include burial cement fabrics.

Another modelling prospect is flow-dependent cement growth, similar to the contact-cement scheme implemented by Sain (2010) for synthetic sandstone and by Keehm (2003) for sandstone CT scans (see Section 1.7.3). This scheme replicates geologic scenarios where super saturated pore fluids preferentially deposit cement at low flux zones. The idea is that every cementation step is preceded by a flow simulation (with Lattice Boltzmann) and only pore voxels with flow velocity below a given threshold are allowed to be transformed into a solid voxel (Figure 7.2). This requires a significant number of LB simulations for a single sample, which is computationally expensive.

A modification of this model can be implemented, which takes into account syntaxial cement development on monocrystalline grains. It would involve

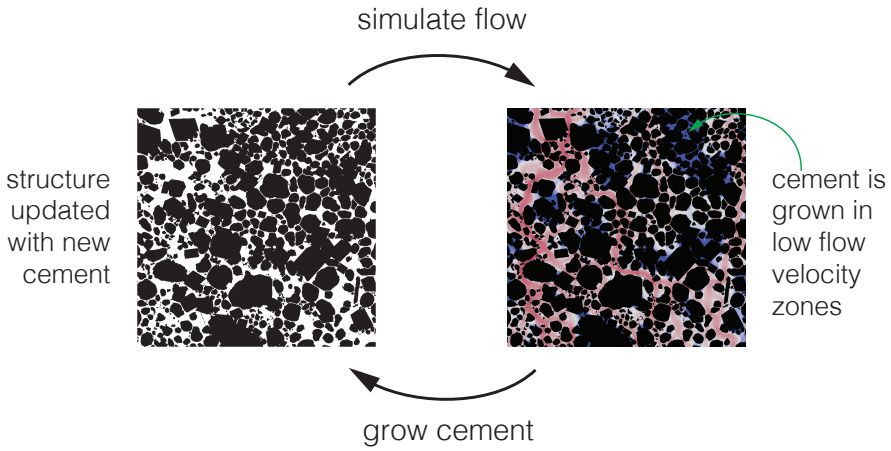

Figure 7.2: Potential flow-dependent modelling set-up. Each cementation step is preceded by a flow simulation and only the pore space where the flow velocity is below a given threshold is allowed to be transformed into solid.

prohibition of cement growth in pore voxels with flow velocity below a given threshold even if they lie inside the bounding crystal of monocrystalline grains.

7.4.4 Simulation of multiphase low

Other further work will involve simulation of multi-phase flow on the synthetic samples generated in this thesis using Lattice Boltzmann method. In order to obtain relative permeability curves, several simulations must be performed with various ratios of the two fluids. This causes the computational cost of such simulations quite high. However, we have secured sufficient computational time (111,716 kAU) on Archer through the University of Edinburgh Supercomputing Call Award for a project titled 'Impact of sediment type on single-phase and multi-phase flow properties in cemented rocks'.

References

Adler, P., Jacquin, C. and Quiblier, J. (1990). Flow in simulated porous media. *International Journal of Multiphase Flow*, **16**, 691 – 712.

Adler, P.M., Jacquin, C.G. and Thovert, J.F. (1992). The formation factor of reconstructed porous media. *Water Resources Research*, **28**, 1571–1576.

Ahr, W. (2008). *Geology of Carbonate Reservoirs: The Identification, Description, and Characterization of Hydrocarbon Reservoirs in Carbonate Rocks*. Wiley.

Ahrenholz, B., Tölke, J., Lehmann, P., Peters, A., Kaestner, A., Krafczyk, M. and Durner, W. (2008). Prediction of capillary hysteresis in a porous material using lattice-boltzmann methods and comparison to experimental data and a morphological pore network model. *Advances in Water Resources*, **31**, 1151 – 1173, quantitative links between porous media structures and flow behavior across scales.

Anderson, M.P., Grest, G.S. and Srolovitz, D.J. (1989). Computer simulation of normal grain growth in three dimensions. *Philosophical Magazine Part B*, **59**, 293–329.

Angelikopoulos, P., Papadimitriou, C. and Koumoutsakos, P. (2012). Bayesian Uncertainty Quantication and propagation in molecular dynamics simulations: a high performance computing framework. *Journal of Chemical Physics*, **137**, 144103.

Arns, C.H., Knackstedt, M.A. and Mecke, K.R. (2003). Reconstructing complex materials via effective grain shapes. *Phys. Rev. Lett.*, **91**, 215506.

Auzerais, F.M., Dunsmuir, J., Ferréol, B.B., Martys, N., Olson, J., Ramakrishnan, T.S., Rothman, D.H. and Schwartz, L.M. (1996). Transport in sandstone: A study based on three dimensional microtomography. *Geophysical Research Letters*, **23**, 705–708.

Bakke, S. and Øren, P.E. (1997). 3-d pore-scale modelling of sandstones and flow simulations in the pore networks. *Society of Petroleum Engineers*.

Bear, J. (1972). *Dynamics of Fluids in Porous Media*. Elsevier.

Beavers, G.S. and Joseph, D.D. (1967). Boundary conditions at a naturally permeable wall. *Journal of Fluid Mechanics*, 197–207.

Beck, J. and Katafygiotis, L. (1998). Updating Models and Their Uncertainties. I: Bayesian Statistical Framework. *Journal of Engineering Mechanics*, **124**, 455–461.

Beck, J. and Yuen, K. (2004a). Model selection using response measurements: Bayesian probabilistic approach. *Journal of Engineering Mechanics*.

Beck, J.L. and Yuen, K.V. (2004b). Model selection using response measurements: Bayesian probabilistic approach. *Journal of Engineering Mechanics-ASCE*, **130**, 192–203.

Bernabé, Y., Li, M. and Maineult, A. (2010). Permeability and pore connectivity: A new model based on network simulations. *Journal of Geophysical Research: Solid Earth*, **115**, n/a–n/a, b10203.

Bhattacharya, S. and Gubbins, K.E. (2006). Fast method for computing pore size distributions of model materials. *Langmuir*, **22**, 7726–7731.

Biswal, B., Manwart, C., Hilfer, R., Bakke, S. and Øren, P. (1999). Quantitative analysis of experimental and synthetic microstructures for sedimentary rock. *Physica A: Statistical Mechanics and its Applications*, **273**, 452 – 475.

Biswal, B., Øren, P.E., Held, R.J., Bakke, S. and Hilfer, R. (2007). Stochastic multiscale model for carbonate rocks. *Physical Review E*, **75**, 061303–.

Biswal, B., Held, R.J., Khanna, V., Wang, J. and Hilfer, R. (2009a). Towards precise prediction of transport properties from synthetic computer tomography of reconstructed porous media. *Physical Review E - Statistical, Nonlinear and Soft Matter Physics*, **80**.

Biswal, B., Øren, P.E., Held, R.J., Bakke, S. and Hilfer, R. (2009b). Modeling of multiscale porous media. *Image Analysis & Stereology*, **28**, 23–34.

Bjorlykke, K. (2010). *Petroleum Geoscience From Sedimentary Environments to Rock Physics Petroleum Geoscience From Sedimentary Environments to Rock Physics*. Springer.

Blikstein, P. and Tschiptschin, A.A.P. (1999). Monte Carlo simulation of grain growth. *Materials Research*, **2**, 133 – 137.

Blunt, M.J., Bijeljic, B., Dong, H., Gharbi, O., Iglauer, S., Mostaghimi, P., Paluszny, A. and Pentland, C. (2013). Pore-scale imaging and modelling. *Advances in Water Resources*, **51**, 197 – 216, 35th Year Anniversary Issue.

Boek, E.S. and Venturoli, M. (2010). Lattice-Boltzmann Studies of Fluid Flow in Porous Media with Realistic Rock Geometries. *Computers & Mathematics with Applications*, **59**, 2305–2314.

Breitmoser, E., Chin, J., Dan, C., er, F.D., Frijters, S., Giupponi, G., Gonzalez-Segredo, N., Gunther, F., Harting, J., Harvey, M., Hecht, M., Jha, S., Janoschek, F., Jansen, F., Kunert, C., Lujan, M., Murray, I., Narvaez, A., Nekovee, M., Porter, A., Raischel, F., Saksena, R., Schmieschek, S., Sinz, D., Venturoli, M. and Zauner, T. (2012). *LB3D V7: A Parallel Implementation of the Lattice-Boltzmann Method for Simulation of Interacting Amphiphilic Fluids*.

Brown, A. (1997). Porosity variation in carbonates as a function of depth: Mississippian madison group, williston basin. In J.A. Kupecz, J. Gluyas and S. Bloch, eds., *AAPG Memoir 69: Reservoir Quality Prediction in Sandstones and Carbonates*, AAPG Special Volumes.

Budd, D.A. (2001). Permeability loss with depth in the cenozoic carbonate platform of west-central florida. *AAPG Bulletin*, **85**, 1253–1272.

Budd, D.A. (2002). The relative roles of compaction and early cementation in the destruction of permeability in carbonate grainstones: A case study from the paleogene of west-central florida, u.s.a. *Journal of Sedimentary Research*, **72**, 116–128.

Burke, J. (1949). Some factor affecting the rate of grain growth in metals. *Transactions of the American Institute of Mining and Metallurgical Engineers*, **180**.

Camargo, M.A., Facin, P.C. and Pires, L.F. (2012). Lattice Boltzmann Method for Evaluating Hydraulic Conductivity of Finite Array of Spheres. *The Scientific World Journal*, **2012**, 8.

Carman, P.C. (1937). Fluid flow through granular beds. *Transactions of the Institution of Chemical Engineers*.

Chen, S. and Doolen, G.D. (1998). Lattice Boltzmann Method for Fluid Flows. *Annual Review of Fluid Mechanics*, **30**, 329–364.

Cheung, S.H., Oliver, T.A., Prudencio, E.E., Prudhomme, S. and Moser, R.D. (2011). Bayesian uncertainty analysis with applications to turbulence modeling. *Reliability Engineering & System Safety*, **96**, 1137–1149.

Ching, J. and Chen, Y.C. (2007). Transitional Markov Chain Monte Carlo method for Bayesian model updating, model class selection, and model averaging. *Journal or Engineering Mechanics*, **133**, 816–832.

Chopard, B. and Droz, M. (1998). *Cellular Automata Modeling of Physical Systems*. Cambridge Univeristy Press.

Choquette, P.W. and Pray, L.C. (1970). Geologic nomenclature and classification of porosity in sedimentary carbonates. *AAPG Bulletin*, **54**, 207–244.

Choquette, P.W. and Steinen, R.P. (1985). Mississippian oolite and non-supratidal dolomite reservoirs in the ste. genevieve formation, north bridgeport field, illinois basin,. In P.O. Roehl and P.W. Choquette, eds., *Carbonate Petroleum Reservoirs*, 207–225, Springer New York.

Coles, M.E., Hazlett, R.D., Muegge, E.L., Jones, K.W., Andrews, B., Dowd, B., Siddons, P., Peskin, A., Spanne, P. and Soll, W.E. (1996). Developments in Synchrotron X-Ray Microtomography with Applications to Flow in Porous Media. *Society of Petroleum Engineers*.

Congedo, P.M., Colonna, P., Corre, C., Witteveen, J.A.S. and Iaccarino, G. (2012). Backward uncertainty propagation method in flow problems: Application to the prediction of rarefaction shock waves. *Computer Methods in Applied Mechanics and Engineering*, **213–216**, 314–326.

Coon, E., Porter, M. and Kang, Q. (2014). Taxila lbm: a parallel, modular lattice boltzmann framework for simulating pore-scale flow in porous media. *Computational Geosciences*, **18**, 17–27.

Coumans, E. (2015). *Bullet 2.83 Physics SDK Manual*. bulletphysics.org.

Curtis, A. and Wood, R. (2004). Optimal elicitation of probabilistic information from experts. *Geological Society, London, Special Publications*, **239**, 127–145.

Daian, J.F., Fernandes, C.P., Philippi, P.C. and Bellini da Cunha Neto, J.A. (2004). 3d reconstitution of porous media from image processing data using a multiscale percolation system. *Journal of Petroleum Science and Engineering*, **42**, 15–28.

de Monte, F., Pontrelli, G. and Becker, S. (2013). Chapter 3 - drug release in biological tissues. In S.M. Becker and A.V. Kuznetsov, eds., *Transport in Biological Media*, 59 – 118, Elsevier, Boston.

D'Errico, J. (06.09.2012). *Inhull*. Matlab Central File Exchange, http://ch.mathworks.com/matlabcentral/fileexchange/10226-inhull.

Dickson, J. (1983). Graphical modelling of crystal aggregates and its relevance to cement diagnosis. *Philosophical Transactions of the Royal Society of London. Series A, Mathematical and Physical Sciences*, **309**, 465–502.

Doyen, P.M. (1988). Permeability, conductivity, and pore geometry of sandstone. *Journal of Geophysical Research: Solid Earth*, **93**, 7729–7740.

Duda, A., Koza, Z. and Matyka, M. (2011). Hydraulic tortuosity in arbitrary porous media flow. *Physical Review E*, **84**, 036319–.

Dullien, F.A. (1991). *Porous Media: Fluid Transport and Pore Structure*. Elsevier.

Ehrenberg, S.N. and Nadeau, P.H. (2005). Sandstone vs. carbonate petroleum reservoirs: A global perspective on porosity-depth and porosity-permeability relationships. *AAPG Bulletin*, **89**, 435–445.

Elsey, M., Esedoglu, S. and Smereka, P. (2009). Diffusion generated motion for grain growth in two and three dimensions. *J. Comput. Phys.*, **228**, 8015–8033.

Elsey, M., Esedoglu, S. and Smereka, P. (2011). Large-scale simulation of normal grain growth via diffusion-generated motion. *Royal Society of London Proceedings Series A*, **467**, 381–401.

Enos, P. and Sawatsky, L.H. (1981). Pore networks in holocene carbonate sediments. *Journal of Sedimentary Research*, **51**, 961–985.

Esedoglu, S. (2010). Large-scale simulations of grain boundary motion in polycrystals. *SIAM News*, **43**.

Esedoglu, S., Ruuth, S. and Tsai, R. (2010). Diffusion generated motion using signed distance functions. *J. Comput. Phys.*, **229**, 1017–1042.

Fauzi, U., Hoerdt, A. and Neubauer, F.M. (2002). Influence of coordination number and percolation probability on rock permeability estimation. *Geophysical Research Letters*, **29**, 78–1–78–4.

Fernandes, C.P., Magnani, F.S., Philippi, P.C. and Daïan, J.F. (1996). Multiscale geometrical reconstruction of porous structures. *Physical Review E*, **54**, 1734–1741.

Ferréol, B. and Rothman, D. (1995). Lattice-Boltzmann simulations of flow through Fontainebleau sandstone. *Transport in Porous Media*, **20**, 3–20.

Flügel, E. (2010). *Microfacies of Carbonate Rocks Analysis, Interpretation and Application*. Springer.

Forrest, B. and Tang, L.H. (1990). Hypercube stacking: A potts-spin model for surface growth. *Journal of Statistical Physics*, **60**, 181–202.

Gao, Y., Zhang, X., Rama, P., Liu, Y., Chen, R., Ostadi, H. and Jiang, K. (2012). Calculating the Anisotropic Permeability of Porous Media Using the Lattice Boltzmann Method and X-ray Computed Tomography. *Transport in Porous Media*, **92**, 457–472.

Garcia, X., Akanji, L.T., Blunt, M.J., Matthai, S.K. and Latham, J.P. (2009). Numerical study of the effects of particle shape and polydispersity on permeability. *Physical Review E*, **80**, 021304–.

Ghassemi, A. and Pak, A. (2011). Pore scale study of permeability and tortuosity for flow through particulate media using Lattice Boltzmann method. *International Journal for Numerical and Analytical Methods in Geomechanics*, **35**, 886–901.

Gibson, P., Schreuder-Gibson, H. and Rivin, D. (2001). Transport properties of porous membranes based on electrospun nanofibers. *Colloids and Surfaces A: Physicochemical and Engineering Aspects*, **187–188**, 469 – 481.

Ginzburg, I. (2008). Consistent lattice boltzmann schemes for the brinkman model of porous flow and infinite chapman-enskog expansion. *Phys. Rev. E*, **77**, 066704.

Ginzburg, I., d'Humières, D. and Kuzmin, A. (2010). Optimal stability of advection-diffusion lattice boltzmann models with two relaxation times for positive/negative equilibrium. *Journal of Statistical Physics*, **139**, 1090–1143.

Gomes, J.S., Ribeiro, M.T., Strohmenger, C.J., Naghban, S. and Kalam, M.Z. (2008). Carbonate reservoir rock typing - the link between geology and scal. *Society of Petroleum Engineers*.

Grader, A., Mu, Y., Toelke, J., Baldwin, C., Fang, Q., Carpio, G., Stenger, B.A., Al-Dayyani, T. and Kalam, M.Z. (2010). Estimation Of Relative Permeability Using The Lattice Boltzmann Method For Fluid Flows, Thamama Formation, Abu Dhabi. *SPE Journal*.

Grest, G., Srolovitz, D. and Anderson, M. (1985). Computer simulation of grain growth—iv. anisotropic grain boundary energies. *Acta Metallurgica*, **33**, 509 – 520.

Grodzinsky, A.J. (2011). *Fields, Forces, and Flows in Biological Systems*. Garland Science, 1st edn.

Hadjidoukas, P.E., Lappas, E. and Dimakopoulos, V.V. (2012). A runtime library for platform-independent task parallelism. In *Parallel, Distributed and Network-Based Processing (PDP), 2012 20th Euromicro International Conference on*, 229–236, IEEE Computer Society, Los Alamitos, CA, USA.

Halisch, M. (2013). *Application and Assessment of the Lattice Boltzmann Method for Fluid Flow Modeling in Porous Rocks*. Ph.D. thesis, Technischen Universität Berlin.

Halley, R.B. and Schmoker, J.W. (1983). High-porosity cenozoic carbonate rocks of south florida: Progressive loss of porosity with depth1 high-porosity cenozoic carbonate rocks of south florida: Progressive loss of porosity with depth1. *The American Association of Petroleum Geologists Bulletin*, **67**.

Hammou, H., Ginzburg, I. and Boulerhcha, M. (2011). Two-relaxation-times lattice boltzmann schemes for solute transport in unsaturated water flow, with a focus on stability. *Advances in Water Resources*, **34**, 779 – 793.

Hamon, G. (2003). Two-phase flow rock-typing: Another perspective. *Society of Petroleum Engineers*.

Hao, L. and Cheng, P. (2010). Pore-scale simulations on relative permeabilities of porous media by lattice Boltzmann method. *International Journal of Heat and Mass Transfer*, **53**, 1908 – 1913.

Harland, S., Wood, R., Curtis, A., van Dijke, M., Stratford, K., Jiang, Z., Kallel, W. and Sorbie, K. (2015). Quantifying flow in variably wet microporous carbonates using object-based geological modelling and both lattice-boltzmann and pore network fluid flow simulations. *AAPG Bulletin*.

Hazlett, R. (1997). Statistical characterization and stochastic modeling of pore networks in relation to fluid flow. *Mathematical Geology*, **29**, 801–822.

Hazlett, R., Chen, S. and Soll, W. (1998). Wettability and rate effects on immiscible displacement: Lattice Boltzmann simulation in microtomographic images of reservoir rocks. *Journal of Petroleum Science and Engineering*, **20**, 167 – 175.

Hebert, V., Garing, C., Luquot, L., Pezard, P.A. and Gouze, P. (2014). Multi-scale x-ray tomography analysis of carbonate porosity. *Geological Society, London, Special Publications*, **406**.

Helfferich, F.G. (1985). Principles of adsorption and adsorption processes. *AIChE Journal*, **31**, 523–524.

Hilfer, R. and Zauner, T. (2011). High-precision synthetic computed tomography of reconstructed porous media. *Physical Review E*, **84**, 062301.

http://www.blender.org (2015). *Blender - a 3D modelling and rendering package*. Blender Foundation, Blender Institute, Amsterdam.

Imperial College Rock Library (10.08.2015). https://wwwf.imperial.ac.uk/earth scienceandengineering/rocklibrary.

James, N.P. and Jones, B. (2015). *Origin of Carbonate Sedimentary Rocks*. Wiley.

Jeffreys, H. (1961). *Theory of Probability*. Oxford University Press, USA, 3rd edn.

Jeong, N. (2010). Advanced Study About the Permeability for Micro-Porous Structures Using the Lattice Boltzmann Method. *Transport in Porous Media*, **83**, 271–288.

Jiang, Z., van Dijke, M., Wu, K., Couples, G., Sorbie, K. and Ma, J. (2011). Stochastic pore network generation from 3d rock images. *Transport in Porous Media*, 1–23, 10.1007/s11242-011-9792-z.

Jin, G., Patzek, T.W. and Silin, D.B. (2003). Physics-based reconstruction of sedimentary rocks. *Society of Petroleum Engineers*, **SPE 83587**.

Jin, G., Patzek, T.W. and Silin, D.B. (2004). Direct prediction of the absolute permeability of unconsolidated and consolidated reservoir rock. *Society of Petroleum Engineers*.

Jin, G., Patzek, T.W. and Silin, D.B. (2012). Modeling the impact of rock formation history on the evolution of absolute permeability. *Journal of Petroleum Science and Engineering*, **100**, 153 – 161.

Kang, Q., Lichtner, P.C. and Janecky, D.R. (2010). Lattice Boltzmann Method for Reacting Flows in Porous Media. *Advances in Applied Mathematics and Mechanics*, **2**, 545–563.

Katafygiotis, L.S. and Beck, J.L. (1998). Updating models and their uncertainties. II: Model identifiability. *Journal of Engineering Mechanics-ASCE*, **124**, 463–467.

Keehm, Y. (2003). *Computational rock physics: Transport properties in porous media and applications*. Ph.D. thesis, Stanford University.

Kelly, A. and Knowles, K. (2012). *Crystallography and Crystal Defects*. Wiley.

Khaled, A.R. and Vafai, K. (2003). The role of porous media in modeling flow and heat transfer in biological tissues. *International Journal of Heat and Mass Transfer*, **46**, 4989 – 5003.

Knoerich, A.C. and Mutti, M. (2006). Epitaxial calcite cements in earth history: a cooler-water phenomenon during aragonite-sea times? *Geological Society, London, Special Publications*, **255**, 323–335.

Kozeny, J. (1927). Ueber kapillare leitung des wassers im boden. *Sitzungsber Akad. Wiss*.

Kroon, D.J. (02.06.2009). *Patch Normals*. Matlab Central File Exchange, http://uk.mathworks.com/matlabcentral/fileexchange/24330-patch-normals.

Kroon, D.J. (09.09.2011). *Wavefront OBJ toolbox*. Matlab Central File Exchange, http://ch.mathworks.com/matlabcentral/fileexchange/27982-wavefront-obj-toolbox.

Lander, R., Larese, R. and Bonnell, L. (2008). Toward more accurate quartz cement models: The importance of euhedral versus noneuhedral growth rates. *AAPG Bulletin*, **92**, 1537–1563.

Latief, F., Biswal, B., Fauzi, U. and Hilfer, R. (2010). Continuum reconstruction of the pore scale microstructure for fontainebleau sandstone. *Physica A: Statistical Mechanics and its Applications*, **389**, 1607 – 1618.

Legland, D. (20.05.2015). *geom3d*. Matlab Central File Exchange, http://uk.mathworks.com/matlabcentral/ fileexchange/24484-geom3d.

Li, X., Huang, H. and Meakin, P. (2008). Level set simulation of coupled advection-diffusion and pore structure evolution due to mineral precipitation in porous media. *Water Resour. Res.*, **44**.

Liang, Z., Ioannidis, M. and Chatzis, I. (2000a). Geometric and topological analysis of three-dimensional porous media: Pore space partitioning based on morphological skeletonization. *Journal of Colloid and Interface Science*, **221**, 13 – 24.

Liang, Z., Ioannidis, M. and Chatzis, I. (2000b). Permeability and electrical conductivity of porous media from 3d stochastic replicas of the microstructure. *Chemical Engineering Science*, **55**, 5247 – 5262.

Libbrecht, K.G. (2007). Physically derived rules for simulating faceted crystal growth using cellular automata. *Department of Physics, California Institute of Technology*.

Lønøy, A. (2006). Making sense of carbonate pore systems. *AAPG Bulletin*, **90**, 1381–1405.

Lorna J. Gibson, B.A.H., Michael F. Ashby (2010). *Cellular Materials in Nature and Medicine*. Cambridge University Press.

Lucia, F. (2007). *Carbonate Reservoir Characterization An Integrated Approach*. Springer, 2nd edn.

Lucia, F.J. (1995). Rock-fabric/petrophysical classification of carbonate pore space for reservoir characterization. *AAPG Bulletin*, **79**, 1275–1300.

Lucia, F.J. and Conti, R.D. (1987). *Rock Fabric, Permeability, and Log Relationships in an Upward-Shoaling, Vuggy Carbonate Sequence*. Univ of Texas Bureau of Economic Geology Geological Circular.

Lucia, F.J. and Murray, R.C. (1967). Origin and distribution of porosity in crinoidal rock. *World Petroleum Congress*.

Ma, J., Wu, K., Jiang, Z. and Couples, G.D. (2010). SHIFT: An implementation for lattice Boltzmann simulation in low-porosity porous media. *Physical Review E*, **81**, 056702.

Ma, X. and Zabaras, N. (2011). A stochastic mixed finite element heterogeneous multiscale method for flow in porous media. *Journal of Computational Physics*, **230**, 4696–4722.

Mahmoudi, S., Hashemi, A. and Kord, S. (2013). Gas-liquid relative permeability estimation in 2d porous media by lattice boltzmann method: Low viscosity ratio 2d lbm relative permeability. *Iranian Journal of Oil & Gas Science and Technology*.

Makhloufi, Y., Collin, P.Y., Bergerat, F., Casteleyn, L., Claes, S., David, C., Menendez, B., Monna, F., Robion, P., Sizun, J.P., Swennen, R. and Rigollet, C. (2013). Impact of sedimentology and diagenesis on the petrophysical properties of a tight oolitic carbonate reservoir. the case of the oolithe blanche formation (bathonian, paris basin, france). *Marine and Petroleum Geology*, **48**, 323 – 340.

Manwart, C., Torquato, S. and Hilfer, R. (2000). Stochastic reconstruction of sandstones. *Physical Review E*, **62**, 893–899.

Massaro, F., Pastero, L., Rubbo, M. and Aquilano, D. (2008). Theoretical surface morphology of 01(1)2 acute rhombohedron of calcite - a comparison with experiments and 10(1)4 cleavage rhombohedron. *Journal of Crystal Growth*.

McBride, E.F. (1989). Quartz cement in sandstones: a review. *Earth-Science Reviews*, **26**, 69 – 112.

Melzer, S.E. and Budd, D.A. (2008). Retention of high permeability during shallow burial (300 to 500 m) of carbonate grainstones. *Journal of Sedimentary Research*, **78**, 548–561.

Merriman, B., Bence, J.K. and Osher, S.J. (1994). Motion of multiple junctions: A level set approach. *Journal of Computational Physics*, **112**, 334–363.

Moore, C. (1989). *Carbonate Diagenesis and Porosity*. Elsevier, 2nd edn.

Moore, C. (2001). *Carbonate Reservoirs: Porosity, Evolution and Diagenesis in a Sequence Stratigraphic Framework*. Elsevier.

Moshier, S.O., Handford, C.R., Scott, R.W. and Boutell, R.D. (1988). Giant gas accumulation in "chalky"-textured micritic limestones, lower cretaceous shuaiba formation, eastern united arab emirates. In A.J. Lomando and P.M.

Harris, eds., *Giant oil and gas fields*, Society of Economic Paleontologists and Mineralogists Core Workshop 12.

Mousavi, M. (2010). *Pore Scale Characterization and Modeling of Two- Phase Flow in Tight Gas Sandstones*. Ph.D. thesis, The University of Texas at Austin.

Mousavi, M.A., Prodanovic, M. and Jacobi, D. (2013). New classification of carbonate rocks for process-based pore-scale modeling. *Society of Petroleum Engineers*.

Mullin, J. (2001). *Crystallization, fourth edition*. Butterworth Heinemann.

Münster, S. and Fabry, B. (2013). A simplified implementation of the bubble analysis of biopolymer network pores. *Biophysical Journal*, **104**, 2774–2775.

Narváez, A., Zauner, T., Raischel, F., Hilfer, R. and Harting, J. (2010). Quantitative analysis of numerical estimates for the permeability of porous media from lattice-Boltzmann simulations. *Journal of Statistical Mechanics: Theory and Experiment*, **2010**, P11026.

Neilson, J.E., Oxtoby, N.H., Simmons, M.D., Simpson, I.R. and Fortunatova, N.K. (1998). The relationship between petroleum emplacement and carbonate reservoir quality: examples from abu dhabi and the amu darya basin. *Marine and Petroleum Geology*, **15**, 57 – 72.

Nelson, P.H. (1994). Permeability-porosity relationships in sedimentary rocks. *Society of Petrophysicists and Well-Log Analysts*.

Oden, J.T., Hawkins, A. and Prudhomme, S. (2010). General Diffuse Interface Theories and an approach to predictive tumor growth modeling. *Mathematical Models and Methods in Applied Sciences*, **20**, 477–517.

O'Hagan, A., Buck, C., Daneshkhah, A., Eiser, J., Garthwaite, P., Jenkinson, D., Oakley, J. and Rakow, T. (2006). *Uncertain Judgements: Eliciting Experts' Probabilities*. Wiley.

Okabe, H. (2004). *Pore-Scale Modelling of Carbonates*. Ph.D. thesis, Imperial College London.

Okabe, H. and Blunt, M.J. (2004). Prediction of permeability for porous media reconstructed using multiple-point statistics. *Physical Review E*, **70**, 066135–.

Okabe, H. and Blunt, M.J. (2007). Pore space reconstruction of vuggy carbonates using microtomography and multiple-point statistics. *Water Resources Research*, **43**, n/a–n/a.

Øren, P. and Bakke, S. (2002). Process based reconstruction of sandstones and prediction of transport properties. *Transport in Porous Media*, **46**.

Øren, P.E. and Bakke, S. (2003). Reconstruction of berea sandstone and pore-scale modelling of wettability effects. *Journal of Petroleum Science and Engineering*, **39**, 177 – 199, reservoir Wettability.

Øren, P.E., Bakke, S. and Arntzen, O.J. (1998). Extending predictive capabilities to network models. *Society of Petroleum Engineers*.

Oyewole, E., Saneifar, M. and Heidari, Z. (2015). Multi-scale characterization of pore structure in carbonate formations: Application to the sacroc unit. *Society of Petrophysicists and Well-Log Analysts*.

Pak, T., Butler, I.B., Geiger, S., van Dijke, M.I.J. and Sorbie, K.S. (2015). Droplet fragmentation: 3d imaging of a previously unidentified pore-scale process during multiphase flow in porous media. *Proceedings of the National Academy of Sciences*, **112**, 1947–1952.

Pan, C., Luo, L.S. and Miller, C.T. (2006). An evaluation of lattice boltzmann schemes for porous medium flow simulation. *Computers and Fluids*, **35**, 898 – 909.

Papadimitriou, C. and Papadioti, D.C. (2013). Component mode synthesis techniques for finite element model updating. *Computers & Structures*, **126**, 15–26.

Papadimitriou, C., Beck, J.L. and Katafygiotis, L.S. (2001). Updating robust reliability using structural test data. *Probabilistic Engineering Mechanics*, **16**, 103–113.

Pastero, L., Costa, E., Alessandria, B., Rubbo, M. and Aquilano, D. (2003). The competition between 1 0 1 4 cleavage and 0 1 1 2 steep rhombohedra in gel grown calcite crystals. *Journal of Crystal Growth*, **247**, 472 – 482.

Patrick A. Domenico, F.W.S. (1997). *Physical and Chemical Hydrogeology*. Wiley, 2nd edn.

Pilotti, M. (1998). Generation of realistic porous media by grains sedimentation. *Transport in Porous Media*, **33**, 257–278, 10.1023/A:1006598029153.

Pyle, D.M., Lu, J., Littlewood, D.J. and Maniatty, A.M. (2013). Effect of 3d grain structure representation in polycrystal simulations. *Comput. Mech.*, **52**, 135–150.

Rabbani, A., Jamshidi, S. and Salehi, S. (2014). An automated simple algorithm for realistic pore network extraction from micro-tomography images. *Journal of Petroleum Science and Engineering*, **123**, 164 – 171, neural network applications to reservoirs: Physics-based models and data models.

Radhakrishnan, B. and Zacharia, T. (1995). Simulation of curvature-driven grain growth by using a modified monte carlo algorithm. *Metallurgical and Materials Transactions A*, **26**, 167–180.

Ramstad, T., Øren, P.E. and Bakke, S. (2010). Simulation of Two-Phase Flow in Reservoir Rocks Using a Lattice Boltzmann Method. *SPE Journal*.

Reiter, C.A. (2005). A local cellular model for snow crystal growth. *Chaos, Solitons & Fractals*, **23**, 1111–1119.

Roberts, A.P. (1997). Statistical reconstruction of three-dimensional porous media from two-dimensional images. *Physical Review E*, **56**, 3203–3212.

Roth, S., Biswal, B., Afshar, G., Held, R.J., Øren, P.E., Inge Berge, L. and Hilfer, R. (2011). Continuum-based rock model of a reservoir dolostone with four orders of magnitude in pore sizes. *AAPG Bulletin*, **95**, 925–940.

Sain, R. (2010). *Numerical Simulation of Pore-Scale Heterogeneity and Its Effects on Elastic, Electrical and Transport Properties*. Ph.D. thesis, Stanford University.

Sayers, C.M. (2008). The elastic properties of carbonates. *The Leading Edge*, **27**, 1020–1024.

Schmoker, J.W. and Halley, R.B. (1982). Carbonate porosity versus depth; a predictable relation for south florida. *AAPG Bulletin*, **66**, 2561–2570.

Scholle, P.A. (1977). Chalk diagenesis and its relation to petroleum exploration; oil from chalks, a modern miracle? *AAPG Bulletin*, **61**, 982–1009.

Scholle, P.A. and Halley, R.B. (1985). Burial diagenesis: out of sight, out of mind! **36**, 309–334.

Schwartz, L.M. and Kimminau, S. (1987). Analysis of electrical conduction in the grain consolidation model. *Geophysics*, **52**, 1402–1411.

Scoffin, T. (1987). *An Introduction to Carbonate Sediments and Rocks*. Blackie.

Seaton, M.A., Anderson, R.L., Metz, S. and Smith, W. (2013). DL_MESO: highly scalable mesoscale simulations. *Molecular Simulation*, **39**, 796–821.

Seiler, A., Aanonsen, S.I., Evensen, G. and Rivenæs, J.C. (2010). Structural surface uncertainty modeling and updating using the ensemble kalman filter. *Society of Petroleum Engineers*.

Silverman, B. (1986). *Density Estimation for Statistics and Data Analysis*. Springer.

Sok, R.M., Knackstedt, M.A., Varslot, T., Ghous, A., Latham, S. and Sheppard, A.P. (2010). Pore scale characterization of carbonates at multiple scales: Integration of micro-ct, bsem, and fibsem. *Society of Petrophysicists and Well-Log Analysts*.

Subbey, S., Christie, M. and Sambridge, M. (2004). Prediction under uncertainty in reservoir modeling. *Journal of Petroleum Science and Engineering*, **44**, 143 – 153, risk Analysis Applied to Petroleum Exploration and Production.

Sukop, M.C. and Thorne, D.T. (2006). *Lattice Boltzmann Modeling, An Introduction for Geoscientists and Engineers*. Springer.

Sun, C., Jain, R. and Munn, L. (2007). Non-uniform plasma leakage affects local hematocrit and blood flow: Implications for inflammation and tumor perfusion. *Annals of Biomedical Engineering*, **35**, 2121–2129.

Sun, S. and Sloan, R. (2003). Quantification of uncertainty in recovery efficiency predictions: Lessons learned from 250 mature carbonate fields. *Society of Petroleum Engineers*.

Thompson, K.E., Willson, C.S. and Zhang, W. (2006). Quantitative computer reconstruction of particulate materials from microtomography images. *Powder Technology*, **163**, 169–182.

Thovert, J.F., Yousefian, F., Spanne, P., Jacquin, C.G. and Adler, P.M. (2001). Grain reconstruction of porous media: Application to a low-porosity fontainebleau sandstone. *Phys. Rev. E*, **63**, 061307.

Tucker, M. and Wright, V. (1990). *Carbonate Sedimentology*. Blackwell Science.

Tucker, M.E. and Bathurst, R.G.C., eds. (2009). *Carbonate Diagenesis*. Blackwell Publishing Ltd.

van der Land, C., Wood, R., Wu, K., van Dijke, M.I., Jiang, Z., Corbett, P.W. and Couples, G. (2013). Modelling the permeability evolution of carbonate rocks. *Marine and Petroleum Geology*, **48**, 1 – 7.

Walker, K., Jernigan, D. and Weber, L. (1990). Petrographic criteria for the recognition of marine, syntaxial overgrowths, and their distribution in geologic time. *Carbonates and Evaporites*, **5**, 141–152.

Wang, Z., Li, Y. and Adams, J.B. (2000). Kinetic lattice monte carlo simulation of facet growth rate. *Surface Science*, **450**, 51–63.

White, J., Borja, R. and Fredrich, J. (2006). Calculating the effective permeability of sandstone with multiscale lattice Boltzmann/finite element simulations. *Acta Geotechnica*, **1**, 195–209.

Wu, K., Nunan, N., Crawford, J., Young, I. and Ritz, K. (2004). An efficient markov chain model for the simulation of heterogeneous soil structure. *Soil Science Society of America Journal*.

Wu, K., Dijke, M.I.J.V., Couples, G.D., Jiang, Z., Ma, J., Sorbie, K.S., Crawford, J., Young, I. and Zhang, X. (2006). 3d stochastic modelling of heterogeneous porous media – applications to reservoir rocks. *Transport in Porous Media*, **65**, 443–467.

Yeong, C.L.Y. and Torquato, S. (1998a). Reconstructing random media. *Physical Review E*, **57**, 495–506.

Yeong, C.L.Y. and Torquato, S. (1998b). Reconstructing random media. II. Three-dimensional media from two-dimensional cuts. *Physical Review E*, **58**, 224–233.

Yuen, K.V. (2010). *Bayesian Methods for Structural Dynamics and Civil Engineering*. Wiley-Vch Verlag.

Zalzale, M. (2014). *Water dynamics in cement paste: insights from lattice Boltzmann modelling*. Ph.D. thesis, École Polytechnique Federeale de Lausanne.

Zhang, M., Ye, G. and van Breugel, K. (2013). Microstructure-based modeling of permeability of cementitious materials using multiple-relaxation-time lattice boltzmann method. *Computational Materials Science*, **68**, 142 – 151.

Zhang, X., Bengough, A.G., Crawford, J.W. and Young, I.M. (2002). A lattice BGK model for advection and anisotropic dispersion equation. *Advances in Water Resources*, **25**, 1 – 8.

Zhang, X., Deeks, L.K., Bengough, A.G., Crawford, J.W. and Young, I.M. (2005). Determination of soil hydraulic conductivity with the lattice Boltzmann method and soil thin-section technique. *Journal of Hydrology*, **306**, 59 – 70.

Zinszner, B. and Pellerin, F.M. (2007). *A geoscientist's guide to petrophysics*. Editions Technip, Paris.

Zou, Q. and He, X. (1997). On pressure and velocity boundary conditions for the lattice boltzmann bgk model. *Physics of Fluids (1994-present)*, **9**, 1591–1598.